Travelling Waves in the Middle Atmosphere

Maria Heloisa Rojas Corradi

Lincoln College

A thesis submitted for the degree of Doctor of Philosophy in the University of Oxford

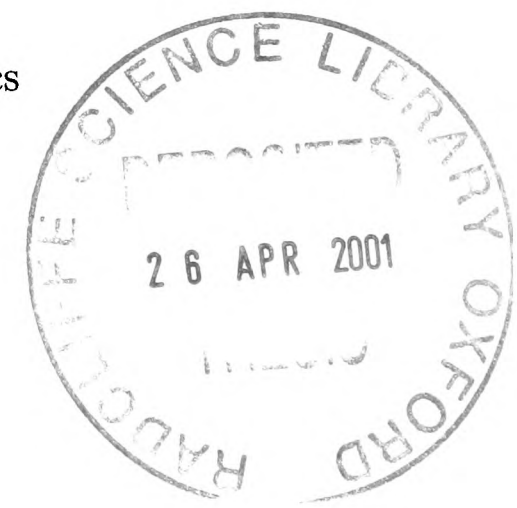
Hilary Term 2000



Atmospheric, Oceanic and Planetary Physics

Department of Physics

University of Oxford



Acknowledgments

First of all I would like to sincerely thank my supervisor Dr. Warwick Norton for tremendous input into this work, lots of encouragement and particularly for his help in finishing this thesis. Thanks for trying to make this thesis readable.

Many thanks go to all the people in MAD group, to Dr. David Andrews for many very interesting discussion about atmospheric Dynamics, thanks to Martin as well. To all the fellow student in the group and in AOPP, in particular many thanks have to go Alan Iwi for too many things, for keeping MADPO running and endless questions about Unix, IDL, Latex, etc....

Thanks to the runners in AOPP (especially to Victoria, my running partner) for trying to keep me fit and distracted! I have had some very good years in AOPP and in Oxford.

Lots of thanks to everybody who proved read parts of this thesis.

But most importantly, I have to thank Simon, my best friend, for thinking that planetary waves are great, and for taking care of me not only during the writing up!

Maisa

To Simon

Planetary Waves in the Middle Atmosphere

Maisa Rojas Corradi

Lincoln College



Atmospheric, Oceanic and Planetary Physics

Department of Physics

University of Oxford

February 28, 2001

Contents

1 Introduction **5**

1.1 The middle atmosphere 6

1.2 Review of planetary waves in the middle atmosphere 10

1.2.1 The quasi 2-day wave 10

1.2.2 The polar winter 4-day wave 12

1.2.3 Other travelling waves, Rossby normal modes 14

1.3 Outline 15

2 Basic atmospheric dynamics **17**

2.1 Governing equations 17

2.1.1 Potential temperature and potential vorticity 19

2.1.2 The geostrophic approximation and thermal wind equation. 20

2.2 Zonal-mean flows 22

2.2.1 Quasi-geostrophic zonal-mean equations 23

2.2.2 The transformed Eulerian mean equations 25

2.2.3 The linearized disturbances to zonal-mean flows 28

2.3 Instability Mechanism 30

2.3.1 Condition for instability 30

2.3.2 Critical lines 33

2.3.3 Barotropic and Baroclinic instability 34

3 Wave spectra in the EUGCM compared with meteor-radar data **37**

3.1 Introduction 37
3.2 EUGCM description 38
3.3 Meteor-radar data 40
3.4 Comparison with meteor-radar data. 40
3.5 Further diagnostics for EUGCM data 48
3.5.1 Winter/Spring months in the EUGCM 49
3.5.1.1 JANUARY 49
3.5.1.2 FEBRUARY 51
3.5.1.3 MARCH 57
3.5.1.4 APRIL 58
3.5.2 Summer months in the EUGCM 61
3.5.2.1 JUNE 61
3.5.2.2 JULY 65
3.5.2.3 AUGUST 70
3.6 Summary of chapter 76

4 Wave spectra in the EUGCM compared with UKMO data 80
4.1 The UKMO Assimilation dataset 81
4.2 UKMO wave spectra 84
4.2.1 1992 data 84
4.2.2 1993 data 88
4.2.3 1996 data 90
4.3 The polar winter 4-day wave in the EUGCM 93
4.4 Summary of chapter 99

5 Linear instability calculation 103
5.1 2-dimensional instability analysis 104
5.2 Results for isothermal atmosphere with no winds 108
5.3 Results for the quasi 2-day wave 109
5.3.1 July background state 109

5.3.2 June background state 111
5.4 Results for the 4-day wave 118
5.4.1 September background state 119
5.4.2 August background state 120
5.5 Calculation of stable modes 124
5.5.1 June background state 127
5.5.2 July background state 128
5.5.3 August background state 129
5.6 Summary of chapter 130

6 SMM runs for the quasi 2-day wave **133**
6.1 Description of the model 134
6.2 Set up of the SMM for quasi 2-day wave experiments 136
6.2.1 Initial balancing run, SMM0 137
6.3 Experiment 1: SMM1, run day 189 138
6.3.1 Period: day 200 - day 224 139
6.3.2 Period: day 224 - day 247 141
6.3.3 Period: day 247 - day 265 144
6.3.4 Changes to the mean flow 147
6.3.5 Growth rates 148
6.3.6 Sensitivity to initial conditions 150
6.4 Experiment 2: runs with Rayleigh friction (SMM2) 151
6.4.1 Inertial instability 156
6.4.2 Kelvin Wave 156
6.5 Experiment 3: runs with radiation 158
6.5.1 SMM3: run with radiation and no Rayleigh friction 158
6.5.2 SMM4: run with radiation and Rayleigh friction 159
6.6 Experiment 4: SMM5, run day 180 162

6.7 Summary of chapter 166

7 SMM runs for the 4-day wave **168**

7.1 Setup of the SMM for 4-day wave experiments 168

7.2 SMM6: day 248 170

7.2.1 Effects on the mean flow 174

7.3 SMM7: day 226 177

7.3.1 Effects on the mean flow 180

7.4 Runs with perturbation at the bottom boundary 183

7.4.1 SMM8: wave 1 perturbation 184

7.4.1.1 Effects on the mean flow 187

7.4.2 SMM9: wave 2 perturbation 190

7.4.2.1 Effects on the mean flow 193

7.5 Summary of chapter 193

8 Conclusions **197**

A Laplace's tidal equation **205**

B List of symbols **214**

C Numerical solution **216**

References **219**

Chapter 1

Introduction

The earth's atmosphere is a thin fluid layer covering our planet. As a fluid, it has the important characteristic of supporting wave motions. It is this aspect of the atmosphere which constitutes the subject of this thesis. In this introduction, some basic definitions about our atmosphere will be introduced.

The earth's atmosphere is conventionally divided into layers based on the vertical gradient of temperature (see Figure 1.1). The first 9-15 km correspond to the troposphere in which temperature decreases with height. The next layer, called the stratosphere where temperature increases, extends from about 9-15 km to 50 km. The mesosphere, from 50 km to about 85 km has decreasing temperatures again. And finally in the thermosphere temperature again increases. The troposphere and the stratosphere are separated by the tropopause, a level of temperature minimum which varies in height from about 15 km at the equator to 9 km at the poles. The level of temperature maxima at about 50 km between the stratosphere and the mesosphere is called the stratopause. Finally the mesosphere is separated from the thermosphere at about 85 km by the mesopause. From the previous definition, atmospheric scientists use the term 'middle atmosphere' to refer to the stratosphere, mesosphere and lower thermosphere, i.e., the atmosphere between the tropopause (10-15 km) and the homopause (110 km)[1].

[1]The homopause divides the atmosphere into the region where the constituents are well mixed, due to eddies, in the lower and middle atmosphere, and the region above the homopause, where molecular

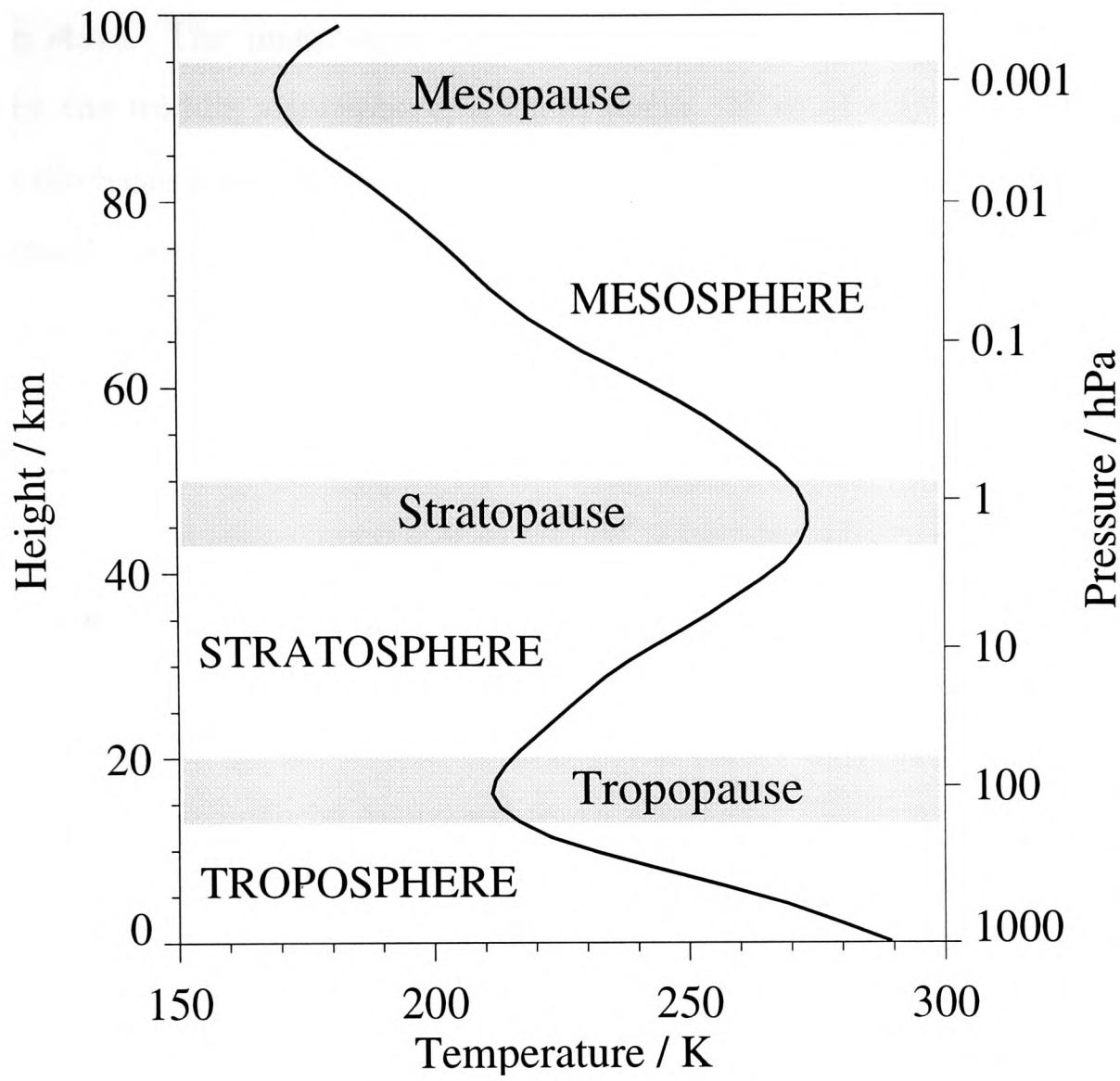


Figure 1.1: A typical midlatitude temperature profile, indicating the levels and names of the different atmospheric layers. Courtesy of D.G. Andrews, from An Introduction to Atmospheric Physics (Cambridge University Press, to appear 2000).

In section 1.1 a few more general remarks about the middle atmosphere are given, followed by a review of waves in the middle atmosphere in section 1.2. This introductory chapter finishes with an outline of the work presented in the rest of the thesis in section 1.3.

1.1 The middle atmosphere

As mentioned above, the earth's atmosphere, being a fluid, has the capability to support different kinds of wave motion. The term 'wave' will be used in this context as the deviation

diffusion begins to dominate over the eddy mixing. Electromagnetic forces play a significant role in the dynamics of the upper atmosphere.

from a mean state. The mean state can be either a temporal mean, or as is used more commonly for the middle atmosphere, a zonal mean. Most of the work presented in this thesis makes the basic assumption that the relevant atmospheric fields - winds, temperature and geopotential- can be represented as a zonal-mean part independent of longitude and small disturbances to this mean, or eddies. This is a reasonable approximation for the middle atmosphere, where the asymmetries to the zonal state induced by land-sea contrast or thermal forcing found in the troposphere are not directly felt. In the middle atmosphere the disturbances to the zonal-mean flow or eddies consist primarily of planetary scale waves which can approximately be described in terms of linear wave dynamics. The observed general circulation of the middle atmosphere is driven by the breaking of these planetary scale waves and the breaking of small-scale gravity waves. This gives rise to a body force on the mean flow (which can be expressed as an Eliassen-Palm flux divergence, see section 2.2.2), which forces the mean meridional circulation. The mean meridional circulation drives temperatures away from radiative equilibrium values, and the radiation responds giving diabatic motion. The large annual change in radiative equilibrium temperatures produces a strong annual cycle in the extratropics. This includes easterlies (westward winds) in the summer hemisphere and westerlies (eastward winds) in the winter hemisphere.

Figure 1.2 shows the meridional cross section of the zonal mean u-wind and zonal mean temperature for January and July taken from CIRA data[2]. From the surface up to 100 hPa the tropospheric subtropical jets can be seen in January and July, the winds are eastward, with larger values found for the winter hemisphere. Above 100 hPa and up to about 0.01 hPa the stratospheric jets can be seen. During winter, the winds are eastwards (westerlies) and in the summer the winds are westwards (easterlies). Although this is true for both hemispheres, some hemispheric differences, especially for the winter months can be noticed. The southern hemisphere winter stratospheric jet in general has larger values than its equivalent northern hemisphere, and also persists for longer throughout the winter. The southern hemisphere winter stratospheric jet has large values until September, whereas the northern hemisphere polar night jet is often weak in January, because of large amplitude

[2]this is climatological data.

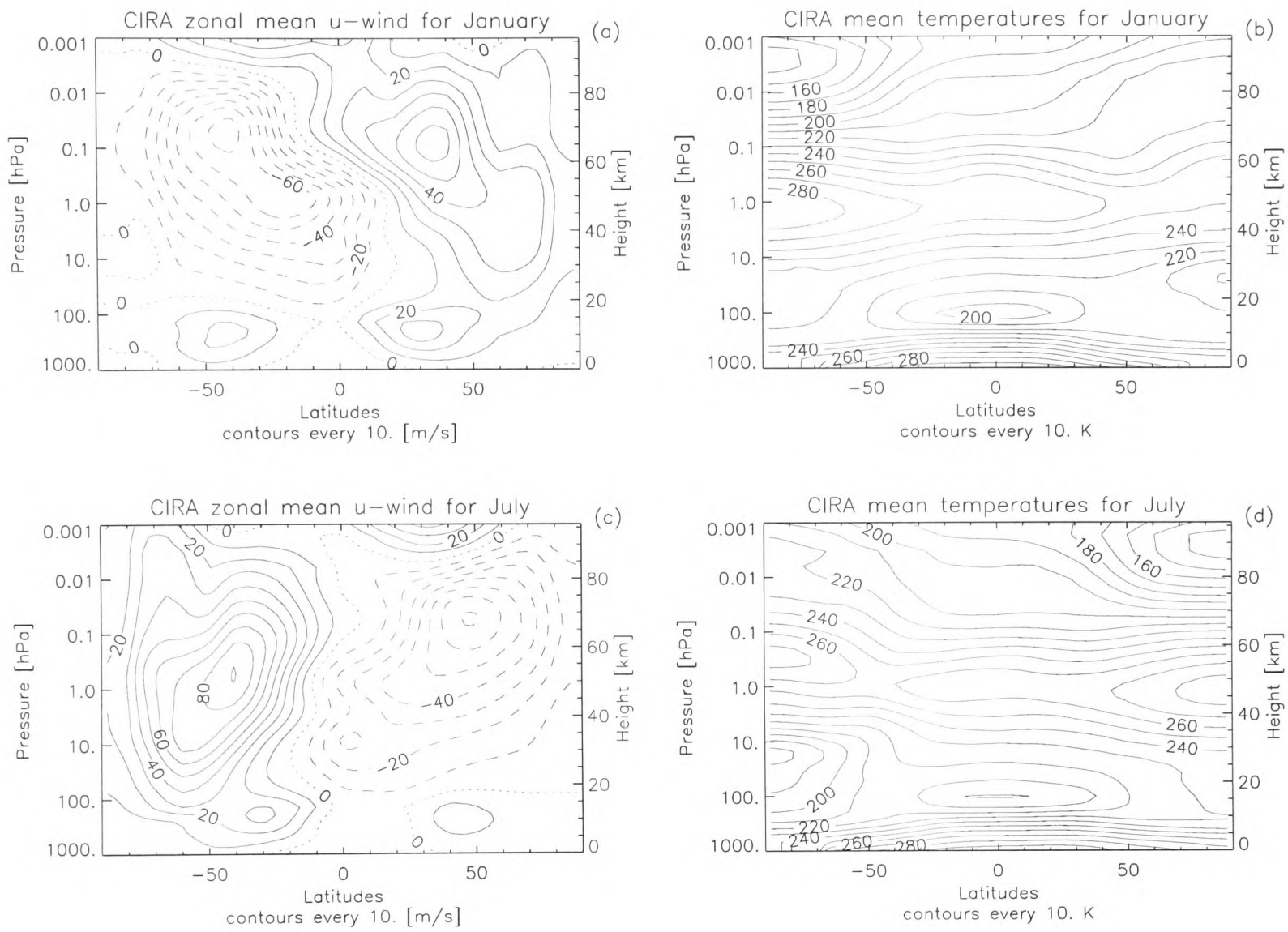


Figure 1.2: (a) CIRA zonal mean u-wind for January, (b) CIRA zonal mean temperature for January. (c) same as (a) but for July, (d) same as (b) but for July.

wave activity associated with stratospheric warmings. Both winter jets show a downward and poleward shift throughout the winter associated with wave driving. But stronger wave driving has been found for the northern hemisphere. In the northern hemisphere, the wave driving is due to both wave 1 and 2 quasi-stationary waves, while in the southern hemisphere eastwards travelling wave 2 is often dominant (e.g. Hirota *et al.*, 1982), until the final warming, when wave 1 dominates (e.g. Lahoz *et al.*, 1995). In the temperature fields differences are found as well, with upper stratospheric temperatures in polar regions higher in the southern hemisphere than in the northern hemisphere, but lower stratosphere polar temperatures colder in the southern hemisphere compared to northern hemisphere (Figures 1.2b and 1.2d).

Large scale waves are recurrent features in the atmosphere and have been of interest to atmospheric physicists from the time of Laplace in his Mécanique Céleste (1799). One property of waves which makes them an important subject of study is that they propagate information without producing a whole displacement of the medium. Due to this property, waves forced in the troposphere can propagate into the stratosphere and mesosphere transporting energy and momentum into the middle atmosphere. There are many classifications of waves, first to distinguish stationary waves from travelling waves. Stationary waves have zero phase speed and remain stationary with respect to longitude. Travelling waves have non-zero phase speeds. Travelling waves can be further classified into free and forced waves. Forced waves, like atmospheric tides, need a continuous forcing mechanism (the sun in the case of tides) whereas free travelling planetary (Rossby) waves, or normal global modes of the atmosphere, are not maintained by travelling forcing effects.

This thesis is centred on studying large-scale travelling waves. Since data from the middle atmosphere have been available, numerous wave-like patterns have been recognized in winds, temperature and other atmospheric fields. In particular the work presented here will examine two travelling planetary waves observed in the middle atmosphere. These are the quasi 2-day wave observed in both hemispheres during the summer months in the upper mesosphere, and the 4-day wave, observed mostly in the southern hemisphere at high latitudes during the winter months in the upper stratosphere/lower mesosphere.

One hypothesis for the origin of these waves is that they arise from an instability of the stratospheric jets, the summer easterly jet for the quasi 2-day wave and the winter westerly jet for the 4-day wave. This hypothesis will be tested in this thesis by examining the patterns of EP flux and their relationship to the potentially unstable regions (indicated by $\bar{q}_y$, see section 2.3.1), as well as the critical lines of the waves. Further evidence is gained by performing a linear instability analysis of the zonal-mean flow and by studying the non-linear evolution of the unstable modes with a mechanistic model. The quasi 2-day wave has also been hypothesized to be a normal mode Rossby wave; evidence for this is carefully examined and characterized. Other normal mode Rossby waves will also be examined as

to their forcing mechanism. The quasi 2-day wave, 4-day wave and normal mode Rossby waves are reviewed in the next section.

1.2 Review of planetary waves in the middle atmosphere

1.2.1 The quasi 2-day wave

The first report of an oscillation with a period of 2 days in the mesosphere was given by Muller (1972) who analyzed wind measurements from a meteor radar at Sheffield in 1968. Apart from the diurnal and semi-diurnal tides, he found an oscillation of 51 hrs during August. Subsequent analysis of meteor winds identified an oscillation with period of approximately 2 days in the northern hemisphere (Clark, 1975; Muller and Kingsley, 1974) as well as in the southern hemisphere (Craig *et al.*, 1980). This wave has been termed the quasi 2-day wave. Use of meteor-radar data from more than one station revealed this wave to be westward propagating with zonal wavenumber 3 (Glass *et al.*, 1975; Muller and Nelson, 1978). Other works have reported this wave to have wavenumber ranging from 2 to 4 (Meek *et al.*, 1996; Tsutsumi *et al.*, 1996). In addition to the large quasi 2-day wave literature in meteor-radar data, the wave has been found in rocketsonde observations (Coy, 1979) as well as with radio wave partial reflection techniques (Stenning *et al.*, 1976). The wave has been recognized as being a large-scale planetary wave, appearing recurrently after the summer solstice at midlatitudes (July and August in the northern hemisphere and January and February in the southern hemisphere). With the satellite coverage of the middle atmosphere in more recent years, the spatial structure of the wave has been further delineated (e.g. Rodgers and Prata, 1981; Wu *et al.*, 1993). The signature is largest in meridional wind, which peaks near the equator (Harris and Vincent, 1993), and both zonal wind and temperature show maxima at midlatitudes with larger values in the summer hemisphere. The wave, although observed in both hemispheres, shows larger amplitude in the southern hemisphere summer (with amplitudes larger by as much as a

factor of two). In the northern hemisphere summer zonal and meridional wind amplitude are about $15\,\mathrm{m\,s^{-1}}$ and $20\,\mathrm{m\,s^{-1}}$ respectively, whereas in the southern hemisphere summer the values are between $20\,\mathrm{m\,s^{-1}}$ and $30\ \mathrm{m\,s^{-1}}$ respectively. At the equator the values are $10\,\mathrm{m\,s^{-1}}$ and $40\,\mathrm{m\,s^{-1}}$ for January/February and somewhat smaller for July/August. The temperature amplitude is found to be between 1-4 K at midlatitudes. The period in the southern hemisphere is found to be about 48 hrs $\pm$ 3 hrs, whereas the period in the northern hemisphere is found more consistently to be 51 hrs. As for the origin of the wave, at first it was thought to be some kind of wave propagating from the troposphere (Muller and Kingsley, 1974) due to its large-scale structure. However this was quickly disregarded[3].

Currently there are two theories for the forcing mechanism of the wave. One theory is that the wave is a manifestation of the third Rossby-gravity normal mode (Salby and Roper, 1980) of a windless and isothermal atmosphere (Laplace's tidal equation, see Appendix A). This (3,0) mode (in Longuet-Higgins (1968) notation[4], zonal wavenumber = 3) has a period of about 52 hrs, and a spatial structure which includes meridional wind with maxima at the equator and zonal wind, and temperature with minima at the equator and maxima at both midlatitudes. The normal mode theory can account for the global structure as well as for the sharply defined peak and repeatability of the period. Since a steady forcing mechanism of this time scale does not exist, it is natural to think of the quasi 2-day wave as a free travelling normal mode. Salby (1981a) uses a linearized primitive equation model with realistic background fields and found a resonant response at 2.25 days for solstice conditions with reasonable structure with enhanced values in the summer mesosphere. Hagan *et al.*, (1993) confirmed these results with a global scale wave model. The fact that the wave's period in the southern hemisphere is often found to be exactly 48 hrs and phase locked with local time, has led to suggestion that the wave is forced by the diurnal tide (e.g Craig and Elford, 1981; Walterschield and Vincent, 1996).

[3]Because the wave is only observed in the summer months, propagation of planetary waves from the troposphere is not possible because of the easterly winds during summer (Charney and Drazin, 1961).

[4]In this notation (k,n-k), k is the zonal wavenumber and n the meridional index. Symmetric and antisymmetric refers to the phase structure with respect to the equator of the zonal wind and temperature. See appendix A for the spatial structure and phase of some Rossby normal modes.

While many aspects of the wave might be explained by a normal mode, other aspects, such as the seasonality and the hemispheric differences, as well as structure indicate that the wave is produced by a baroclinic instability of the summer jet (Plumb, 1983). This second theory accounts for the observed eddy momentum and temperature fluxes and Eliassen-Palm (EP) fluxes associated with the wave, which are quite irreconcilable with the idea of a normal mode (Lieberman, 1999; Fritts *et al.*, 1999). Plumb (1983) performed a 1-dimensional stability analysis with the quasi-geostrophic equations and found a mode with similar characteristics to the quasi 2-day wave. Pfister (1985) extended the analysis to 2 dimensions for one hemisphere. Even though he found unstable modes with the correct wavenumbers and period range, their spatial structure were confined to midlatitudes and high latitudes. Randel (1994) examined global NMC analysis where, in addition to identifying the quasi 2-day wave, the background zonal-mean fields were analyzed. He showed that large amplitude quasi 2-day wave events coincide with periods of negative gradients of potential vorticity (near the stratopause at $\sim$ 1 hPa). This is a necessary condition for instability to occur (see section 2.3.3). These studies (see also Wu *et al.*, 1993) have therefore suggested that the wave is a near-resonant mode forced by an instability, i.e., they propose a combination of the two theories. The question about the forcing mechanism of this wave is still open. As was described above, there are aspects of the wave that agree with it being a normal mode and others that are better explained with the instability theory. In this thesis both the instability and the normal mode hypothesis will be tested, to provide a better understanding of the dynamics of the wave.

1.2.2 The polar winter 4-day wave

A recurrent feature of the polar winter upper stratosphere is an eastward moving wave of zonal wavenumber 1 and a period of around 4 days. The wave was first reported by Venne and Stanford (1979, 1982) when analyzing brightness temperature from satellite measurements. Subsequent studies of satellite measurements as well as radar data found that there are also other wavenumber components present (wavenumbers 2-4), all circulating with same phase speed as a 'warm pool' in temperature around the pole (Prata,

1984; Fraser *et al.*, 1993). The wave is seen in both hemispheres at high latitudes with maximum amplitude at 70°S and 65°N. The spatial structure of the wave is confined to polar latitudes and has a double peak in altitude in temperature (Allen *et al.*, 1997). Larger amplitudes are observed in the southern hemisphere and most of the studies have focused there. The wave shows very small vertical phase tilt, suggesting that the dynamics is mostly barotropic. However equatorwards heat fluxes have been diagnosed for some wave events (Randel and Lait, 1991), implying a baroclinic component of the wave. The horizontal phase structure is variable and both equatorwards and polewards momentum fluxes are found (Venne and Stanford, 1982; Prata, 1984; Manney, 1991).

The theoretical studies upon the forcing mechanism of the wave have focused on barotropic instability of the stratospheric westerly jet. Several modelling studies have performed instability calculations and found unstable modes with similar characteristics to the 4-day wave, including the spatial structure, position of the peak amplitude and the momentum flux (Hartmann, 1983; Manney *et al.*, 1993). Two different regions of instability seem to be important for the growth of the 4-day wave. Hartman (1983) and Manney *et al.*, (1988), showed that episodes of the 4-day wave associated with poleward momentum fluxes are consistent with barotropic instability of the polar night jet, the so called 'polar-modes'. Other episodes, where the momentum fluxes are found to be equatorwards can be associated with barotropic instability of the 'double jet' structure observed in the upper stratosphere and and mesosphere (Manney, 1991; Randel and Lait, 1991), these modes are called 'midlatitude-modes'.

The representation of this wave in a global circulation model (GCM) will be investigated in this thesis, better delineating its spatial structure. Particular attention will be paid to the mesosphere, where few observations have been available. The same method used to study the quasi 2-day wave will be employed to test the instability hypothesis for this wave with a complete 3-dimensional dataset the GCM provides.

1.2.3 Other travelling waves, Rossby normal modes

Since the work of Laplace it is known that the atmosphere, like any other fluid, supports various kinds of wave solutions. Theoretical studies on the solutions of Laplaces's tidal equation extend back two hundred years. But it was not until Rossby *et al.*, (1939) which sought a theoretical explanation to observed eddies in the troposphere, that the solutions were simplified to a straightforward physical principle. The single point of view which provided the solution to the problem was the conservation of potential vorticity, which gave the Rossby wave dispersion relation. Global scale travelling waves have been reported from observations since the 1950's. Work focussed on whether the calculated phase speeds and wavenumber from the observations were consistent with the dispersion relation of Rossby waves. The work on Rossby waves centred mainly around the first three zonal wavenumbers. Madden (1979) presents an extensive tabulation of observational reports of travelling planetary scale wave, with data from a variety of sources over almost 3 decades. Later a survey of planetary scale waves, comprising theory and observations was presented by Salby (1984). From these works, and references therein, the observed wave spectra can be summarized as follows. For zonal wavenumber 1, waves are seen to migrate westward with periods clustering around 5-days and 16-days. A zonal wavenumber 1 wave with period close to 5 days was first reported by Eliassen and Machenhauer (1965), who analyzed northern hemisphere geopotential fluctuations and projected daily streamfunctions at 1000 hPa and 500 hPa onto spherical harmonics. The phase speeds found in those data agreed very well with those obtained from Laplace's tidal equation with a 10 km equivalent depth (Dikki and Golitsyn, 1968), the first symmetric Rossby normal mode, (1,1) in Longuet-Higgins notation. Madden and collaborators worked on the characterization of the global structure of the wave and it was Madden who finally coined it the 5-day wave. The first coherent global scale measurement was presented by Rodgers (1976) who found the (1,1) mode as retrieved from temperature satellite measurements. Further evidence of a 5-day wave in the stratosphere was given in Hirota and Hirooka (1984).

Kubota and Iida (1954) were the first in identifying a zonal wavenumber 1 wave with

wave	zonal wavenumber	phase speed c m s^{-1} at 45°N	first observed by	coined by	identified with mode	observed
5-day wave	k=1	7.7	Eliassen and Machenhauer 1965	Madden	(1,1)	Throughout the year, in general with larger values found in the NH.
10-day wave	k=1	3.9	Hirota and Hirooka 1984	Hirota and Hirooka	(1,2)	Largest amplitudes found for equinox conditions.
16-day wave	k=1	2.4	Kubota and Iida 1954	Madden	(1,3)	Largest values in winter and spring.
4-day wave	k=2	4.8	Eliassen and Machenhauer 1965	Hirota and Hirooka	(2,1)	Throughout the year, in general with larger values found in the NH.

Table 1.1: Table summarizing the main characteristics of observed planetary scale waves.

period close to 16 days. Their observations were later confirmed by other studies, and identified with the second symmetric Rossby normal mode, the (1,3) mode. The wave was coined by Madden (1978) as the 16-day wave, although the period ranges between 11 and 21 days. Eliassen and Machenhauer (1965) also identified the 16-day wave with zonal wavenumber 1. In the same study, a wave with zonal wavenumber 2 was found with period about 4 days.

For zonal wavenumber 2, all the waves found have westward propagation, with periods clustering around 3-7 days. The wave with period 4 days was then identified by Hirota and Hirooka (1981) with the first symmetric Rossby normal mode for k=2, the (2,1) mode and coined by them as the 4-day wave. Hirota and Hirooka (1984) found evidence of a global mode with period between 8-12 days, observed throughout the year but with greater amplitude for equinox conditions. They identified this wave with the second antisymmetric Rossby normal mode for k=1, the (1,2) and coined it the 10-day wave. A summary of all observed Rossby normal modes is presented in table 1.1.

1.3 Outline

A brief introduction of the observed large-scale circulation in the middle atmosphere was presented in section 1.1. Then followed a summary of the work done on travelling planetary waves in the middle atmosphere, which is the main subject of this thesis. Sections 1.2.1 and 1.2.2 discussed the observational and theoretical work done on the quasi 2-day wave and for the polar winter 4-day wave, respectively. These two waves are the main travelling

planetary waves discussed in this thesis. Section 1.2.3 briefly summarized the work on other travelling wave, all identified with Rossby normal modes.

In chapter 2 a resume of the relevant theoretical concepts in atmospheric physics necessary for the understanding of the atmospheric phenomena presented in this thesis are presented. These include the governing equations and a series of approximations leading to the linearized equations of disturbances to zonal-mean flows. The instability mechanisms present in the atmosphere are discussed in this chapter

A large part of the work in this thesis was based on the analysis of data from a GCM. The model used is the UK Universities Global Atmospheric Modelling Programme (UGAMP) GCM, in its extended version (called the EUGCM). In chapters 3 and 4 the wave spectra in the upper stratosphere and mesosphere of a three year run of the EUGCM are analyzed and compared with two different observational datasets. In chapter 3 the EUGCM is compared with a timeseries of meteor-radar data in the northern hemisphere. For the southern hemisphere (and to a small extent the northern hemisphere), the model output is compared with UKMO assimilation data in chapter 4. Here the attention is paid to the southern hemisphere winter 4-day wave. In chapter 5, linear instability calculations are performed for background conditions chosen to represent the middle atmospheric conditions and are solved numerically. Different runs are performed to study the quasi 2-day wave and the 4-day wave. To extend the analysis of the linear instability calculation, chapters 6 and 7 present the results of a mechanistic model used to perform initial value experiments, which allowed the study of the non-linear evolution of the modes found in chapter 5. The model used is the Stratosphere Mesosphere Model (SMM). Chapter 6 describes the runs performed for the quasi 2-day wave and chapter 7 describes the runs performed to study the 4-day wave. Finally in chapter 8 the conclusions of the work are presented and lines of further work are discussed.

Chapter 2

Basic atmospheric dynamics

In this chapter, some fundamental concepts of atmospheric dynamics are reviewed and description is given of some atmospheric phenomena, which are relevant to the work described later in this thesis. Topics covered include the governing equations of the atmosphere under a series of approximations, and instability of zonal-mean flows.

2.1 Governing equations

The earth's atmosphere is a fluid and can therefore be treated as a continuum and hence the Navier-Stokes equation describes atmospheric motions. Together with a continuity equation and a thermodynamic equation they describe the evolution of the atmospheric state. However, the Navier-Stokes equation allows for the whole spectra of atmospheric motions, from small-scale eddies to the large-scale circulation which has scales comparable with the earth dimensions itself. For the purpose of studying large-scale atmospheric dynamics, as is the interest of this thesis, it is therefore necessary to simplify these equations via a scale analysis to arrive to a set of equations which are valid in the spatial scales we are interested in.

Investigating the order of magnitude of the different terms involved in the atmospheric equations, reveals that the atmospheric motion is strongly influenced by gravity and rotation. A detailed scale analysis can then lead to a set of equations valid for large-scale

motions. By neglecting vertical accelerations, the vertical part of the momentum equation can be simplified to the hydrostatic equation. The Coriolis force is an important part of the large-scale dynamics. Scale analysis allows to neglect the horizontal component of the earth's rotation vector, Ω[1]. Under these assumptions, and other minor simplifications we arrive at the so called primitive equations for the atmospheric variables, zonal wind, meridional wind, vertical wind, temperature and geopotential (e.g. Andrews *et al.*, 1987). Using spherical coordinates with longitude and latitude (λ, ϕ) and log-pressure as the vertical coordinate, defined as: $z \equiv -H \log(p/p_s)$ as our vertical coordinate, where p_s is a reference pressure level usually taken as 1000 hPa, the set of primitive equations take the following form:

$$\frac{Du}{Dt} - (f + \frac{u \tan\phi}{a})v + \frac{1}{a\cos\phi}\frac{\partial\Phi}{\partial\lambda} = X, \tag{2.1}$$

$$\frac{Dv}{Dt} + (f + \frac{u \tan\phi}{a})u + \frac{1}{a}\frac{\partial\Phi}{\partial\phi} = Y, \tag{2.2}$$

$$\frac{\partial\Phi}{\partial z} = \frac{RT}{H}, \tag{2.3}$$

$$\frac{1}{a\cos\phi}\frac{\partial u}{\partial\lambda} + \frac{1}{a}\frac{\partial v}{\partial\phi} + \frac{1}{\rho_o}\frac{\partial(\rho_o w)}{\partial z} = 0 \tag{2.4}$$

$$\frac{DT}{Dt} + \frac{\kappa T w}{H} = \frac{J}{c_p}, \tag{2.5}$$

where X and Y represent unresolved physical forces (e.g. friction). All other symbols used are standard, see Appendix B. These equations express, respectively, momentum balance in the zonal and meridional direction, hydrostatic balance in the vertical, mass continuity and the first law of thermodynamics, which relates the change of temperature to diabatic

[1] so that the Coriolis force is calculated as: $-2\Omega(0, 0, \sin\phi) \times (u, v, w)$.

and adiabatic heating. These are a closed set of equations for the relevant atmospheric variables. Further simplification to this set of equations can be performed under various approximations. Before introducing any approximations two new variables will be defined in the next section.

2.1.1 Potential temperature and potential vorticity

The thermodynamic equation (equation 2.5) expresses that the temperature of an air parcel following its motion can only change as a result of vertical motion, leading to heating (cooling) via adiabatic compression (expansion), or as a result of diabatic heating. In the middle atmosphere diabatic processes are small (latent heat or thermal emission), this motivates the introduction of a new variable, the potential temperature θ, which is conserved under an adiabatic process. The potential temperature is defined as the temperature assumed by a system when compressed or expanded adiabatically to a reference pressure p_s =1000 hPa. Mathematically this is expressed in the following way:

$$\theta = T\left(\frac{p_s}{p}\right)^{\kappa}. \tag{2.6}$$

With this definition, the thermodynamic equation (equation 2.5) can be rewritten as:

$$\frac{D\theta}{Dt} = Q, \tag{2.7}$$

where $Q = (J/c_p)e^{\kappa z/H}$.

For a statically stable atmosphere the potential temperature is a monotonically increasing function of height. Therefore it can be used as an independent vertical coordinate instead of pressure or log-pressure.

Another conserved quantity under adiabatic (and frictionless) processes is the *potential vorticity*, or PV, defined as the dot product of the absolute vorticity and the gradient of the potential temperature:

$$PV = \frac{1}{\rho_o}\vec{\zeta}\cdot\nabla\theta, \tag{2.8}$$

here $\vec{\zeta}$ is the absolute vorticity, defined as the vorticity apparent to an observer in an inertial frame of reference[2].

In the stratosphere, where both θ and PV are conserved, maps of potential vorticity on potential temperature levels (isentropic levels, IPV hereafter) show important dynamical features. Isentropic maps of potential vorticity show the large-scale balanced circulation in the atmosphere. Ideas of IPV can also lead to the understanding of Rossby waves and flow instability as will be shown in section 2.3.3.

2.1.2 The geostrophic approximation and thermal wind equation.

A first order approximation of the horizontal momentum equations (equations 2.1 and 2.2) indicates that the Coriolis force is in balance with the pressure gradient force (represented by the geopotential gradient term). Retaining only these two terms leads to the *geostrophic* approximation:

$$u \approx u_g \equiv -\frac{1}{af}\frac{\partial \Phi}{\partial \phi}, \tag{2.9}$$

$$v \approx v_g \equiv \frac{1}{af\cos\phi}\frac{\partial \Phi}{\partial \lambda}. \tag{2.10}$$

These are diagnostic equations, i.e., they give the relation between the geostrophic wind (u_g and v_g) and the geopotential field. The geostrophic balance does not hold in the tropics because f is small there.

Because the geostrophic wind is non-divergent, it is possible to introduce a geostrophic streamfunction Ψ, in cartesian coordinates:

$$(u_g, v_g) \equiv (-\Psi_y, \Psi_x), \tag{2.11}$$

[2]The vertical component of the absolute vorticity is defined as the relative vorticity plus the planetary vorticity, $\zeta = (\nabla \times \vec{U}) \cdot \hat{k} + f$.

where

$$\Psi \equiv \frac{1}{f_o}(\Phi - \Phi_o). \tag{2.12}$$

$\Phi_o(z)$ is a reference geopotential profile. With this definition the potential temperature can also be written in terms of the geostrophic streamfunction:

$$\theta_e \equiv \theta - \theta_o = \frac{H f_o}{R} e^{\kappa z/H} \frac{\partial \Psi}{\partial z}, \tag{2.13}$$

where θ_o is a reference potential temperature profile.

Because the geopotential field is related to the temperature (equation 2.3), the temperature and winds also have to be in balance under the geostrophic approximation. By combining equations 2.9 and 2.10 with equation 2.3, the thermal wind equation is obtained for the zonal and meridional wind, respectively:

$$\frac{\partial u_g}{\partial z} = -\frac{R}{afH} \frac{\partial T}{\partial \phi}, \tag{2.14}$$

$$\frac{\partial v_g}{\partial z} = \frac{R}{afH \cos\phi} \frac{\partial T}{\partial \lambda}. \tag{2.15}$$

These equations state that if there is a horizontal temperature gradient, there must be a vertical wind shear and vice-versa. For example, this relationship can be used to qualitatively explain the observed winter westerlies and summer easterlies in the stratosphere and mesosphere due to the seasonal horizontal temperature gradients (see Figure 1.2). This approximation and balance of forces holds for large-scale motions.

The term 'large-scale' can be quantified by scale analysis. A 'large-scale' motion will be referred to motions that are large enough to feel the influence of the earth rotation. Let a typical lengths scale of the motions be **L** and a velocity **U**, so that the time taken to traverse a distant **L** is **L/U**. If this time is much less than the rotation period of the earth, then the motion is not influenced by the earth rotation and hence is not 'large-scale'. Using this criteria, a motion is considered large-scale if:

$$\frac{L}{U} \geq \frac{1}{\Omega}. \tag{2.16}$$

Or equivalently:

$$R_o \equiv \frac{U}{fL} \leq 1. \tag{2.17}$$

This is a non-dimensional number called the 'Rossby' number, R_o. Motions with small Rossby number are considered in the atmosphere, and in the ocean, to be large-scale motions.

2.2 Zonal-mean flows

As was stated in the introduction, the main assumption used in the analysis of the atmosphere in this thesis is that the atmospheric flow can be divided into a zonally symmetric part and small amplitude longitudinally varying deviations. In this section these ideas will be formalized mathematically and in this way a series of equations will be derived that describe the relations between the zonal-mean flow and the eddies and their time evolution. This will also lead to the framework to discuss ideas about flow instability.

All the atmospheric variables shall be represented as a mean part plus a disturbance to this mean flow, where the disturbance is a small amplitude departure from the mean state. The zonal-mean state is defined as follows:

$$\overline{X}(\phi, z, t) = \frac{1}{2\pi} \int_0^{2\pi} X(\lambda, \phi, z, t) d\lambda, \tag{2.18}$$

so that all the variables might be written as:

$$X(\lambda, \phi, z, t) = \overline{X}(\phi, z, t) + X'(\lambda, \phi, z, t). \tag{2.19}$$

Separating each variable into a zonal-mean part and a disturbance part, and substituting into equations 2.1 –2.5 leads to two sets of equations. In section 2.2.1 the equations for the zonal-mean flow will be obtained, they describe the time evolution of the zonal-mean flow ($\bar{u}$, $\bar{v}$ and $\bar{T}$) in relation to the eddy fluxes. In section 2.2.3 the set of equations will be derived for the linearized disturbances to zonal-mean flows.

2.2.1 Quasi-geostrophic zonal-mean equations

In equations 2.9 and 2.10 the dominant terms in the momentum equations were retained and the geostrophic approximation introduced. Those equations are diagnostic equations and cannot be used to predict the flow evolution. To determine the evolution of the fields some ageostrophic effects must be retained. By doing so, a set of equations is obtained valid for the large-scale motions called the quasi-geostrophic equations. As for the geostrophic approximation, the quasi-geostrophic equations are not valid in the tropics where the Coriolis parameter becomes very small. The assumptions involved in the quasi-geostrophic approximation are therefore that the Rossby number is small, which implies that the motions are slow compared with the earth rotation and therefore the material derivative of the velocity is smaller than the advection due to the Coriolis force[3]. Together with these dynamical approximations, a geometric approximation is also introduced. Geostrophic balance only holds in the extratropics and the horizontal scales are small compared with the earth dimensions. This means that cartesian coordinates (x,y) can be used instead of spherical coordinates, then a Taylor expansion to first order of the Coriolis force can be introduced:

$$f = f_o + \beta y, \tag{2.20}$$

where β is meridional derivative of f. This is called the β-plane approximation.

Let us first separate the horizontal velocity field into geostrophic and ageostrophic parts,

$$u = u_g + u_a, \quad v = v_g + v_a, \tag{2.21}$$

and the vertical velocity is:

$$w = w_a, \tag{2.22}$$

here the assumption is that:

$$|\vec{U_g}| \gg |\vec{U_a}|. \tag{2.23}$$

[3]This is actually another way to define the Rossby number and leads directly to equation 2.17.

Inserting this approximation into equations 2.1, 2.2, 2.3, 2.4 and 2.7, the set of equations describing the quasi-geostrophic flow on a β-plane are obtained (not shown). They consist of a x-momentum equation, a y-momentum equation, a continuity equation and a thermodynamic equation describing the evolution of θ_e, defined in equation 2.13.

Now the Eulerian mean equation from the quasi-geostrophic equations on a β-plane can be obtained. The variables u, v, w and θ are expanded as in equation 2.19, with the definition 2.21 and 2.22 for the winds, and the zonal mean is taken. This leads to the following equations, assuming that $\overline{Q}=\overline{X}=0$[4],

$$\frac{\partial \bar{u}}{\partial t} - f_o \bar{v}_a = -\frac{\partial}{\partial y}\overline{v'u'}, \tag{2.24}$$

$$\frac{\partial \bar{v}_a}{\partial y} + \frac{1}{\rho_o}\frac{\partial}{\partial z}\left(\rho_o \bar{w}_a\right) = 0, \tag{2.25}$$

$$\frac{\partial \bar{\theta}}{\partial t} + \bar{w}_a \frac{\partial \theta_o}{\partial z} = -\frac{\partial}{\partial y}\overline{v'\theta'}. \tag{2.26}$$

These equations describe the time evolution of the quasi-geostrophic zonal-mean flow[5].

Now, by adding the x derivative of the y-momentum equation to minus the y derivative of the x-momentum equation, eliminating the terms involving the vertical velocities, using some identities, end after some manipulation, the quasi-geostrophic potential vorticity equation can be obtained:

$$\left(\frac{\partial}{\partial t} + \bar{u}\frac{\partial}{\partial x}\right) q' + v'\frac{\partial \bar{q}}{\partial y} + \left(v'\frac{\partial q'}{\partial y} + u'\frac{\partial q'}{\partial x}\right) = 0, \tag{2.27}$$

where:

$$q' = \frac{\partial v'}{\partial x} - \frac{\partial u'}{\partial y} + \frac{f_o}{\rho_o}\frac{\partial}{\partial z}\left(\rho_o \frac{\theta'_e}{\theta_{oz}}\right), \tag{2.28}$$

[4]Note that $\bar{v}_g \equiv 0$, so that the zonal-mean geostrophic wind is purely zonal.

[5]Note that the subscript g has been dropped from the geostrophic quantities.

is the perturbation potential vorticity. And

$$\bar{q} = f_o + \beta y - \frac{\partial \bar{u}}{\partial y} + \frac{f_o}{\rho_o}\frac{\partial}{\partial z}\left(\rho_o \frac{\bar{\theta}_e}{\theta_{oz}}\right), \tag{2.29}$$

is the potential vorticity of the basic state.

From these equations it can be seen that the mean flow can be changed by a number of different ways. For example the mean velocity (equation 2.24) may be altered by the mean meridional wind via the Coriolis force, or by the meridional gradient of the zonal-mean eddy momentum flux. If, for example, the flux is divergent (i.e., $\overline{(u'v')}_y > 0$) then more zonal momentum leaves local latitudes than enters and the flow gets decelerated. In a similar way the zonal-mean potential temperature of the flow can be changed by the temperature flux or by small vertical velocities. For example a mean upward motion would tend to lower the mean temperature as air of lower potential temperature is moved upwards. But it is in general not possible to say which of these effects is playing the most important role in a particular situation, i.e., if it is the zonally averaged meridional circulation (terms on the left hand side of the equations) or the eddy forcing (terms on the right hand side of the equations). Hence in the next section the transformed Eulerian mean formulation is introduced.

2.2.2 The transformed Eulerian mean equations

As this thesis deals with waves in the atmosphere it is important to say something about wave-mean flow interaction. It is easy to realize that once the waves have gained large amplitude they might affect the background flow and vice-versa. Work developed by Andrews and McIntyre (1976) and others gives good insight into these problems by introducing the Transformed Eulerian Mean equations or TEM equations (e.g. Pedlosky, 1986).

As was stated above, from the zonal-mean Eulerian mean equations it is not possible to say how the eddy forcing terms and the zonal-mean meridional velocities may act upon the mean flow.

From equations 2.24 and 2.26 it can be seen that no changes to the mean flow (i.e., $\bar{u}_t$=$\bar{\theta}_t$=0) can only occur if:

$$\bar{w}_a = -\frac{1}{\theta_{oz}}\frac{\partial \overline{v'\theta'}}{\partial y}, \tag{2.30}$$

and

$$\bar{v}_a = \frac{1}{f_o}\frac{\partial \overline{v'u'}}{\partial y}. \tag{2.31}$$

By continuity (equation 2.25) this means:

$$\frac{\partial}{\partial y}\left(-\frac{\partial(\rho_o \overline{v'u'}/f_o)}{\partial y} + \frac{\partial(\rho_o \overline{v'\theta'}/\theta_{oz})}{\partial z}\right) = 0. \tag{2.32}$$

If v' vanishes at some latitude it follows that for all y the condition that the mean flow does not change is that:

$$-\frac{\partial(\rho_o \overline{v'u'}/f_o)}{\partial y} + \frac{\partial(\rho_o \overline{v'\theta'}/\theta_{oz})}{\partial z} = 0. \tag{2.33}$$

In other words there should be a balance between the horizontal gradient of the eddy momentum fluxes with the vertical gradient of the eddy temperature fluxes. In general there will be an imbalance and changes to the mean flow will arise. A better way to see this is by calculating the so-called Transformed Eulerian mean equations. This is done by defining the residual meridional mean circulation ($\bar{w}^*$,$\bar{v}^*$): as the difference between the actual vertical and meridional velocity and the portion whose effect on the mean field is cancelled by the eddy effects:

$$\bar{w}^* = \bar{w}_a + \frac{\partial}{\partial y}\frac{\overline{v'\theta'}}{\theta_{oz}}. \tag{2.34}$$

In order that the residual circulation also satisfy the continuity equation (equation 2.25) we define

$$\bar{v}^* = \bar{v}_a - \frac{1}{\rho_o}\frac{\partial}{\partial z}\frac{\rho_o \overline{v'u'}}{f_o}, \tag{2.35}$$

$$= \bar{v}_a - \frac{1}{\rho_o}\frac{\partial}{\partial y}\frac{\rho_o \overline{v'\theta'}}{\theta_{oz}}, \tag{2.36}$$

by using equation 2.33.

Replacing these definitions into equations 2.24 – 2.26 leads to the **transformed Eulerian mean equations** of the quasi-geostrophic form:

$$\frac{\partial \bar{u}}{\partial t} - f_o \bar{v}^* - \bar{X} = \frac{1}{\rho_o} \nabla \cdot \mathbf{F}, \tag{2.37}$$

$$\frac{\partial \bar{\theta}}{\partial t} + \bar{w}^* \theta_{oz} = 0, \tag{2.38}$$

$$\frac{\partial \bar{v}^*}{\partial y} + \frac{1}{\rho_o} \frac{\partial}{\partial z} (\rho_o \bar{w}^*) = 0 \tag{2.39}$$

$$f_o \frac{\partial \bar{u}}{\partial z} + \frac{Re^{-\kappa z/H}}{H} \frac{\partial \bar{\theta}}{\partial y} = 0, \tag{2.40}$$

where

$$\mathbf{F} = (0, -\rho_o \overline{u'v'}, \rho_o f_o \overline{v'\theta'}/\theta_{oz}), \tag{2.41}$$

and

$$\frac{1}{\rho_o} \nabla \cdot \mathbf{F} = -\frac{\partial \overline{v'u'}}{\partial y} + \frac{1}{\rho_o} \frac{\partial}{\partial z} \left(\frac{\rho_o f_o \overline{v'\theta'}}{\theta_{oz}} \right). \tag{2.42}$$

$\mathbf{F}$ is the Eliassen-Palm flux, or EP flux and $\nabla \cdot \mathbf{F}$ the EP flux divergence.

Note that in this set of equations, only in the mean zonal momentum equation (equation 2.38) do eddy terms appear, in the form of the divergence of the Eliassen-Palm flux. The advantage of these equations over the Eulerian mean equations is that, in contrast to the momentum and temperature fluxes, the EP flux divergence depends on certain physical properties of the eddies.

Eliassen and Palm (1961) considered steady, linear waves on a basic zonal flow $\bar{u}(\phi, z)$, with no frictional or diabatic effects (X=Y=Q=0) and using a set of linear equations of disturbances on a β-plane, proved that:

$$\nabla \cdot \mathbf{F} = 0. \tag{2.43}$$

Thus, for linear, steady, conservative waves on a zonal flow, the EP flux divergence vanishes. This theorem was later extended to include spherical geometry, transient waves and X, Y, $Q \neq 0$. The generalized Eliassen-Palm theorem for small amplitude waves takes the form:

$$\frac{\partial \mathbf{A}}{\partial t} + \nabla \cdot \mathbf{F} = \mathbf{D}, \tag{2.44}$$

where $\mathbf{A}$ and $\mathbf{D}$ are mean quadratic functions of disturbances quantities. $\mathbf{D}$ vanishes for conservative waves (it depends on frictional and diabatic effects). $\mathbf{A}$ is called the wave activity. Thus, the time evolution of the wave activity depends on the divergence of the EP flux, and the non-conservative wave effects act as a source or sink of wave activity. In general analytical expressions for these terms are difficult to obtain (e.g. Andrews, 1987). For quasi-geostrophic theory, however, some expressions are found. For quasi-geostrophic theory the wave activity takes the following form:

$$\mathbf{A} = \frac{1}{2}\rho_o \overline{q'^2}/\overline{q}_y. \tag{2.45}$$

If the non-conservative effects are represented by Rayleigh friction and Newtonian cooling (with coefficient γ), then $\mathbf{D}$ is given by:

$$\mathbf{D} = -2\gamma\mathbf{A}. \tag{2.46}$$

If a time mean is now taken (as is done in chapter 3 and chapter 4), so that the first term in equation 2.44 is zero, then the $\nabla \cdot F$ must be produced by non-conservative effects. If, for example, $\nabla \cdot F > 0$ is found in a region where $\overline{q}_y < 0$ then this region is a source of wave activity and vice-versa.

2.2.3 The linearized disturbances to zonal-mean flows

By substituting 2.19 for u, v, w, T and Φ into the primitive equations (equations 2.1-2.5), and assuming that the disturbances or eddies to the zonal-mean quantities are small, so that terms which are of second order in the disturbances can be neglected, the following set of linearized equations for the perturbations are obtained:

$$\frac{\overline{D}u'}{Dt} + \frac{v'}{a}\frac{\partial\overline{u}}{\partial\phi} + w'\frac{\partial\overline{u}}{\partial z} - (f + \frac{\overline{u}tan\phi}{a})v' + \frac{1}{a\cos\phi}\frac{\partial\Phi'}{\partial\lambda} = X', \tag{2.47}$$

$$\frac{\overline{D}v'}{Dt} + (f - \frac{\overline{u}tan\phi}{a})u' + \frac{1}{a}\frac{\partial\Phi'}{\partial\phi} = Y', \tag{2.48}$$

$$\frac{\partial\Phi'}{\partial z} = \frac{RT'}{H}, \tag{2.49}$$

$$\frac{1}{a\cos\phi}\frac{\partial u'}{\partial\lambda} + \frac{1}{a}\frac{\partial v'}{\partial\phi} + \frac{1}{\rho_o}\frac{\partial(\rho_o w')}{\partial z} = 0, \tag{2.50}$$

$$\frac{DT'}{Dt} + \frac{v'}{a}\frac{\partial T}{\partial\phi} + w'\frac{\partial T}{\partial z} + \frac{\kappa w'T}{H} = \frac{J'}{c_p}, \tag{2.51}$$

where

$$\frac{\overline{D}}{Dt} = \frac{\partial}{\partial t} + \frac{\overline{u}}{a\cos\phi}\frac{\partial}{\partial\lambda}, \tag{2.52}$$

and $\bar{v}$=$\bar{w}$=0. This set of linearized equations for the disturbances is still very complicated and can in general only be solved by numerical solutions. Under certain simplifications, analytical solutions to these equations can be found. For example, if disturbances with very small meridional scale are considered, so that the curvature of the earth can be ignored, then the equations can be written in cartesian coordinates and the Coriolis force can be considered constant. If then wave solutions are imposed to the equations, a dispersion relation is obtained corresponding to internal gravity waves. Less simplified, in spherical geometry with $\bar{u}$=$\bar{T}$=0, equations 2.47-2.51 lead to the Laplace tidal equation (see appendix A). This formulation originated with Laplace and has given much insight into atmospheric behavior, in particular in the study of atmospheric tides and global normal modes.

2.3 Instability Mechanism

Atmospheric flow shows aperiodic, or transient fluctuations over a wide range of both spatial and time scales, e.g. from small turbulent eddies at the boundary layer, to tropospheric synoptic scale disturbances, and to planetary scale waves in the mesosphere. The transient fluctuations may arise through instability of the mean flow and in particular from the strong horizontal and vertical shear in the tropospheric and stratospheric jets. The basic state can be regarded as a zonally symmetric state and the instabilities can be associated with asymmetric perturbation to the zonally symmetric basic flow. Although this is an idealization of the true atmospheric state, it has been able to reveal the mechanisms that give rise to the instability processes and is capable of predicting the general character of the observed fluctuations.

In section 2.2.3 the linearized equations for small disturbances to zonal-mean flows were given with a brief description on how solutions can be sought, appendix A gives an example. In both of the cases mentioned (gravity waves and Laplace's tidal equation), the procedure is to look for stable solutions, i.e., assuming a sinusoidal time dependence where the frequency or period of the wave is real. However, the above equations have the possibility to develop instability, i.e., they allow for wave solutions that grow or decay in time. In this case the frequency has an imaginary part as well.

2.3.1 Condition for instability

Analytical analyses of instability (or stability) of realistic zonal wind profiles where $\bar{u}=\bar{u}(y,z)$ are difficult because the horizontal and vertical part of the problem cannot be separated (as is usually done when trying to solve eigenvalue problems). However, progress was made by Charney and Stern (1962), whose theorem provides *necessary conditions* for an instability to occur given a basic zonal mean state and the quasi-geostrophic set of equations on a β-plane.

Following Charney and Stern, the question which is addressed here is whether a

particular background state is unstable or not with respect to small perturbations, or, for a given perturbation, will this tend to grow or decay?

Following their discussion, consider the time evolution of a quantity related to the quasi-geostrophic wave activity: $q'^2/2\bar{q}_y$ (see equation 2.45), assuming that $\bar{q}_y \neq 0$ in the domain of interest.

$$\frac{\partial}{\partial t}\left(\frac{q'^2}{2\bar{q}_y}\right) = \frac{q'}{\bar{q}_y}\frac{\partial q'}{\partial t}, \tag{2.53}$$

because $\bar{q}_t = 0$. Substitute the evolution of the quasi-geostrophic potential vorticity (equation 2.27) into the right hand side of equation 2.53:

$$\frac{\partial}{\partial t}\left(\frac{q'^2}{2\bar{q}_y}\right) = \frac{q'}{\bar{q}_y}(-u\cdot\nabla q' - v'\bar{q}_y) \;=\; -\bar{u}\frac{\partial}{\partial x}\left(\frac{q'^2}{2\bar{q}_y}\right) - v'q', \tag{2.54}$$

using the fact that $\bar{v}$=0. Now the first term on the right hand side is be moved to the left hand side, and the zonal mean is taken:

$$\left(\frac{\partial}{\partial t} + \bar{u}\frac{\partial}{\partial x}\right)\frac{\overline{q'^2}}{2\bar{q}_y} = -\overline{v'q'}, \tag{2.55}$$

$$= -\overline{v'\left(\frac{\partial v'}{\partial x} - \frac{\partial u'}{\partial y} + \frac{1}{\rho_o}\frac{\partial(\theta'_e/\theta_{oz})}{\partial z}\right)}, \tag{2.56}$$

$$= \overline{u'_y v'} - \frac{1}{\rho_o}\overline{v'(\theta'_e/\theta_{oz})_z}, \tag{2.57}$$

$$= \overline{(u'v')}_y - \overline{u'v'_y} - \frac{1}{\rho_o}\overline{(v'(\theta'_e/\theta_{oz}))_z} + \frac{1}{\rho_o}\overline{v'_z\theta'}. \tag{2.58}$$

[6] So, we end up with the following expression:

$$\left(\frac{\partial}{\partial t} + \bar{u}\frac{\partial}{\partial x}\right)\frac{\overline{q'^2}}{2\bar{q}_y} = \nabla\cdot(\overline{u'v'}, -\frac{1}{\rho_o}\overline{v'(\theta'_e/\theta_{oz})}) + \overline{u'u'_x} + \frac{1}{(\rho_o\theta_{oz})^2}\overline{\theta'_e\theta'_{ex}}. \tag{2.59}$$

The last two terms on the rhs are zero. Now apply the divergence theorem to equation

[6] the density factors have been omitted here to shorten the calculation.

2.59:

$$\begin{aligned}\int_V \left(\frac{\partial}{\partial t} + \bar{u}\frac{\partial}{\partial x}\right)\frac{\overline{q'^2}}{2\bar{q}_y}\mathrm{dV} &= \int_V \nabla\cdot(\overline{u'v'}, -\frac{1}{\rho_o}\overline{v'(\theta'_e/\theta_{oz})}\mathrm{dV} \\ &= \int_{boundary}(\overline{u'v'}, -\frac{1}{\rho_o}\overline{v'(\theta'_e/\theta_{oz})})\cdot\hat{n}dA \\ &= 0. \end{aligned} \tag{2.60}$$

Up to now it has been assumed that $\bar{q}_y$ is different from zero all the time. To overcome this restriction, define the perturbation potential vorticity in terms of the northwards displacement η[7]:

$$q' = -\eta'\bar{q}_y, \tag{2.61}$$

with this definition equation 2.60 becomes:

$$\frac{\partial}{\partial t}\int \eta'^2\bar{q}_y dxdy = 0. \tag{2.62}$$

Equation 2.62 states that, if $\bar{q}_y$ is positive everywhere, then η'^2 is bounded, but if $\bar{q}_y$ changes sign somewhere in the domain, then η'^2 can have unbounded growth. Therefore the necessary conditions for an instability to occur is that the meridional gradient of the quasi-geostrophic potential vorticity of the basic flow has to change sign. Because the potential vorticity grows northwards, the meridional gradient is usually positive, therefore the condition is usually fulfilled if there is a region where $\bar{q}_y$ is negative. This is a very powerful theorem; although it does not state whether a basic flow is unstable or not to small perturbation, it states that if there are regions where $\bar{q}_y$ is negative, a potentially unstable region has been found.

There are two basic sources for instability in the basic flow: the vertical shear of the basic flow and the horizontal shear. The presence of vertical shear implies horizontal

[7]eta is defined as follows:

$$\eta'_t + \bar{u}\eta'_x = v'$$

.

temperature gradients and therefore the presence of available potential energy. When the perturbation grows by transforming the available potential energy of the background flow, the instability process is called baroclinic instability. The other source of instability is associated with the horizontal shear of the basic flow, here perturbations are able to extract energy of the basic flow independent of height and therefore this process is called barotropic instability.

2.3.2 Critical lines

In linear wave theory critical lines appear when the phase speed of a wave matches the local zonal mean u-wind.

Consider the potential vorticity equation for linear disturbances, i.e., neglect the last two terms in equation 2.27:

$$\left(\frac{\partial}{\partial t} + \bar{u}\frac{\partial}{\partial x}\right) q' + v'\bar{q}_y = 0, \tag{2.63}$$

where q' is the eddy potential vorticity. Written in terms of the geostrophic streamfunction (by replacing definitions 2.11 and 2.12 into 2.28)

$$q' = \frac{\partial^2 \Psi'}{\partial x^2} + \frac{\partial^2 \Psi'}{\partial y^2} + \frac{1}{\rho_o}\frac{\partial}{\partial z}\left(\rho_o \frac{f_o^2}{N^2(z)}\frac{\partial \Psi'}{\partial z}\right). \tag{2.64}$$

Wave solutions will now be sought of equation 2.63. For simplicity assume that $\bar{u}$= $\bar{u}(z)$ only. The wave solution is in the form of:

$$\Psi' = \hat{\Psi}(z) e^{ik(x-ct)} \sin ly. \tag{2.65}$$

Substitution of equation 2.65 into equation 2.63 leads to:

$$\frac{1}{\rho_o}\frac{\partial}{\partial z}\left(\rho_o \frac{f_o^2}{N^2(z)}\frac{\partial \hat{\Psi}}{\partial z}\right) + \left[\frac{\bar{q}_y}{\bar{u}(z) - c} - (k^2 + l^2)\right]\hat{\Psi} = 0. \tag{2.66}$$

Now, if c is real and $\bar{q}_y \neq 0$, then at a level where $\bar{u}$=c, the coefficient of $\hat{\Psi}$ will be infinite in equation 2.66. This level is called the critical level or critical line of the stable linear wave. The singularity is removed by including wave transience, dissipation or nonlinearity.

Because of all these different factors, to understand what happens at a critical level is not easy. Work on the theory of critical layers show that in these regions wave activity is either reflected or absorbed (e.g. Andrews *et al*, 1987, section 5.6).

If the wave is not stable, i.e., c is complex then something different occurs. In section 2.3.1 the necessary condition for instability to occur was obtained form the linearized potential vorticity equation. If, as above, a wave solution is introduced, then equation 2.60 (without the zonal mean taken) can be rewritten (after considering the appropiate boundary conditions and some integration by part) as:

$$c_i \left(\int \int \bar{q}_y \frac{\rho_o |\Psi|^2}{|\bar{u} - c|^2} dy dz - \int \left[\frac{f_o^2}{N^2} \frac{\rho_o |\Psi|^2}{|\bar{u} - c|^2} \frac{\partial \bar{u}}{\partial z} \right]_{z=0} dy \right) = 0. \tag{2.67}$$

Equation 2.67 is equivalent to equation 2.60. If the wave is stable c_i=0 and the equality holds. If $c_i \neq 0$, i.e., the wave is unstable, and if $\partial\bar{u}/\partial z$ vanishes at the bottom boundary then $\bar{q}_y$ must change sign somewhere in the domain. But equation 2.67 also implies that the critical region can be removed by making $c_i > 0$ in equation 2.67, and therefore also in equation 2.66. When boundaries do not play an important role, amplifying solutions usually have a critical line inside the unstable region (Dickinson, 1973), so that the unstable region acts as a source of wave activity, instead of a sink as occurs for stable waves.

2.3.3 Barotropic and Baroclinic instability

A number of idealized mathematical models of the baroclinic instability problem have been derived, in which most of the models assume quasi-geostrophic theory. The simplest model was derived by Eady (1949), which assumes u independent of y (i.e., u=u(z)) and the meridional derivative of the potential temperature is constant, it also ignores the β effect. Charney's (1947) model of baroclinic instability is similar to Eady's model but retains the β effect.

One way to understand baroclinic instability which does not depend on the constraints imposed by quasi-geostrophic theory is to use a potential vorticity anomaly viewpoint

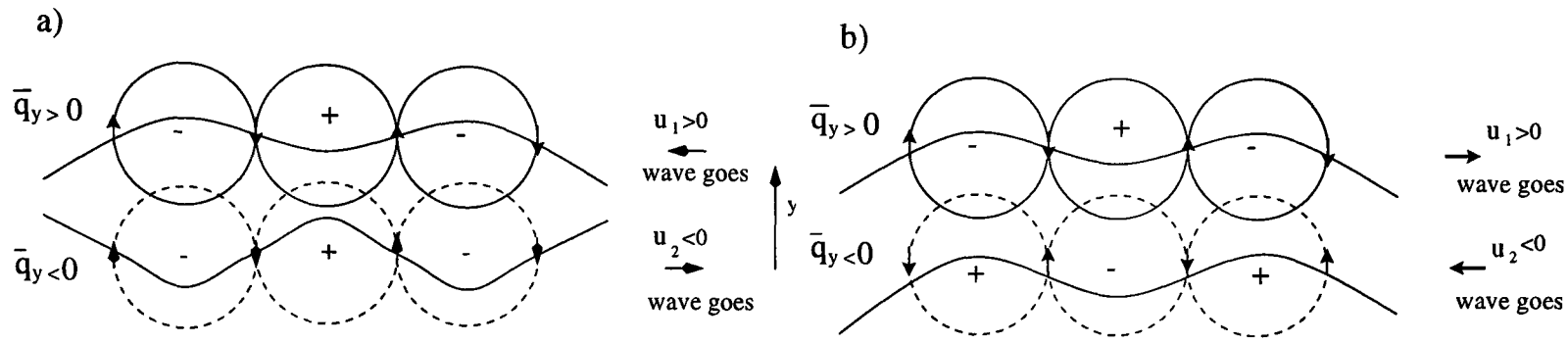


Figure 2.1: (a) PV anomalies representing a westward and a eastward propagating Rossby wave in the northern hemisphere. The waves are out of phase so that their velocity fields add up and reinforce each other. (b) same as in (a) but this time the waves are out of phase, so that they velocity fields oppose each other and they propagation decreases.

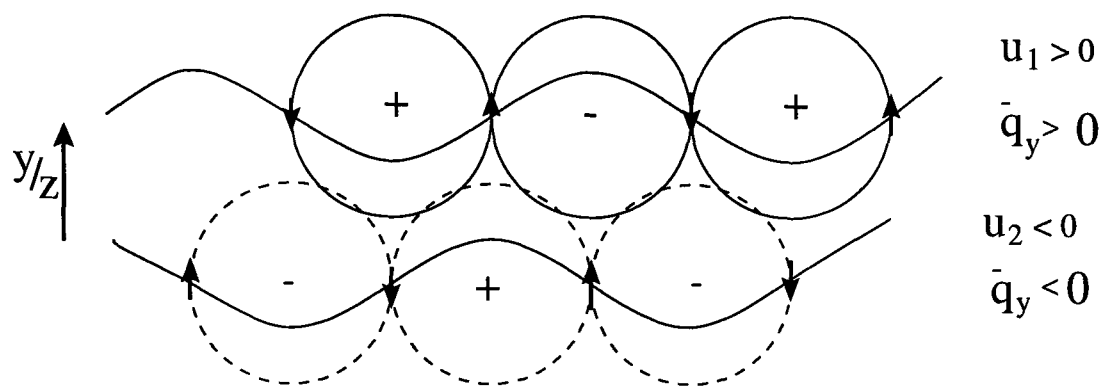


Figure 2.2: Barotropic/Baroclinic instability as seen from PV anomalies for the northen hemisphere.

(Hoskins *et al.*, 1985). The idea here is to think about Rossby waves as potential vorticity anomalies.

In Figure 2.1a the undulating lines represent isopleths of PV anomalies. If PV increases northward (as is usually the case), i.e., $\bar{q}_y > 0$, a northward displacement of a PV isopleth will imply a negative PV anomaly in that region, as indicated by the minus sign in the top part of the figure. A southward displacement will be a positive PV anomaly. This anomaly pattern will induce anticyclonic circulation for the negative PV anomaly and cyclonic circulation for the positive PV anomaly (as indicated by the arrows in the figure). Conversly, if $\bar{q}_y < 0$ (as shown in the bottom part of Figure 2.1a), then a northwards displacement of a PV isopleth will imply a positive PV anomaly, and the induced circulations are reversed as well.

From Figure 2.1a it can be seen that the regions of PV displacement are 90° out of phase with the velocity field. Lets say the wavelength of the anomaly is L, i.e., goes

from the centre minus sign to the next minus sign, then the velocity field is a quarter wavelength out of phase of the displacement field. The maximum northward velocity is located a quarter of wavelength westward of the maximum northward displacement and the same phase relationship is true for the southward velocity and displacements fields. One can picture that this velocity field will advect the PV displacements westward, i.e., a westward propagating Rossby wave. Now consider both PV isopleths, the same arguments can be applied to show that the wave pictured in the lower part of Figure 2.1a propagates eastwards. Now assume a background flow, with $u_1 > 0$ and $u_2 < 0$, so to keep both waves stationary, i.e., the phase speeds $c_1 = c_2 = 0$. Now consider the combined effects of both waves in Figure 2.1a. The displacements of the two waves are completely out of phase and therefore the velocity fields add together and strengthen the wave propagation (i.e., $c_1 < 0$, $c_2 > 0$). On the other hand Figure 2.1b shows waves that are completely in phase and it can be seen that the induced velocity fields oppose each other and the wave propagation decreases (i.e., $c_1 > 0$, $c_2 < 0$). There is a configuration in between these two extremes in which the waves 'phase lock' and will grow in phase, as in Figure 2.2c. Then it can be seen that the velocity field of one wave is in phase with the displacement of the other wave and vice-versa. This configuration will therefore reinforce the displacement of the other wave, and lead to a growing disturbance, i.e., an instability (in this case barotropic instablity). Note, this PV argument does not rely on small amplitude quasi-geostropic approximations.

The waves can also be arranged in the vertical, i.e., consider a region of $\bar{q}_y > 0$ below a region where $\bar{q}_y < 0$. The waves can then be arranged such that the velocity field of one is in phase with the displacement of the other. In this case the instability is called baroclinic instability. This pattern of $\bar{q}_y$ is associated with the vertical shear present in the background flow.

Chapter 3

Wave spectra in the EUGCM compared with meteor-radar data

3.1 Introduction

In this and the following chapter the wave spectra found in a three year run of the Extended UGAMP model (EUGCM) will be examined.

The EUGCM produces a wide range of travelling waves in the upper stratosphere and mesosphere, where the interest of this thesis lies. For validation, the waves in the EUGCM have been compared with two different observational datasets. In this chapter waves in the EUGCM are compared with meteor-radar data taken over Sheffield (53°25'N, 1°35'W). Previous studies of meteor-radar data at this location (e.g. Muller, 1972) have shown strong quasi 2-day wave activity in the summer mesosphere; it is therefore a suitable dataset to study this wave. In chapter 4 the waves in the EUGCM southern hemisphere are compared with UK Met. Office analysis data. Previous studies (e.g. Stanford, 1997) have observed travelling waves (e.g. the 4-day wave) in the upper stratosphere and lower mesosphere in the winter southern hemisphere.

The chapter begins by giving a description of the EUGCM (section 3.2), and of the meteor-radar data (section 3.3). The comparison between model and meteor-radar data (section 3.4) shows generally good agreement. This motivates further diagnostics which

are carried out with the EUGCM data (section 3.5), as to the forcing mechanism of the waves.

3.2 EUGCM description

The UGAMP GCM was developed from the 19 level 'cycle 27' forecast model of the European Centre for Medium Range Weather Forecasts (ECMWF), which had a lid at approximately 30 km. The UGAMP GCM is a spectral model; the variables vorticity, divergence, temperature, moisture and the logarithm of the surface pressure coordinates are represented by truncated series of spherical harmonics. The model runs used in this thesis are at T42, which means a triangular truncation of spherical harmonics at $N{=}M{=}42$, where M is the maximum zonal wavenumber and N is the maximum total wavenumber. This horizontal resolution gives a grid spacing of approximately 3°. The extended version of the UGAMP GCM (EUGCM, hereafter) has 47 levels in the vertical and a model upper lid at about 100 km. Vertical levels are given by hybrid $\sigma - p$ coordinates. Hybrid $\sigma - p$ means that the first few levels are in σ coordinates, which is the pressure normalized to the surface pressure, $\sigma = p/p_s$. In this way the vertical coordinate in the lower troposphere is 'terrain-following'. Then there is a smooth transition to purely pressure levels in the stratosphere. Vertical terms of the equations are calculated using a second order finite-difference scheme (Simmons and Burridge, 1981), with the exception of the vertical advection terms which are given by a 4th order finite difference scheme (Thuburn and McIntyre, 1997). The vertical resolution ranges from 2 km (lower stratosphere) to 3 km (upper mesosphere).

The parameterized processes in the model include large-scale condensation, boundary layer processes, and surface processes, as described by Tiedke *et al.*, 1988. Deep and shallow convection are represented by the adjustment scheme of Betts and Miller (1993). The EUGCM has two separate radiation schemes, Morcette's (1990) for the troposphere and lower stratosphere up to 74 hPa, Shine (1987) and Shine and Rickaby (1989) for above 28 hPa. At intermediate levels the heating rate is given by a weighted mean of the heating rates from the two schemes.

For the representation of the unresolved gravity waves, the EUGCM uses a modified version of the gravity wave scheme of Palmer *et al.*, 1986. This includes sources of stationary gravity waves forced by orography and non-stationary gravity waves (with non-zero phase speeds) which are included as an isotropic, uniform source at every grid-box to crudely represent gravity waves forced by frontal disturbances, convective activity, geostrophic adjustment and shear instability. Note that the waves forced by orography only act below 100 hPa, otherwise it was found they produce too much drag in the stratosphere. For more details on the gravity wave drag scheme see Norton and Thuburn (1997) (NT97, hereafter) and Norton and Thuburn (1999) (NT99).

Norton and Thuburn have worked extensively with the EUGCM and documented their results in a series of articles (NT96, NT97 and NT99). In NT96 initial results of the quasi 2-day wave were presented from a T21 version of the EUGCM. In NT97 the quasi 2-day wave, mesopause temperature and diurnal tide were presented from a T42 version of the EUGCM. In NT99 results were presented from a T21 version of the EUGCM where the upper lid had been extended to approximately 125 km (52 levels in total). In the latter study the importance of the parameterization of the gravity wave drag in getting the observed mean structure and waves in the mesosphere was demonstrated; this included the cold summer mesopause, the realistic structure and strength of the jets and the appearance of important planetary scale travelling waves (like the quasi 2-day wave), as well as the diurnal tide.

In this thesis, a recently completed integration of the EUGCM at T42 with 47 levels is analysed, where 6 hourly output is available for three complete years. This allows a much more thorough analysis of the waves present in the EUGCM (including interannual variability) than was done in NT97. Earlier analysed runs at T21 of the EUGCM do not exhibit the interannual variability found in the T42 run.

3.3 Meteor-radar data

A meteor is a particle from the solar system dust cloud that enters the atmosphere. Heating and ablating due to friction with the atmosphere, produce an ionized trail along its path. Most trails are formed in the height range 75-105 km. Meteor trails are expected to move with the local wind, and therefore act as natural wind tracers. The free electrons in the meteor trail reflect radio waves, and can be detected by radar, providing a means of measuring the radial drift velocity. The radar measurements involve emitting periodic pulses (at 300 Hz in this case) and receiving the Doppler shifted echoes from the meteor trail.

Data taken from the meteor radar at Sheffield (53°25'N, 1°35'W) are used for this work. The data are taken to represent the region above 53°25'N, 3°53'W, the position of the midpoint of the collecting volumes. Although no height finding was used, it is believed that more than 90% of the data come from a height between 85 km and 95 km (Mitchell, 1991). The data were acquired between the 30th of June 1989 and the 6th of October 1994 (Muller *et al.*, 1995).

3.4 Comparison with meteor-radar data.

In this section, 6 hourly data for three complete years of the EUGCM have been compared with the meteor-radar data set obtained and analysed by the University of Aberystwyth. The Aberystwyth data consist of a five year long timeseries of zonal and meridional wind taken every hour by the meteor-radar in Sheffield, i.e., a timeseries at one particular location. The data were kindly provided by G. Beard. Meteor-radar observations have been almost continuous from 1989 until 1994, with some spurious periods in 1989, 1990 and 1994, when data were spoiled by glitches on one of the aerials of the radar. Therefore the years used for the comparison are 1991, 1992 and 1993. For both the EUGCM and the meteor-radar data frequency versus time plots have been calculated to show the waves present. This was done by taking a 32 day window and Fourier transforming it in time,

the window is then moved by one day and the same procedure is applied. This is repeated for the three complete years[1].

Figures 3.1 and 3.3 show the frequency versus time plots of the meteor zonal and meridional wind respectively, Figures 3.2 and 3.4 show the frequency versus time plots of the EUGCM zonal and meridional wind respectively at 54°N, 3°W and 0.003 hPa height (about 90 km). This point corresponds to the nearest grid point to the coordinates at which the meteor-radar data were taken, and therefore provides the best possible comparison.

A first look at the zonal wind spectra, Figures 3.1 and 3.2, and the meridional wind spectra, Figures 3.3 and 3.4, shows remarkable agreement between the meteor-radar and EUGCM data. In both datasets there are periods of strong wave activity in July and August, with frequencies between 0.2 and 0.6 cycles per day, and in January to April, with frequencies less than 0.2 cycles per day. Both meteor-radar data and EUGCM show no wave activity (dark blue colours) of frequencies above 0.2 cycles per day during the equinox months (March/April and October/November).

From Figures 3.1 to 3.4 it is apparent that both the meteor-radar and the EUGCM show interannual variability. The EUGCM shows a somewhat greater spread of frequencies in the June, July and August period (JJA, hereafter), this is especially true for Year 3 (see Figure 3.4c), but the EUGCM also shows a clearer differentiation between the summer months and the winter/equinox months when no wave activity is seen above 0.2 cycles per day. In this sense the interannual variability in the EUGCM is less than in the meteor-radar data. In the meteor-radar data, much less wave activity is found for 1993, while in 1991 more waves, and over a longer period in the summer (from May to September) are found. With respect to the corresponding amplitudes, there is also generally good agreement, perhaps with a tendency for larger amplitude in the EUGCM. Maximum amplitudes for JJA in zonal and meridional wind in the EUGCM reach $17\,\mathrm{m\,s^{-1}}$ and $25\,\mathrm{m\,s^{-1}}$ respectively (this high value corresponds to the quasi 2-day wave in Year 1), whereas maximum amplitudes

[1]To avoid the first few points in the window producing a spurious influence in the Fourier transform (via the Gibbs phenomena), a smoothing to the first 5 and last 5 points was imposed in the following form: the data are multiplied by: $\frac{1}{2}(1-\cos\theta)$, where $\theta = i\pi/5$ for i from 0 to 5.

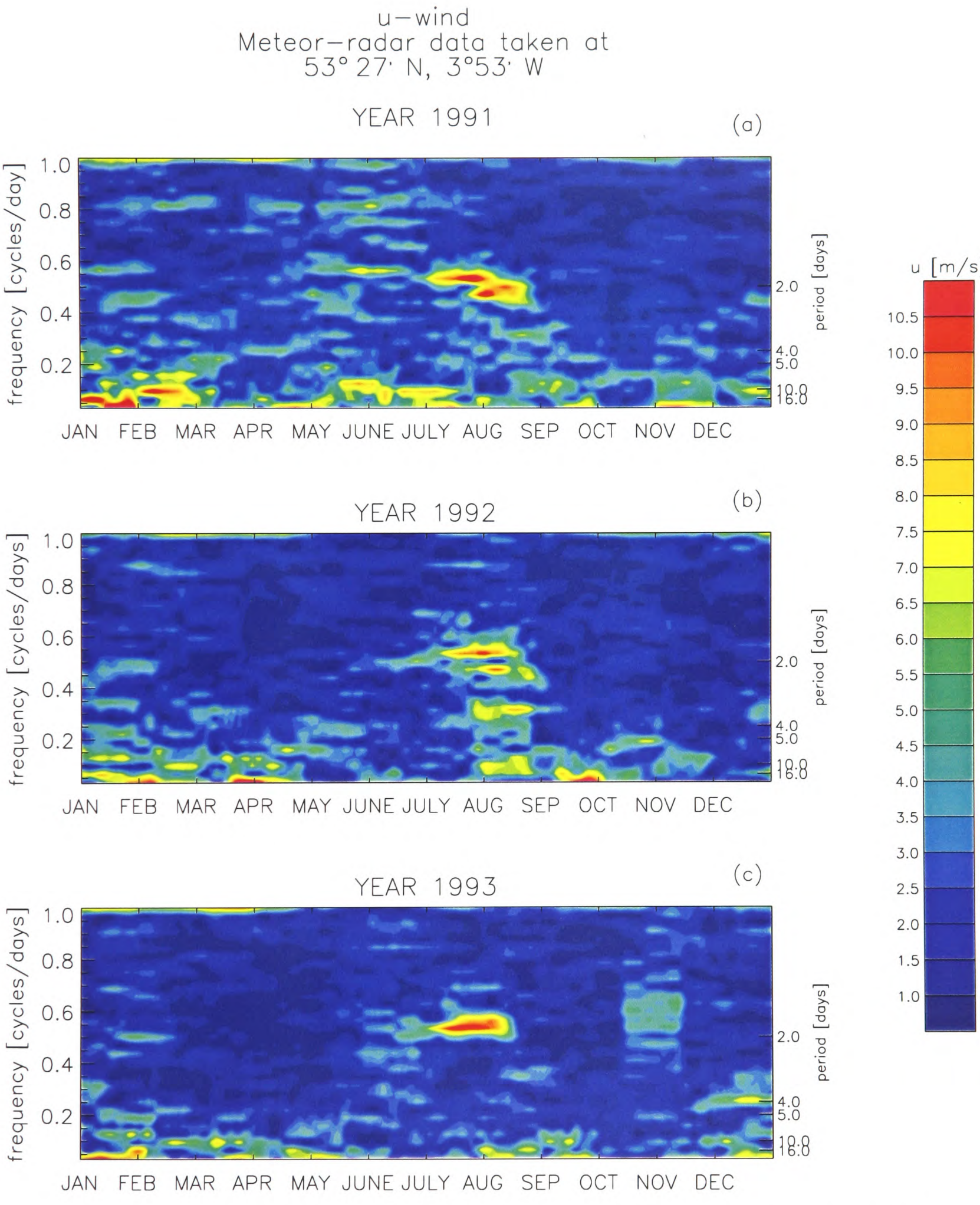


Figure 3.1: Plots of frequency vs time of zonal wind of meteor-radar data for 1991 (a), 1992 (b) and 1993 (c), taken at 53°25′N, 3°53′W and about 90 km of altitude.

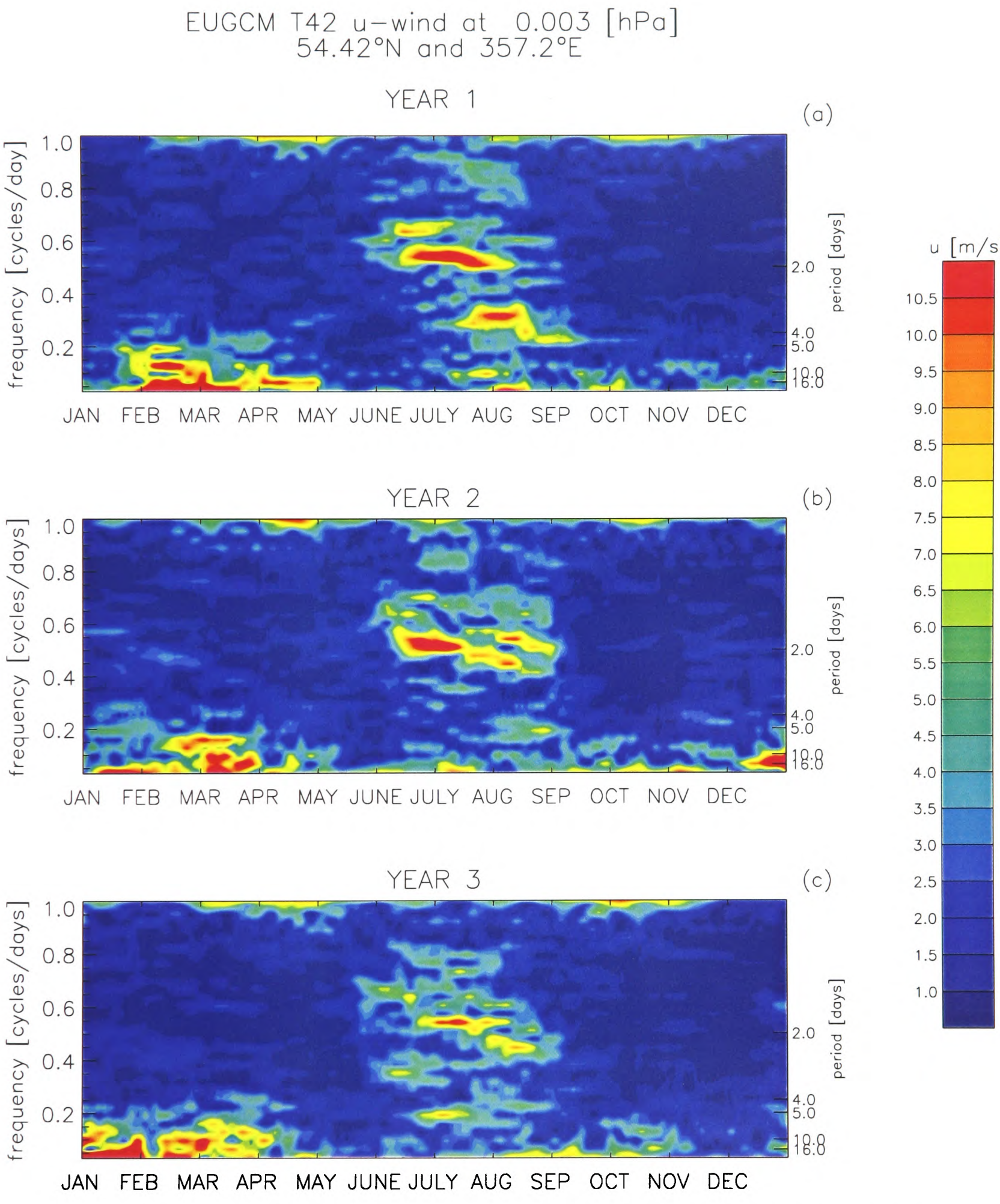


Figure 3.2: Three years of frequency vs time plots of zonal wind from EUGCM integration at 54.4°N and 357.2°E and 0.003 hPa. To compare with Figure 3.1.

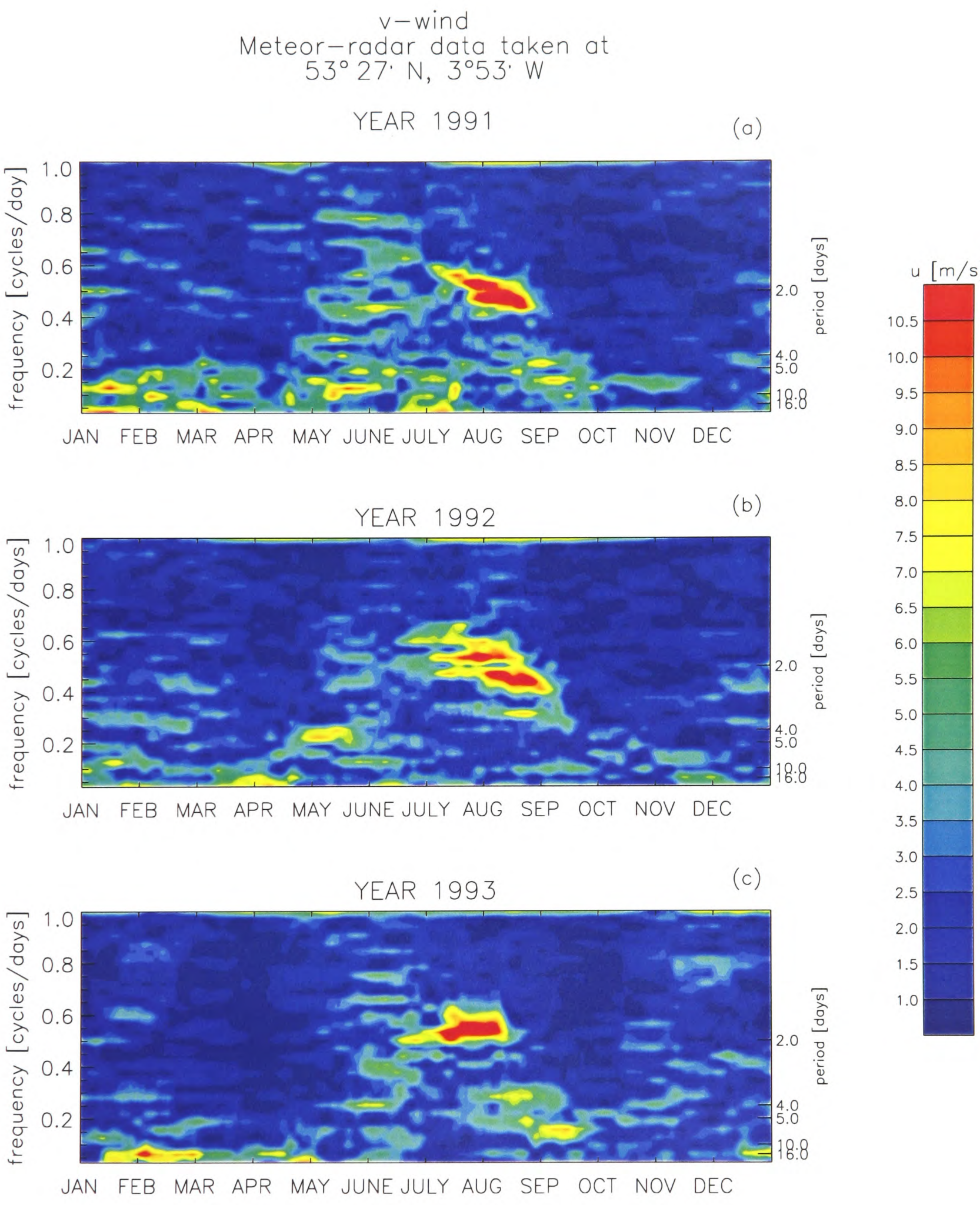


Figure 3.3: Same as figure 3.1 but for meridional mean wind.

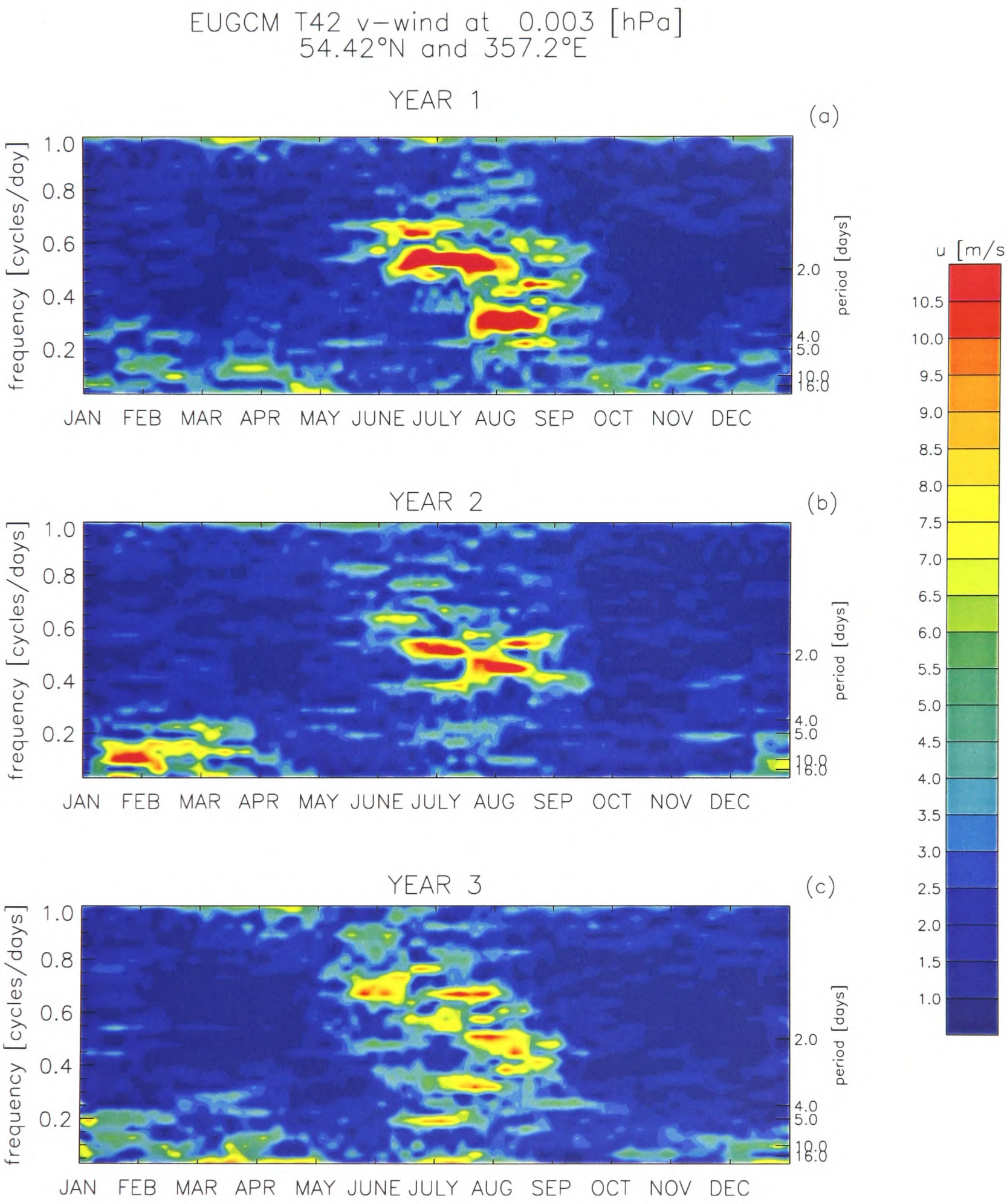


Figure 3.4: Same as figure 3.2 but for meridional mean wind.

in the meteor-radar data are of $13\,\mathrm{m\,s^{-1}}$ and $14\,\mathrm{m\,s^{-1}}$, for zonal wind and meridional wind, respectively. During the winter/spring months meteor-radar data shows maximum wind amplitudes of approximately $14\,\mathrm{m\,s^{-1}}$ for zonal mean wind. The maximum zonal wind amplitude in the EUGCM is about $28\,\mathrm{m\,s^{-1}}$ (the agreement is better for the meridional wind).

In the meteor-radar data the overall pattern during the JJA period starts with waves of frequencies of about 0.6 cycles per day in June, changing to 0.5 cycles per day (the quasi 2-day wave) during July and August, when the wave activity in both data sets is strongest. Then later in August waves with frequencies of 0.3 to 0.2 cycles per day are observed (periods between 3 and 5 days), this pattern can especially be recognized for the years 1991 and 1992 (see Figure 3.3a and 3.3b). This pattern of frequency change with month is also well reproduced by the EUGCM. The strong quasi 2-day wave is seen every year in both datasets, this wave is known from numerous other observational studies to be a recurrent feature of the summer mesosphere (see section 1.2.1). The wave has been reported in the northern hemisphere around July and August (e.g. Muller 1972; Glass *et al.*, 1975) and in the southern hemisphere in January and February (e.g. Craig *et al.*, 1980; Harris and Vincent, 1993). There have been very few studies of the quasi 2-day wave with GCM's (see NT96), in this sense the EUGCM represents an important method for studying the dynamics of the wave. In the meteor-radar data the quasi 2-day wave tends to occur more into August, whereas the EUGCM tends to produce a quasi 2-day wave in July.

The overall pattern in the winter/spring months (December, January, February and March) in the meteor-radar data shows low frequency waves (periods around 10-16 days), which the EUGCM reproduces well, albeit with somewhat larger amplitude (red colours).

There is a marked difference between the winter months and the summer months. During the winter month the wave activity is centered at period between 6 to 16 days, whereas during the summer the periods lie between 1.5 and 5 days. Figure 3.5 shows the timeseries of the zonal mean u-wind, as a function of height, at 54°N (Note that EUGCM years are labelled as 1994, 1995 and 1996). An important difference between winter and summer is the change in the background winds, from westerlies (red colours) to easterlies

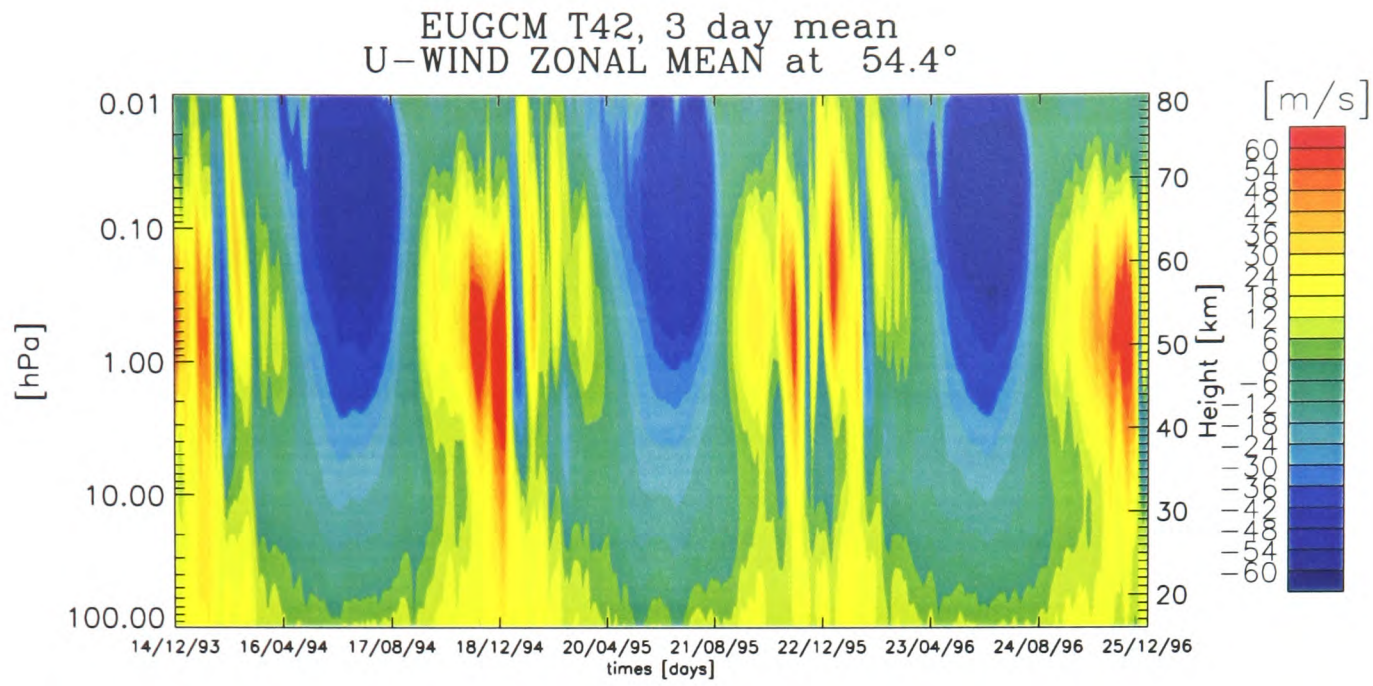


Figure 3.5: Zonal mean u-wind [$\mathrm{m\,s^{-1}}$] at 54°N for the 3 year period of the model integration.

(blue colours) in the stratosphere. In westerlies (winter time) Rossby waves can propagate up from the troposphere through the stratosphere and disturb the mesosphere. This can be seen in Figure 3.6 which shows the timeseries as a function of height of the vertical component (F_z) of the Eliassen-Palm flux (EP flux, see section 2.2.2) at 54°N. It is possible to see how during the winter months there is an increase in F_z in the upper stratosphere as Rossby waves propagate upwards from the troposphere into the stratosphere. In the stratosphere they break producing large variability in the westerlies wind (see red colours in Figure 3.5), including stratospheric warmings. One hypothesis is that the waves seen during the winter are upward propagating Rossby waves from the lower atmosphere. But for the JJA period a different mechanism must operate, since Rossby waves cannot propagate through easterlies.

The good agreement between the two datasets described above gives confidence that the EUGCM produces a good simulation of the observed wave activity of the mesosphere. To further investigate the structure and forcing mechanism of the waves seen, different diagnostics are applied in detail to the 3 year long EUGCM output in the next section.

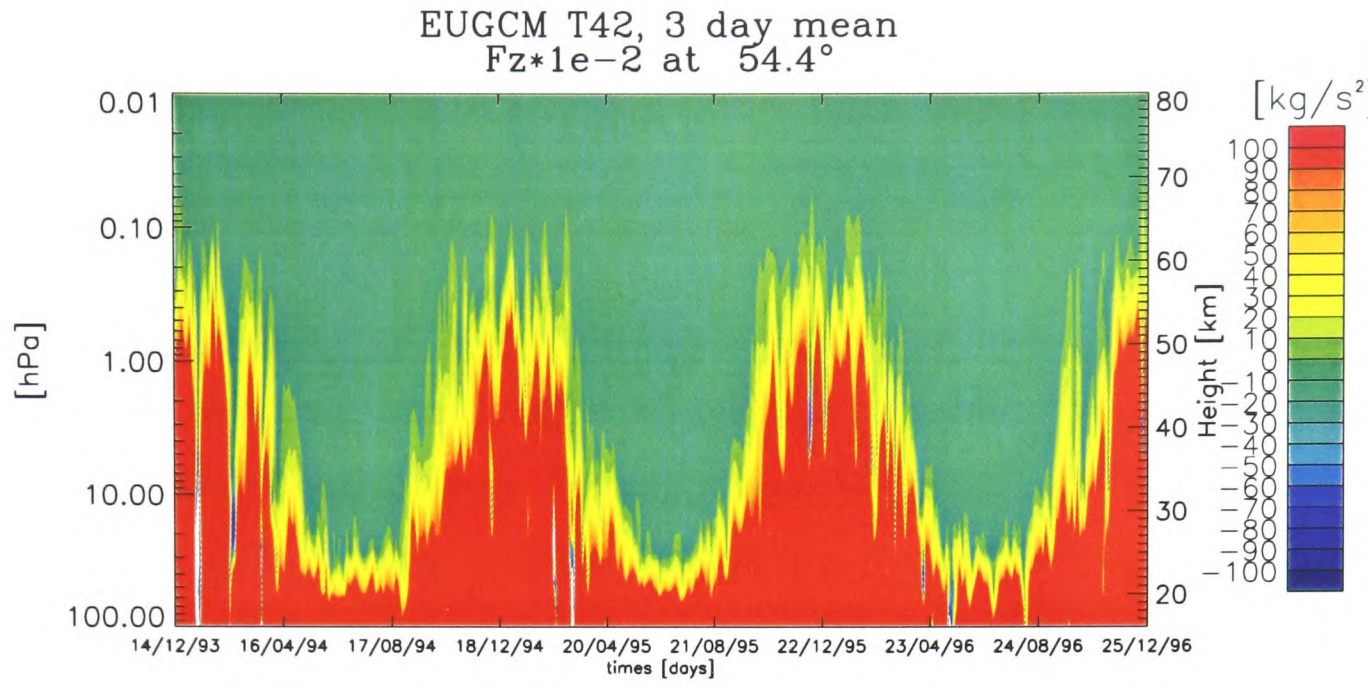


Figure 3.6: F_z $[kg/s^2]$ at 54°N for the 3 year period of the model integration.

3.5 Further diagnostics for EUGCM data

To examine the spatial structure of the waves in the EUGCM data, plots of zonal wavenumber versus frequency are constructed for a 32 day length window, this is done by taking Fourier transforms in time and longitude at 54°N and 0.003 hPa (see Figure 3.7d for example). Information is thus obtained about frequency, zonal wavenumber and direction of propagation (westward or eastward). The latitude-height amplitude and phase of the corresponding harmonics can then be calculated. Typically a wave has large amplitude over a small range of frequencies, as opposed to a well defined single peak. In this thesis, unless otherwise stated, amplitudes are calculated for a single frequency, which has the local maxima in amplitude.

The description which follows will be divided between the winter/spring period and the summer period for the three years of the EUGCM integration, where the most significant peaks in Figures 3.2 and 3.4 will be analysed. For each of the analysed months, plots of zonal mean u-wind and temperature will be produced. Superimposed on the zonal mean u-wind are shaded regions where $\overline{q}_y$ is negative. This indicates the location of potentially unstable regions. In addition, the EP flux components and divergence will be shown for

each month to see where wave activity is produced. Finally a wavenumber-frequency plot will be shown to find the dominant travelling waves for that period.

3.5.1 Winter/Spring months in the EUGCM

In this section the strong wave activity in the winter/spring time will be analysed. This includes January, February, March and April (JFMA, hereafter). No 3-dimensional data are available for December. During the winter months (JFMA) the waves present have periods ranging from 5 or 7 days to 15 or 16 days (e.g. Figure 3.2), i.e., frequencies of less than 0.2 cycles per day[2]. They generally show a similar spatial structure; very 'noisy'[3] in u-wind, 2 peaks in v-wind at very high latitudes. Temperature has a more global structure, with a minimum at the equator and peaks at midlatitudes.

3.5.1.1 JANUARY

Figures 3.7a and 3.7b show the zonal mean u-wind and temperatures for January in Year 1, respectively. The southern hemisphere summer jet is very strong, with values up to -100 $\mathrm{m\,s^{-1}}$ at its core. The shaded regions on the plot represent regions where the meridional gradient of quasi-geostrophic potential vorticity ($\bar{q}_y$) is significantly negative (less than $-1 \times 10^{-11}\mathrm{m^{-1}s^{-1}}$). These regions are seen at the core of the jet and in the northern hemisphere, at polar latitudes above the polar night jet. As was explained in section 2.3.1, $\bar{q}_y < 0$ is a necessary condition for an instability to occur. Figure 3.7c shows in arrows the EP flux and in contours the EP flux divergence. Much stronger wave activity is seen in the winter hemisphere (northern hemisphere on the plot), where arrows point upwards and then equatorwards. Due to the large hemispheric differences, the EP flux for the first 3 levels in the northern hemisphere has been set to zero in Figure 3.7c.

In Figure 3.2a a small amplitude wave with a period of 5 days is apparent in

[2]Because all of the observed waves in the middle atmosphere are named after their period, from here onwards periods of the waves, rather than their frequency, will be used to refer to them. This will be the case even though in plots it is the frequency which is calculated.

[3]Where 'noisy' means a not very coherent spatial structure, as in the case of Figure 3.14a.

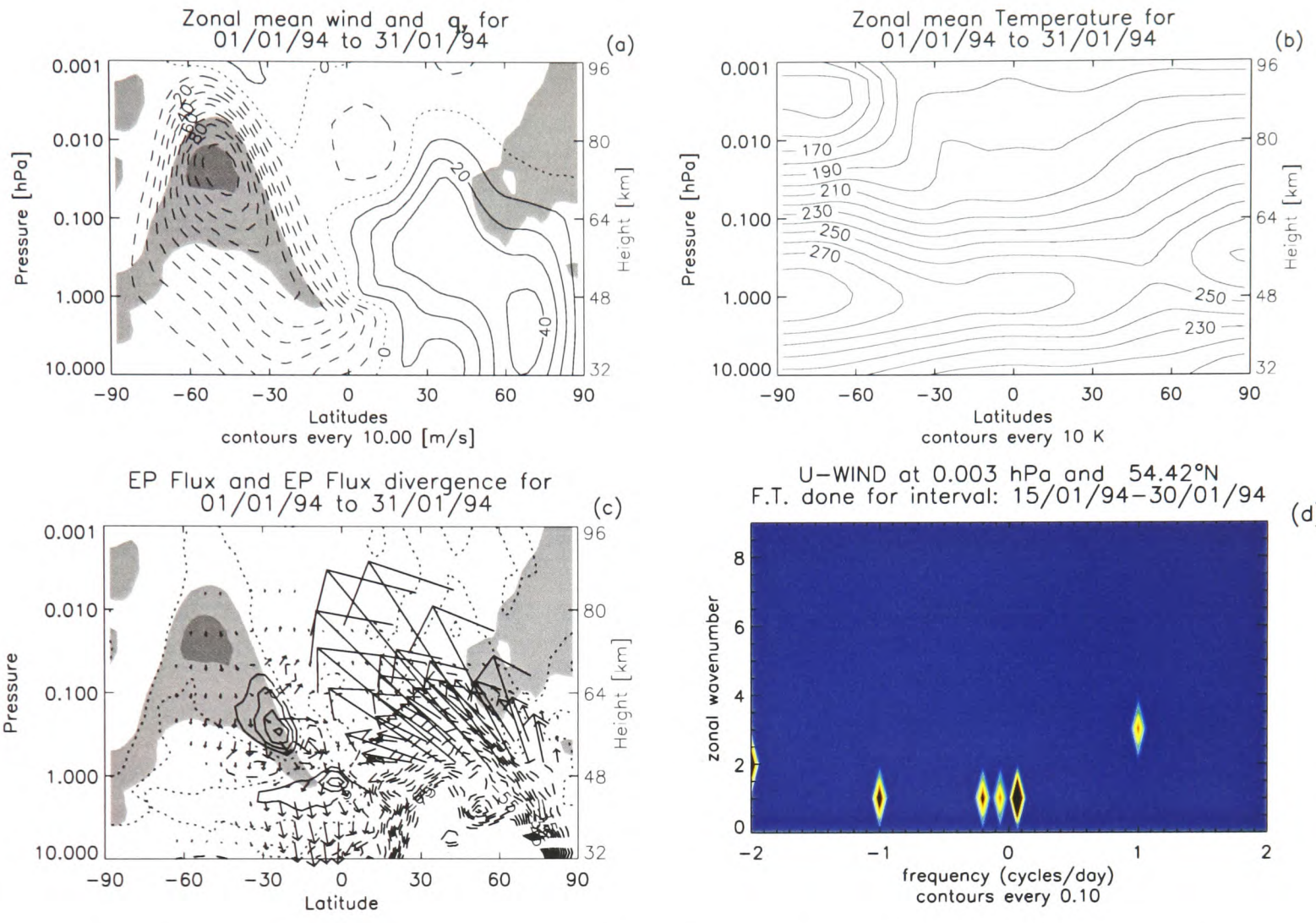


Figure 3.7: (a) Zonal mean u-wind for January Year 1. Shaded regions are where $\overline{q}_y < -1 \times 10^{-11}$ [$\mathrm{m^{-1}s^{-1}}$], with light grey for values between -1 to -5×10^{-11} and dark grey for values less than -5×10^{-11}. (b) zonal mean temperature for the same period. (c) Contours of $\nabla \cdot F$ in units of [$\mathrm{kgm^{-1}s^{-1}day^{-1}}$], arrows of the EP flux for same period. The EP flux for the first 3 levels in the winter hemisphere have been set to zero. (d) zonal wavenumber versus frequency plot of u-wind at 54.4°N and 0.003 hPa.

January/February of Year 1 (labelled as 1994). In Figure 3.7d Fourier transform in time and longitude of u-wind reveals that this 5 day wave is a zonal wavenumber 1 westward propagating wave (negative frequencies in the figure indicate westward propagation). Figure 3.8 shows the spatial structure and temperature phase of the 5-day wave. A 5-day wave has been found in observation (e.g. Rodgers, 1976; Hirota and Hirooka, 1984) and has been identified with the (1,1) Rossby normal mode. In Appendix A the latitude-height structure and phase of a few Rossby normal modes are presented. They have been used to identify the EUGCM waves. From Figure 3.8, it is not entirely clear that the structure pictured there corresponds to a single, global wave. The southern and northern hemisphere amplitudes could correspond to two independent waves. If we believe they

corresponds to one wave, then the structure of the 5-day wave in the EUGCM, although quite distorted, does resemble the gravest Rossby normal mode (1,1) (compare Figure 3.8 with Figure A.1). The bold dot-dashed line in Figure 3.8 is the critical line of the wave, i.e., the phase speed of the wave matches the local background wind at those points. As was explained in section 2.3.2, critical lines are associated with unstable modes, and should not appear for stable Rossby normal modes.

On Figure 3.7d at k=1 there is a bigger peak at frequency around +0.1 cycles per day (period between 7 and 15 days). This is an eastward propagating wave and its structure (not shown) has large amplitudes in the lower stratosphere, northern hemisphere. The EP flux in Figure 3.7c indicates it is an upward propagating planetary wave in the winter hemisphere.

3.5.1.2 FEBRUARY

Figure 3.9a shows the zonal mean u-mean wind for February of Year 1. In the northern hemisphere, winds are very weak and westerly (the polar night jet has disappeared). In the southern hemisphere, the easterly jet wind amplitudes are up to $-60\,\mathrm{m\,s^{-1}}$, less intense than in January. The shading in that plot indicates the region where $\overline{q}_y$ is significantly negative (less than $-1 \times 10^{-11}\mathrm{m^{-1}s^{-1}}$), a region potentially unstable. The region is at the core of the southern hemisphere easterly jet and is smaller than in January.

The zonal wavenumber-frequency spectra calculated from meridional wind during February (Figure 3.9d) reveals the presence of two other waves apart from the 5-day wave already discussed for January (and the beginning of February). These are a zonal wavenumber 2 (k=2) westward propagating wave with period around 4 days and a zonal wavenumber 1 (k=1) westward propagating wave with period around 7 days. The amplitude of the 4-day wave is shown in Figure 3.10, the bold dot-dashed contour on the figures represents the critical line for that wave, i.e., regions where the phase speed matches the mean wind. Figure 3.10a shows the zonal wind amplitude and Figure 3.10b the meridional wind amplitude, Figure 3.10c shows temperature amplitude and Figure 3.10d the temperature phase. The temperature structure is approximately

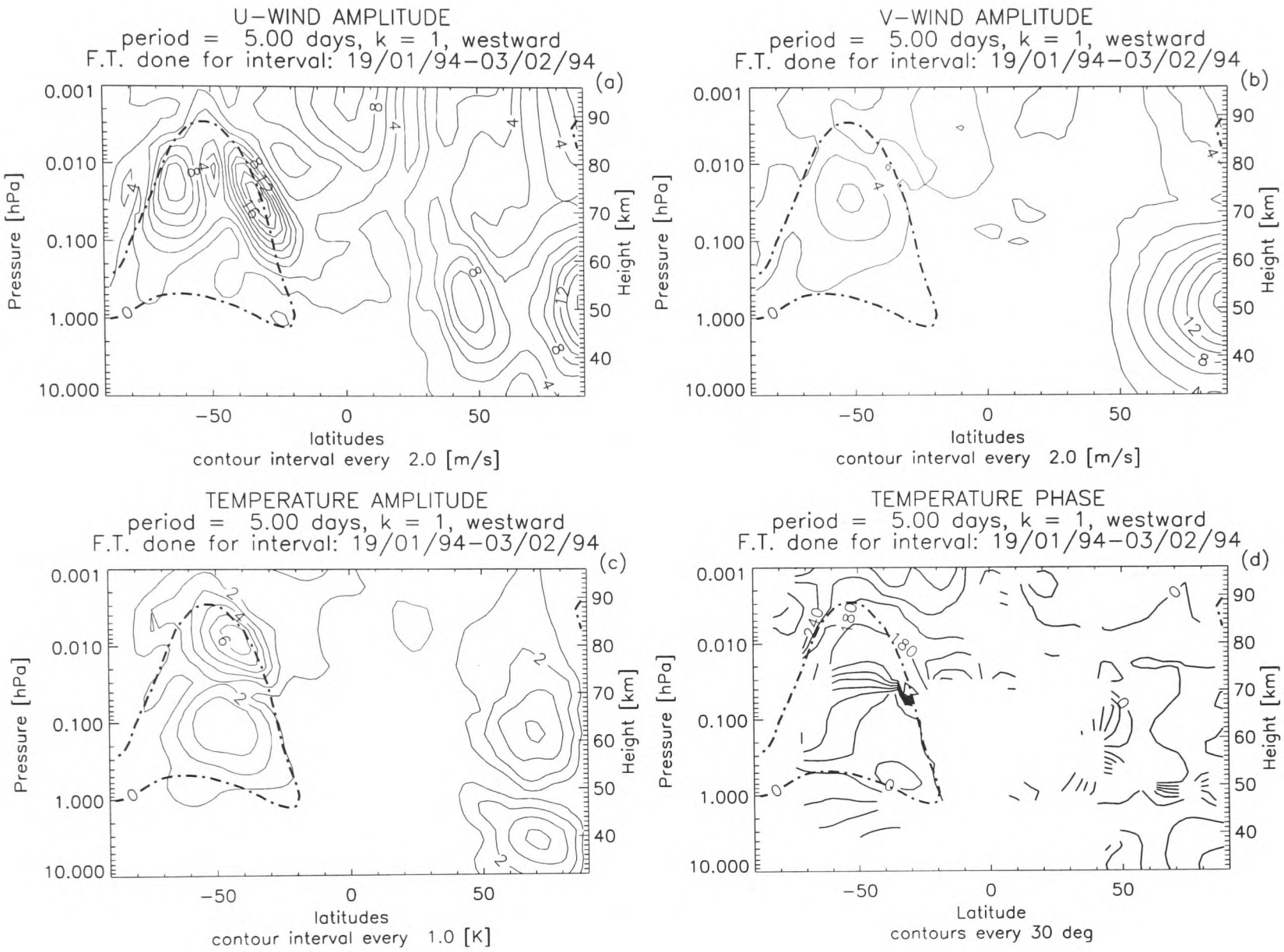


Figure 3.8: (a) u-wind amplitude of the westward propagating 5-day wave during January of Year 1. The bold dot-dashed line is the critical line for this wave ($u-c=0$). (b) v-wind amplitude, (c) temperature amplitude and (d) temperature phase.

symmetric about the equator, with enhanced amplitude in the summer hemisphere. These characteristics agree well with the 4-day wave proposed by Hirota and Hirooka (1984). They identify the 4-day wave with the (2,1) Rossby normal mode (compare with the (2,1) mode in Figure A.4). This wave should not be confused with the polar winter 4-day wave described in the section 1.2.2. The wave in Figure 3.10 will be refered to as the 'normal mode 4-day wave'. Some characteristics of the normal mode 4-day wave and the 5-day wave in the model agree with theoretical results for normal modes modified by realistic background flows (Salby, 1981b), e.g. the vertical phase tilt is increased in the presence of easterlies and veers towards the critical region (see Figures 3.8d and 3.10d). The presence of easterlies in solstice conditions gives the potential for critical regions,

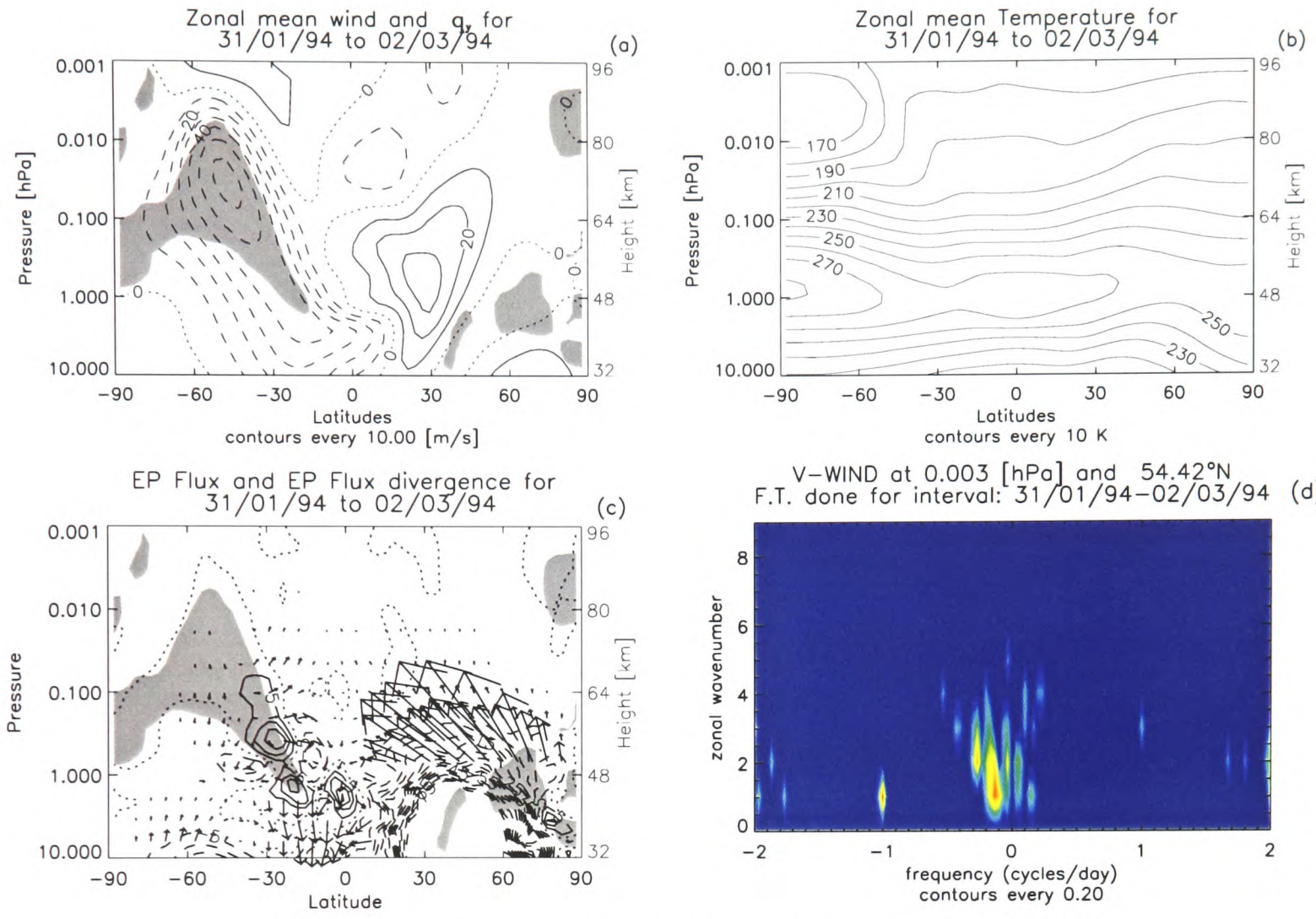


Figure 3.9: (a) Zonal mean u-wind for February Year 1. Shaded regions are where $\overline{q}_y < -1 \times 10^{-11}$ [$\mathrm{m^{-1}s^{-1}}$], with grey for values between -1 to -5×10^{-11}. (b) zonal mean temperature for the same period. (c) Contours of $\nabla \cdot F$ in units of [$\mathrm{kgm^{-1}s^{-1}day^{-1}}$], arrows of the EP flux for same period. The EP flux for the first 3 levels in the winter hemisphere have been set to zero.(d) zonal wavenumber versus frequency plot of v-wind at 54.4°N and 0.003 hPa.

as indicated by the bold dot-dashed line in the Figures. Salby (1981b) finds that the amplitude of normal modes should decay in this region. This is not the case for either the 5-day wave nor the normal mode 4-day wave, their amplitude is actually largest in the critical region (Figures 3.8c and 3.10c). Notice that the region of large 4-day wave u-wind amplitude coincides with the region where $\overline{q}_y$ is negative (see Figure 3.9a and Figure 3.10a).

Year 2 (1995) exhibits a normal mode 4-day wave again. The wave has a period between 3.7 and 4.3 days with k=2 (figure not shown). As in Year 1 (1994) this wave is identified with the first symmetric (2,1) Rossby normal mode for zonal wavenumber 2 (the 'normal mode 4-day wave'). The mode is global, symmetric about the equator with larger amplitude

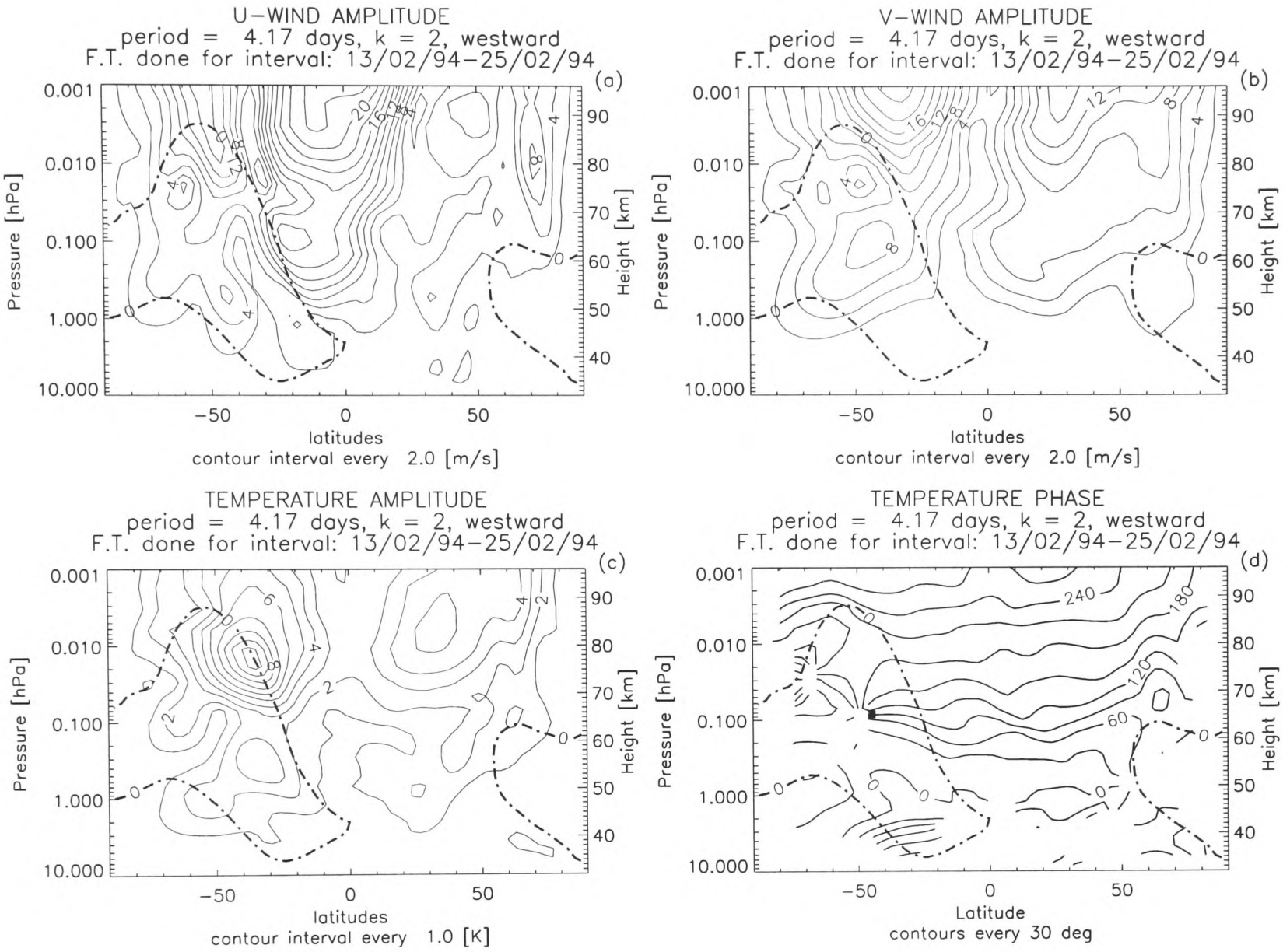


Figure 3.10: (a) u-wind amplitude of the westward propagating 4-day wave during February year 1. The bold dot-dashed line is the critical line for this wave ($u-c=0$). (b) v-wind amplitude, (c) temperature amplitude and (d) temperature phase.

in the summer hemisphere (i.e., southern hemisphere). The wave has a critical line due to the summer easterlies over a large region of the southern hemisphere, the amplitude is enhanced just above this region and the phase lines veer towards the critical region. But again the normal mode 4-day wave in the EUGCM has large amplitude within the critical region (especially in u-wind and temperature, as in Figures 3.10a and 3.10c), this does not agree with the apparent observed reduction in amplitude in critical regions for normal modes (Hirooka, 1999).

As mentioned before, during February of Year 1 (1994), Figure 3.9d shows a peak at frequency -0.12 and k=1. This is a westward propagating wave with period between 6 and 8 days. In Figure 3.11 the amplitude of the winds and temperature, and the phase

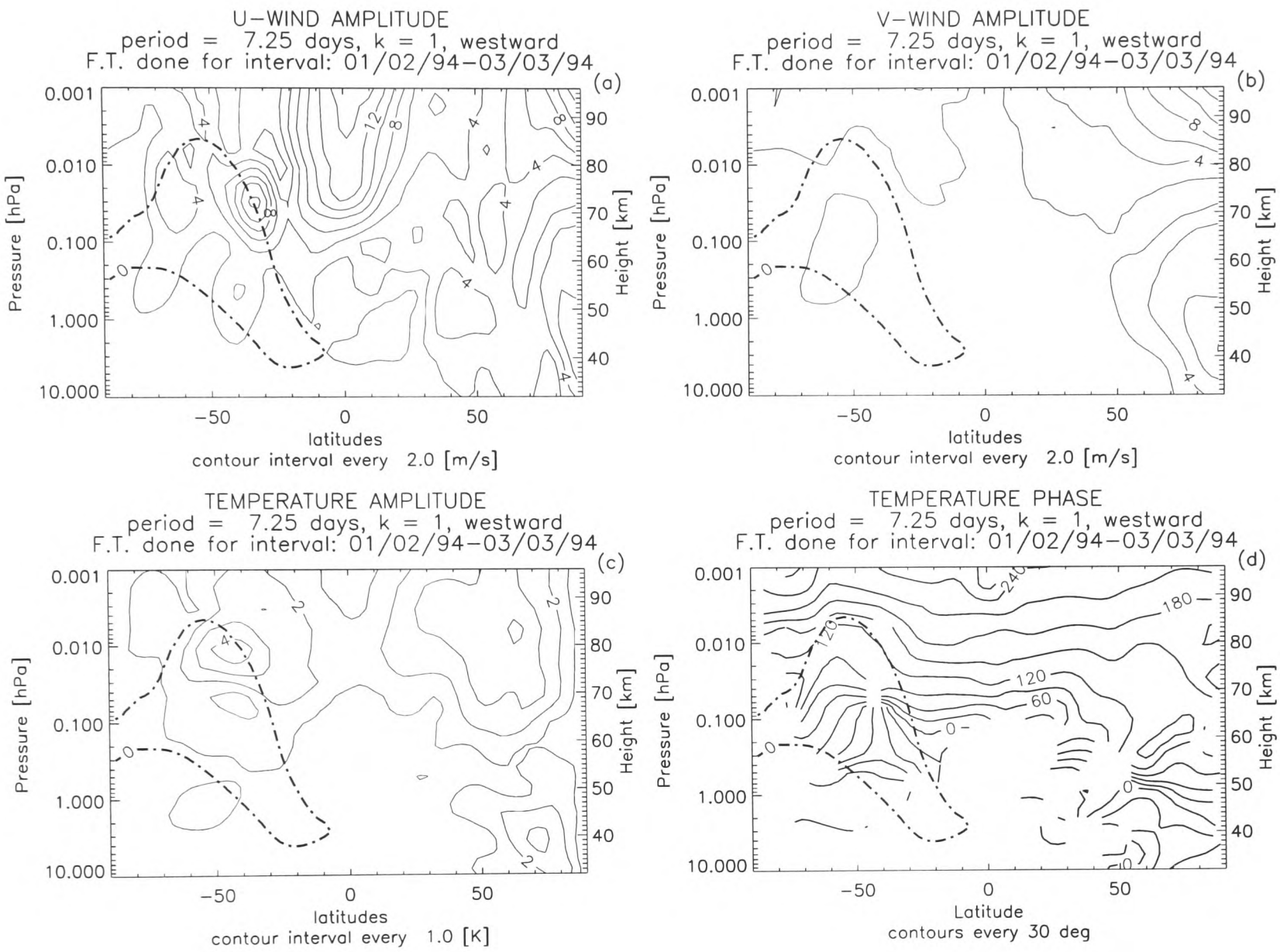


Figure 3.11: (a) u-wind amplitude of the westward propagating 7.25 day wave during February Year 1. The bold dot-dashed line is the critical line for this wave ($u - c = 0$). (b) v-wind amplitude, (c) temperature amplitude and (d) temperature phase.

of the temperature are shown at period 7.25 days. The most coherent structure for zonal wind is found at this period, although temperature and meridional wind have a coherent structure all through the periods between 6 days and 8 days. Overall the wave's spatial structure is similar to the 5-day wave. The zonal wind (Figure 3.11a) has a maximum at the equator, the meridional wind component (Figure 3.11b) has large amplitude at high latitudes northern hemisphere, with 2 maxima at 50 km and 90 km. Temperature amplitude (Figure 3.11c) peaks on both sides of the equator with large amplitude at about 80 km height in both hemispheres and the phase structure symmetric about the equator. Plotted on the same Figure is the line where the phase speed of the wave matches the

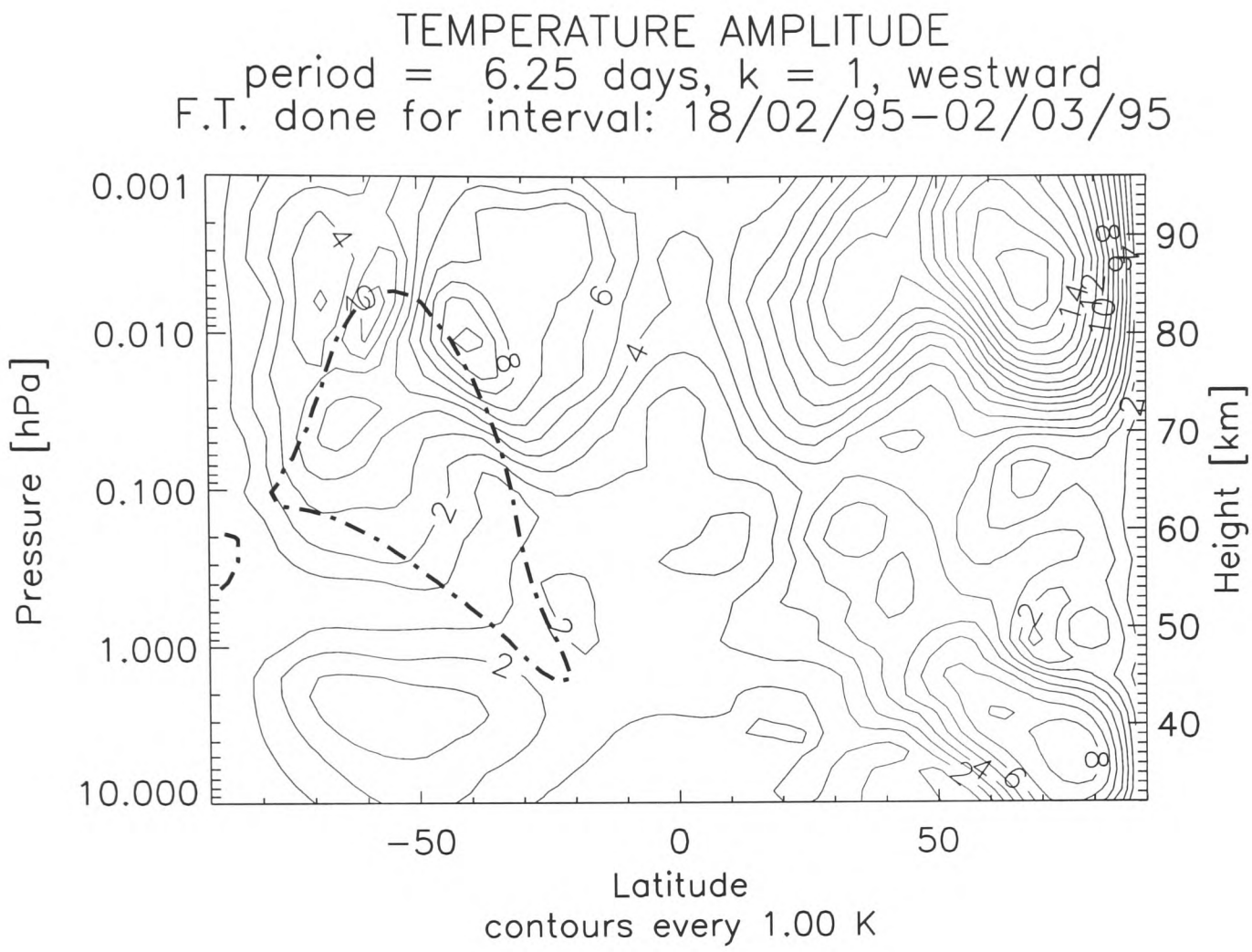


Figure 3.12: Temperature amplitude of the 6.2 day wave during February Year 2. The bold dot-dashed line is the critical line for this wave ($u - c = 0$).

zonal mean wind, the wave has no significant amplitude in the region of the critical line in meridional wind, but it has in zonal wind and temperature. The peak in temperature coincides with the region where $\overline{q}_y$ is negative (see Figure 3.9a), as the case for the normal mode 4-day wave and the 5-day wave.

A wave of period between 6 and 8 days is seen again during February of Year 2 (1995). Its spatial structure is very similar to the one identified in Year 1 (1994), except for the temperature amplitude, which in this case has a larger amplitude in the northern hemisphere (see Figure 3.12 and compare with Figure 3.11c). Also the period is more sharply defined, having the most coherent structure and largest amplitude at 6.2 days. The last wave to see during February Year 2 (1995) is a wave of period about 16 days lasting until the end of March. The wave has k=1 and propagates westward. Its structure is somewhat noisy, with large amplitude in the northern hemisphere high latitudes (Figure 3.14 shows the amplitude of the wave for March).

In Year 3 (1996) the wave activity of the model at 54.4°N and 0.003 hPa is seen over a wide range of frequencies (Figure 3.2c and 3.4c). Large wave amplitudes are present almost continuously from periods of 6 days to 14 days. Two different structures can be distinguished. Around 6-8 days zonal mean wind peaks at the equator at the highest levels, temperature peaks symmetrically at midlatitudes with larger values in the southern hemisphere, the wave looks like the 7 day wave found in Year 1 (see Figure 3.11). Towards slower periods (13 to 16 days) the zonal wind loses its coherent structure and the temperature amplitude is largest in the northern hemisphere. In meridional wind the structure does not change much, maintaining its double peak structure at very high latitudes.

3.5.1.3 MARCH

Figure 3.13a shows the zonal mean u-wind for March of Year 2. No significant waves are seen in March of Year 1 of the EUGCM integration (see Figures 3.2a and 3.4a). In Year 2 very weak winds are present during this month and there is not much wave activity, as inferred from the small values of the EP flux in both hemisphere (Figure 3.13c)[4].

During March of Year 2 (1995) there is a 16-day, k=1 westward propagating wave, whose structure is approximately global but with larger amplitude and coherence in the northern hemisphere (Figure 3.14). Both wind components have large values (up to $30\,\mathrm{m\,s^{-1}}$). Meridional wind peaks at very high latitudes in the northern hemisphere. Zonal wind shows large values, but not very coherent structure, whereas temperature structure is symmetric about the equator, and peaks at midlatitudes with enhanced values in the northern hemisphere. The wave has no significant amplitude in the critical regions. Repeatedly observed since the 1960's is a wave with period between 11 and 20 days and large amplitude at high latitudes. The wave was coined by Madden (1978) as the '16-day wave', and identified with the second symmetric zonal wavenumber 1 Rossby normal mode (1,3) (see Figure A.3 in Appendix A). Waves of period close to 16 days are also clearly seen

[4]The zonal mean wind for March in Year 1 and 2 are very similar.

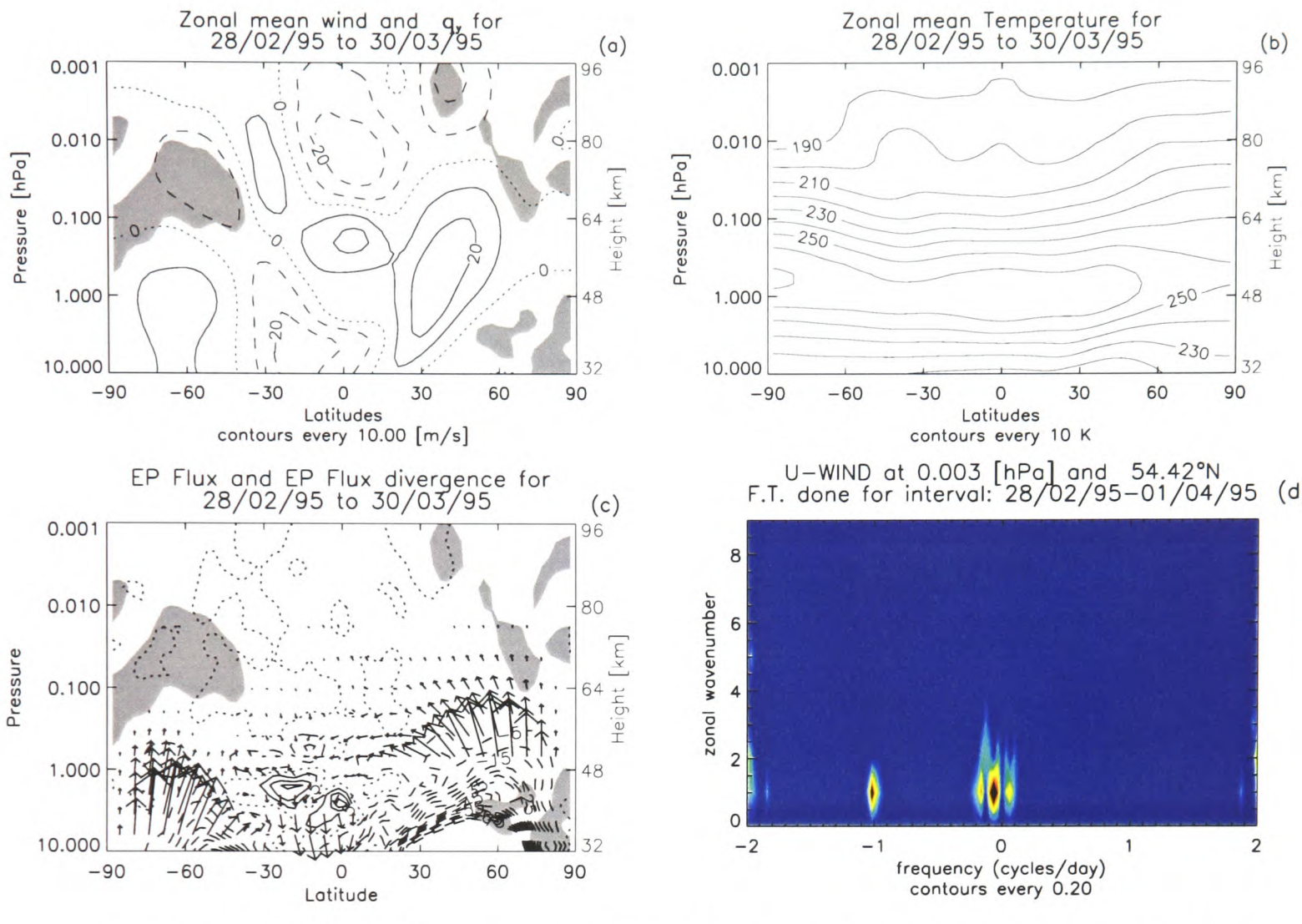


Figure 3.13: (a) Zonal mean u-wind for March Year 2. Shaded regions are where $\bar{q}_y < -1 \times 10^{-11}$ [$m^{-1}s^{-1}$], with grey for values between -1 to -5×10^{-11}. (b) zonal mean temperature for the same period. (c) Contours of $\nabla \cdot F$ in units of [$kgm^{-1}s^{-1}day^{-1}$], arrows of the EP flux for same period. The EP flux for the first 3 levels in the winter hemisphere have been set to zero. (d) zonal wavenumber versus frequency plot of u-wind at 54.4°N and 0.003 hPa.

in the meteor-radar data. Mitchell *et al.*, 1999, find 16-day wave activity for December to mid-April in the meteor-radar data.

In March of Year 3 a 13-16 day wave is found again, its spatial structure is similar to previous years; u-wind structure is not very coherent, large amplitude in v-wind at high northern latitudes and two peaks in temperature at about 50 km and 80 km and 60°N.

3.5.1.4 APRIL

The zonal mean wind in the southern hemisphere during April is westerly (Figure 3.15a), so that planetary waves can propagate upwards from the troposphere into the middle stratosphere. The EP flux components for this month have positive values in both

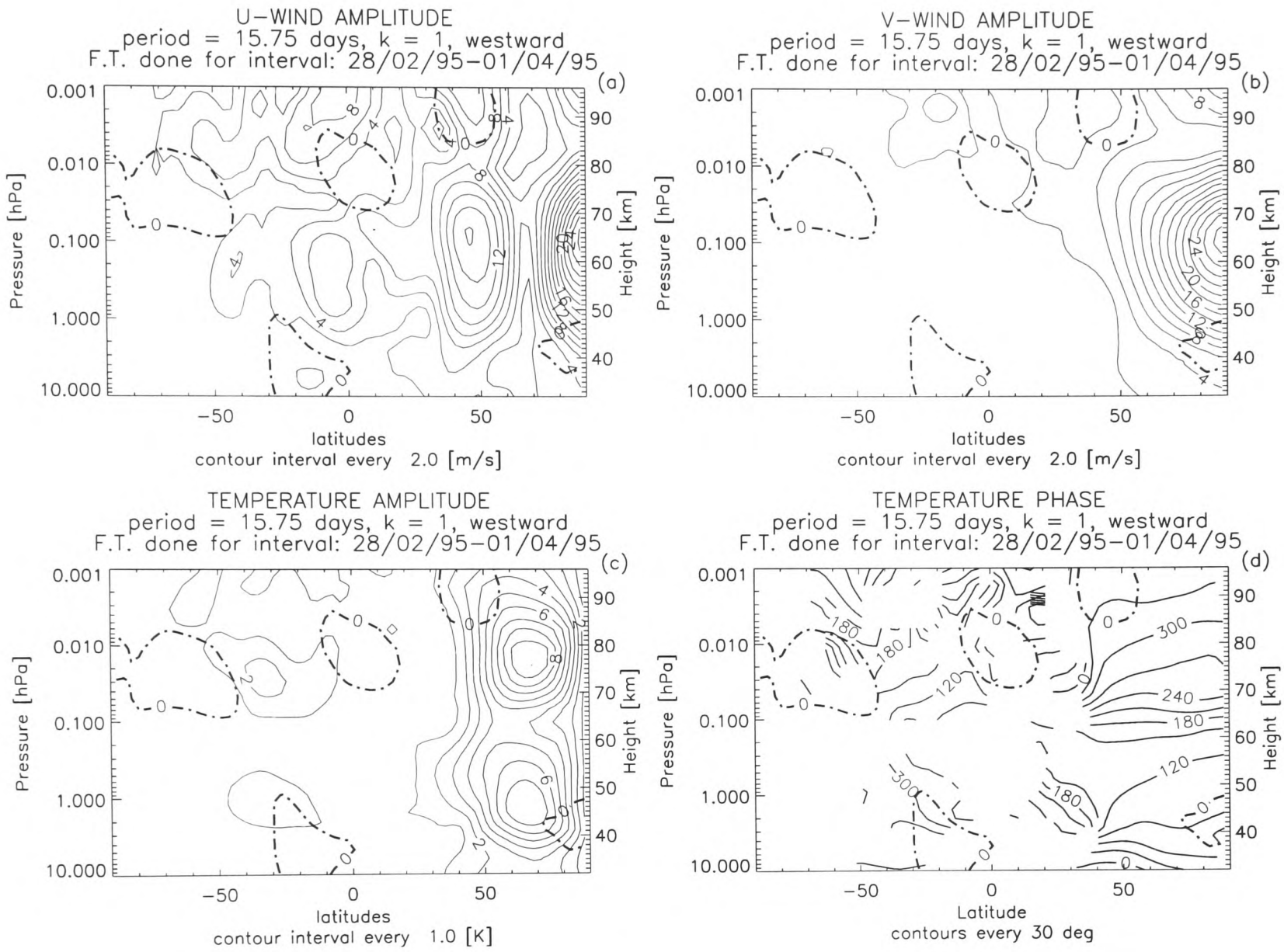


Figure 3.14: (a) u-wind amplitude of the westward propagating 16-day wave during March Year 2. The bold dot-dashed line is the critical line for this wave ($u - c = 0$). (b) v-wind amplitude, (c) temperature amplitude and (d) temperature phase.

hemispheres. In the northern hemisphere between 30°N and 60°N, the EP flux points upwards and equatorwards. The divergence of the EP flux does not show any major values in the whole domain (see Figure 3.15c). The frequency versus time plot for April Year 1 shows a 8-10 day wave, with k=1 and westward propagating (Figure 3.15d). Its spatial structure resembles a Rossby wave (compare Figure 3.16 of this wave with Figure A.2 of the Rossby normal mode). The wave has a critical line in the northern hemisphere. The phase structure has, for instance, a jump across the equator, as expected for the (1,2) normal mode, the second antisymmetric mode with respect to the equator. This wave was coined by Hirota and Hirooka (1984) the '10-day wave'.

There is no wave activity during April of Year 2.

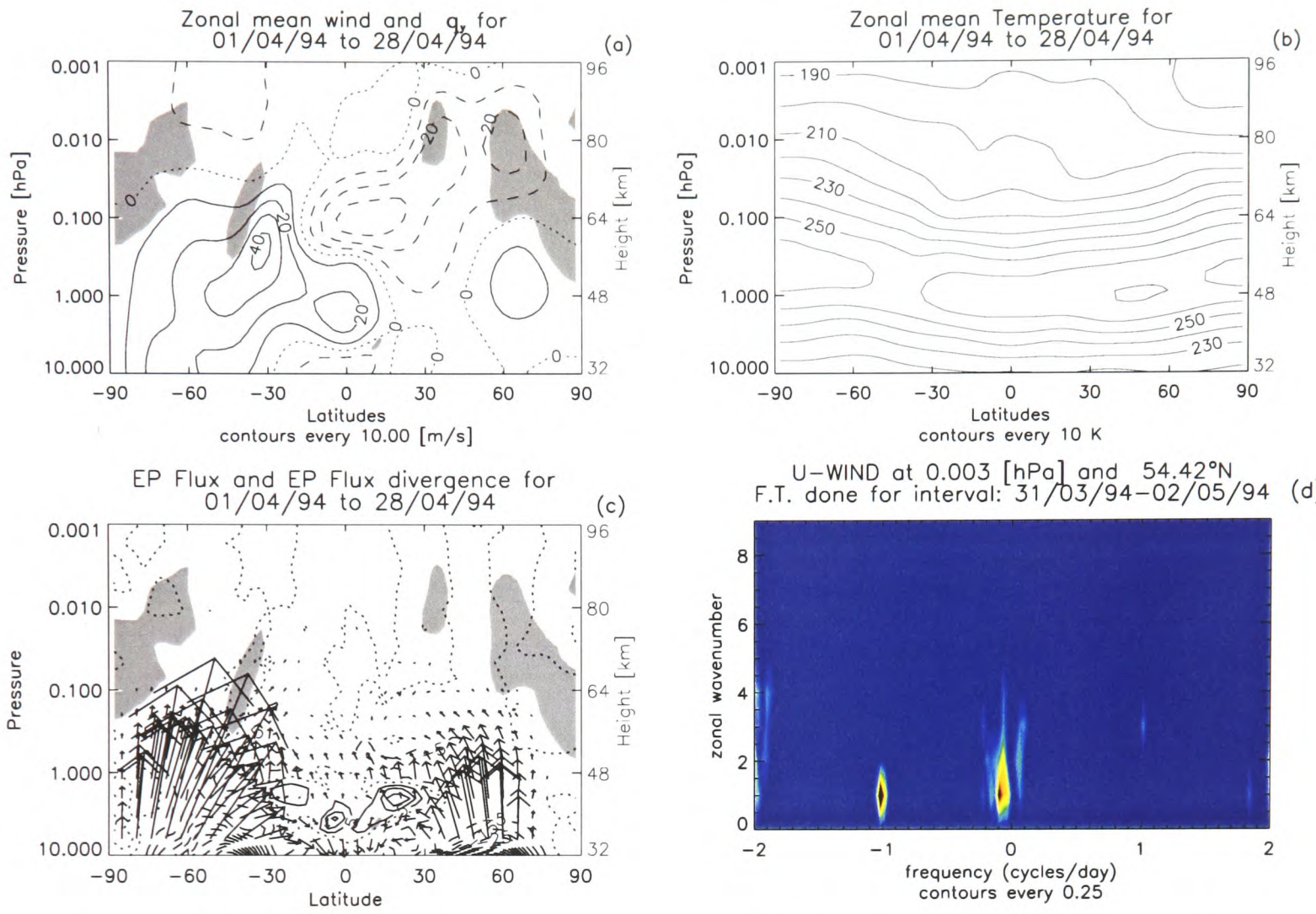


Figure 3.15: (a) Zonal mean u-wind for April Year 1.Shaded regions are where $\overline{q}_y < -1 \times 10^{-11}$ [$\mathrm{m^{-1}s^{-1}}$], with grey for values between -1 to -5×10^{-11} . (b) zonal mean temperature for the same period. (c) Contours of $\nabla \cdot F$ in units of [$\mathrm{kgm^{-1}s^{-1}day^{-1}}$], arrows of the EP flux for same period. (d) zonal wavenumber versus frequency plot of u-wind at 54.4°N and 0.003 hPa.

A smaller amplitude 10-day wave is seen in April of Year 3 (1996). Again the spatial structure shows little coherence in zonal wind, symmetric about the equator in meridional wind and temperature with larger amplitude in the northern hemisphere. Phase structure is symmetric about the equator, and there is a small region where the phase speed equals the zonal mean wind. The phase structure of the wave does not agree with that expected for the (1,2) Rossby normal mode and is different from the one found for the 10-day wave in Year 1. The temperature phase structure of the (1,2) mode, and of the 10-day wave found in Year 1 is antisymmetric about the equator.

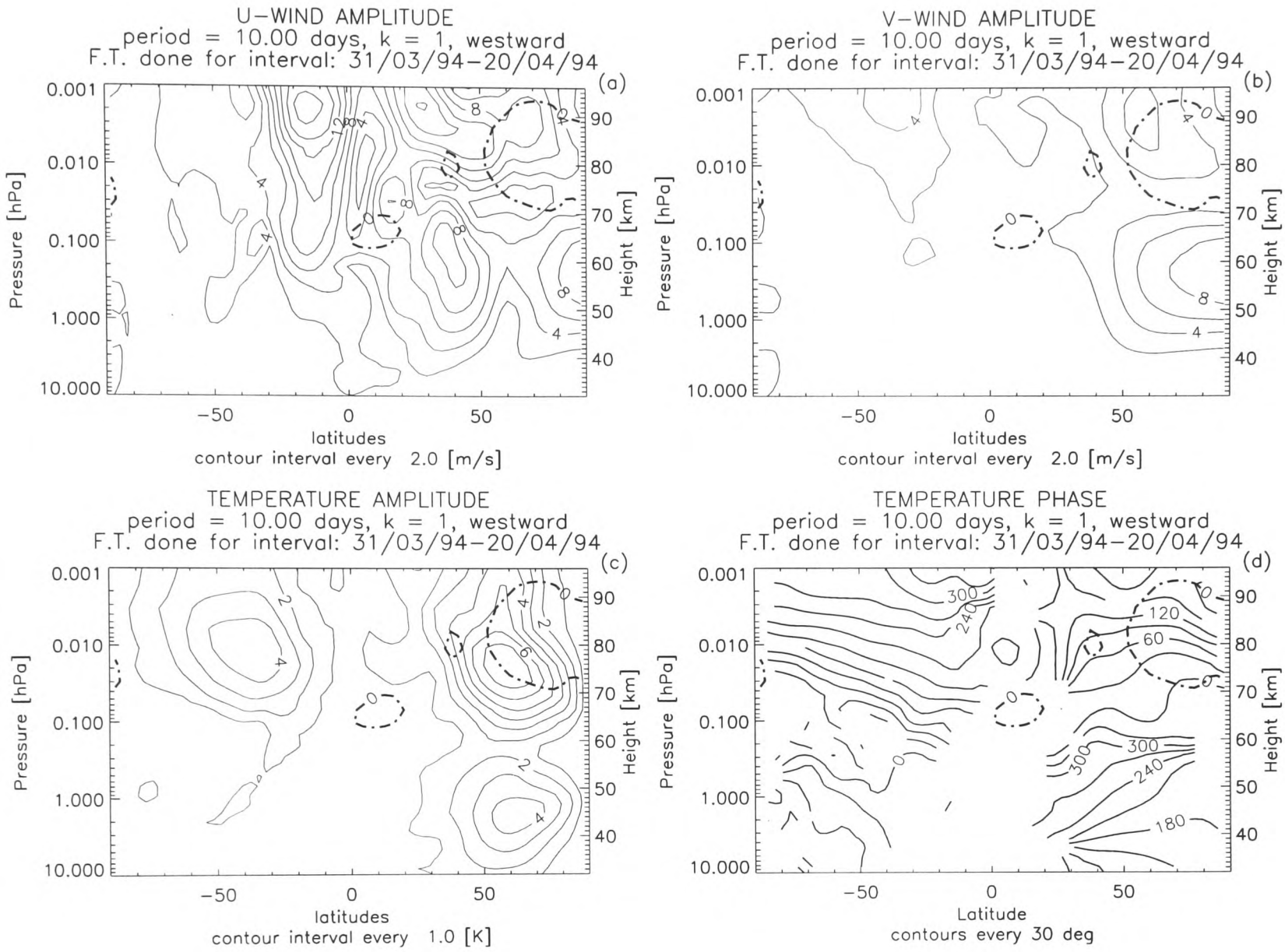


Figure 3.16: (a) u-wind amplitude of the westward propagating 10-day wave during April Year 1. The bold dot-dashed line is the critical line for this wave ($u - c = 0$). (b) v-wind amplitude, (c) temperature amplitude and (d) temperature phase.

3.5.2 Summer months in the EUGCM

The months analysed in this section are June, July and August, the period of strongest wave activity in the EUGCM as well as in the meteor-radar data. Most waves in this season have periods of 1.5 to 5 days (frequencies lying in the range between 0.2 to 0.7 cycles per day).

3.5.2.1 JUNE

Figure 3.17a shows the zonal mean u-wind for June, the summer jet is well developed, with values at the core reaching $-80\,\mathrm{m\,s^{-1}}$. On the same plot shaded are the regions where $\overline{q}_y$ is significantly negative (less than $-1 \times 10^{-11}\mathrm{m^{-1}s^{-1}}$). The meridional gradient of quasi-

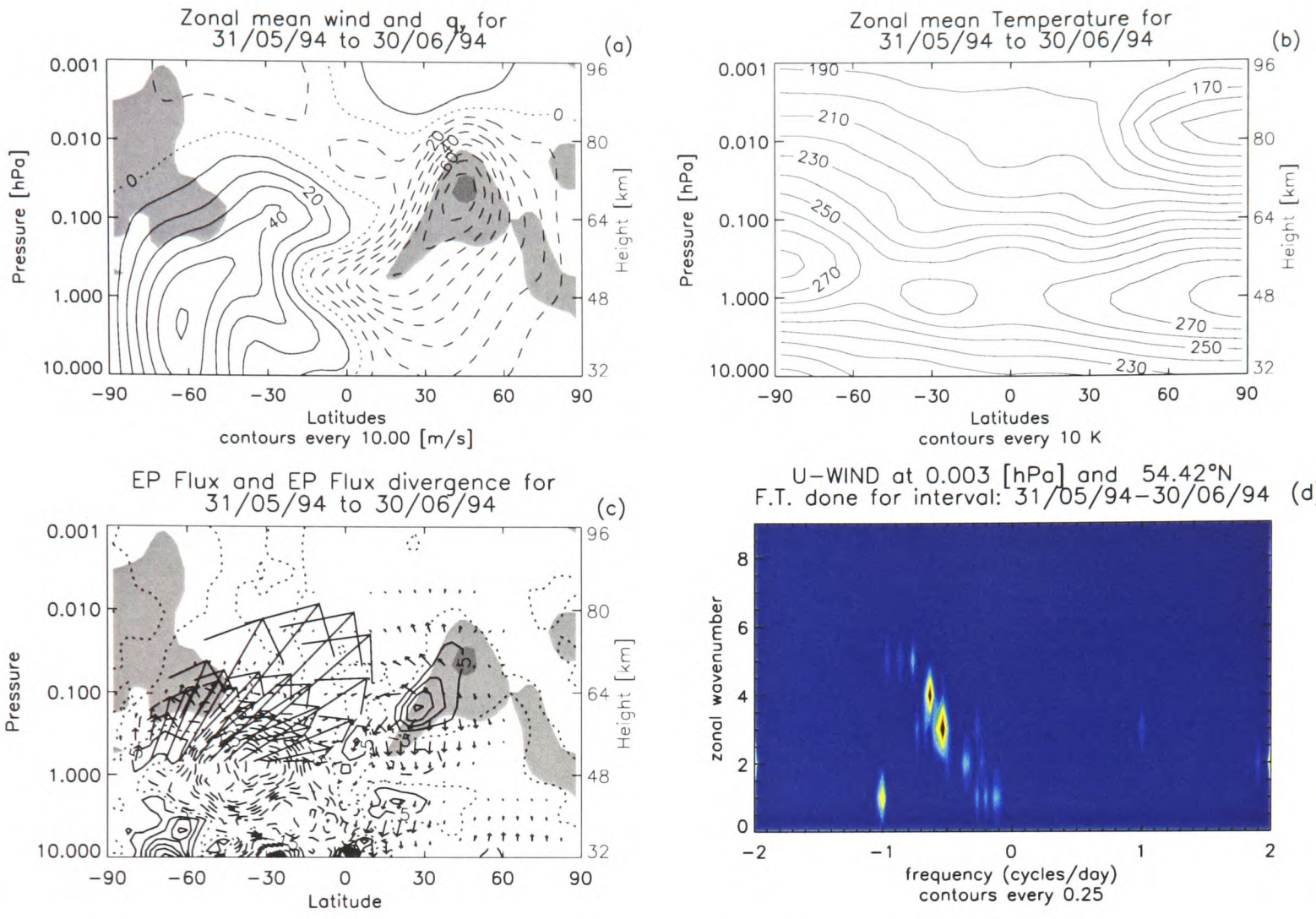


Figure 3.17: (a) Zonal mean u-wind for June Year 1. Shaded regions are where $\overline{q}_y < -1 \times 10^{-11}$ [$\mathrm{m^{-1}s^{-1}}$], with light grey for values between -1 to -5×10^{-11} and dark grey for values less than -5×10^{-11}. (b) zonal mean temperature for the same period. (c) Contours of $\nabla \cdot F$ in units of [$\mathrm{kgm^{-1}s^{-1}day^{-1}}$], arrows of the EP flux for same period. The EP flux for the first 3 levels in the winter hemisphere have been set to zero. (d) zonal wavenumber versus frequency plot of u-wind at 54.4°N and 0.003 hPa.

geostrophic potential vorticity ($\overline{q}_y$) of the background flow for that month shows a negative region at the top of the summer jet (around 45°N and 70 km).

The first wave to note during June of Year 1 (1994) in Figures 3.2 and 3.4 is a wave of period about 38 hrs (1.58 days). A wavenumber versus frequency plot indicates that the wave has a zonal structure of k=4 (see Figure 3.17d). Its amplitude is confined to the northern hemisphere from middle to high latitudes (Figure 3.18). The wave has large amplitude within the critical line (the bold dot-dashed line on Figure 3.18), an indication of an unstable wave. Furthermore, the divergence of the EP flux (see Figure 3.17c) is consistent with the dynamics of this wave being an unstable growing disturbance, i.e., there

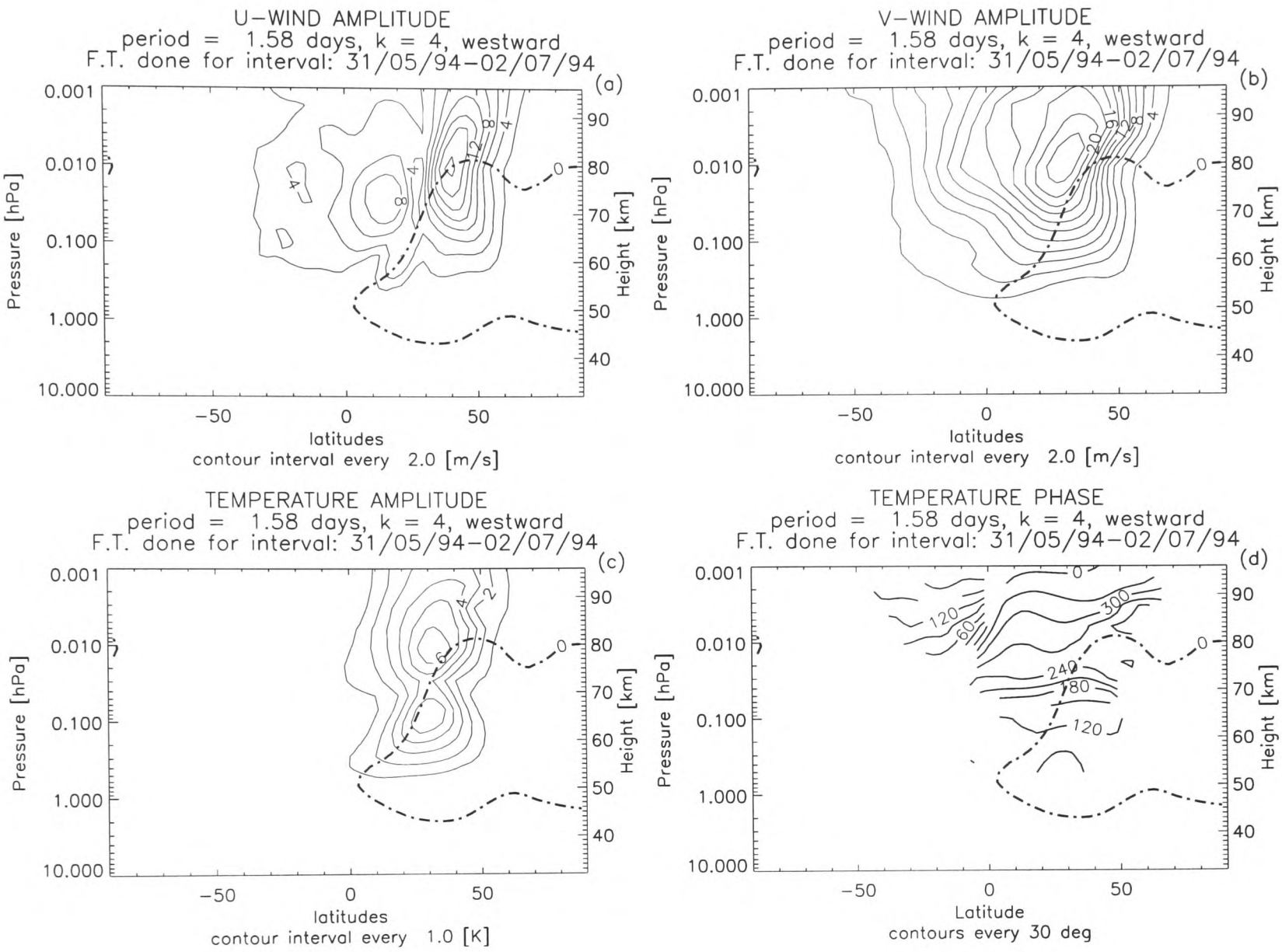


Figure 3.18: (a) u-wind amplitude of the westward propagating 1.5 day wave, k=4 during June Year 1. The bold dot-dashed line is the critical line for this wave ($u-c=0$). (b) v-wind amplitude, (c) temperature amplitude and (d) temperature phase.

is $\nabla \cdot F > 0$ where $\overline{q}_y < 0$ and vice versa, as expected from quasi-geostrophic theory (see section 2.2.2). Later during June in Year 1 the quasi 2-day wave starts to appear.

In early June of Year 2 zonal wavenumber versus frequency plots for winds and temperature all show a wave of period around 38 hrs and k=4. The wave has the same spatial structure as in Year 1, in temperature the structure is very similar to the quasi 2-day wave, but with maximum amplitude at around 30°N instead of 40°N. Winds peak at 30°N as well. Later in the month the quasi 2-day wave grows in amplitude and stays until the beginning of August.

Waves of shorter period are also seen in June (and August) of Year 2, their spatial structure resemble results obtained from the linear instability calculation described in

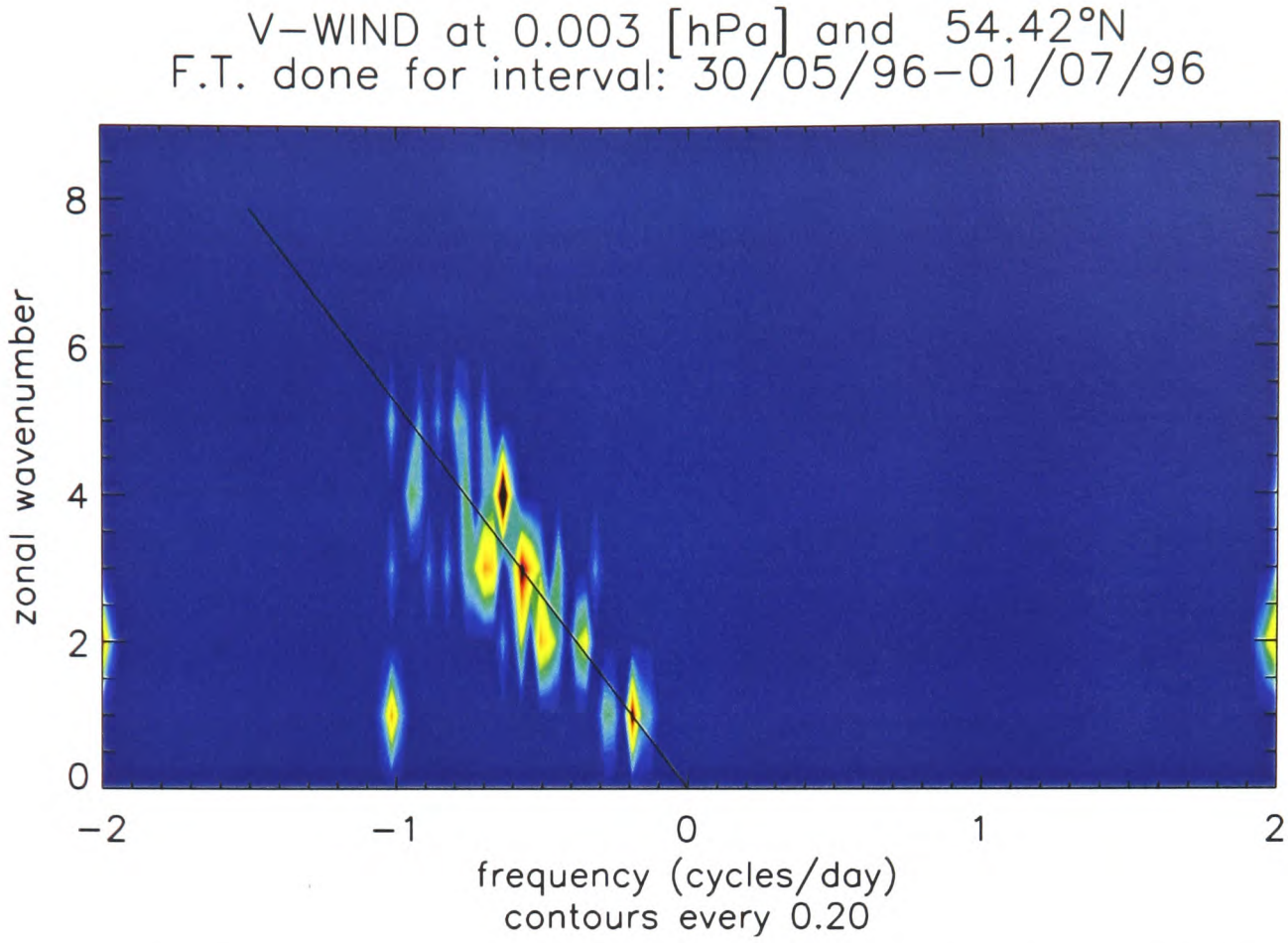


Figure 3.19: Zonal wavenumber versus frequency plot of v-wind at 54.4°N and 0.003 hPa for June Year 3 (1996). Positive (negative) frequencies indicate eastward (westward) propagation. Peaks on the straight line travel westward with the same phase speed.

chapter 5. In the zonal wavenumber versus frequency plot for meridional wind for the first half of June a peak is seen at k=3 and period 35 hrs. The wave is a high latitude localized wave (the spatial structure for this wave as seen in August Year 2 is shown in Figure 3.28). This wave is also seen in June of a shorter run of the EUGCM (which was first available and upon which some instability calculation were based on). Waves at these periods are also present in the meteor-radar data (see Figure 3.1b for example).

A different behaviour to the two previous years is apparent in the summer of Year 3 (e.g. compare Figures 3.2a, 3.2b and 3.2c). The amplitude of the quasi 2-day wave is smaller and various smaller amplitude, shorter lived waves in the range of 0.6 to 0.2 cycles per day are present. In Figure 3.19 frequency versus zonal wavenumber spectra is calculated from meridional wind at 54.4°N and 0.003 hPa for June of Year 3. A few peaks can be seen. With k=1 (apart of the diurnal tide) there is a peak at frequency -0.2 (5 day period), the black diagonal line on the plot is the phase speed of this wave and it can be seen

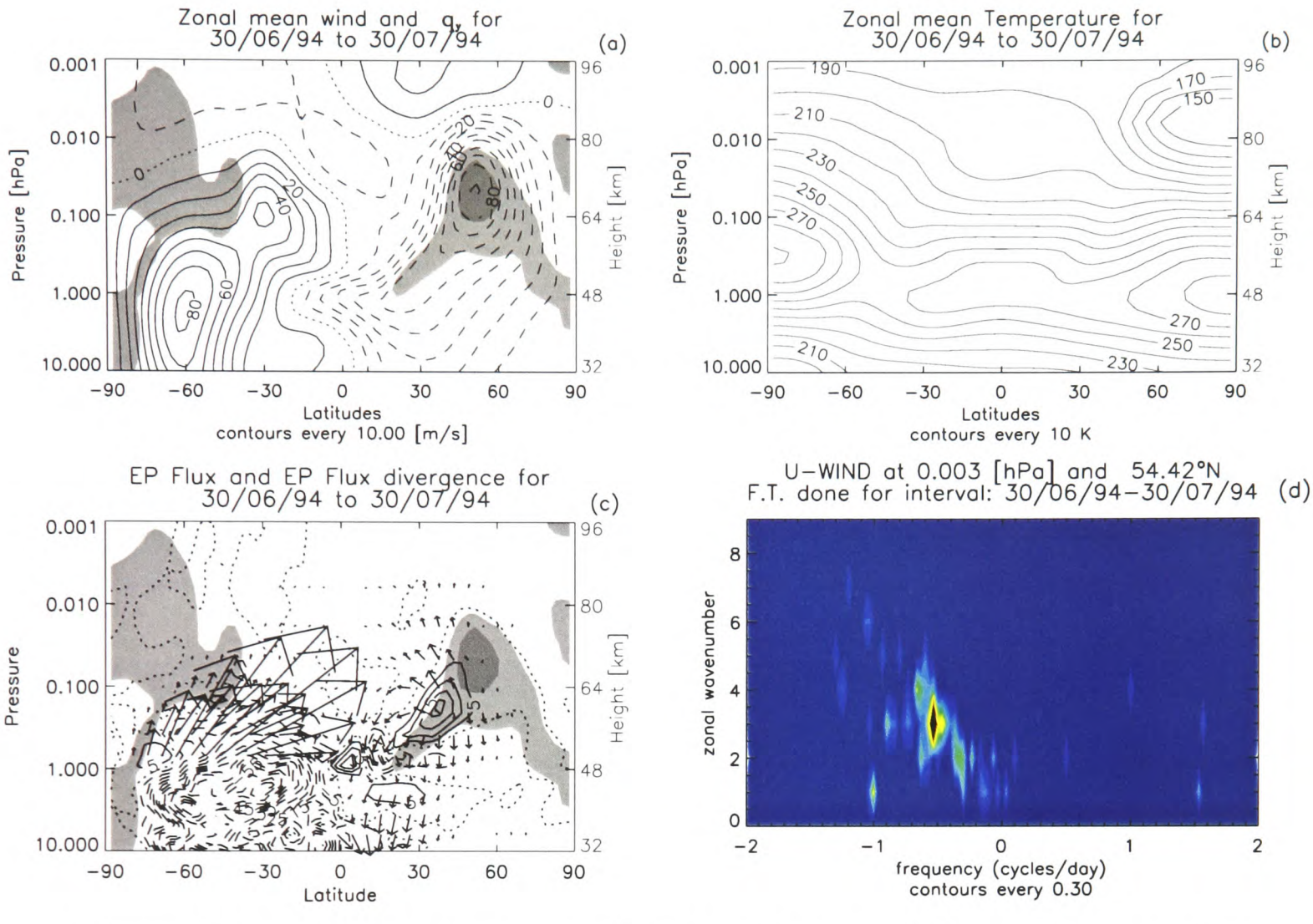


Figure 3.20: (a) Zonal mean u-wind for July Year 1. Shaded regions are where $\bar{q}_y < -1 \times 10^{-11}$ [$m^{-1}s^{-1}$], with light grey for values between -1 to -5×10^{-11} and dark grey for values less than -5×10^{-11}. (b) zonal mean temperature for the same period. (c) Contours of $\nabla \cdot F$ in units of [$kgm^{-1}s^{-1}day^{-1}$], arrows of the EP flux for same period. The EP flux for the first 3 levels in the winter hemisphere have been set to zero. (d) zonal wavenumber versus frequency plot of u-wind at 54.4°N and 0.003 hPa.

that the peaks at k=2 and k=3 lie on this line; these 'waves' have the same phase speed. Therefore there is either a 'blob' of air going round at a given phase speed, but with no distinguishable zonal structure or the wave is non-linear. Two peaks in Figure 3.19 that do have a coherent linear wave structure associated to them, are a wave of period 38 hrs and k=4 (as in the previous years), with the same spatial structure but smaller amplitude. And a wave with k=3 and period 1.4 days which is also seen in Year 2.

3.5.2.2 JULY

The zonal mean u-wind for this month has intensified with respect to June, and again negative values of $\bar{q}_y$ can be seen (see Figure 3.20a). The main wave seen in all the three

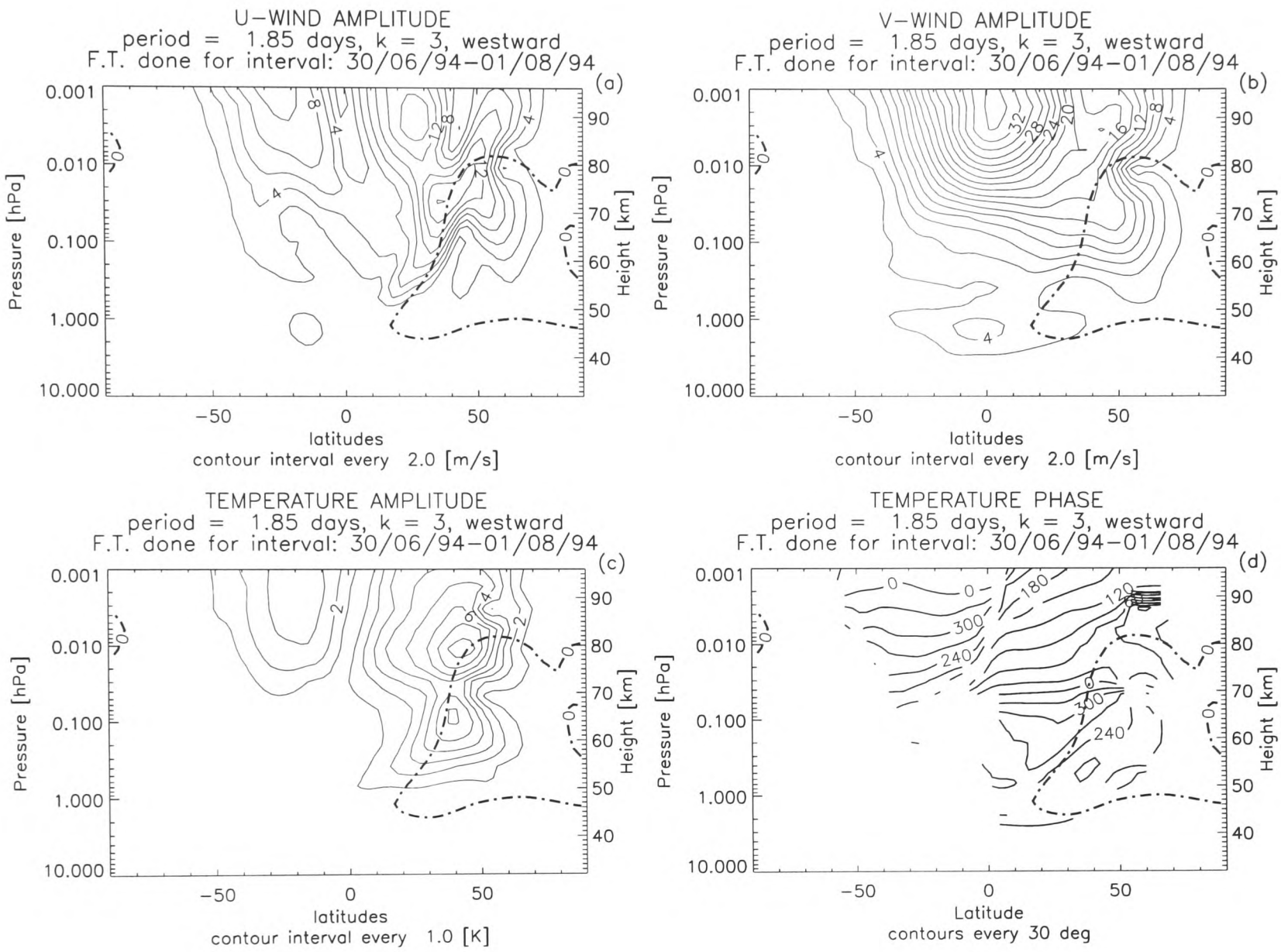


Figure 3.21: (a) u-wind amplitude of the westward propagating quasi 2-day wave during July Year 1, The bold dot-dashed line is the critical line for this wave ($u - c = 0$). (b) v-wind amplitude, (c) temperature amplitude and (d) temperature phase.

years of the EUGCM during July is the quasi 2-day wave. The quasi 2-day wave can be seen both in Figure 3.2a and Figure 3.4a. The wave is the largest feature during July in Year 1 and in Year 2. For Year 1 (1994) a frequency versus zonal wavenumber plot reveals the k=3 structure of the wave (Figure 3.20d). Its spatial structure is shown in Figure 3.21. Zonal wind has a minimum at the equator and peaks at both hemispheres midlatitudes. Meridional wind presents a maximum at the equator and temperature has two maxima at midlatitudes, at 40° in the northern hemisphere and 20° in the southern hemisphere, with larger values in the northern hemisphere. This structure agrees well with previous observations of the wave (e.g. Rodgers and Prata, 1981). As mentioned previously the quasi 2-day wave is a recurrent feature of the mesosphere, the wave appears in every

year of the meteor-radar data as well as in the EUGCM. The exact period of the wave in the meteor-radar data is 1.88 days (45 hrs), this is true for the EUGCM in Year 1 as well (as indicated in Figure 3.21). In Year 2 the wave has a period of 1.97 days and in Year 3 the period changes from 1.85 days to 1.97 days. As the 38 hrs wave seen in June, the quasi 2-day wave has a critical line. Figure 3.20c shows in contours the EP flux divergence, in arrows the EP flux and in shades regions of negative $\overline{q}_y$. In the northern hemisphere the EP flux is divergent (positive values) in most of the region where $\overline{q}_y < 0$, indicating the wave most likely arises from an instability. The EP flux vectors point upwards and equatorwards from the region of divergence, indicating heat and momentum transport by the wave away from the unstable region.

In Year 2 there is an interesting difference from July in Year 1; the quasi 2-day wave undergoes a zonal wavenumber change from k=3 to k=4 (Figure 3.29). In July of Year 2 the main feature in Figure 3.2b is a large amplitude quasi 2-day wave, the period of which changes throughout the month, starting at 1.85 days and ending up at 2.1 days (at the start of August). The spatial structure (not shown) is the same as for Year 1.

The zonal wavenumber versus frequency plot calculated for temperature show two waves with k=2 and period of about 2.5 days and 3.5 days respectively (Figures not shown). Their height-latitude amplitudes are similar to the quasi 2-day wave. Combining all the waves with same phase speed as the quasi 2-day wave gives a wave which is predominantly with k=2 and k=3. By the end of August of this year, the quasi 2-day wave has a less coherent spatial structure, with a mixture of wavenumbers present.

Figure 3.22 shows frequency versus wavenumber of v-wind during July of Year 3 (1996). In the plot several peaks can be identified. At k=4 is a maximum with frequency -0.64 cycle per day (1.55 days), with k=2 there is a peak at frequency -0.3 cycles per day (period of 3.1 days). These two peaks have the same phase speed and therefore are either two harmonics of a wave-like pattern going round the globe at that phase speed with a zonal wavenumber of 2 and 4 or a non-linear wave. In the same plot peaks that do represent waves are the one at k=3 and period of 1.97 days; this is the quasi 2-day wave. The period of the quasi 2-day wave is different from the two previous years, but the spatial

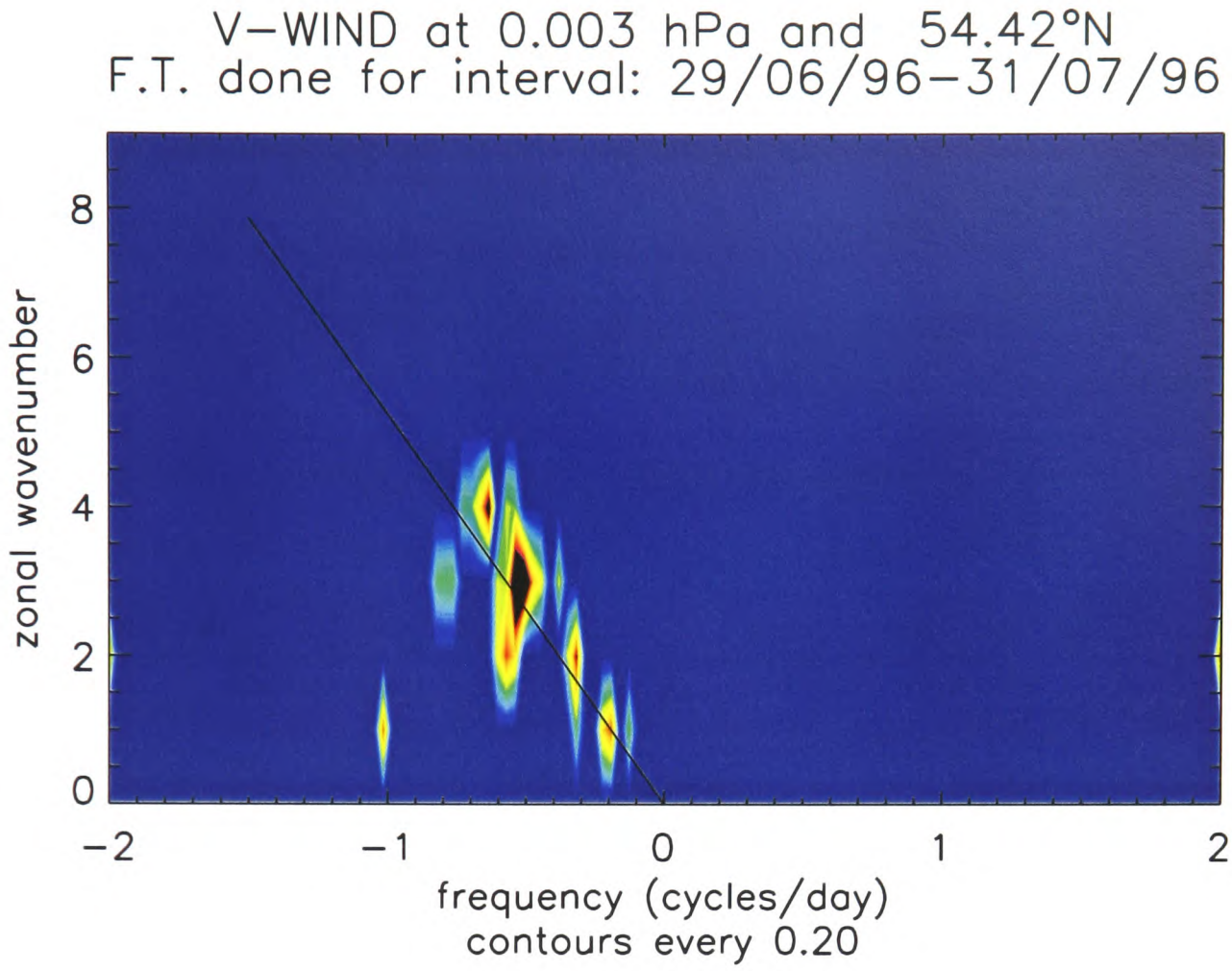


Figure 3.22: Zonal wavenumber versus frequency plot of v-wind at 54.4°N and 0.003 hPa for July Year 3. Positive (negative) frequencies indicate eastward (westward) propagation. Peaks on the straight line travel westward with the same phase speed of 0.19 rad per day.

structure is the same, although the amplitude of the quasi 2-day wave is smaller during Year 3 (compare Figures 3.2a, 3.2b and 3.2c).

The largest peak in Figure 3.22 at zonal wavenumber 1 is at frequency -0.2 cycles per day (5-day wave). The spatial structure of the wave is shown in Figure 3.23; some differences in comparison with the 5-day wave in Year 1 are seen (Figure 3.8). Mainly in zonal and meridional wind. The amplitudes are only present in the northern hemisphere and the characteristic maxima at the equator of the zonal wind component is not observed. The meridional component of the (1,1) Rossby normal mode has a minimum at the equator and maxima at the poles, this again is not the case for this 5-day wave. Only the temperature amplitude does agree with the expected structure of the (1,1) Rossby normal mode, apart from the fact that again the wave has large amplitude inside the critical region, as was the case for the 5-day wave in Year 1.

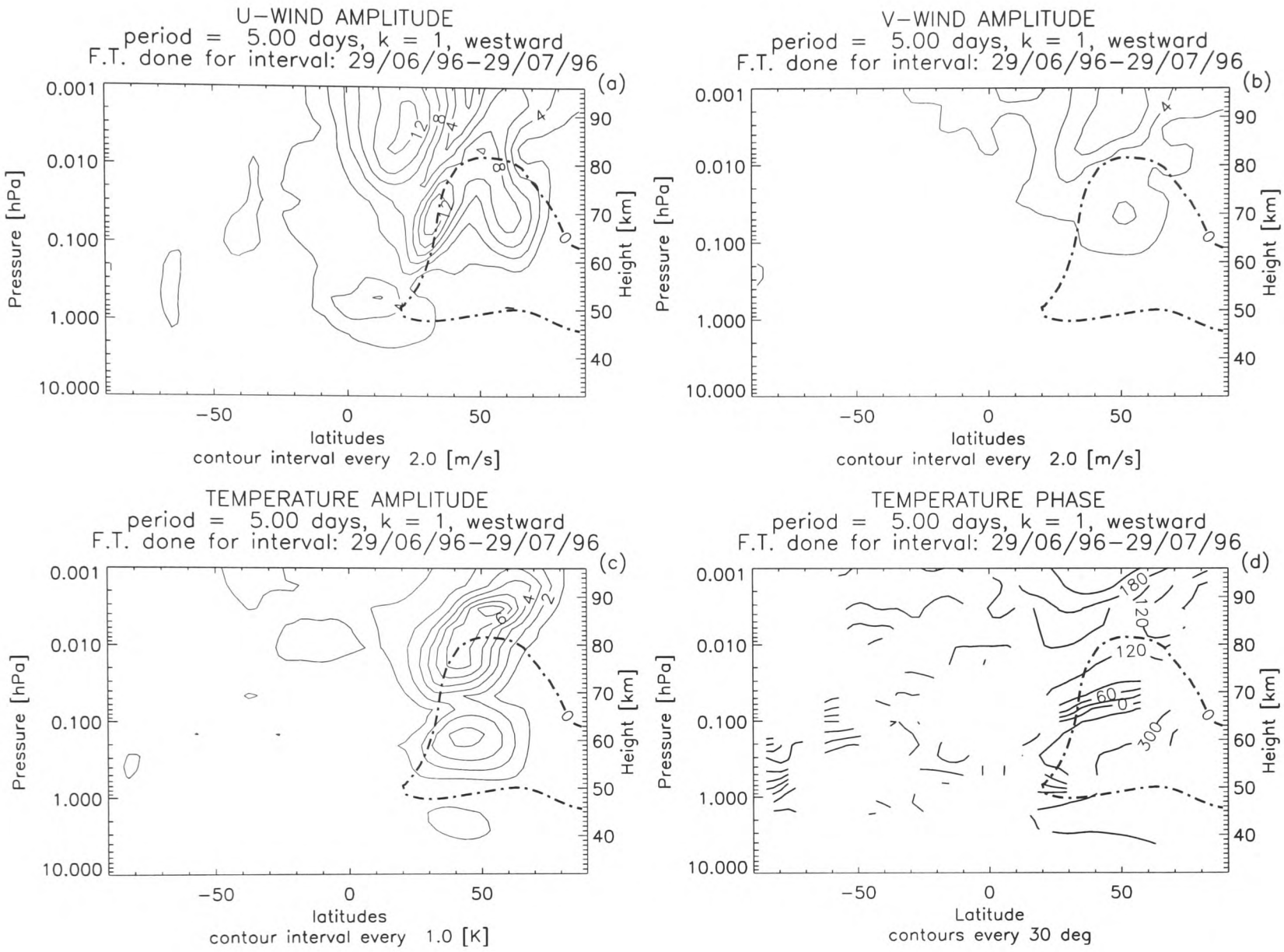


Figure 3.23: (a) u-wind amplitude of the westward propagating 5-day wave during July Year 3. The bold dot-dashed line is the critical line for this wave ($u - c = 0$). (b) v-wind amplitude, (c) temperature amplitude and (d) temperature phase.

Finally Figure 3.22 has a peak at k=2 and frequency -0.57 cycles per day (period of 1.75 days). The amplitude of the wave is shown in Figure 3.24. The zonal wind has a double peak at around 50°N and 70°N, v-wind has a maximum at the equator and a maximum at 65°N, temperature has a localized peak at 65°N. The structure and period of this wave closely resembles the fastest growing mode with k=2 obtained in the instability calculation described in chapter 5 (Figure 5.3).

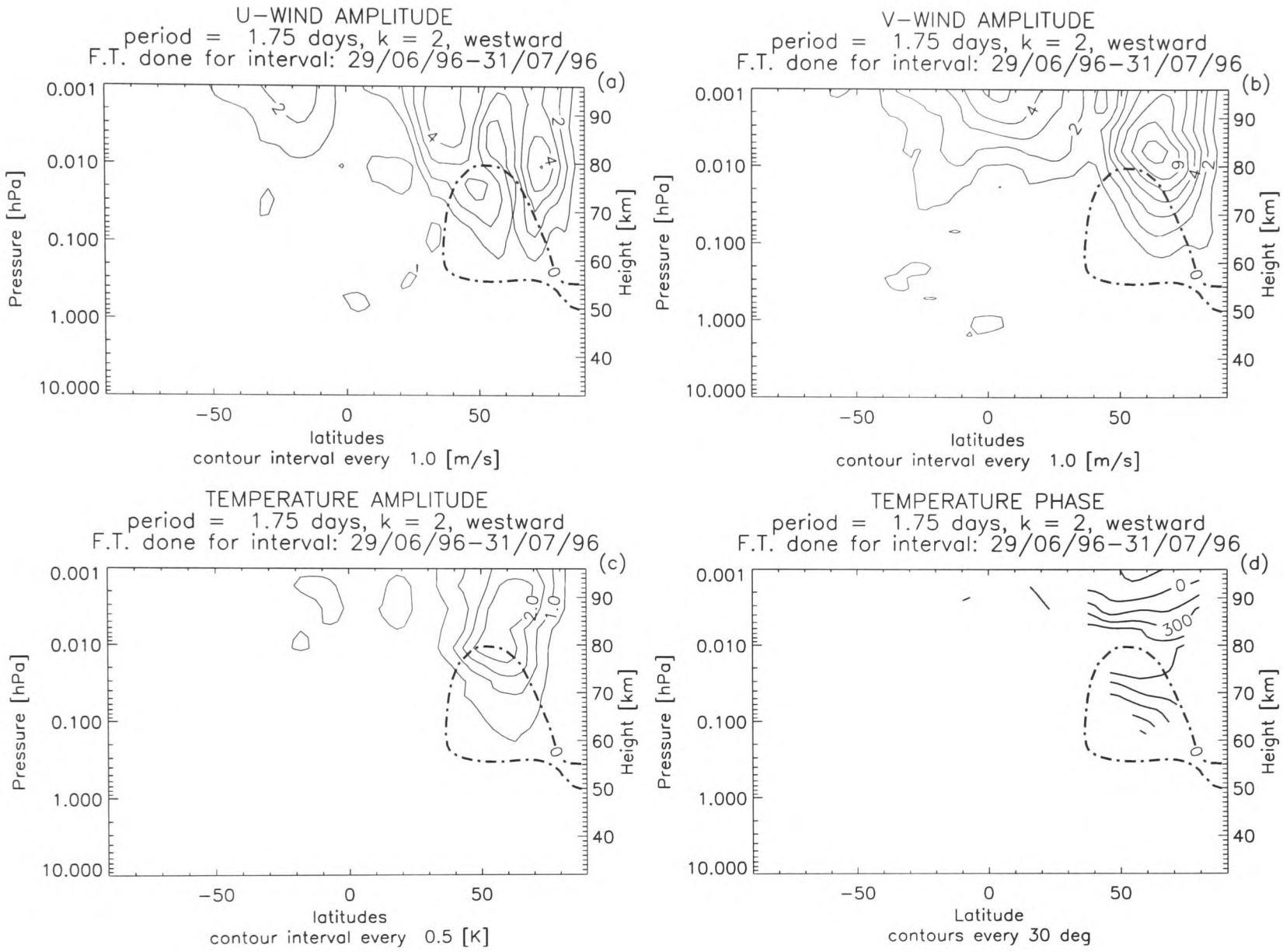


Figure 3.24: (a) u-wind amplitude of the westward propagating 1.75 day wave during July Year 3. The bold dot-dashed line is the critical line for this wave ($u - c = 0$). (b) v-wind amplitude, (c) temperature amplitude and (d) temperature phase.

3.5.2.3 AUGUST

In August the northern hemisphere jet has reduced values with respect to July, but still shows regions where $\overline{q}_y < 0$. In the southern hemisphere a strong polar night jet can be seen (Figure 3.25a).

A wave of period about 3.5 days and k=2 is seen in August of Year 1 (1994) (see Figure 3.25d). Its structure is global and symmetric about the equator, like the normal mode 4-day wave discussed for February of Year 1 and Year 2. Figure 3.26 shows its spatial structure, having maximum amplitude again in the summer hemisphere (the northern hemisphere at this time of year, compare with Figure 3.10). Figure 3.25c shows $\nabla \cdot F > 0$ again coinciding with regions where $\overline{q}_y < 0$ in the northern hemisphere. Although values are

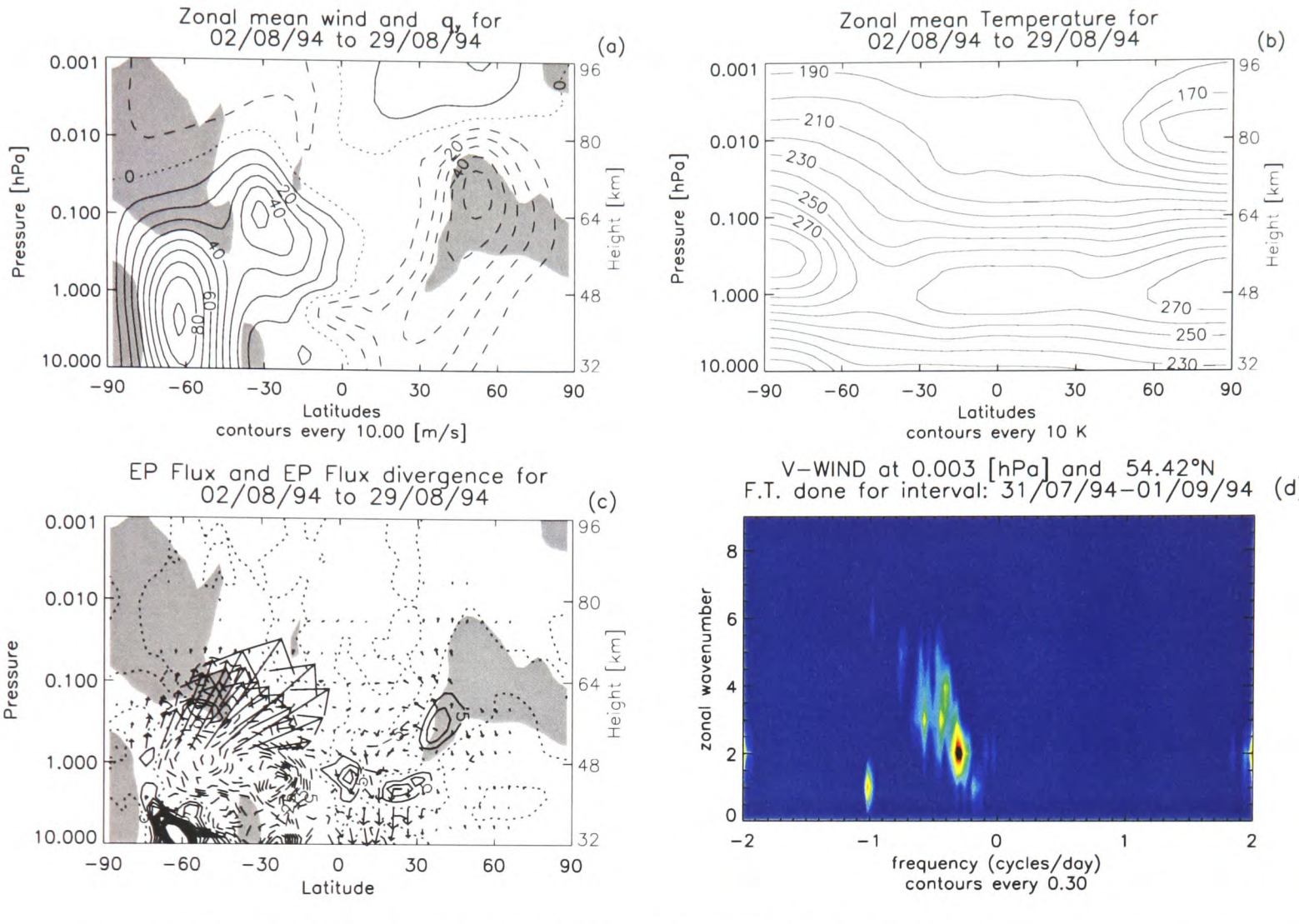


Figure 3.25: (a) Zonal mean u-wind for August Year 1. Shaded regions are where $\overline{q}_y < -1 \times 10^{-11}$ [$m^{-1}s^{-1}$], with grey for values between -1 to -5×10^{-11}. (b) zonal mean temperature for the same period. (c) Contours of $\nabla \cdot F$ in units of [$kgm^{-1}s^{-1}day^{-1}$], arrows of the EP flux for same period. The EP flux for the first 3 levels in the winter hemisphere have been set to zero. (d) zonal wavenumber versus frequency plot of v-wind at 54.4°N and 0.003 hPa.

smaller compared to those found in June and July, the EP flux vector and divergence are similar to July, when the quasi 2-day wave is seen (see Figure 3.20).

In August of Year 2 spectral analysis reveals a change from k=3 to k=4 in the quasi 2-day wave going through a very noisy period. The period of the wave changes from 2.1 days (k=3) to 1.85 days (k=4). The k=4 wave has a different spatial structure than the k=3 wave as seen in Figure 3.27, with the location of larger amplitudes shifting into higher latitudes of the northern hemisphere.

Daily PV maps reveal from 24/6 to 11/07 a clear wavenumber 3 pattern, followed by a period of transition to wavenumber 4. Then k=4 is very clearly seen between 10/08 and 15/08. Figure 3.29 shows Ertel's PV on the 3000 K isentrope (about 60 km, polar

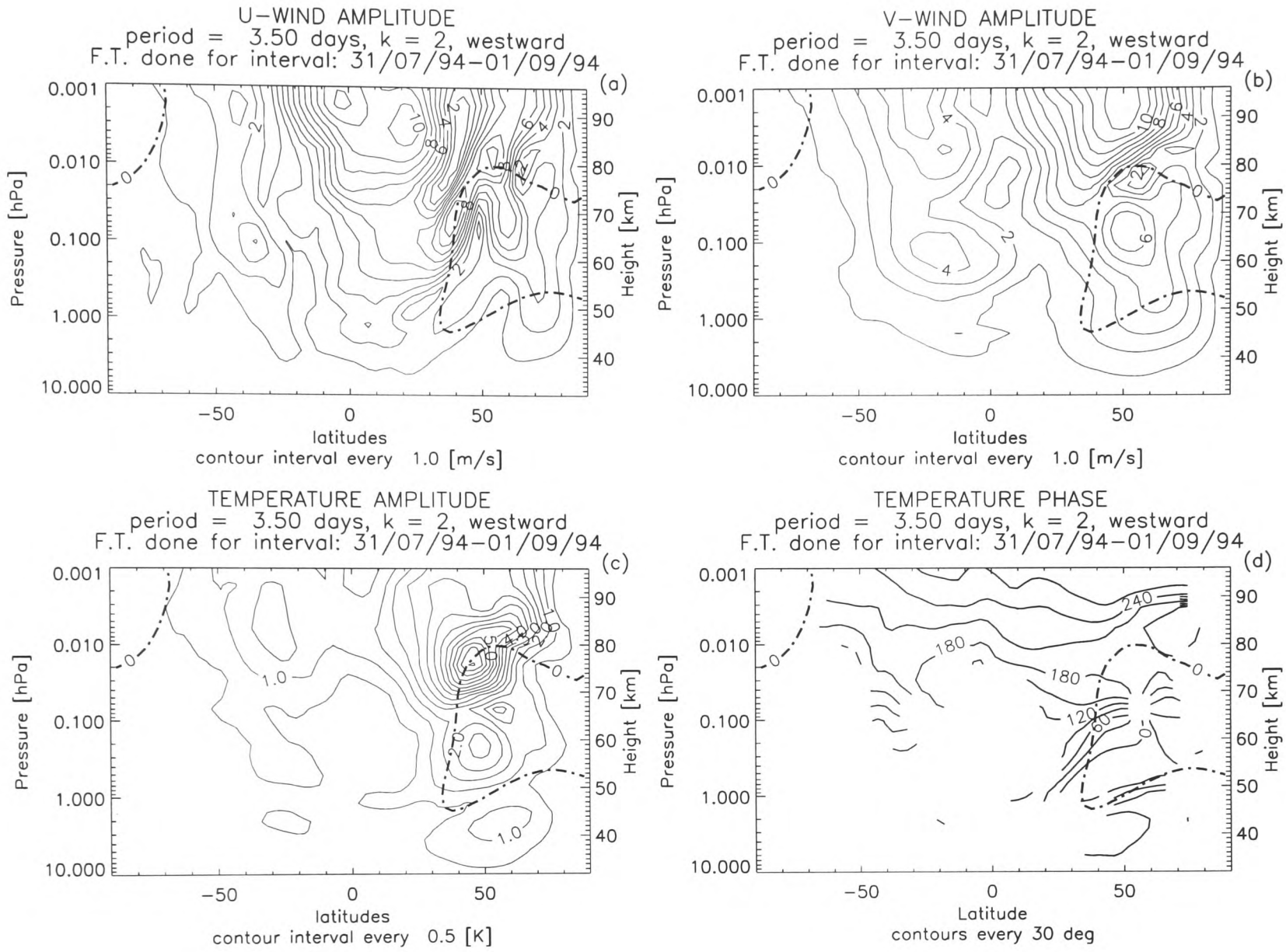


Figure 3.26: (a) u-wind amplitude of the westward propagating 4-day wave during August Year 1. The bold dot-dashed line is the critical line for this wave ($u - c = 0$). (b) v-wind amplitude, (c) temperature amplitude and (d) temperature phase.

stereographic projection of the northern hemisphere). The first 5 plots (from left to right) correspond to PV from the 03/07 to 07/07 where a clear wave 3 pattern can been seen propagating westward with a period close to 2 days. Plots 6 to 9 of the same Figure show consecutive days from the 10th of August[5] onwards, a striking wave 4 pattern is observed, again moving westwards with a period close to 2 days. Notice that the maxima of PV has shifted from midlatitudes for k=3 to higher latitudes for the k=4 pattern, as can be seen from the latitude-height plots of the waves (Figures 3.21 and 3.27).

With k=3, but with a smaller amplitude, is a wave of period 35 hrs and spatial structure localized to 60°N. The spatial structure of this wave as well as the 35 hrs wave seen during

[5]my birthday!

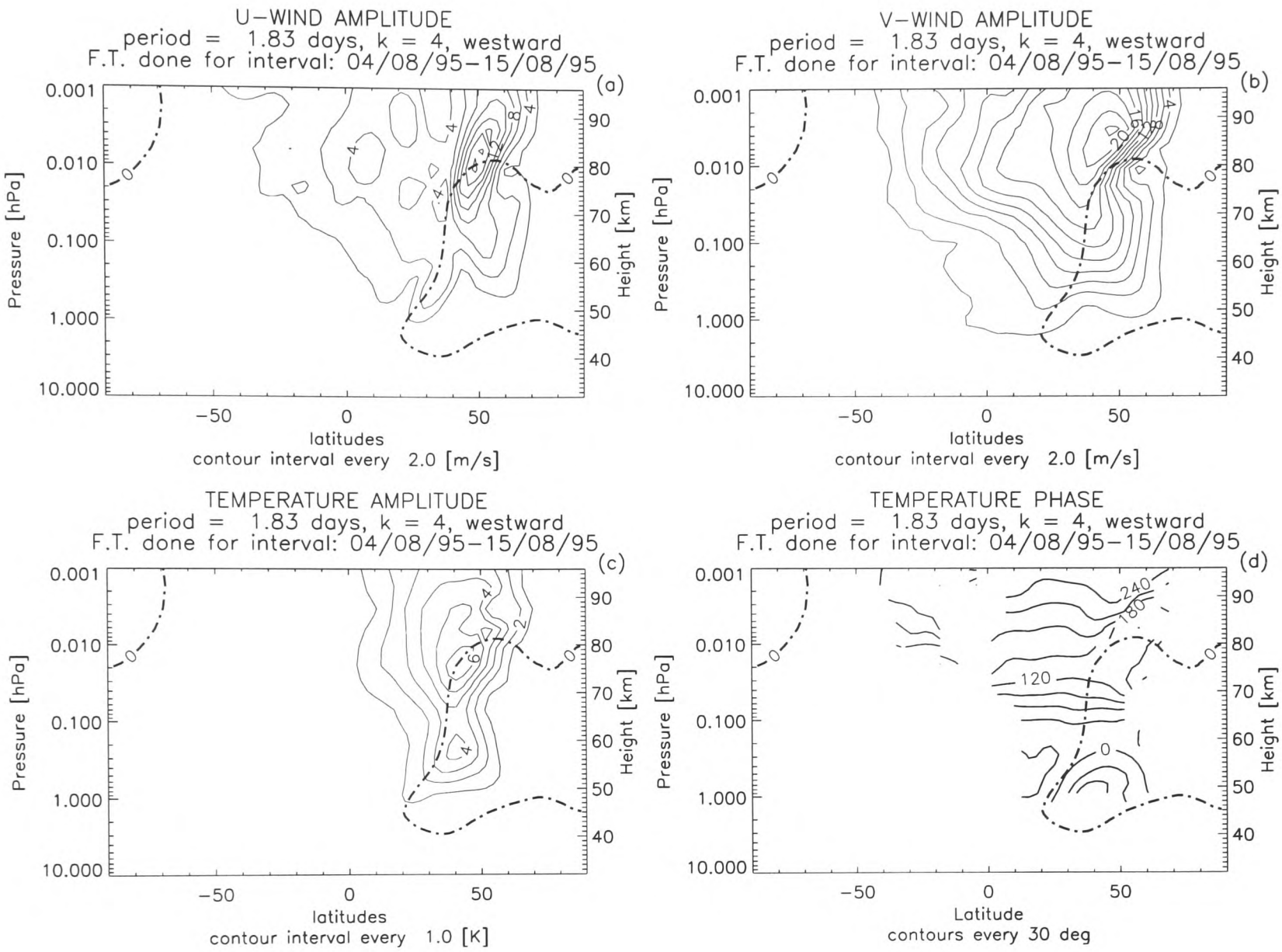


Figure 3.27: (a) u-wind amplitude of the westward propagating quasi 2-day wave k=4, during August Year 2. The bold dot-dashed line is the critical line for this wave ($u - c = 0$). (b) v-wind amplitude, (c) temperature amplitude and (d) temperature phase.

June of Year 2 resembles remarkably the fastest growing mode obtained in the linear instability analysis described in chapter 5. Figure 3.28 shows the spatial structure of this wave.

In Year 3 the spectral analysis for August shows that the period of quasi 2-day-wave does not have a so well defined peak, finding amplitude between 1.95 days and 2.2 days. PV plots show a zonal wavenumber change from k=3 to k=4 at the beginning of August (not shown). As for June and July of Year 3 the wave spectra in the model for August is less clear than in the two previous years, with more transient waves.

The structure of the EP fluxes, the appearance of critical lines, etc; suggest the waves

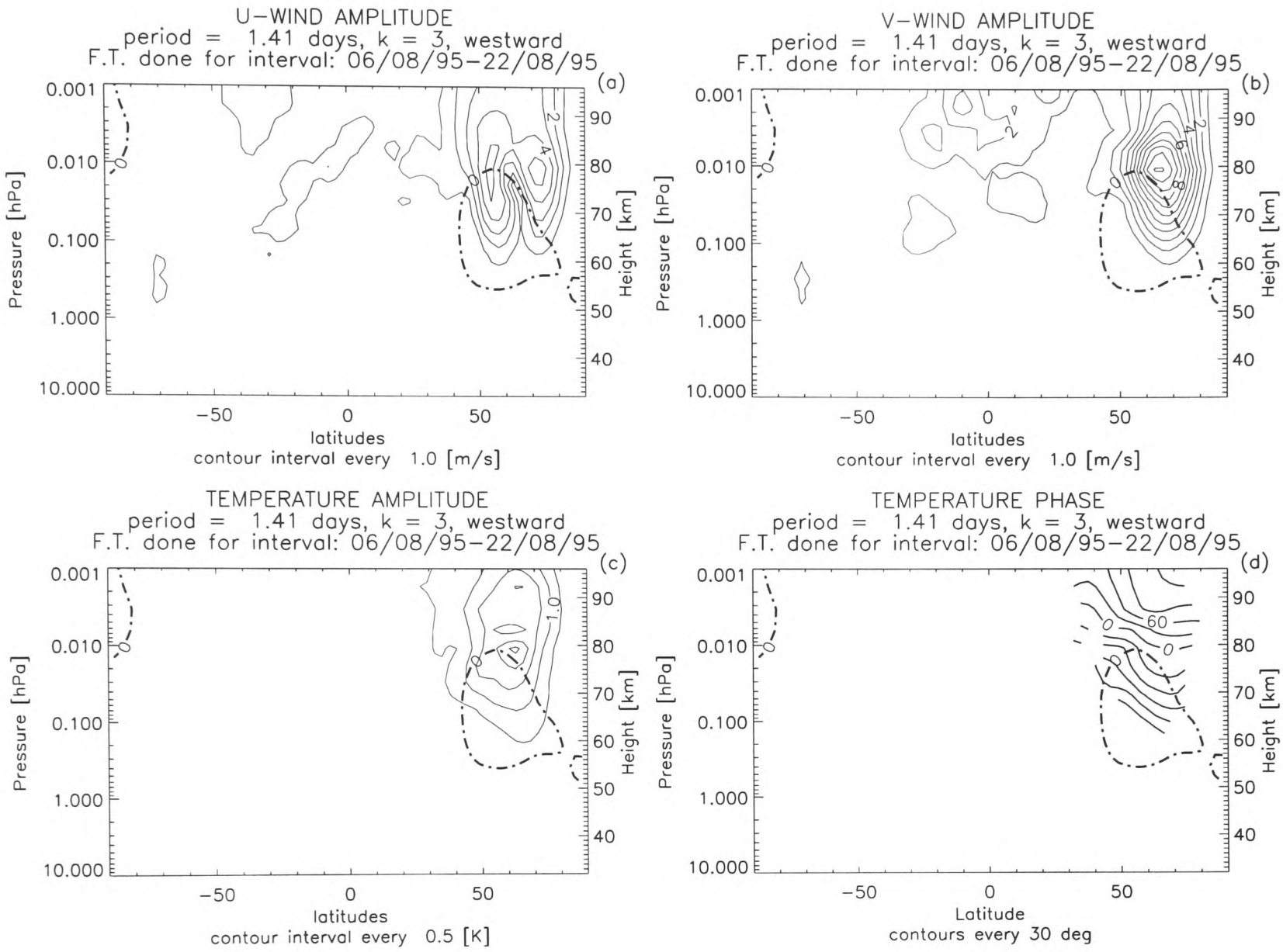


Figure 3.28: (a) u-wind amplitude of the westward propagating 35 hrs wave during August Year 2. The bold dot-dashed line is the critical line for this wave ($u - c = 0$). (b) v-wind amplitude, (c) temperature amplitude and (d) temperature phase.

seen during the JJA period are generated in-situ by some instability process in the summer jet[6].

Throughout the JJA period regions with negative meridional gradients of mean potential vorticity are observed in the northern hemisphere. In Figure 3.30 an intensification of the zonal mean u-wind at 0.018 hPa can be observed around the 20th of July, at the time of most negative $\overline{q}_y$ values. Corresponding positive values of the EP flux divergence are in agreement with the picture of wave activity being generated by an instability of the summer easterly jet. The time of maximum negative $\overline{q}_y$ values coincides with the time of

[6]This is also the result obtained with the instability code for most of the waves, and which will be presented in chapter 5.

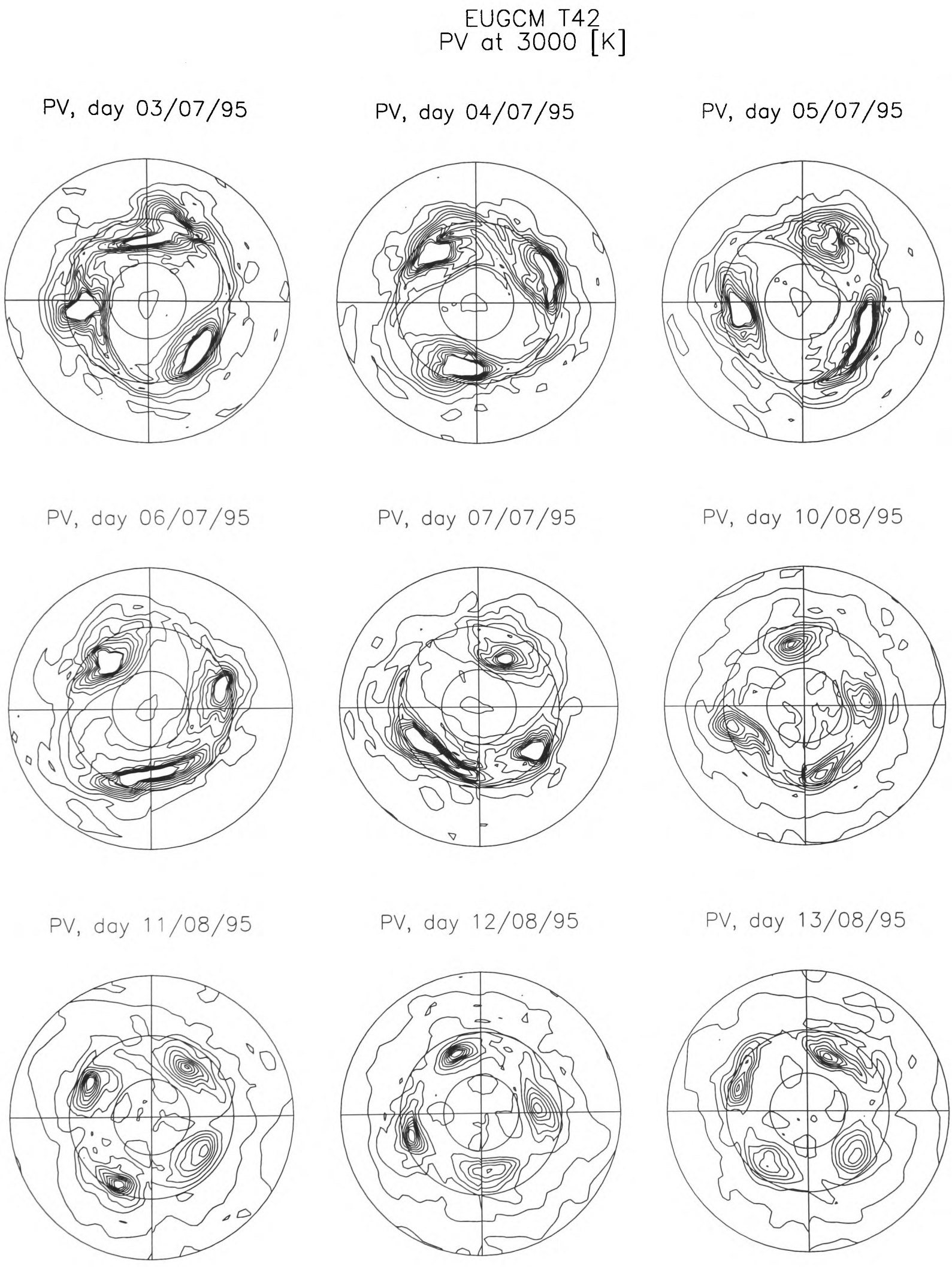


Figure 3.29: Potential vorticity maps at 3000 K for consecutive days from the 3/7/95 to the 7/7/95 (first 5 plots) and then from the 10/08/95 to the 13/8/95.

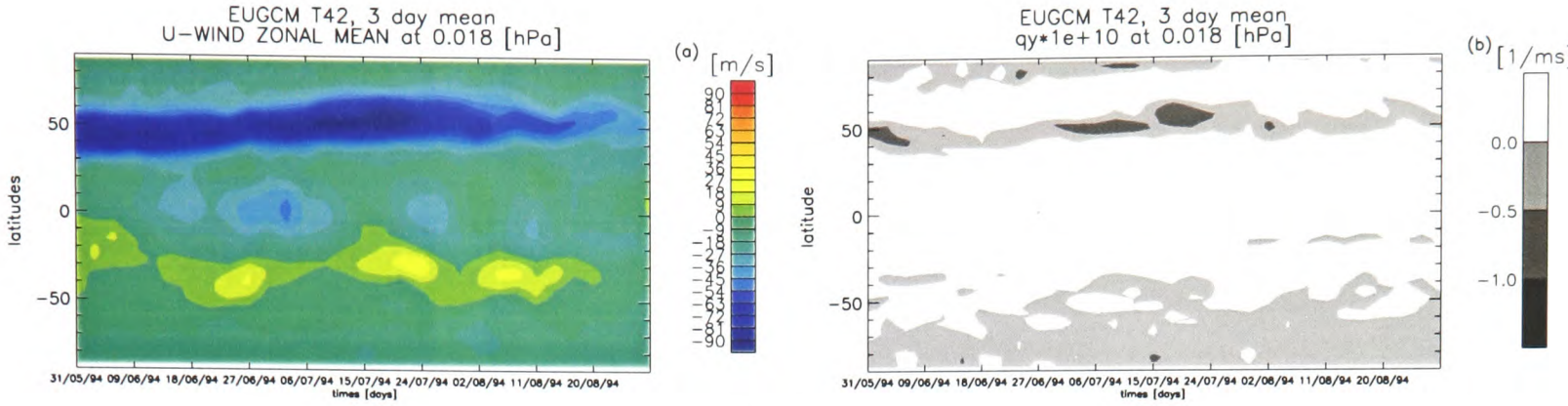


Figure 3.30: (a) Latitude time plot at 0.018 hPa of zonal mean wind, from June Year 1 to September Year 1. (b) same at part (a), but showing $\overline{q}_y$, scaled by $1 \times 10^{+10}$.

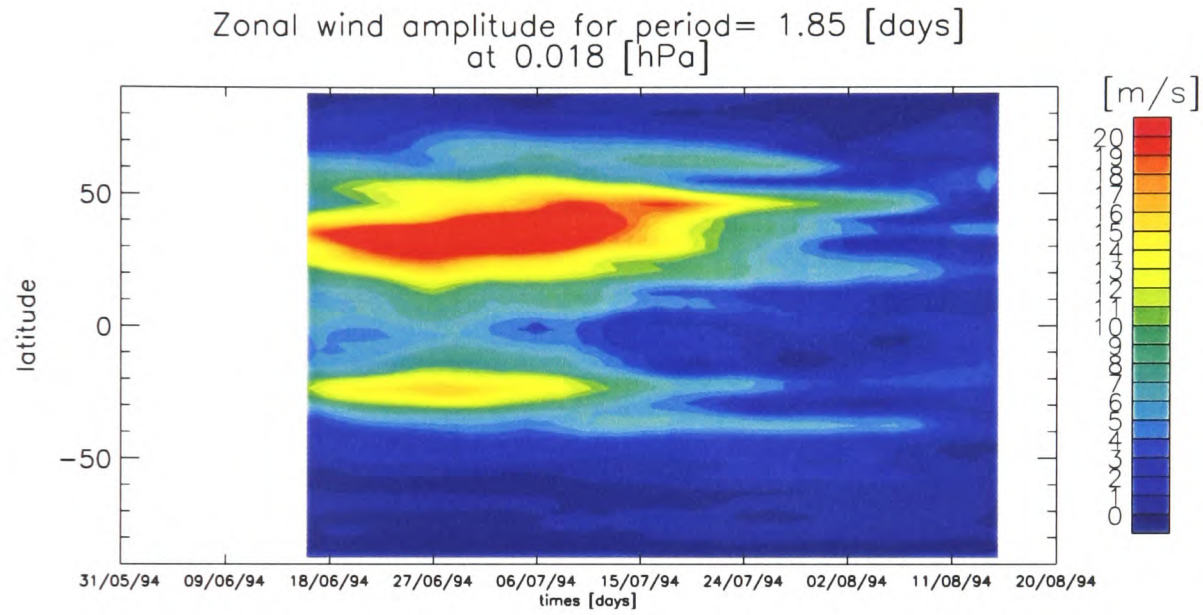


Figure 3.31: Latitude time plot at 0.018 hPa of zonal wind amplitude of period 1.85 days, from June to August Year 1.

large amplitude of the quasi 2-day wave (see Figure 3.31). The positive values of the EP flux divergence associated with the wave then producing an eastward force and reducing the strength of the easterly jet.

3.6 Summary of chapter

In this chapter a comparison between 3 years of EUGCM output with a timeseries of meteor-radar data taken at 53°25'N, 3°53'W and about 90 km height was presented. The comparison showed that the EUGCM is capable of a realistic simulation of the wave activity in the mesosphere. These good results motivated further detailed analysis of the EUGCM. These are summarized as following.

wave	zonal wavenumber	observed in the EUGCM
5-day wave	k=1	Seen around solstice conditions, with larger values in the summer hemisphere. Critical line.
7-day wave	k=1	Not identified with a Rossby normal mode, similar characteristics to 5-day wave. Seen in Feb/March.
16-day wave	k=1	Seen during winter and spring. Large amplitude at high latitudes.
10-day wave	k=1	Seen at equinox in NH. Phase structure not always correct.
4-day wave	k=2	Seen around solstice conditions, with larger values in the summer hemisphere. Critical line.
2-day wave	k=3	Seen in JJA. Critical lines. Similar to (3,0) mode.
1.5-day wave	k=4	Seen in June. Large amplitude in the NH. Critical line.
35 hrs wave	k=3	Seen in June and August. Localized amplitude in the NH. Critical line.

Table 3.1: Table summarising the main characteristics of observed planetary scale waves in the EUGCM.

wave	observed in the meteor-radar data
30-38 hrs wave	Seen in June/August.
2-day wave	Seen in July and August.
4-day wave	Seen around solstice conditions.
5-day wave	Seen around solstice conditions.
6-8 day wave	Seen throughout the year. Larger amplitude found in v-wind.
16-day wave	Seen during winter and spring.
10-day wave	Seen Dec/March. Larger amplitude in u-wind.

Table 3.2: Table summarising the main waves in the meteor-radar data.

In the winter months the diagnosed waves have long periods, ranging from 5 days to 16 days. For the waves with longer periods, characteristics are in agreement with upwards propagating Rossby waves. The EUGCM also produces some waves which can be identified with normal mode Rossby waves, in table 3.1 a summary of the diagnosed waves in the EUGCM is given. The normal mode 4-day wave is seen for both solstice conditions, the 10-day wave and the 16-day wave can be observed during the winter/spring months, in accordance with observations. A 5-day wave is found in the EUGCM as well for both solstice conditions, but the observed characteristics are not as well reproduced as the normal mode 4-day wave. In addition during February/March there is a wave of period around 7 days, with very similar characteristics to the 5-day wave. This wave has not been noted previously, although a wave with period 7 days is found in the UKMO data discussed in chapter 4. In table 3.2 a summary of the waves seen in meteor-radar data is given. A 4-day and 5-day wave are seen for solstice conditions as well. A 16-day and 10-day wave is seen for winter/spring months. The 10-day wave has larger amplitude in the u-wind than in the v-wind, which is the case in the EUGCM as well (and in the UKMO data). Finally throughout the year in the meteor-radar data there are waves with periods between 6-8 days, with larger amplitude in the v-wind. This could be the 7-day wave seen in the EUGCM which also has larger amplitude in the v-wind in the winter hemisphere.

The summer mesosphere produces a variety of waves with periods between 1.5 days and 5 days. Together with evaluating the spatial structure of these waves, the EP fluxes, the background state and critical lines were analysed. All these indicate that these waves are unstable disturbances triggered by baroclinic/barotropic instability of the easterly jet present in summer. The EUGCM produces every year a quasi 2-day wave, which is an ubiquitous feature of the summer mesosphere. The simulation of the wave is realistic in its spatial structure as well as amplitude and period. From global observations this wave is mostly a wavenumber 3 disturbance, but sometimes a wave 4 pattern is seen as well. This feature of the wave is also well reproduced by the EUGCM. The EUGCM shows for June a large amplitude wave of period 1.5 days and for June and August a smaller amplitude

wave with period 35 hrs. Waves with periods between 30-38 hours are also seen in the meteor-radar data for these months.

There is a problem with the waves identified as Rossby normal modes in the EUGCM. From theory and observations the amplitudes of normal modes are greatly reduced in regions of critical lines. This is not the case in the EUGCM, where most of the Rossby normal modes have large amplitude in the critical regions. In particular the amplitude for the normal mode 4-day wave and the 5-day wave is even largest in the critical region. The excitation regions for normal mode-like modes are thought to come from the troposphere and the waves propagate upwards in the atmosphere and upon encountering a critical region cannot propagate further upwards. Theoretical studies find a large amplitude close to the critical line. All this may imply that the excitation of these waves in the EUGCM occur in the critical region, as it is for unstable disturbances. The two hypotheses to explain the large amplitude in the critical region for the Rossby normal modes are then that, either the EUGCM is too unstable and all the waves seen for solstice conditions are forced in the model by instability. The other possibility is that, for large enough amplitudes of the waves (as is the case in the waves found in the EUGCM), these singularities may not exist, since critical lines arise as singularities when doing linear wave analysis.

Chapter 4

Wave spectra in the EUGCM compared with UKMO data

In chapter 3, the wave spectra of the 3-year long EUGCM integration was compared with a timeseries of meteor-radar data taken in the northern hemisphere. In this chapter the output from the EUGCM integration will be compared with UK Meteorological Office (UKMO) assimilation data. The focus will be on the southern hemisphere, where the waves present include the 4-day wave observed at high latitudes in austral winter (see section 1.2.2). Because the UKMO assimilation dataset is global, a more complete comparison can be performed than with the meteor-radar data. However the UKMO assimilation only extends up to 0.3 hPa, and is possibly inaccurate above 1 hPa (Swinbank and O'Neill, 1994). This means that the UKMO assimilation is more useful for studying waves with large amplitude in the upper stratosphere (e.g. the 4-day wave) rather than waves with large amplitude in the upper mesosphere (e.g. the quasi 2-day wave).

The methodology used to study the wave spectra will include, as in chapter 3, the calculation of frequency versus time plots at particular locations. Zonal wavenumber versus frequency plots can then be calculated to obtain information about the zonal structure of the waves and the direction of propagation. The spatial structure, amplitude and phase of the 4-day wave and the other waves found in the EUGCM and the UKMO dataset

will be given, together with the associated background zonal mean wind and temperature structure ($\bar{u}$ and $\overline{T}$).

The chapter starts by giving a short description of the UKMO assimilation data (section 4.1), then the waves in this data (section 4.2) are analysed on a yearly basis and compared with the EUGCM output (section 4.3).

4.1 The UKMO Assimilation dataset

The UK Meteorological Office developed an assimilation system for the stratosphere and mesosphere as part of the Upper Atmosphere Research Satellite (UARS) project. This was done to validate the UARS measurements by providing independent correlative data. The assimilation system was adapted from the UKMO's operational assimilation system used for operational weather forecasting. The numerical model into which the observations are assimilated is the UKMO Unified Model. In the stratosphere, the assimilation system combines a mixture of radiosonde and satellite observations, the main satellite data being the NOAA (National Oceanic and Atmospheric Administration) temperature data from the TIROS-N series of polar orbiter satellites (for further details of the assimilation system see Swinbank and O'Neill, 1994). This provides a self-consistent sequence of three dimensional grid-point analyses of the atmosphere up to the lower mesosphere.

The UKMO dataset includes daily assimilated winds, temperature and geopotential height on 22 levels from the ground to 0.32 hPa. Winds are given at 72 latitudes (from 88.75°S to 88.75°N) and 96 longitudes (from 1.875°E to 358.185°E) and temperature and geopotential at 73 latitudes (from 90°S to 90°N) and 96 longitudes (0°E to 356.25°E). UARS was launched on the 12th of September 1991 and assimilated data are available from October 1991 up to the present date. For this chapter, analysis of winds and temperature data will be presented, on the 10 upper most levels (10 hPa to 0.32 hPa) for the years 1992, 1993 and 1996 (the waves spectra present in the whole lengths of the dataset is well represented by these three years).

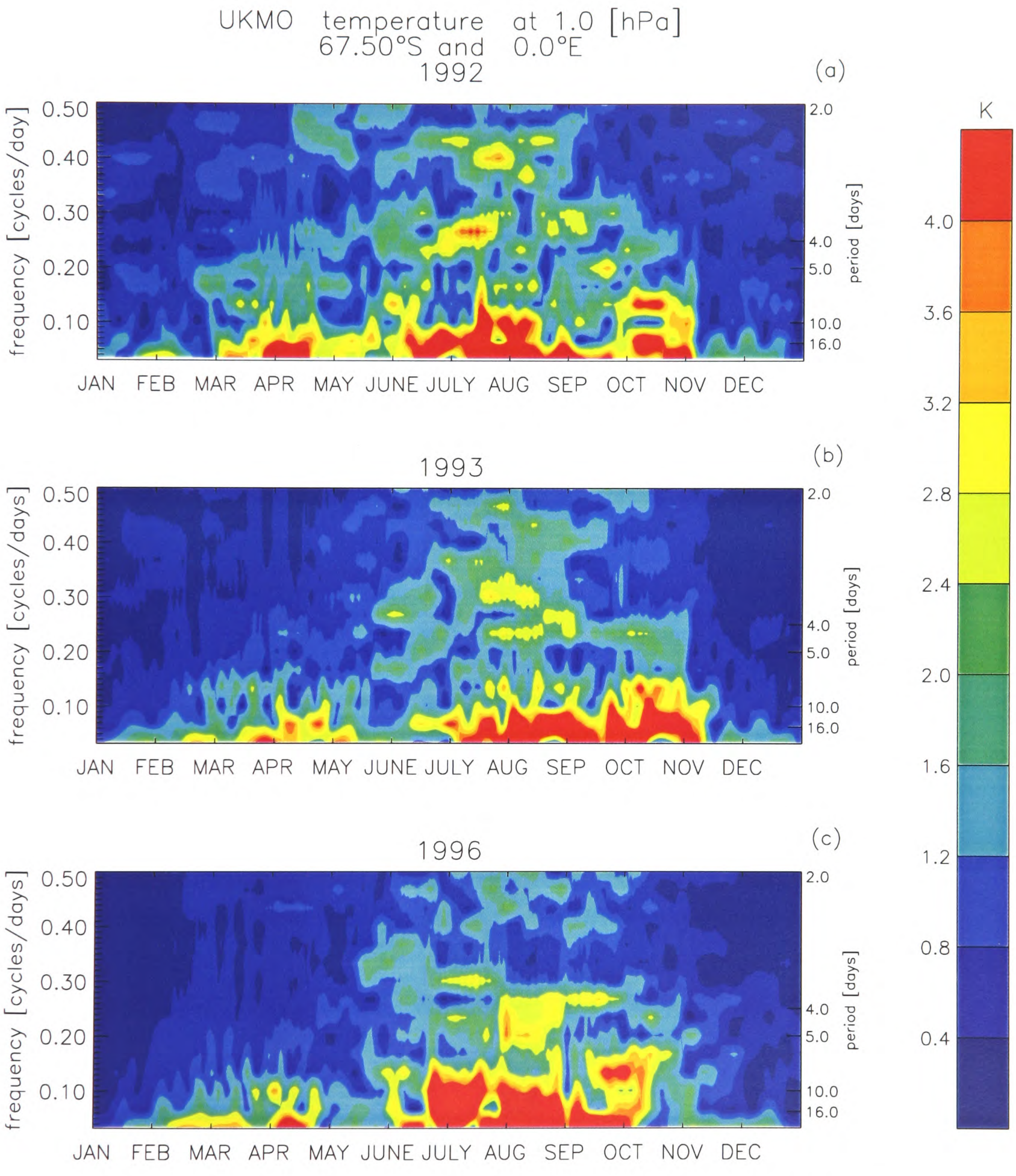


Figure 4.1: Frequency versus time section for temperature of UKMO assimilation data for (a) 1992, (b) 1993 and (c) 1996, at 67.5°S, 0°E and 1.0 hPa altitude.

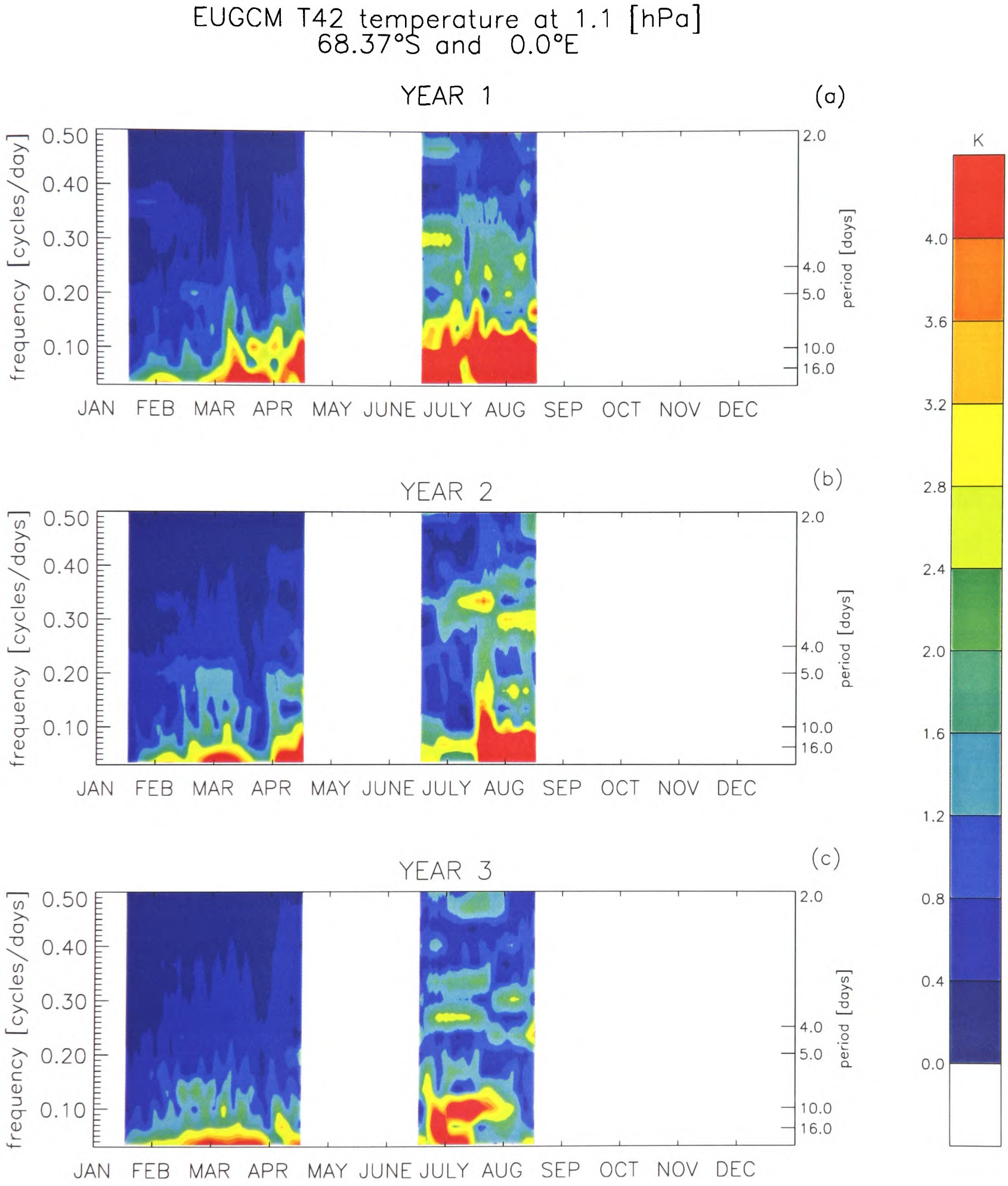


Figure 4.2: Frequency versus time section for temperature for EUGCM data for Year 1 (a), Year 2 (b) and Year 3 (c), at 68.3°S, 0°E and 1.1 hPa of altitude. White denotes times when high frequency data was not kept.

4.2 UKMO wave spectra

As in the comparison of the EUGCM with the meteor-radar data described in chapter 3, frequency versus time plots have been constructed from the UKMO data. A 32 day window is Fourier transformed in time and then moved by one day and Fourier transformed again. The process is repeated for the complete length of the timeseries. Because UKMO data are available only daily, the largest frequency resolved is 0.5 cycles per day, i.e., a period of 2 days. Figure 4.1 shows the timeseries of frequency spectra of temperature at 67.5°S, 0°E and 1 hPa.

The dataset captures some of the known planetary scale waves over the height range analysed, for the case of the low frequency waves (periods greater than 5 days). By calculating frequency versus zonal wavenumber spectra, many waves come out as either stationary waves (represented as an eastward and westward propagating wave by the Fourier transform), or as quasi-stationary waves (very long periods), with mostly zonal wavenumber 1 and less often zonal wavenumber 2 (e.g. in Figure 4.3a waves with frequencies less than 0.2 cycles per day are quasi stationary waves). So, most of the waves in Figure 4.1 are upward propagating Rossby waves, with not very coherent spatial structures.

Due to the height coverage of the UKMO assimilation data, a quasi 2-day wave signal is not found in this dataset with the exception of 1994, when a very weak signal at 2 days and zonal wavenumber 4 was found in geopotential (it could not be seen in temperature and wind, and is therefore not shown).

4.2.1 1992 data

The main waves at 67.5°S seen in Figure 4.1 for 1992 with periods shorter than 5 days are: a 3 day wave in August/September, a 4 day wave in June, and a 2.5 day wave in September.

Analysis of the wavenumber versus frequency spectra (e.g. Figure 4.3a) at a given latitude and altitude reveals the presence, from the beginning of June until the end of August, of an eastward propagating 4-day wave, with zonal wavenumber 1. The wave

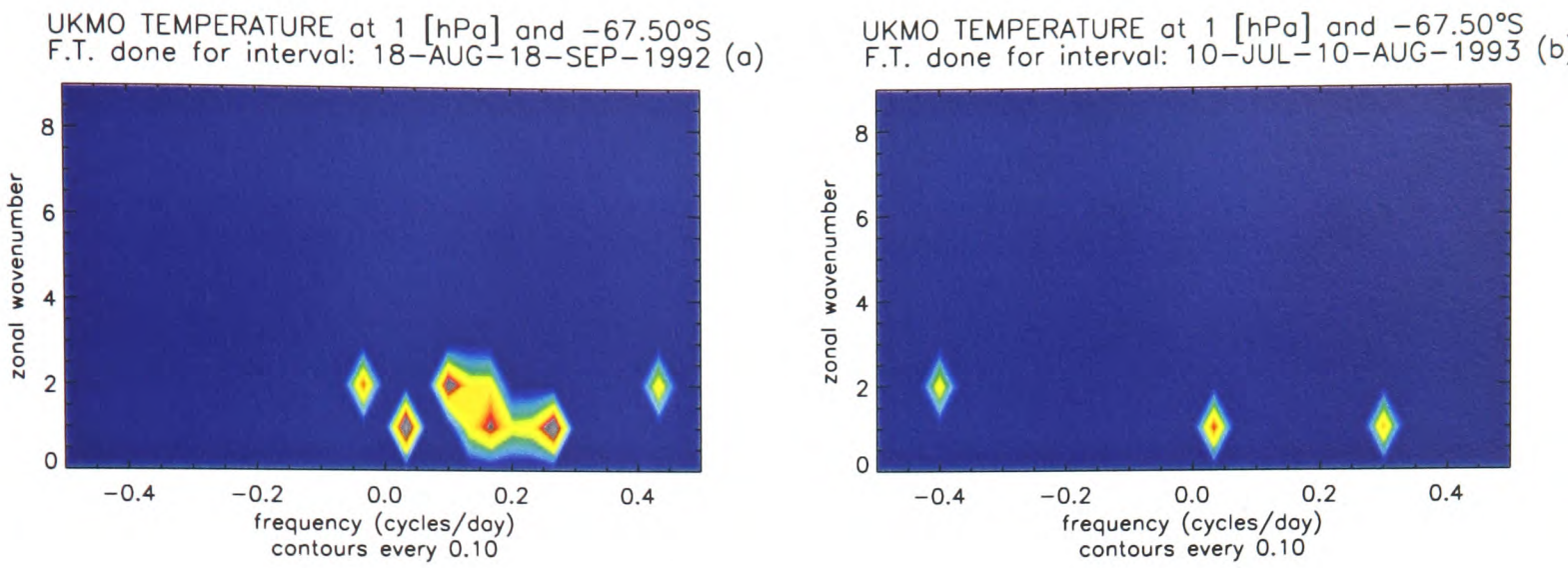


Figure 4.3: (a) zonal wavenumber versus frequency plot of temperature at 67.5°S and 1 hPa for August/September 1992. Positive (negative) frequencies indicate eastward (westward) propagation. (b) same as (a), but for July/August 1993.

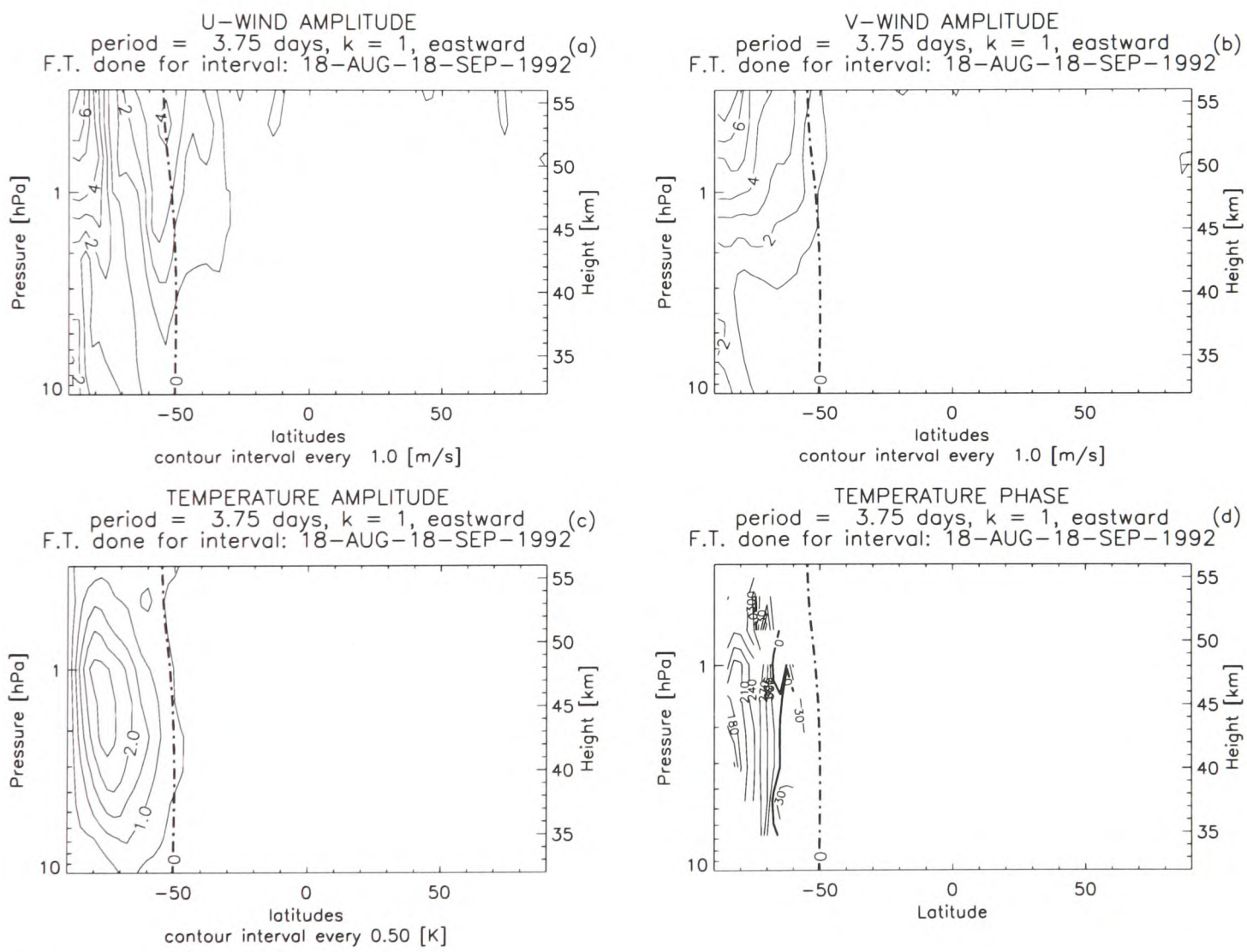


Figure 4.4: (a) u-wind amplitude of the eastward propagating 4-day wave during August/September 1992. In bold dot-dashed line is the critical line for this wave ($u - c = 0$). (b) v-wind amplitude, (c) temperature amplitude and (d) temperature phase.

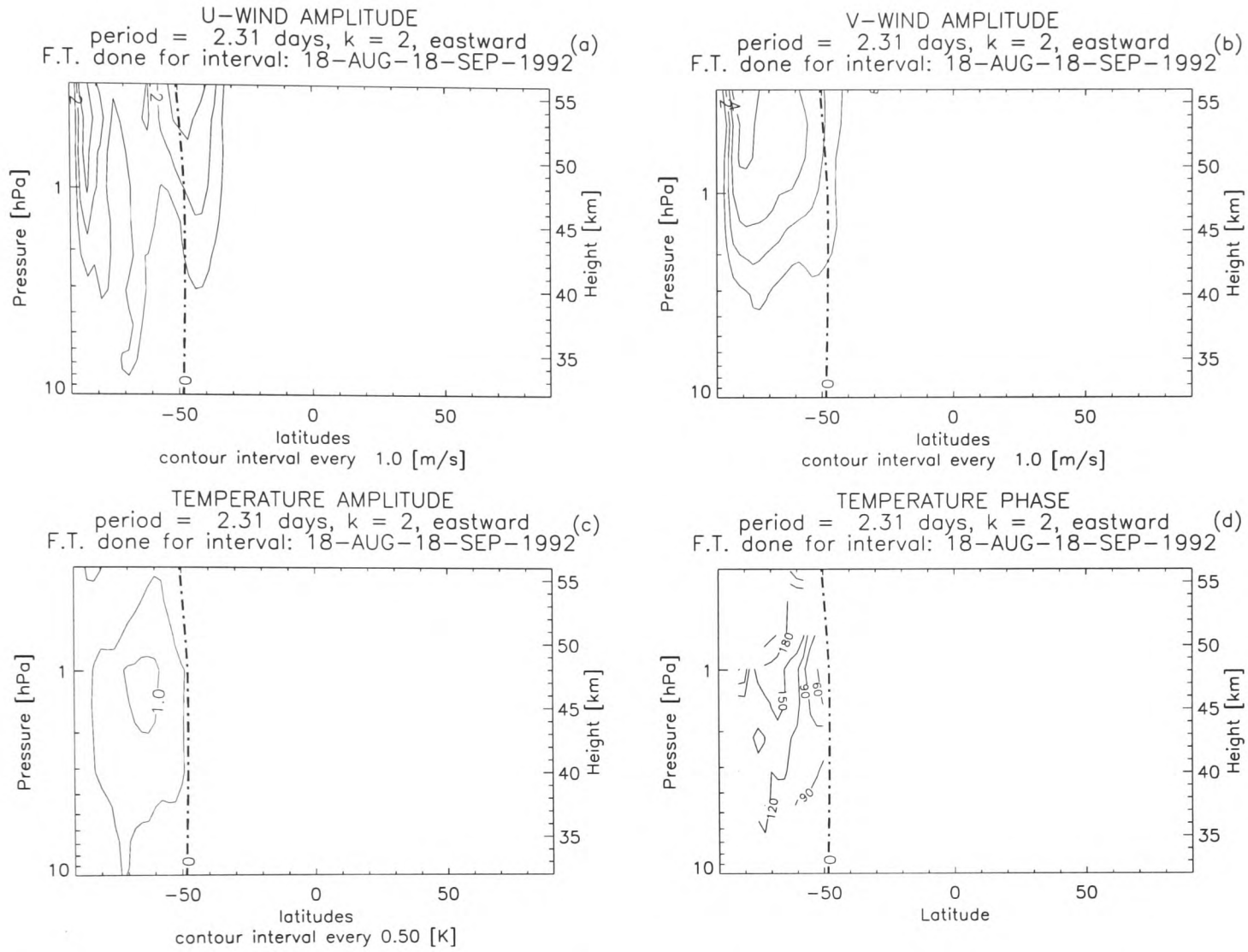


Figure 4.5: (a) u-wind amplitude of the eastward propagating 2.3-day wave during August/September 1992. In bold dot-dashed line is the critical line for this wave ($u - c = 0$). (b) v-wind amplitude, (c) temperature amplitude and (d) temperature phase.

changes from a period of 4.2 days in June to 3.7 days in August. The wave also shifts poleward with time. The maximum amplitude in temperature moves from 60°S in June to almost 80°S in August. Figure 4.3a shows the wavenumber frequency spectra of the temperature field at 67.5°S and 1 hPa calculated for the period 18th of August to 18th of September 1992. Various peaks at zonal wavenumber 1 can be seen in the plot in the range from 0.2 cycles per day to -0.2 cycles per day. From their spatial structures most of them can been identified with upward propagating Rossby waves from the lower atmosphere. At 0.25 cycles per day there is a large peak corresponding to the eastward propagating 4-day wave. Figure 4.4 shows the spatial structure of this wave (which has a period of 3.8 days in this time interval). As reported in other studies, the wave is confined to very high latitudes (Stanford, 1997 and references therein). The phase of temperature is almost

vertical (Figure 4.4d), as are the phases of the wind components of the wave (not shown), indicating that the wave is barotropic. The zonal wind amplitude (Figure 4.4a) shows a double peak in the horizontal at 75°S and 60°S, while there is a single peak in meridional wind and temperature (Figures 4.4b and 4.4c). It has been reported previously that the temperature structure has a double peak in the vertical at around 48 km and 60 km (Allen *et al.*, 1997). Allen *et al.*, (1997) analysed temperature data from the Microwave Limb Sounder (MLS) instrument on the Upper Atmosphere Research Satellite. Their data span the region from 22 hPa to 0.1 hPa (i.e., up to 64 km). The double peak is not seen in the UKMO analysis, because the data only goes up to 56 km; there may be a second peak higher up. Notice that, although the 4-day wave is thought to be generated by barotropic instability, the wave has no significant amplitude at the critical line (Figure 4.4). In Figures 4.6 and 4.7 the background conditions for July and August 1992 are shown respectively. Potentially unstable regions are found for both months on the poleward flank of the polar night jet, most significantly above 50 km south of 70°S.

In Figure 4.3a at zonal wavenumber 2 there is a smaller peak at 0.45 cycles per day, which corresponds to an eastward propagating wave with period 2.3 days. This has also been reported in previous studies (e.g. Prata, 1984). The spatial structure of the 2.3 day wave is shown in Figure 4.5, and it is very similar to the 4-day wave, but with smaller amplitude.

A zonal wavenumber versus frequency of temperature shows for the period from June to September 1992. In addition to the 4-day wave, a '2-day' wave at high latitudes in the southern hemisphere in the data[1]. The wave has a zonal wavenumber 2 and propagates westward (its structure is shown in Figure 4.8). As with the 4-day wave, this wave undergoes a period shift, in this case from 2.2 days to 2.5 days. This is accompanied with a poleward shift in wave amplitude.

During March, a 10-day wave is present (which is better seen in frequency time cross sections of zonal wind than of temperature or meridional wind). The wave is westward propagating with zonal wavenumber 1. The structure of the wave for 1996 is shown in

[1]This wave has nothing to do with the quasi 2-day wave.

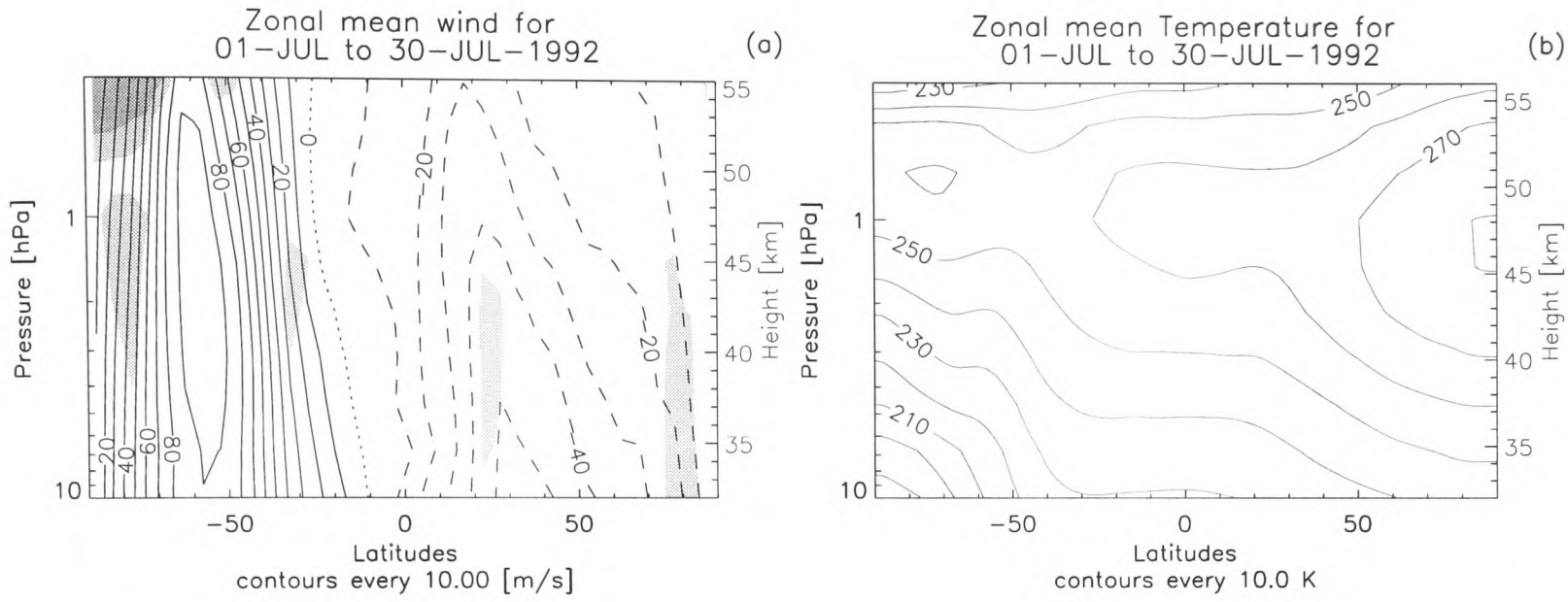


Figure 4.6: (a) zonal mean $u-$wind for July 1992. Shaded regions are where $\overline{q}_y < -1 \times 10^{-11}$ [$m^{-1}s^{-1}$], with light grey for values between -1 to -5×10^{-11} and dark grey for values less than -5×10^{-11}. (b) zonal mean temperature for July 1992.

Figure 4.13. The EUGCM also shows a 10 day wave in March which was identified with a Rossby normal mode wave (section 3.5.1.3). Although the wave in the EUGCM has largest amplitude in the upper mesosphere, the two lower temperature peaks at midlatitudes (at around 60 km in Figure 3.16c) coincide well with the peaks of the UKMO 10-day wave.

4.2.2 1993 data

In 1993, as in 1992, the two main waves present during the JJA season are the eastward propagating 4-day wave and the westward propagating wave with period close to 2 days (Figure 4.3b). Both waves have similar structure peaking at very high latitudes in the southern hemisphere. The '2-day' wave has a zonal wavenumber 2 structure and a period of 2.3 days in June, which then changes to 2.5 days in July/August. Figure 4.8 shows the spatial structure. It can be seen that all the fields show a poleward tilt with height, and the wave has no critical line. This wave has also been reported by Venne and Stanford (1982) and is seen in all years of the UKMO data analyzed. Note though that both the UKMO and the data analyzed in Venne and Stanford (1982) are daily data and therefore the wave could have been aliased. An eastward propagating wave with period less than 2

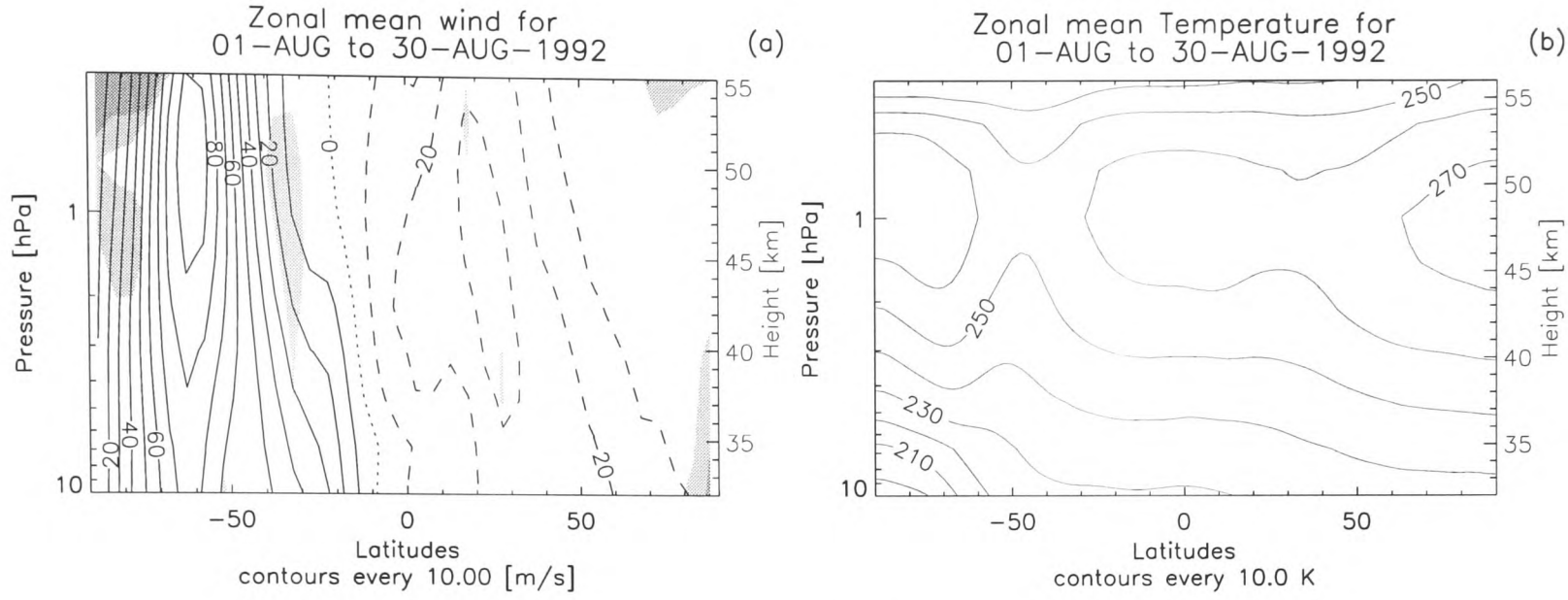


Figure 4.7: (a) zonal mean u-wind for August 1992. Shaded regions are where $\bar{q}_y < -1 \times 10^{-11}$ [$\mathrm{m^{-1}s^{-1}}$], with light grey for values between -1 to -5×10^{-11} and dark grey for values less than -5×10^{-11}. (b) zonal mean temperature for August 1992.

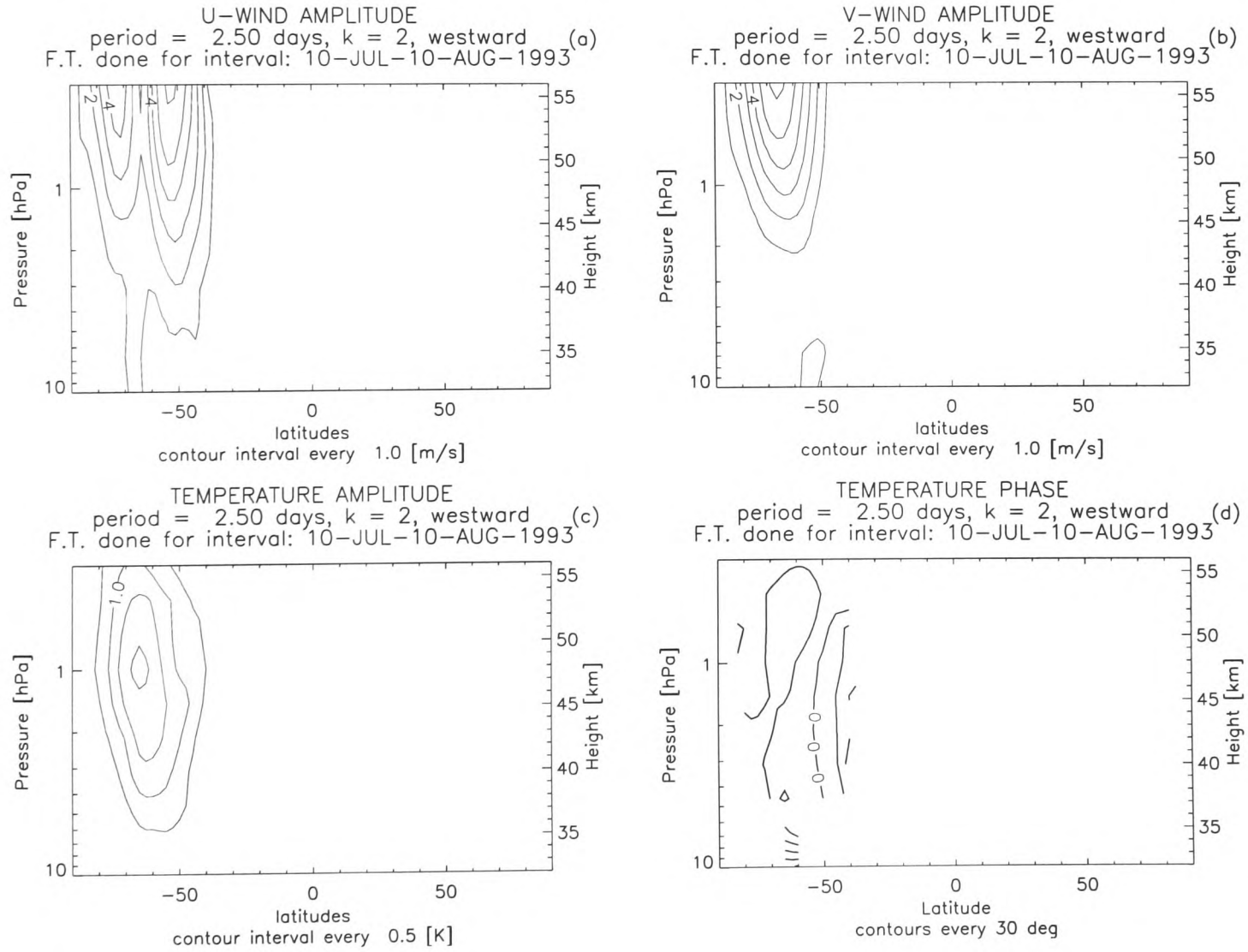


Figure 4.8: (a) u-wind amplitude of the westward propagating 2.5 day wave during July 1993. In bold dot-dashed line is the critical line for this wave ($u - c = 0$). (b) v-wind amplitude, (c) temperature amplitude and (d) temperature phase.

days, say 1.7 days (a period of 2 days corresponds to the Nyquist frequency) would come out in the Fourier transform as a westward propagating wave with period 2.5 days.

Significant wave amplitude is found for periods between 3 and 4 days through July to September in 1993 (see Figure 4.1b). In July, there is large amplitude at 3.3 days, in July/August there is large amplitude at 3 days, for August large amplitude is found at 4 days and finally in September large amplitude at 4.2 days. The structure of the wave in September is shown in Figure 4.9; it differs slightly from the wave seen in 1992 (Figure 4.4). In particular, the wave's amplitude tilts equatorwards with height, as opposed to the slight poleward tilt seen for the wave in 1992. The phase structure remains vertical, similar to the wave in 1992. Also, the amplitude of the wave is slightly greater in 1993 compared with 1992.

Figure 4.10 shows a polar stereographic projection of the southern hemisphere where temperature has been plotted for consecutive days in September 1993 at 1 hPa. At very high latitudes a warm pool of air can be seen to circle the pole eastwards with a period of about 4 days.

4.2.3 1996 data

In 1996, as in 1992 and 1993, there are an eastward propagating 4-day wave and a westward propagating 2-day wave present at high latitudes in the southern hemisphere winter. However, in 1996 there is also a 4-day wave in the northern hemisphere winter, its spatial structure is shown in Figure 4.11. It is an eastward moving wave with zonal wavenumber 1 and its structure is very similar to the equivalent wave in the southern hemisphere (compare with Figure 4.4). The amplitudes are comparable and the phase lines are vertical for the wind components (not shown). However, the phase lines of the temperature seem more noisy and less vertical than the phase lines of the 4-day wave found in the southern hemisphere (e.g. compare Figure 4.11d with Figure 4.4d). One difference with respect to the southern hemisphere 4-day wave is that in the northern hemisphere the wave does have a critical line. The background wind for February, shown in Figure 4.14, in the northern hemisphere has considerably smaller values than in July or August in the

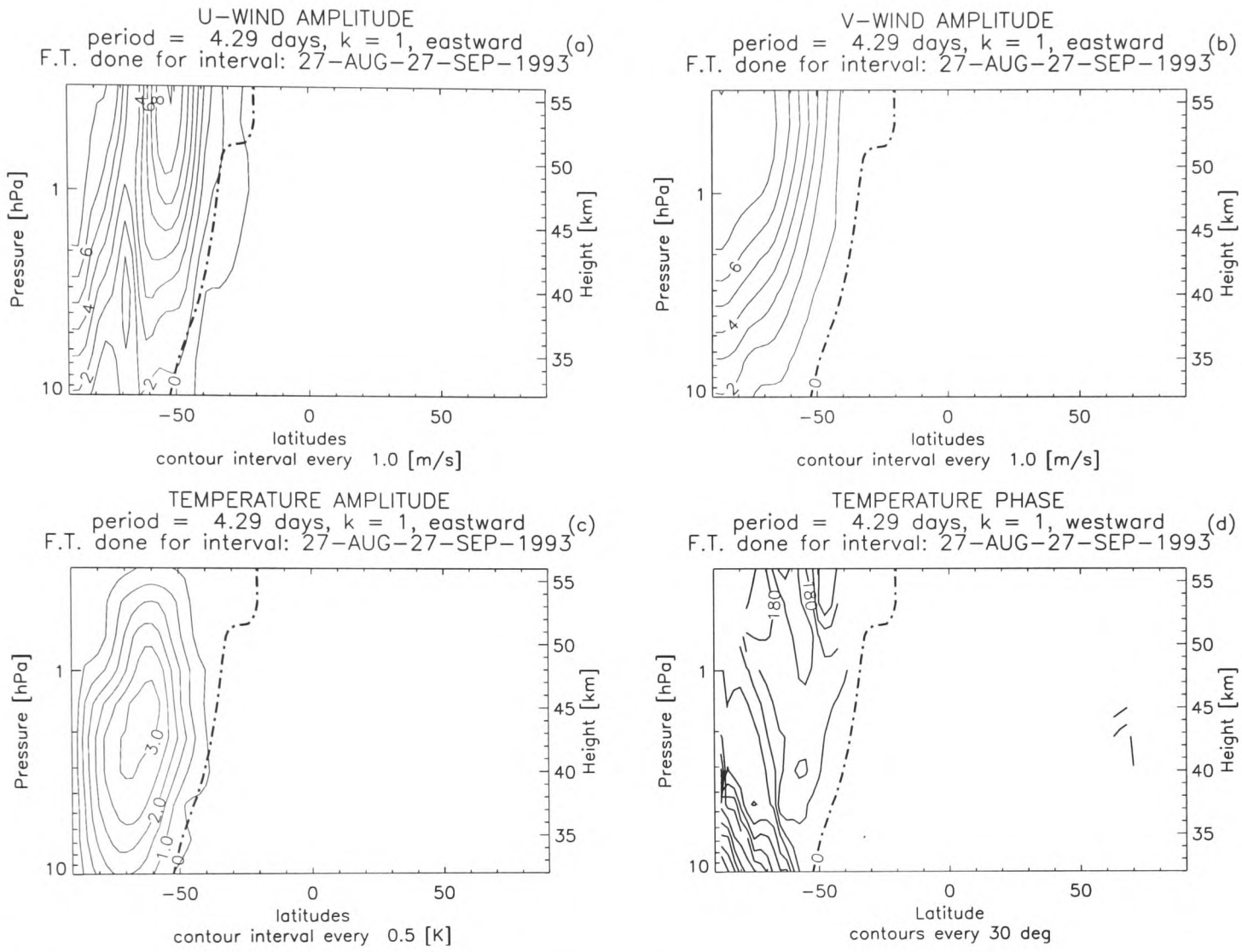


Figure 4.9: (a) u-wind amplitude of the eastward propagating 4-day wave during September 1993. In bold dot-dashed line is the critical line for this wave ($u - c = 0$). (b) v-wind amplitude, (c) temperature amplitude and (d) temperature phase.

southern hemisphere, where winds reached values up to $100\,\mathrm{m\,s^{-1}}$, whereas in February maximum values in the northern hemisphere are about $40\,\mathrm{m\,s^{-1}}$.

In 1996 there are 3 other planetary scale waves found, which have previously been found in the EUGCM. During March there is a wave with period 7.5 days that is westward moving with zonal wavenumber 1 (Figure 4.12). The structure agrees well with the 7 day wave seen in the EUGCM (compare with Figure 3.11).

In April there is a 10-day wave; the amplitude and phase is shown in Figure 4.13. It is westward moving with zonal wavenumber 1. Again, the EUGCM 10-day wave compares well with this wave (see Figure 3.16).

In July 1996 a small amplitude 5-day wave is found, which has zonal wavenumber 1 and propagates westwards. Its spatial structure is shown in Figure 4.15. Although the

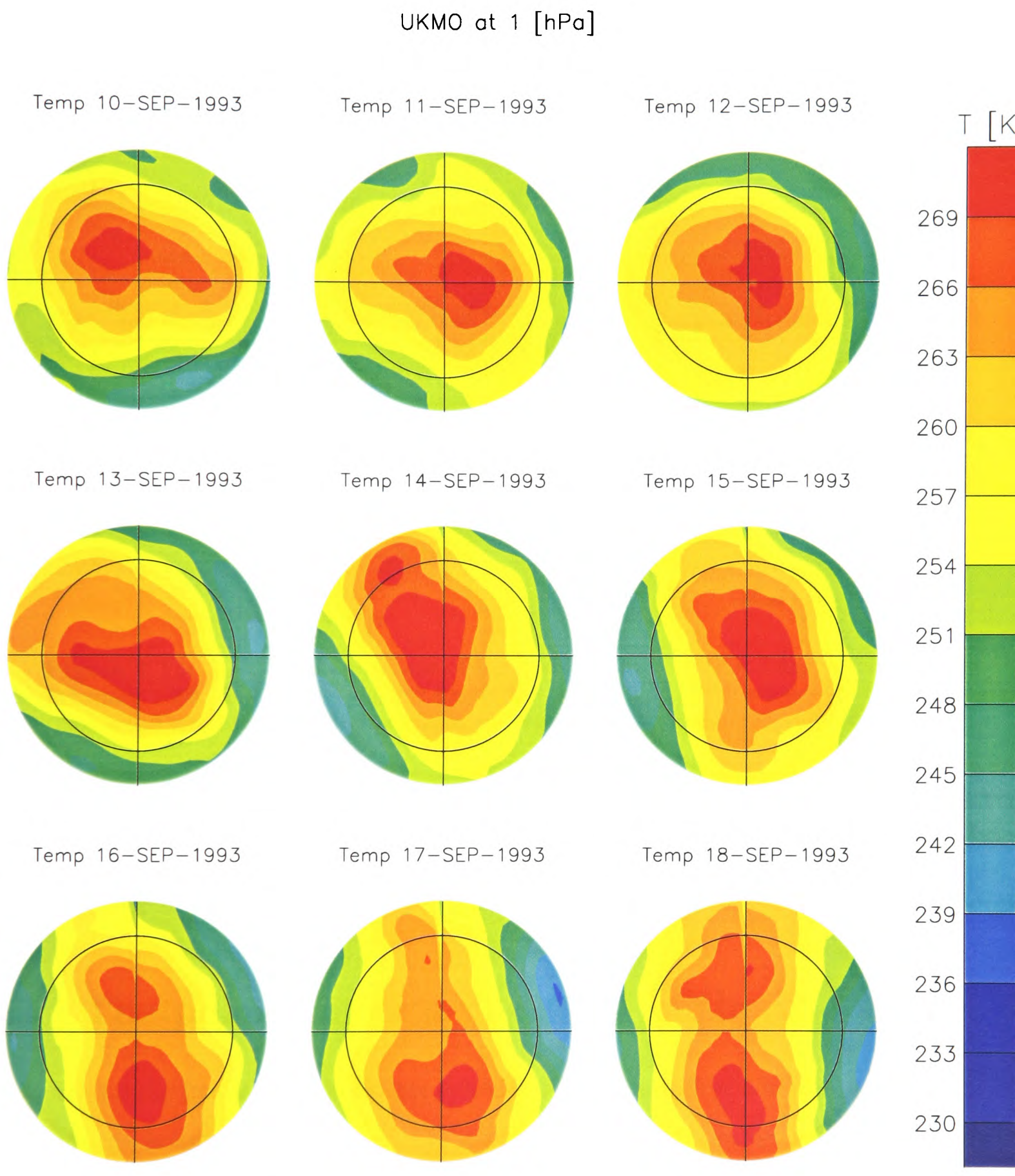


Figure 4.10: Southern hemisphere UKMO temperature for the period 10-18 of September 1993, at 1 hPa. The outer circle is 50°S.

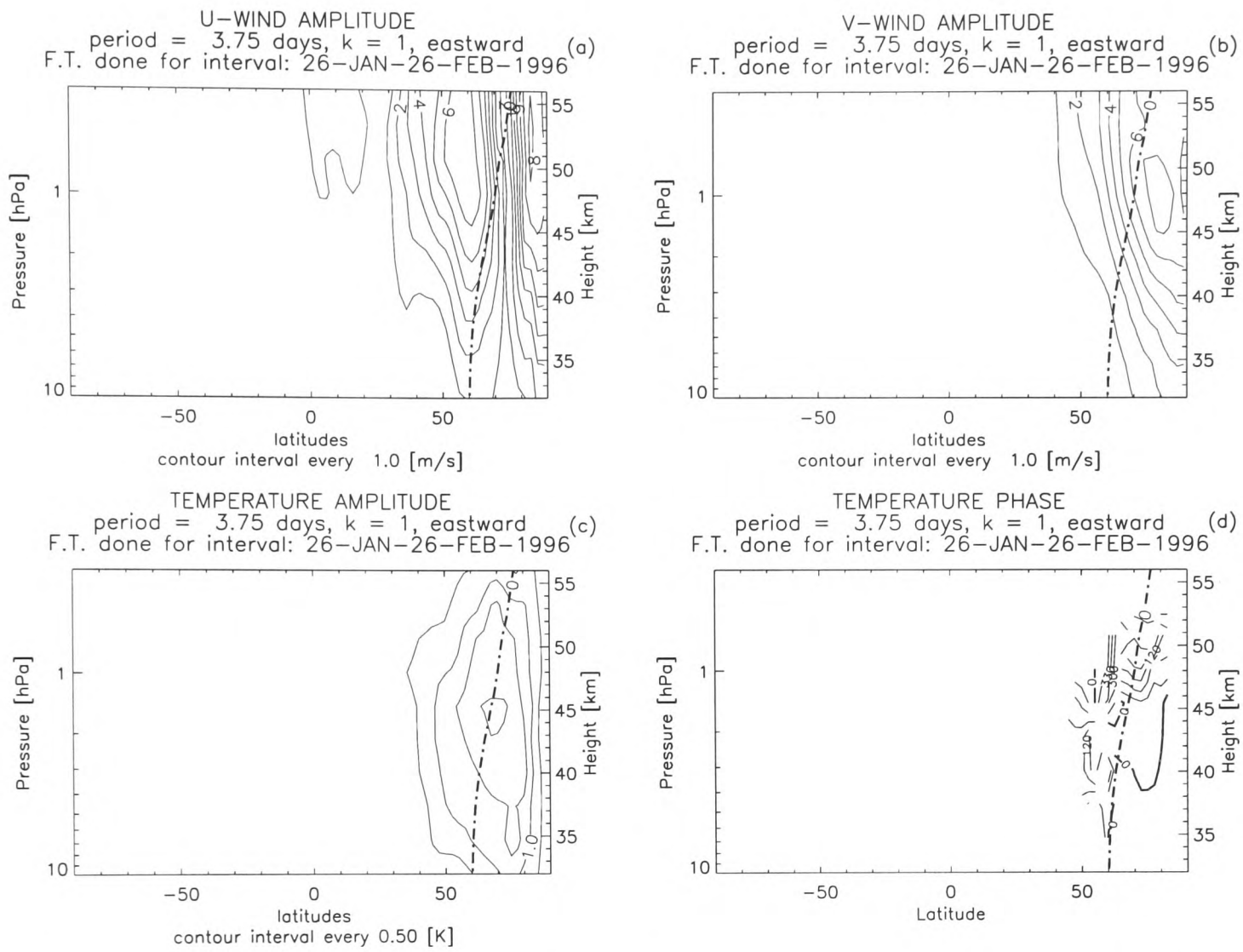


Figure 4.11: (a) u-wind amplitude of the eastward propagating 4-day wave during February 1996. In bold dot-dashed line is the critical line for this wave ($u - c = 0$). (b) v-wind amplitude, (c) temperature amplitude and (d) temperature phase.

amplitude is small, the known characteristics of the 5-day wave can be observed, namely temperature and wind structure peaking at midlatitudes. As opposed to the 7-day wave and the 10-day wave, the 5-day wave has a critical line.

4.3 The polar winter 4-day wave in the EUGCM

In Figure 4.2 the frequency versus time spectra for temperature at 1 hPa from the EUGCM is shown. Six hourly output data at 1 hPa from the EUGCM was not available for May to June and for September to December, because the EUGCM history files could no longer be read after the closure of the J90 Cray computer in March 1999. Figure 4.2 was therefore constructed from the months when 6-hourly data was available. Nevertheless it is possible to see that general features agree in Figures 4.1 and 4.2. During the austral summer and

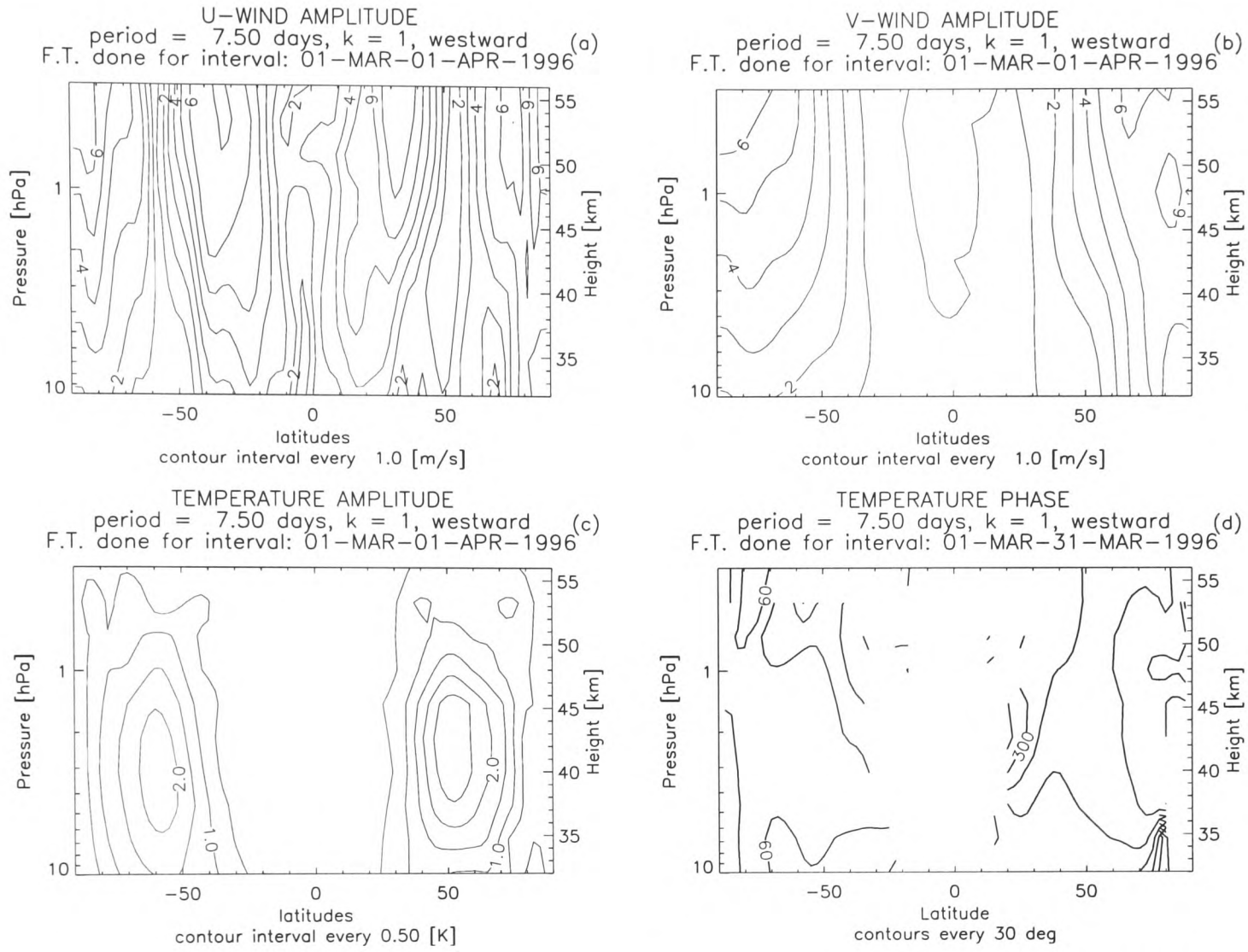


Figure 4.12: (a) u-wind amplitude of the westward propagating 7-day wave during March 1996. In bold dot-dashed line is the critical line for this wave ($u - c = 0$). (b) v-wind amplitude, (c) temperature amplitude and (d) temperature phase.

autumn, wave activity is seen mostly at frequencies less than 0.2 cycles per day. During the JJA season, the characteristic waves with period between 2.5 days and 4.5 days are seen for the three years of the EUGCM data.

Figure 4.16 shows daily synoptic maps of EUGCM temperature in the southern hemisphere from 02/08/93 to 10/08/93 at 0.9 hPa. A warm pool of air can be seen circling the pole eastward with an approximate period of 4 days (this is the same time period as shown in Figure 10 of NT97). The position of the warm pool agrees well with the UKMO data as seen in Figure 4.10; note however that the mean temperature in the EUGCM is about 10 K warmer than the UKMO data.

The 4-day wave at high latitudes in the southern hemisphere winter is seen in the EUGCM in all three years as an eastward propagating wave with zonal wavenumber 1. In

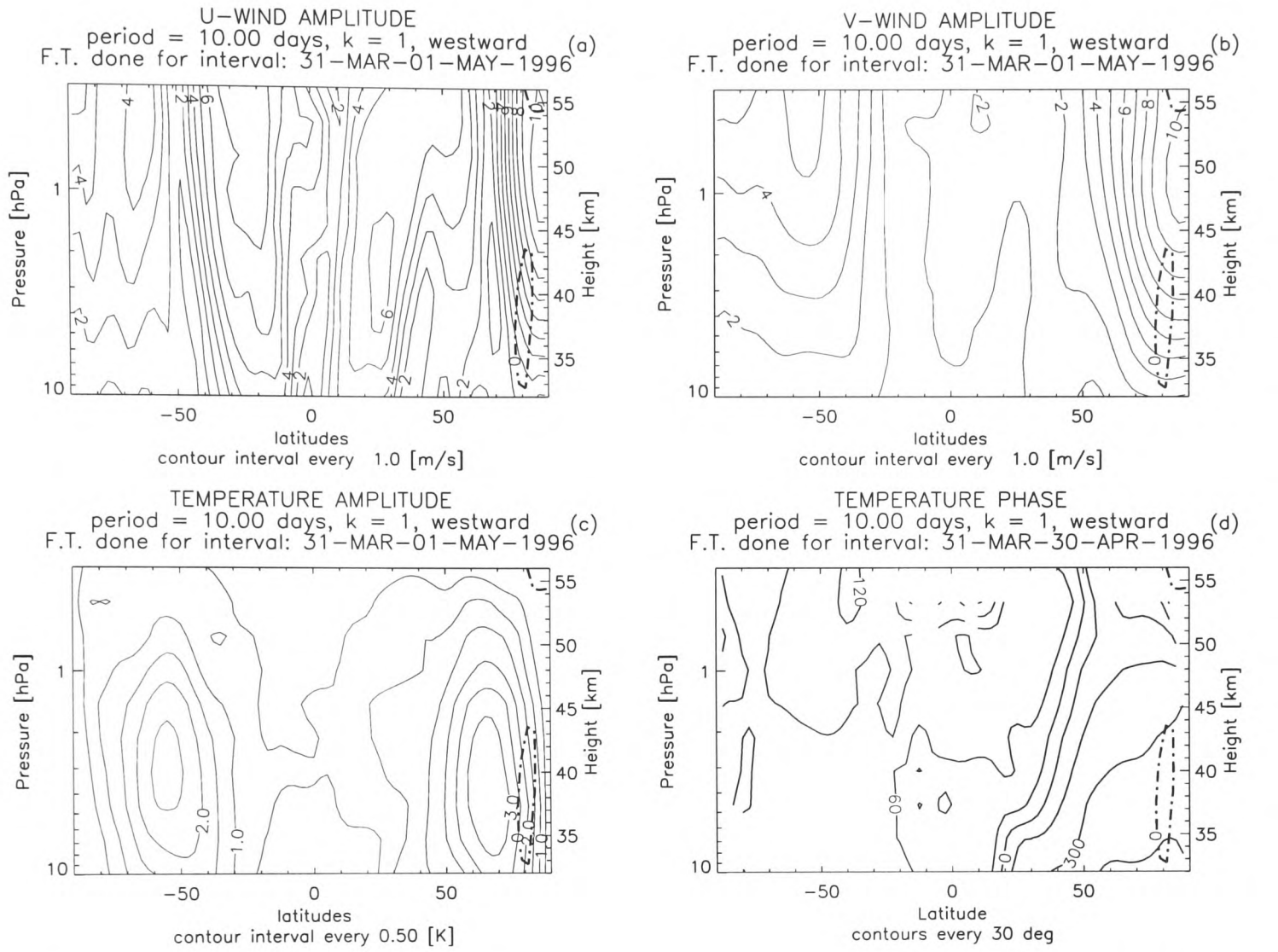


Figure 4.13: (a) u-wind amplitude of the westward propagating 10-day wave during April 1996. In bold dot-dashed line is the critical line for this wave ($u - c = 0$). (b) v-wind amplitude, (c) temperature amplitude and (d) temperature phase.

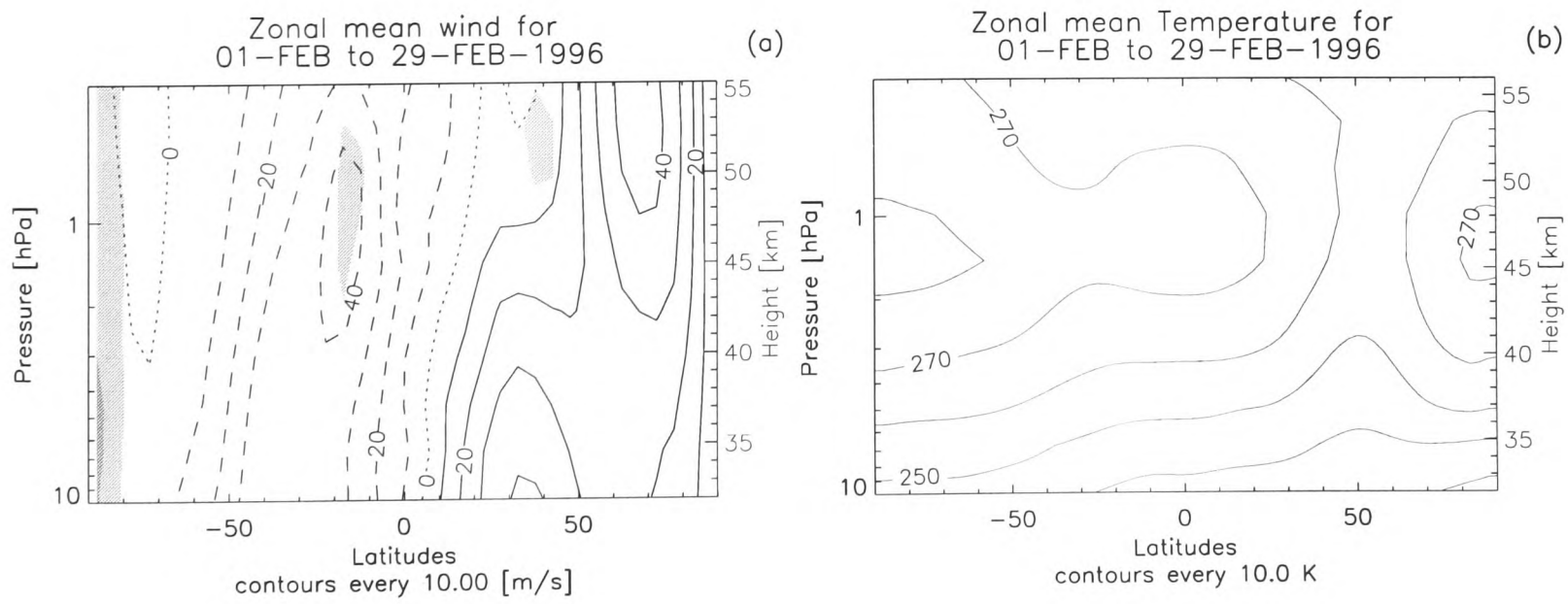


Figure 4.14: (a) zonal mean u-wind for February 1996. Shaded regions are where $\bar{q}_y < -1 \times 10^{-11}$ [$\mathrm{m^{-1}s^{-1}}$], with light grey for values between -1 to -5×10^{-11} and dark grey for values less than -5×10^{-11}. (b) zonal mean temperature for February 1996.

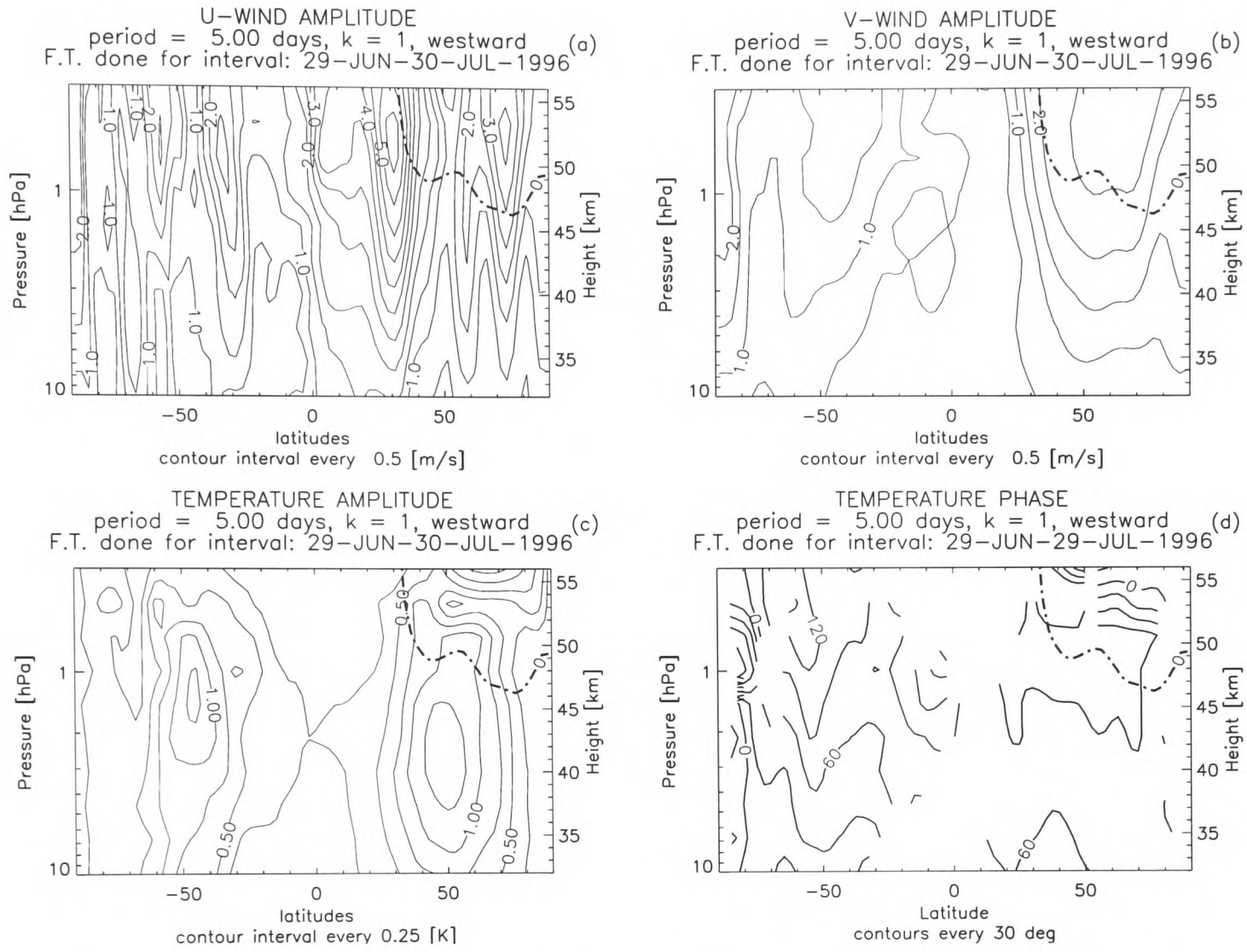


Figure 4.15: u-wind amplitude of the westward propagating 5-day wave during July 1996. In bold dot-dashed line is the critical line for this wave ($u - c = 0$). (b) v-wind amplitude, (c) temperature amplitude and (d) temperature phase.

Year 1 there is a wave with period of 3.5 days present during the last 15 days of June. Figure 4.18 shows the spatial structure and phase of the wave. The wave is plotted for the height range 10 hPa to 0.01 Pa (i.e., extending higher than for the UKMO data). The structure compares remarkably well with the wave in the UKMO assimilation data, over the overlapping height range (compare with Figure 4.4 and 4.11). The wave in the EUGCM extends up into the upper mesosphere. Amplitude of the 4-day wave in the mesosphere has been reported previously by Lawrence *et al.*, (1995), when analysing radar observations in the southern hemisphere. They find meridional wind amplitude between 6-10 $\mathrm{m\,s^{-1}}$ at about 80 km. The 4-day wave has somewhat greater amplitude in the EUGCM compared with the UKMO data (compare with Figures 4.4 and 4.9), and values up to 8 $\mathrm{m\,s^{-1}}$ are found around 80 km. Also the wave in the EUGCM has a critical line. The wave seen in

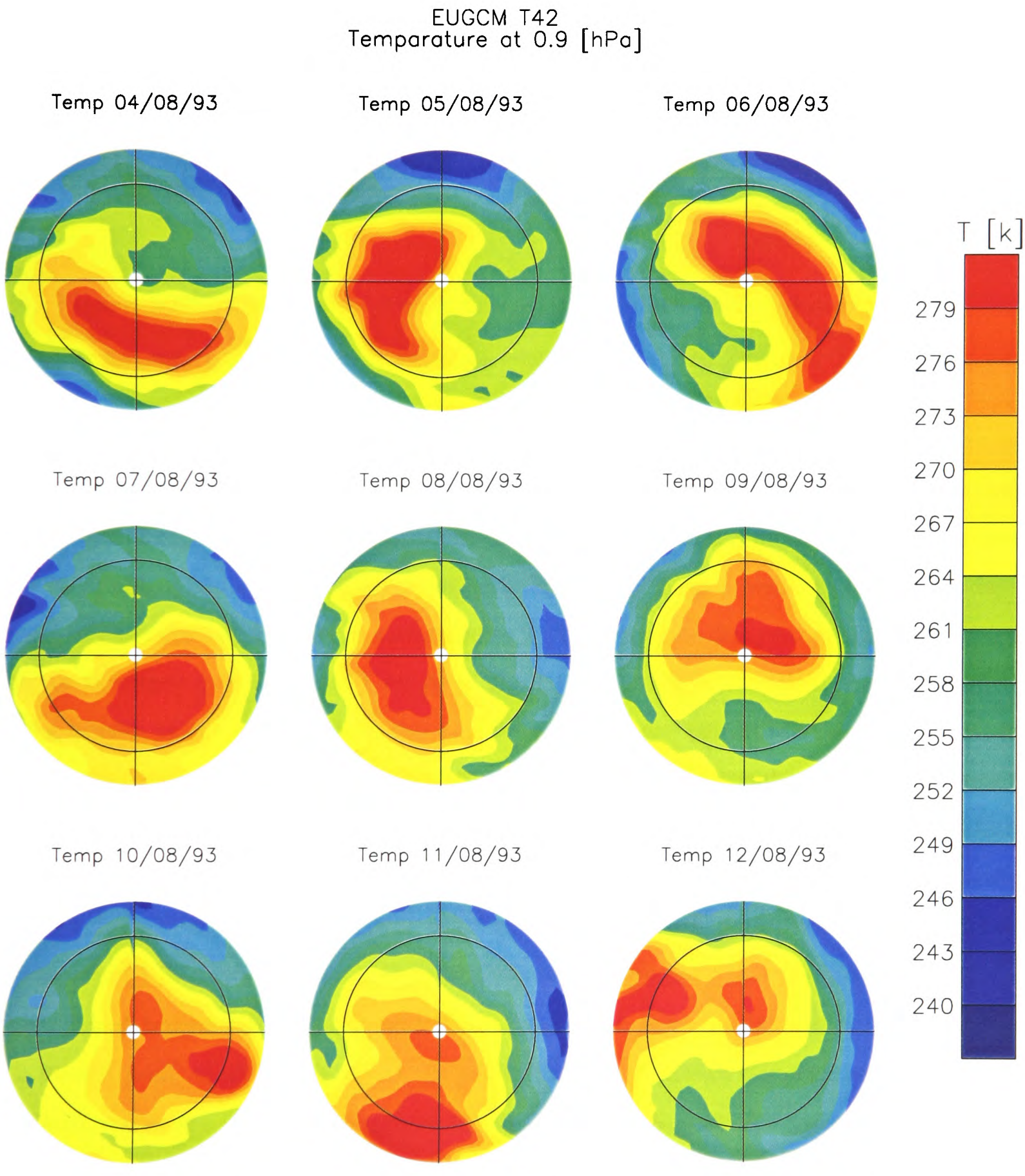


Figure 4.16: Southern hemisphere EUGCM temperature for the period 4-12 of August 1993, at 0.9 hPa. The outer circle is 50°S.

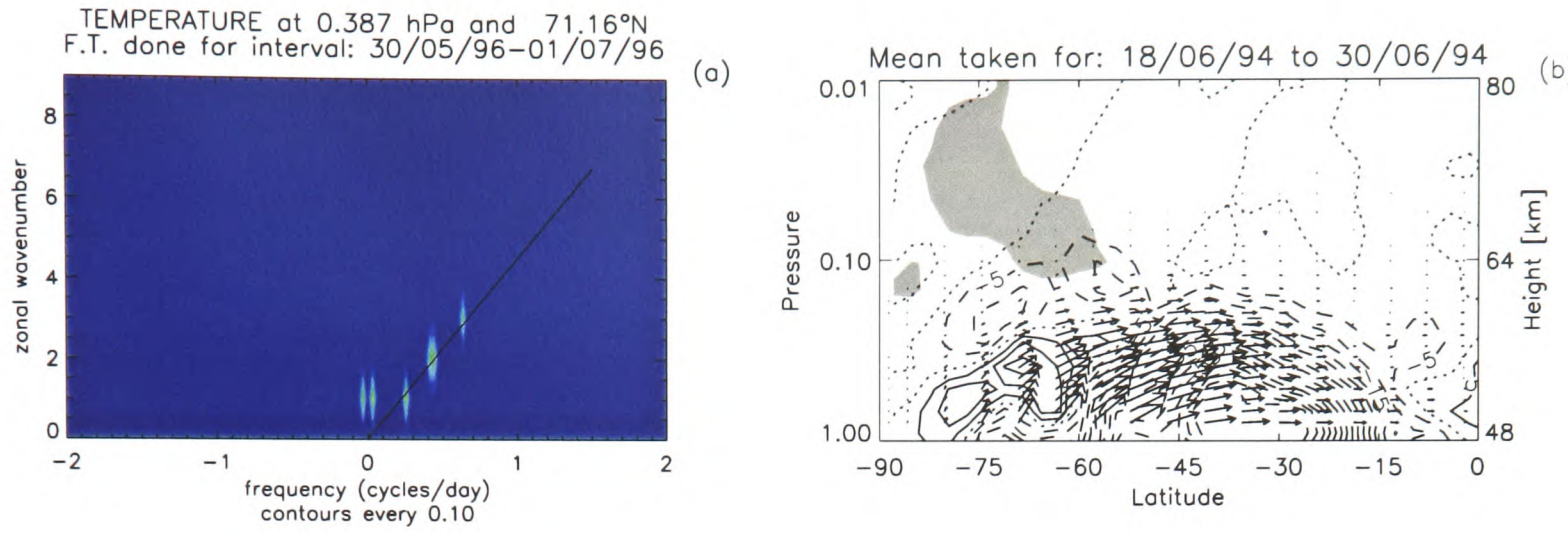


Figure 4.17: (a) zonal wavenumber versus frequency plot of temperature at 71.1°S and 0.38 hPa. (b) Contours of $\nabla \cdot F$ in units of [kg m^{-1}s^{-1}day^{-1}], arrows of the EP flux for same period. Shaded regions are where $\bar{q}_y < -1 \times 10^{-11}$ [m^{-1}s^{-1}].

the larger vertical EUGCM domain (i.e., up to 0.01 hPa) shows for temperature a second peak at around 60 km, as found by Allen *et al.*, (1997). For Year 2, a 4-day wave is seen in July and August. In July the period of the wave is around 3.8 days but then decreases to 3.1 days in August. The 4-day wave is accompanied with a weak signal at 1.7 days, eastward propagating with zonal wavenumber 2. The wave for this year again has a critical line, in this case over the height range of the UKMO data, the critical line seems to be at the border of the region where the 4-day wave has large amplitude (as for the UKMO 4-day wave), but as for Year 1, higher up the critical line veers polewards and intersects the wave, close to the zero wind line seen in the mesosphere when the winds reverse from westerlies to easterlies (see Figures 3.17a, 3.20a and 3.25a). Finally in Year 3, in addition to the 4-day wave, there is a peak in amplitude at k=2 (with period 2 days) and at k=3 (with period 1.57 days) all travelling at almost the same phase speed (Figure 4.17a). These higher zonal wavenumber component waves have been reported before, and can be seen as a 'warm pool' of air going round the pole. The amplitude of temperature for the k=2 and k=3 waves are shown in Figure 4.19. It can be seen that the maximum amplitude shifts to slightly lower latitudes for higher zonal wavenumber (the same is true for the wind amplitudes). This structure is also in agreement with observations (e.g. Prata, 1984).

In NT97 the period of amplification of the 4-day wave seemed to be linked to strong wave activity propagating from the lower atmosphere into the stratosphere. Therefore

wave	zonal wavenumber	phase speed c m s^{-1}at 70°S	observed in the UKMO
4-day wave	k =1	26	Eastwards propagating. Seen at high latitudes, larger values in the SH mostly between July/September. Critical line.
2-day wave	k =2	26	Eastwards propagating. Seen at high latitudes in the SH mostly, between July/September. Seen together with the 4-day wave. Critical line.
2-day wave	k =2	-23	Westward propagating. Seen at high latitudes in the SH, mostly between July/September. Critical line.
5-day wave	k =1	–	Rossby normal mode (1,1). Seen in solstice conditions. This wave has a critical line.
7-day wave	k =1	–	Rossby wave-like structure. Seen around March/April.
10-day wave	k =1	–	Rossby normal mode (1,2). Seen for equinox conditions.

Table 4.1: Table summarising the main characteristics of observed travelling waves in the UKMO data.

they suggest that the wave in the EUGCM is forced by wave activity coming from the lower atmosphere, rather than by an in-situ process such as an instability of the winter jet. Upward propagating planetary waves are found in the 3 years of the EUGCM throughout most of the individual days during JJA in the southern hemisphere, and the EP flux is dominated by these waves. The component of the EP flux tends to be vertical and then points equatorwards north of 75°S (Figure 4.17b). The region between about 80°S and 50°S and about 50 km and 65 km shows convergence of EP flux. The EP fluxes in that region, although small, are almost horizontal, pointing equatorwards with small upwards tilt. Thus the momentum fluxes found in this region could be associated with the barotropic 4-day wave. In most of the observational studies on the 4-day wave, momentum fluxes have been found associated with the wave, and temperature fluxes are very small or nonexistent.

The westward propagating wave k=2 with period around 2 days wave, which is seen in the UKMO assimilation data, is not found in the EUGCM.

4.4 Summary of chapter

The UKMO assimilation data analysed contain a variety of planetary scale waves including the polar winter 4-day wave, table 4.1 summarises the waves found. This wave has been reported from various different observational datasets and is a very recurrent feature of

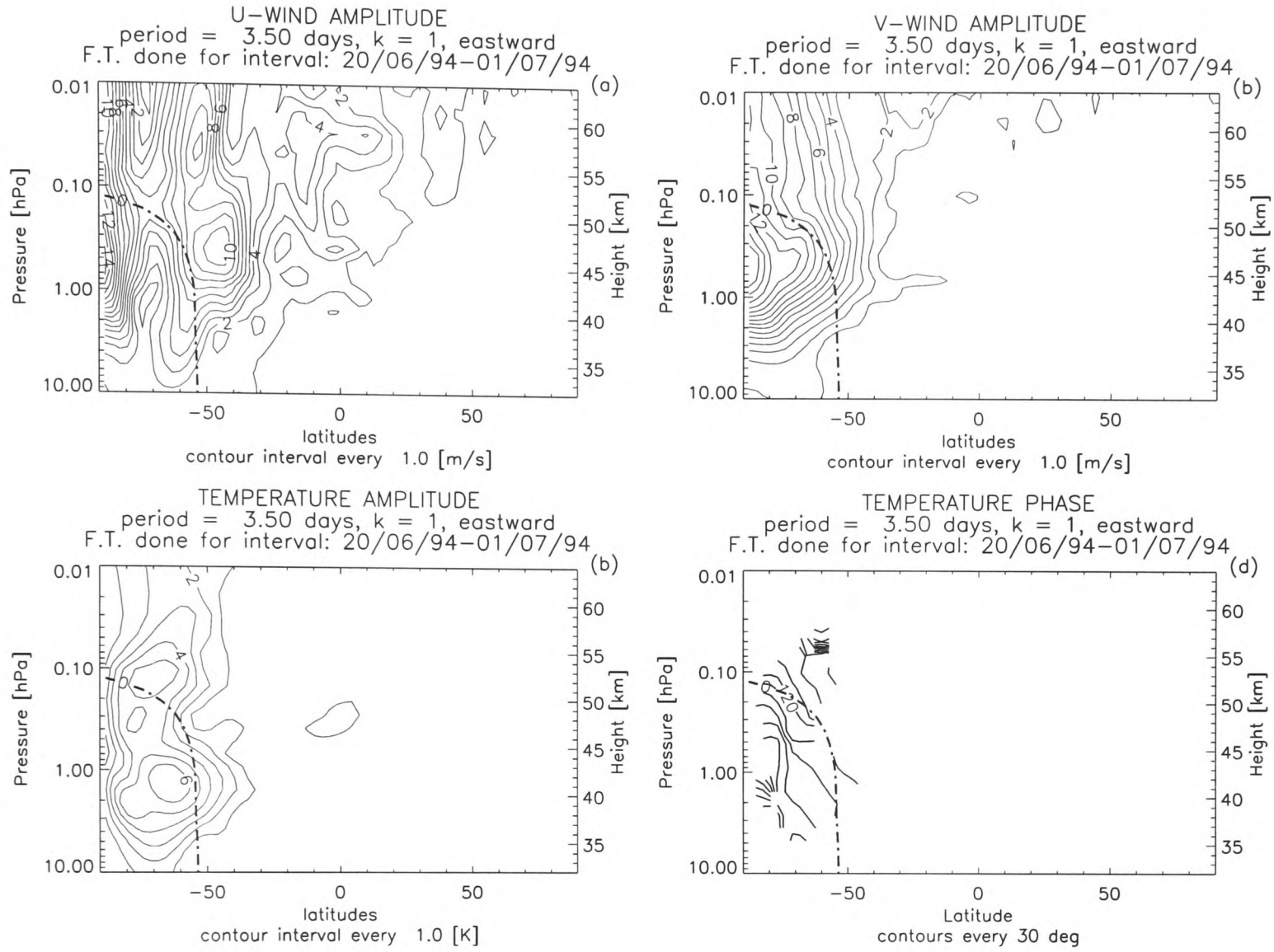


Figure 4.18: (a) u-wind amplitude of the eastward propagating 4-day wave during June Year 1 from the EUGCM. In bold dot-dashed line is the critical line for this wave ($u - c = 0$). (b) v-wind amplitude, (c) temperature amplitude and (d) temperature phase.

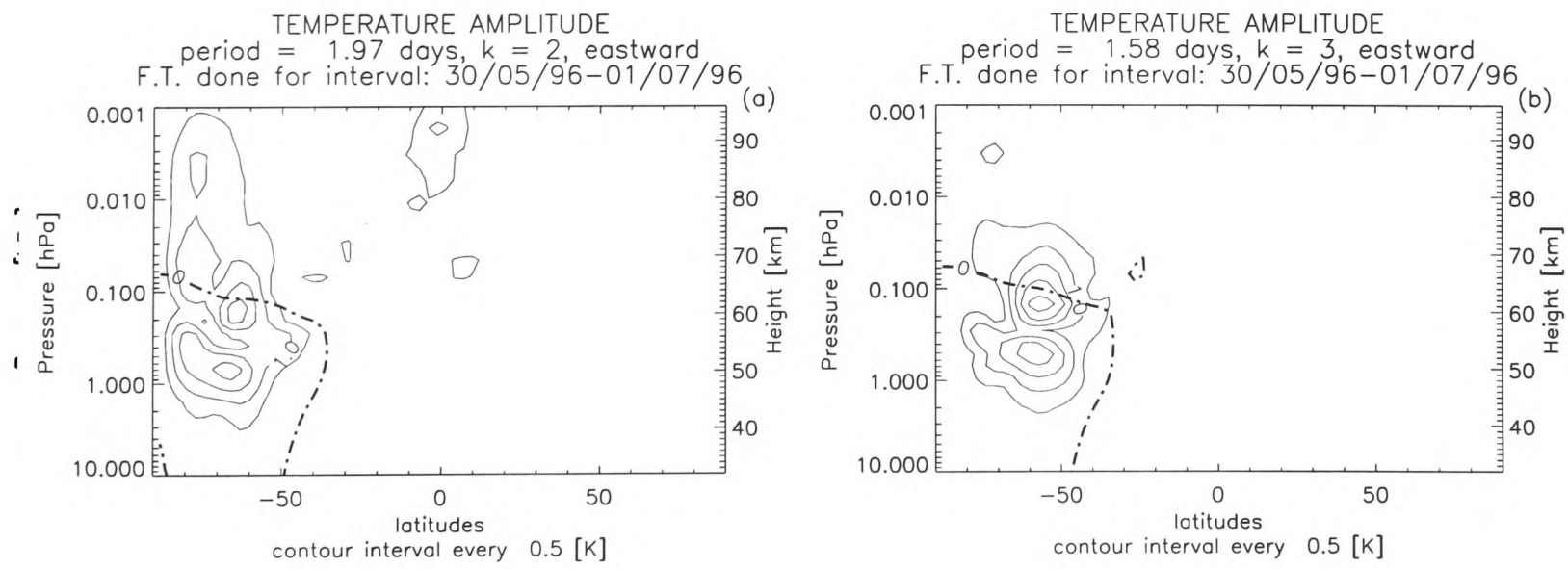


Figure 4.19: (a) temperature amplitude of the eastward propagating 2 day, k=2 wave during June Year 3 from the EUGCM. (b) temperature amplitude for the westward propagating 1.57 day, k=3 wave in June Year 3. In bold dot-dashed line is the critical line for these waves ($u - c = 0$).

wave	zonal wavenumber	phase speed c m s^{-1} at 70°S	observed in the UKMO
4-day wave	k =1	26	Eastwards propagating. Seen at high latitudes, larger values in the SH mostly between June/August. Critical line.
2-day wave	k =2	26	Eastwards propagating. Seen at high latitudes in the SH mostly, between June/August. Seen together with the 4-day wave. Critical line.
1.5-day wave	k =3	23	Eastwards propagating. Seen at high latitudes in the SH mostly, between June/August. Seen toghether with the 4-day wave. Critical line.

Table 4.2: Table summarising the main characteristics of observed polar winter waves in the EUGCCM data.

the polar winter stratosphere. The wave is also present in the EUGCM. Comparison of the wave structure in amplitude and phase shows remarkably good agreement in the range where the UKMO data overlap with the EUGCM, table 4.2 summarises the polar winter waves found in the EUGCM. But there is also evidence that the complete structure of the wave includes large amplitude in the mesosphere (Lawrence *et al.*, 1995), so the structure of the wave in the EUGCM may be correct.

The signature of the wave is seen in all EUGCM years, and the EUGCM picks up the higher wavenumber components (k=2 and k=3). These are seen to travel with the 4-day wave as reported from other observational analyses, at least in Year 3 of the EUGCM. In the EUGCM the appearance of the 4-day wave coincides in location with negative regions of $\overline{q}_y$ and EP flux divergence (see Figure 3.17a). But the EP flux components are dominated by upward propagating Rossby waves, characteristic of the winter hemisphere. In all of the 4-day wave events found in the UKMO data, the wave did not have significant amplitude at the critical line. However, from the EUGCM, where a larger vertical range is available to investigate the waves, we find that the critical line for the 4-day is almost vertical up to about 50 km and then veers towards the pole at about 60 km (Figure 4.18). In this region the EUGCM 4-day wave has large amplitude, and so may have the 4-day wave in the real atmosphere.

The UKMO assimilation data show a strong '2 day' wave which is westward propagating. It has zonal wavenumber 2 and amplitude in the southern hemisphere at high latitudes during winter, similar to the eastward propagating 4-day wave. A wave with

these characteristics has also been reported by Venne and Stanford (1982), but is not seen in the EUGCM. As was mentioned above, both the UKMO data and the data analyzed by Venne and Stanford are daily data, and therefore this wave could possible just the effect of aliasing. If an eastward propagating wave of zonal wavenumber 2 changes period from less than 2 days to above 2 days, the Fourier transform would result in a westward propagating wave for the period less than 2 days (this would not occur in the EUGCM, because the sampling interval of the EUGCM is 6 hours). It is therefore believed, that the westward propagating 2 day wave found in the UKMO is not a real wave, but is the product of aliasing.

Apart from the waves in winter at high latitudes, the 5-day, 7-day and 10-day Rossby normal mode waves were found the UKMO data. Some of these were diagnosed in the EUGCM and discussed in chapter 3. Again the comparison between the UKMO waves and the EUGCM waves shows good agreement in amplitude and structure as well as the time during the year when these waves are observed (see table 4.1). In chapter 3 large amplitudes for normal mode Rossby waves were found in regions where the waves had critical lines. It was then commented that this did not agree with theoretical as well as observational results, which saw reduction in amplitude inside critical regions. However, the 5-day wave found in the UKMO data for 1996 (Figure 4.15) exhibits a critical line in a region where the wave has amplitude. The wave has overall small amplitude, so that arguments for non-linear effects removing the singularity are not applicable.

Chapter 5

Linear instability calculation

The quasi 2-day wave and the polar winter 4-day wave, which were examined in the meteor-radar, UKMO and EUGCM data in chapters 3 and 4 are thought to be generated by instabilities of the summer easterly jet and the winter westerly jet respectively (Plumb, 1983; Stanford, 1997). In this chapter this hypothesis will be tested by describing the results of a 2-dimensional linear instability calculation. Instabilities associated with shears and curvature of the mean wind and temperature fields are relevant for large-scale circulation (see section 2.3.3). Strong vertical (horizontal) velocity shears may be unstable in the sense that any small perturbation to the flow will tend to amplify. This class of instability is called baroclinic (barotropic) instability. The question for this thesis is whether the stratospheric/mesospheric jets are unstable, and if they are, whether they trigger the observed large-scale waves.

As described in chapter 3, the quasi 2-day wave is well represented in the EUGCM (see NT96). However, the forcing mechanisms of this wave have not unambiguously been established. Some aspects of the wave might be explained by a normal mode (Salby, 1981), but other aspects might rather indicate that the wave is produced by a baroclinic instability of the summer jet (Plumb, 1983). The quasi-geostrophic instability analysis by Plumb (1983) in one dimension and Pfister's (1985) in two dimensions for one hemisphere gave modes with similar characteristics to the quasi 2-day wave. The aim of this chapter is to search for the quasi 2-day wave forcing mechanism in a 2-dimensional analysis using the

linearised primitive equations in spherical geometry instead of the much more restrictive analysis of the quasi-geostrophic equations used by Plumb (1983) and Pfister (1985). The same procedure will then be used to see whether the southern hemisphere 4-day wave is an unstable mode.

5.1 2-dimensional instability analysis

The linearised equations for deviations from a zonal-mean background state ($\bar{u}$, $\overline{T}$) are used to perform the instability analysis (see chapter 2, equations (2.47) – (2.51)). Since the EUGCM works on pressure levels rather than log-pressure levels, it is convenient to use pressure as vertical coordinate. Again, in the linearisation the terms involving wave-wave interaction have been neglected, and the terms of background flow-wave interaction have been kept. The 3-dimensional problem is reduced to a 2-dimensional problem by constraining all the variables to have the following zonal structure:

$$A(\lambda) \propto e^{ik\lambda}, \tag{5.1}$$

where A represents any variable (i.e., the problem is solved for a given zonal wavenumber k).

The equations for the linearised disturbances in pressure coordinates are the following, with the zonal variation as defined by equation 5.1,

$$\frac{\partial u'}{\partial t} = -\frac{ik}{a\cos\phi}\bar{u}u' + \left(f + \frac{\overline{u}\tan\phi}{a} - \frac{1}{a}\frac{\partial\overline{u}}{\partial\phi}\right)v' - \frac{\partial\bar{u}}{\partial p}w' - \frac{ik}{a\cos\phi}\Phi', \tag{5.2}$$

$$\frac{\partial v'}{\partial t} = -\left(f + 2\frac{\overline{u}\tan\phi}{a}\right)u' - \frac{ik}{a\cos\phi}\bar{u}v' - \frac{1}{a}\frac{\partial\Phi'_{\phi}}{\partial\phi}, \tag{5.3}$$

$$\frac{\partial\Phi'}{\partial p} = -\frac{RT'}{p}, \tag{5.4}$$

$$\frac{ik}{a\cos\phi}u' + \frac{1}{a}\frac{\partial v'}{\partial \phi} + \frac{\partial w'}{\partial p} = 0, \tag{5.5}$$

$$\frac{\partial T'}{\partial t} = \frac{\kappa \overline{T} w'}{p} - \frac{\partial \overline{T}}{\partial p}w' - \frac{1}{a}\frac{\partial \overline{T}}{\partial \phi}v' - \frac{ik}{a\cos\phi}\bar{u}T'. \tag{5.6}$$

The five unknown fields (u', v', w', T', Φ') can be reduced to three (u', v', T') by integrating the hydrostatic equation (equation 5.4) and the mass continuity equation (equation 5.5):

$$\Phi'(p) = \Phi'(p = p_0) - \int_{p_0}^{p} RT' \mathrm{d}(\ln p), \tag{5.7}$$

$$w'(p) = w'(p = p_0) - \int_{p_0}^{p} \left(\frac{ik}{a\cos\phi}u' + \frac{1}{a}\frac{\partial v'}{\partial \phi} \right) \mathrm{d}p. \tag{5.8}$$

To solve a particular physical problem from a general formulation it is of course necessary to impose boundary conditions. The lower boundary condition in this problem is:

$$\frac{\mathrm{D}}{\mathrm{D}t}(z^* - h) = 0 \quad \text{at} \quad z^* = h(\lambda, \phi), \tag{5.9}$$

where z^* is the geometric height and h is the height of the ground. In terms of geopotential this is:

$$\frac{D\Phi'}{Dt} = g\frac{Dh}{Dt} \quad \text{at} \quad \Phi(p) = \int_0^h g\mathrm{d}z \approx gh. \tag{5.10}$$

As the domain of interest lies in the stratosphere and mesosphere, a flat lower boundary is considered, by which equation (5.10), under linear assumption, reduces to:

$$\frac{D\Phi'}{Dt} = 0 = \frac{\partial \Phi'_{p=p_0}}{\partial t} + \frac{R\overline{T}}{p_o}w'. \tag{5.11}$$

The upper boundary condition is:

$$w' = 0. \tag{5.12}$$

Equations (5.2), (5.3), (5.6) and (5.11) are discretised for a grid of J evenly spaced latitudes and K levels (taken from the EUGCM pressure levels), using second order finite differences and equations 5.7 and 5.8 are evaluated using simple trapezoidal rule (see appendix C for more details about the discretisation and solution of the equations).

The result can be written as:

$$\frac{\partial \mathbf{X}}{\partial t} = \mathbf{M}\mathbf{X}, \tag{5.13}$$

where the vector $\mathbf{X}$ is:

$$\mathbf{X} = (u'_{11}, u'_{21}, .., u'_{jk}, ..., u'_{JK}, v'_{11}, v'_{21}..., v'_{JK}, T'_{11}, ..., T'_{JK}, \Phi'_{1p_o}, \Phi'_{Jp_o}). \tag{5.14}$$

The matrix $\mathbf{M}$ is constructed as follows. The first element of the vector $\mathbf{X}$ is set to one with all the other elements of $\mathbf{X}$ set to zero. Equations 5.2, 5.3, 5.6, 5.7, 5.8 and 5.11 are evaluated, and the result, $\partial\mathbf{X}/\partial t$, gives the first column of the matrix $\mathbf{M}$. Then the second element of the vector $\mathbf{X}$ is set to one, with the other elements zero, the equations are evaluated and the result gives the second column of the matrix. The process is repeated for all the elements of $\mathbf{X}$. This process is much less prone to error than trying to determine the individual elements of $\mathbf{M}$ from the finite difference equations themselves. Note that $\mathbf{M}$ is complex and is of order $\sim 1000 \times 1000$.

If $\mathbf{X}$ is assumed to have a time dependence such that:

$$X(\phi, p, t) = \hat{X}(\phi, p)e^{\nu t}, \tag{5.15}$$

then equation 5.13 reduces to the eigenvalue problem:

$$M\hat{X} = \nu\hat{X}, \tag{5.16}$$

where ν are complex eigenvalues and $\hat{X}$ are complex eigenvectors. The real part of the eigenvalue ν gives the growth rate of the eigenvector mode, the imaginary part of ν gives the frequency of oscillation of the mode. In particular, if the real part of the eigenvalue is positive, then the mode is unstable.

NAG routines[1] are used to calculate the eigenvalues and eigenvectors. The code is written so that first all the eigenvalues are calculated, and then the eigenvectors of

[1] NAG stands for 'Numerical Algorithms Group' and is a library of FORTRAN routines.

particular eigenvalues are obtained. The eigenvectors of interest are those with eigenvalues that have the largest positive real part and so represent the fastest growing modes.

Various calculations were performed to study the influence of resolution on the results. The resolution at which the code can be run is limited by the computer memory required to do the matrix inversion involved in the eigenvalue calculation. To cover most of the upper stratosphere and mesosphere using the EUGCM levels, between 20 and 30 levels are necessary. For the background fields used, levels below 25-30 km do not change the eigenvectors found in the calculations. So the domain was confined to the range 28 km to 96 km. Calculations using from 14 (using one every two levels) to 30 levels were performed. Two different horizontal resolutions were tried, 17 latitudes (from $-80°$ to $+80°$, every 10 degrees) and 35 latitudes (from $-85°$ to $+85°$, every 5 degrees)[2]. With 35 latitudes the fastest growing modes for all the zonal wavenumbers showed small-scale structure at the equator with very long periods, which were identified with inertial instability. These modes will be disregarded.

After some experimentation it was decided to use 35 latitudes and 23 levels, from 6 hPa to 0.001 hPa. To study the quasi 2-day wave, two different sets of background fields ($\bar{u}$ and $\overline{T}$) were constructed using daily data from the EUGCM. The first background state corresponds to a July mean, taken from a shorter EUGCM integration, of which data from June to the end of August are available (labelled as 1993). The second background state was constructed from June 1994 (Year 1), when the three year integration of the EUGCM was available. The instability calculation was performed for the 'June' and 'July' background states, at zonal wavenumbers k= 1, 2, 3 and 4 (sections 5.3.1 and 5.3.2). To study the 4-day wave two background states were used. The first background state corresponds to a September 1993 mean (from the short EUGCM run), and the second state corresponds to an August 1995 mean (Year 2). Instability calculations were performed for the first three wavenumbers for the 'August' and 'September' background states (sections 5.4.1 and 5.4.2).

[2]To make the derivatives at the pole easier, the horizontal discretisation is such that there no grid point at the pole.

5.2 Results for isothermal atmosphere with no winds

To test the code against some analytical solutions, the code was run with background fields of an isothermal atmosphere ($\overline{T}$= 240 K) and no background wind ($\overline{u}$=0). The solutions to this problem are Hough functions $\Theta(k, n)$, hereafter denoted by '(k,n)', which are the eigenvectors to Laplace's tidal equation (see Appendix A and Longuet-Higgins, 1968). The code was run with 35 latitudes (from −85° to 85°) and 23 levels (from 11 hPa to 0.016 hPa), to match the vertical domain for which the Hough functions were obtained by an alternative method[3]. Figure 5.1 shows the temperature component of the zonal wavenumber 1 Θ(1,1) mode, from the alternative method (Figure 5.1a) and from the instability code (Figure 5.1b). The Θ(1,1) mode corresponds to the first component of the diurnal tide and should have a vertical wavelength of 27 km and a period of 24 hrs. The instability code gives a period for this mode of 21.8 hrs instead of 24 hrs and a wavelength of 34 km compared to 27 km. The differences in period and wavelength are due to the fact that the alternative solution assumes a period of 24 hrs and the eigenvalue problem is solved for the vertical wavelength, while in the instability code the vertical wavelength is determined by the size of the domain and boundary conditions, and the eigenvalue problem is solved for the period. Nonetheless the agreement between the structure of the mode in Figures 5.1a and 5.1b is very good. The rest of the modes for the diurnal tide, and for the semi-diurnal tide, also agree very well.

Other solutions of Laplace's tidal equation include Rossby-gravity waves and Rossby waves. Some of the well known solutions are shown in Appendix A, as some observed large-scale waves in the middle atmosphere have been identified with these normal mode structures. Figure A.1 shows the amplitude and phase structure of the first symmetric mode for k=1, the (1,1) mode, which has been identified with the 5-day wave. Figure A.2 shows the second antisymmetric mode for k=1, the (1,2) mode, which has been identified with the 10-day wave. A 16-day wave has been identified with the second symmetric mode for k=1, the (1,3) mode. Figure A.3 shows the structure of the (1,3) mode. Figure A.4

[3]The alternative method calculates Hough functions as a sum of Associated Legendre Polynomials for tidal solutions.

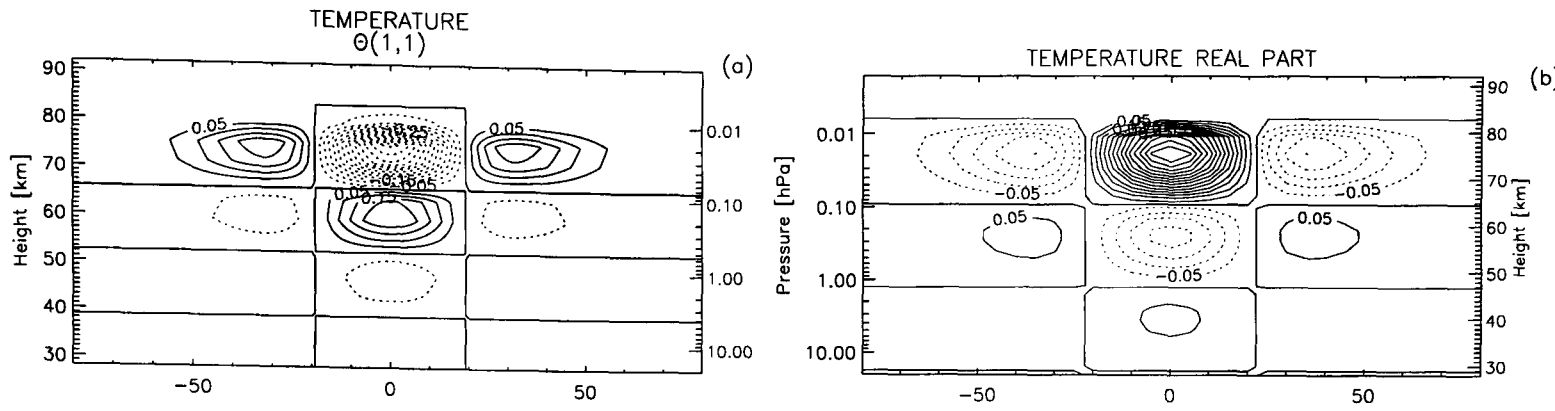


Figure 5.1: (a) Temperature of $\Theta(1,1)$ mode obtained by a numerical solution. (b) Temperature component of the first mode of the diurnal tide calculated by the instability code.

shows the structure of the first symmetric mode for k=2, the (2,1) mode, identified with the 4-day wave. Finally Figure A.5 shows the amplitude and phase structure of the third Rossby-gravity mode, the (3,0) mode, identified by some authors with the quasi 2-day wave.

5.3 Results for the quasi 2-day wave

To study the quasi 2-day wave, in this section results will be presented of the instability calculations for two different background states. The first state is a 'July' mean taken from a shorter run of the EUGCM that was available first (labelled as 1993). The second background state corresponds to a 'June' mean from Year 1 (labelled as 1994). The section will start with the results for the July 1993 background state.

5.3.1 July background state

The 5 day mean from the 1st to the 5th of July 1993 was chosen as likely to represent the most unstable flow for the quasi 2-day wave since it has large amplitude in early July[4]. Figure 5.2 shows the zonal mean u-wind and zonal mean temperature for this period, shaded are regions where $\overline{q}_y$ is less than -1×10^{-11} m^{-1} s^{-1}, indicating the potentially unstable regions.

[4]Different means where tried, from monthly mean to this 5 day mean and the fastest growing modes were found when running the code for this background state.

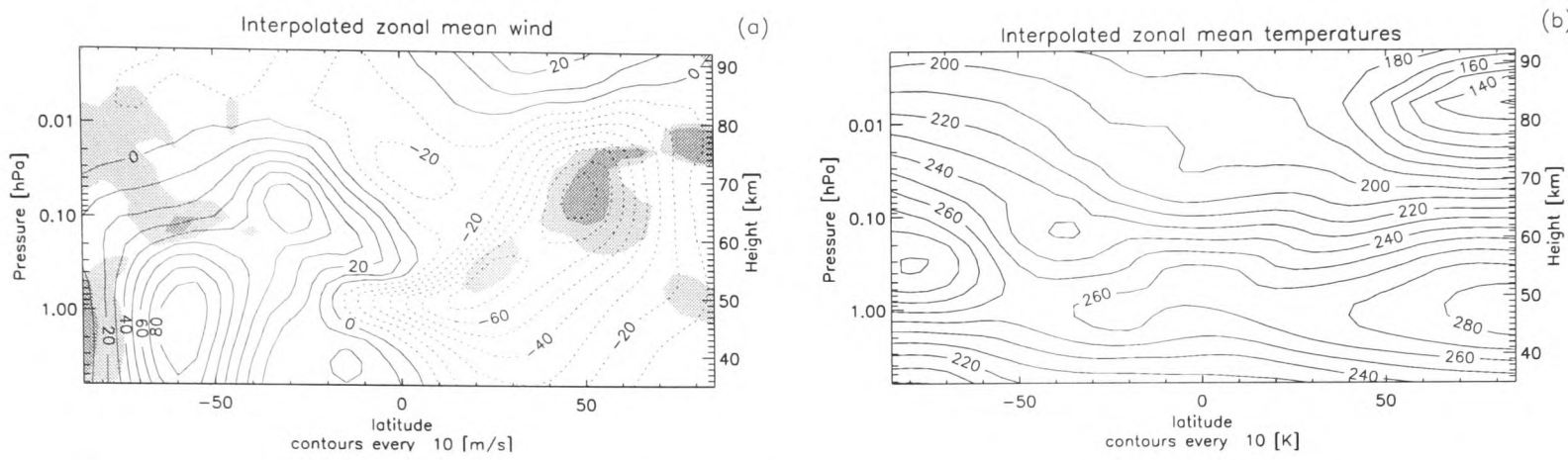


Figure 5.2: (a) EUGCM zonal mean u-wind interpolated onto 35 evenly spaced latitudes, time mean from the 1st to 5th of July 1993, shaded regions are where $\overline{q}_y$ $\mathrm{m}^{-1}\,\mathrm{s}^{-1}$ is less than -1×10^{-11}, with light grey for values between -1 to -5×10^{-11} and dark grey for values less than -5×10^{-11}, contour interval. (b) same as (a) but for zonal mean temperature.

Between 10 and 20 unstable modes are found for each zonal wavenumber for which the instability calculation was performed. As stated above, running the code with 35 latitudes results in the most unstable modes having small-scale structure close to the equator and very long periods (an example of these modes is shown in Figure 5.7 and discussed in section 5.3.2). Disregarding these modes, the most unstable mode was found for zonal wavenumber 3. Results from the instability code for the July background state at different zonal wavenumbers are given in Table 5.1.

Disregarding the inertial-instability-like modes, there is only one unstable mode for k=1. The mode is an eastward propagating mode, with amplitude in the southern hemisphere, with period 108 hrs (about 4.5 days, figure not shown). Its spatial structure is similar to the 4-day wave (figure not shown), its e-folding time is 138 hrs (5.8 days). For k=2, again only one mode is found. It is a westward propagating mode with period -49 hrs. Its spatial structure (shown in Figure 5.3) includes a maximum temperature amplitude in the northern hemisphere (60°N); u-wind with maximum in both midlatitudes and v-wind at the equator. The e-folding time is 94 hrs (about 4 days). For zonal wavenumber 3 there are three unstable modes. The fastest mode for k=3 has a period of -33 hrs and an e-folding time of 78 hrs (3.2 days, the fastest for all wavenumbers). The structure can be seen in Figure 5.4, its amplitude has a very localized peak of all the fields at around 60°N and 80 km height, at the top of the summer jet. The amplitude of the mode in fact

	July		June	
k	*e*-folding time[hrs]	period [hrs]	*e*-folding time[hrs]	period [hrs]
1	138.8	108.6	-	-
2	94.3	-48.9	155.2	-49.7
3	78.7	-33.2	83.0	-43.4
	90.2	-37.7	-	-
	97.6	-42.4	-	-
4	84.5	-28.4	-	-
	125.5	-25.2	-	-

Table 5.1: Table showing results of the instability calculation for July and June background states. Rows show growth rate and period for different wavenumbers.

coincides with the region where $\overline{q}_y$ is negative and the strongest shear zone of the summer jet. The second mode, which has a period of -38 hrs and an *e*-folding time of 90 hrs, has a very similar spatial structure to the 33 hrs mode (Figure not shown). The third fastest growing mode for k=3 has a period of -42 hrs and a more global structure, with some amplitude in the southern hemisphere for u-wind and maxima of v-wind at the equator (Figure not shown). This mode resembles the large-scale quasi 2-day wave. This mode has an *e*-folding time of 98 hrs (4.1 days). Finally for k=4 the fastest growing mode has a very similar spatial structure to the 33 hrs, k=3 mode (Figure not shown). The period of the k=4 mode is -28 hrs and the *e*-folding time is 84 hrs (3.5 days).

5.3.2 June background state

As stated in chapter 3 the largest quasi 2-day wave event in the EUGCM is seen in June/July Year 1 (labelled as 1994), therefore different time means for June and July of that year were tried, to see if different unstable modes could be found. A time mean from the 21st of June to the 24th of June 1994 was chosen. Figure 5.6 shows the zonal mean u-wind and temperature for that period, interpolated onto 35 latitudes and 23 levels.

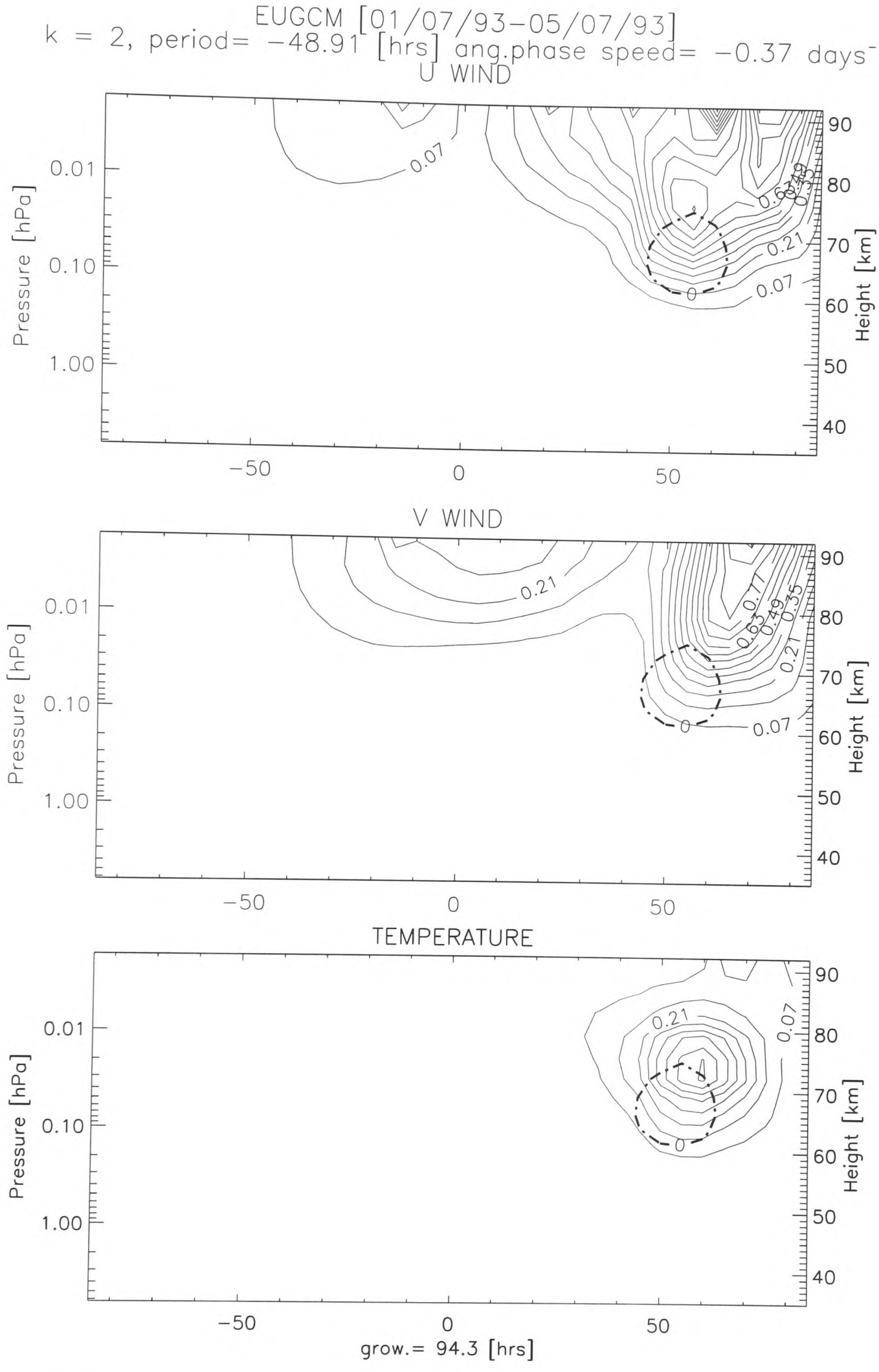


Figure 5.3: Fastest growing mode for k=2 from the 2-dimensional instability calculation. July background state. In bold dot-dashed line is the critical line for the mode.

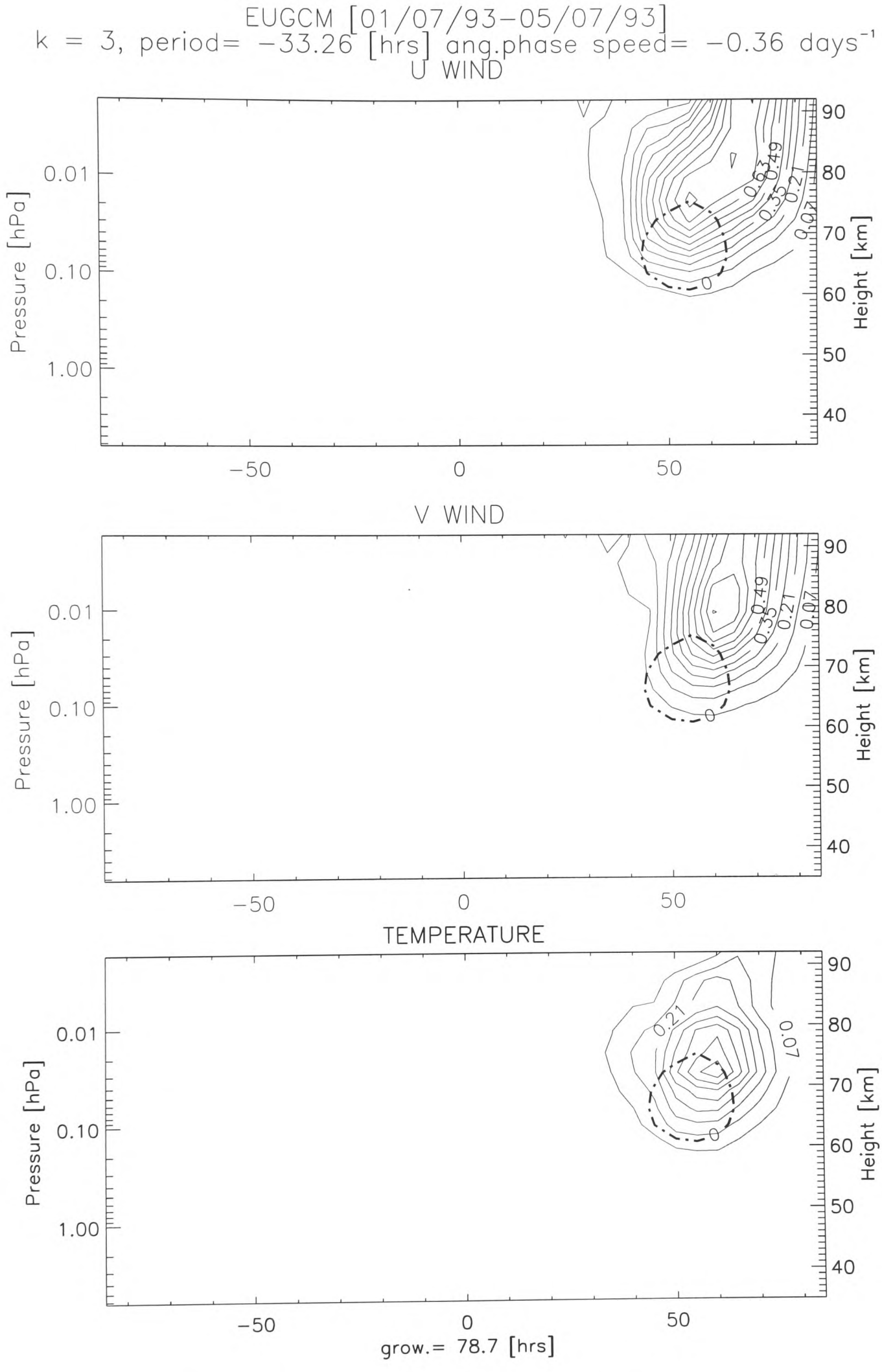


Figure 5.4: Same as Figure 5.3, but k=3.

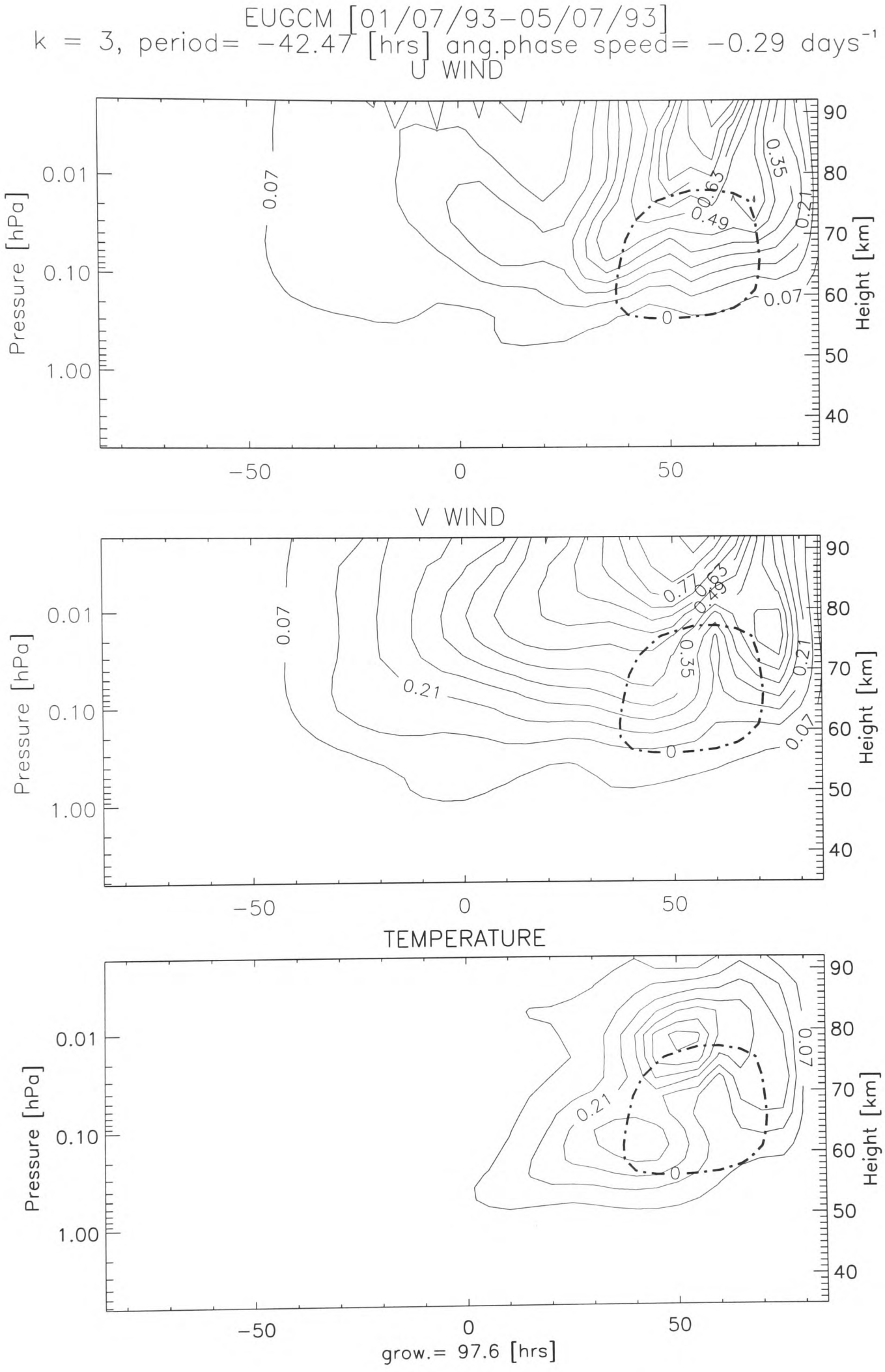


Figure 5.5: Third fastest growing mode for k=3, July background state.

Compared with the background fields for July mean conditions (shown in Figure 5.2), the region where $\overline{q}_y$ is negative is slightly larger for the June mean.

As mentioned in section 5.1 the instability calculation with 35 latitudes gives as fastest growing modes eigenvectors with amplitude at the equator with very small vertical scale 'pancake' like structure, probably associated with inertial instability. An example of this is shown in Figure 5.7, which is the temperature and v-wind amplitude of the fastest growing mode for k=3. The criteria for inertial instability to occur is that the potential vorticity of the mean zonal wind times the Coriolis parameter is negative. In the region 10°S to 20°S and 5 hPa to 0.5 hPa this criteria for inertial instability to occur is satisfied (not shown) and this corresponds to the position of the unstable mode in Figure 5.7. Furthermore the relationship between the winds and temperature fields of the mode agree with the theoretical predictions of Dunkerton (1982)[5].

The periods and e-folding times of the unstable modes found for the June background state are given in table 5.1. Disregarding the inertial instability modes, the fastest growing mode for zonal wavenumber 3 is now a global mode (shown in Figure 5.8), with structure resembling the quasi 2-day wave and with a period of -43 hrs. The maximum amplitude of the mode is in the northern hemisphere, but with some amplitude in the southern hemisphere as well, with an indication of the observed double peak at either side of the equator in zonal wind and maximum at the equator for meridional wind (compare with the spatial structure of the EUGCM quasi 2-day wave, Figure 3.21). For the other zonal wavenumbers (k=1, k=2 and k=4) most of the unstable modes show the inertial instability structure in the tropics. For zonal wavenumber 1, all the 6 unstable modes are localized in the tropics. For zonal wavenumber 2, only one unstable mode is not localized in the tropics. Its structure is similar to the fastest growing mode k=2 found with July background fields (Figure 5.3).

Note that the underlying assumption of the experiments described in this chapter is

[5]Figure 1 of Dunkerton (1982), presents a schematic of the relations between all the fields. In the vertical, for example, temperature anomalies are in between levels of easterly and westerly wind, and zonal and meridional wind anomalies occur at the same level, but at different latitudes.

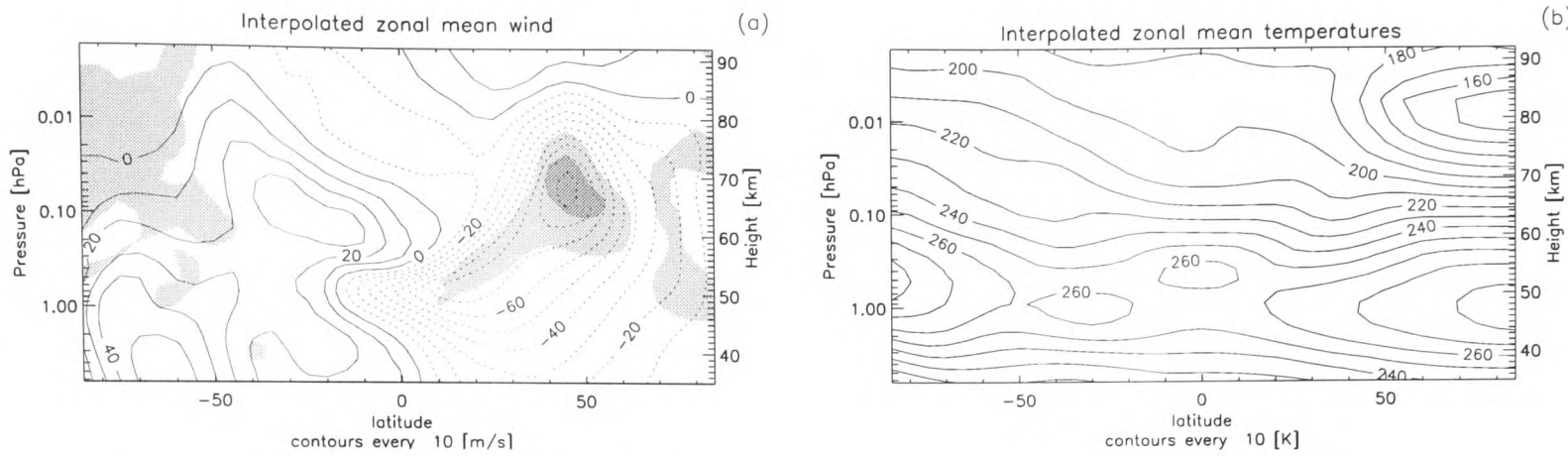


Figure 5.6: (a) EUGCM zonal mean wind interpolated onto 35 evenly spaced latitudes, time mean from the 21-24 June 1994. Shaded regions are where $\bar{q}_y$ is less than -1×10^{-11}, with light grey for values between -1 to -5×10^{-11} and dark grey for values less than -5×10^{-11}. (b) same as (a) but for zonal mean temperature.

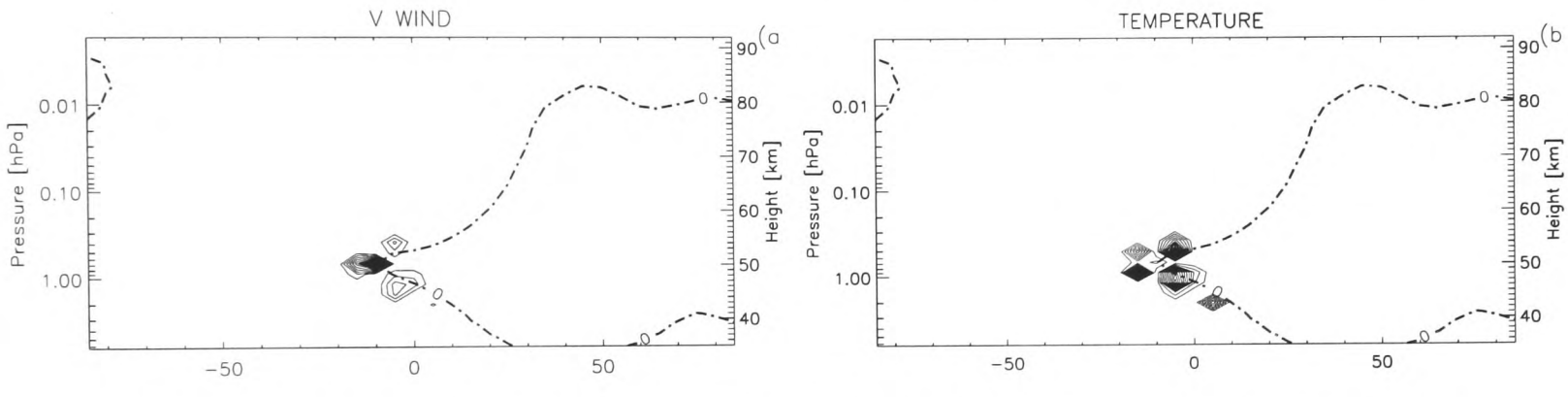


Figure 5.7: (a) Meridional wind amplitude of the fastest growing mode for k=3, period of 127 hrs, for June background conditions. (b) same as (a) but for temperature amplitude. In bold dot-dashed line is the critical line for the mode.

that the zonal mean flow of the summer mesosphere (in the case of the quasi 2-day wave) is unstable, and that unstable modes can grow by perturbing this mean flow. Unstable modes are found to grow from this perturbation (as just shown), but to verify that these modes really need the particular background state used in this section, the instability code was also run with background fields of other months. In Figure 5.9 a EUGGCM May background state is shown. Potentially unstable regions can be seen in the figure, as had the June and July background states. However, when the instability code is run with this background state no significantly unstable modes are found (growth rates are of the order of 50 to 100 days). This assures that the unstable modes found in this section do depend on the background state.

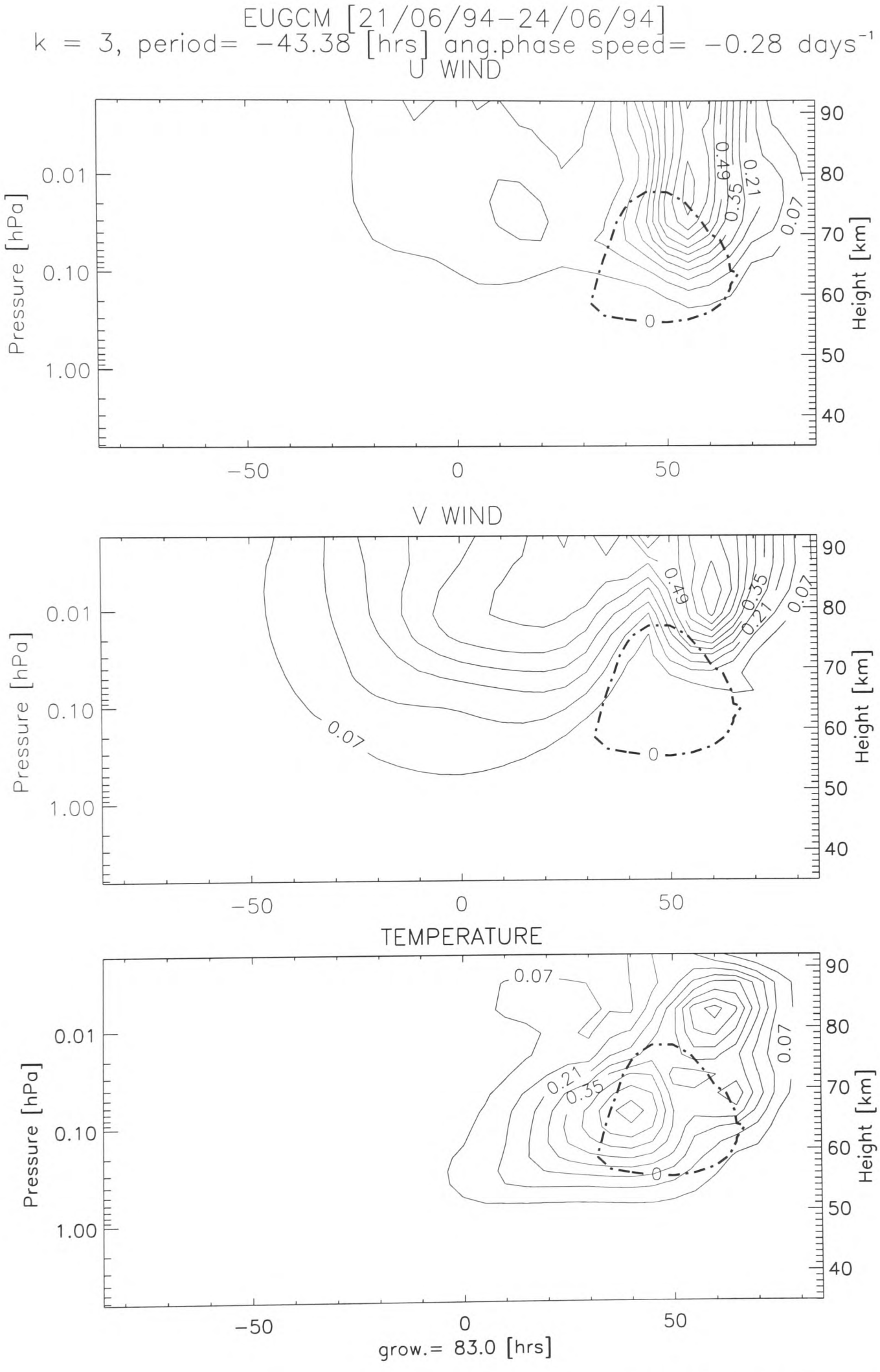


Figure 5.8: Amplitude of the fastest growing mode for k=3 for June background conditions. In bold dot-dashed line is the critical line for the mode.

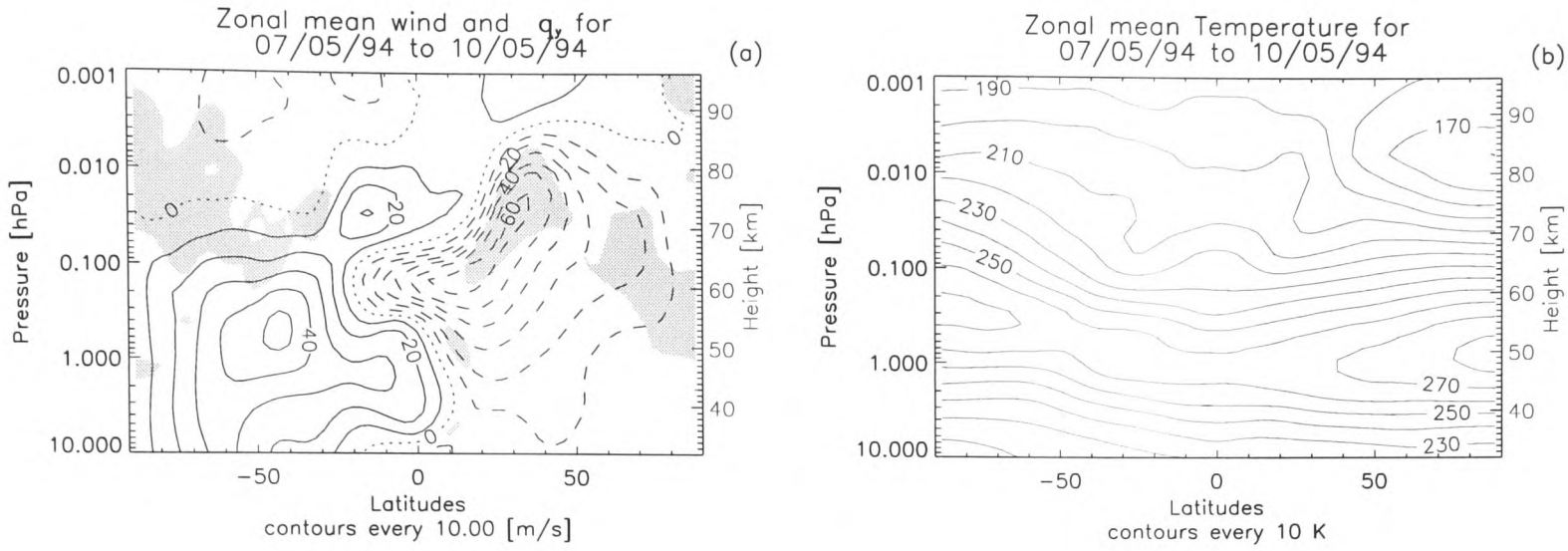


Figure 5.9: (a) EUGCM zonal mean u-wind, time mean 7/05/94-10/05/94. Shaded regions are where $\overline{q}_y$ $\mathrm{m}^{-1}\,\mathrm{s}^{-1}$ is less than -1×10^{-11}. (b) same as (a), but for Temperature.

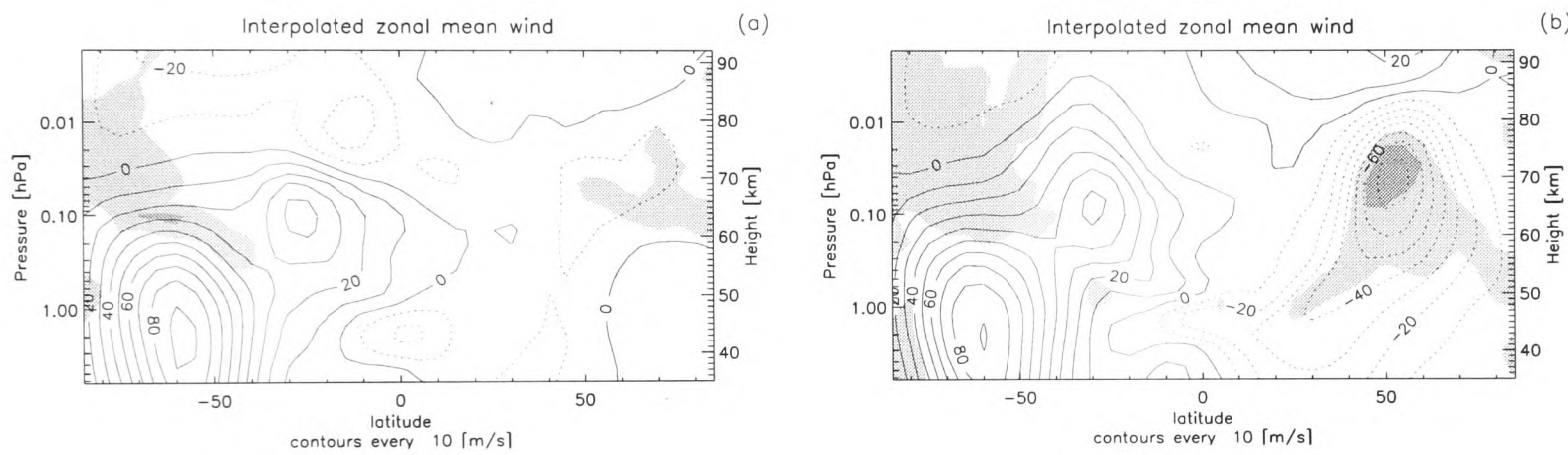


Figure 5.10: (a) EUGCM zonal mean u-wind interpolated onto 35 evenly spaced latitudes time mean 6/09/93-17/09/93. (b) EUGCM zonal mean u-wind interpolated onto 35 evenly spaced latitudes time mean 06/08/95-09/08/95. Shaded regions are where $\overline{q}_y$ $\mathrm{m}^{-1}\,\mathrm{s}^{-1}$ is less than -1×10^{-11}, with light grey for values between -1 to -5×10^{-11} and dark grey for values less than -5×10^{-11}.

5.4 Results for the 4-day wave

The instability code was run with two different background states to study the 4-day wave. First results will be presented for a September 1993 mean state (from the shorter EUGCM run that was available before the 3 year long integration). Then the results for August 1995 mean state will be presented.

	September		August	
k	*e*-folding time [hrs]	period [hrs]	*e*-folding time [hrs]	period [hrs]
1	96.6	98.6	98.6	96.4
2	133.8	54.0	85.7	-52.4
	150.6	50.0	127	-86.6
	—	—	131.9	49.6
3	136.9	36.8	96.2	-36.2
	—	—	109.8	-40.7
	—	—	144.8	-53.1

Table 5.2: Table showing results of the instability calculation for August and September background states. Rows show growth rate and period for different wavenumbers.

5.4.1 September background state

The same procedure as described for the quasi 2-day wave is applied for the 4-day wave. The instability code is run at different zonal wavenumbers for a background state that corresponds to a September mean (9-17 of September 1993). Figure 5.10a shows the zonal mean u-wind. In the southern hemisphere the winter polar night jet still is strong, but the summer jet has almost disappeared, regions where $\bar{q}_y < 0$ are seen in the southern hemisphere above 65 km and south of 60°S. The unstable modes obtained from these instability calculations are mostly confined to the southern hemisphere. Periods and e-folding times for the fastest growing modes are given in Table 5.2. The fastest growing mode is found for k=1 (Figure 5.11), it is an eastward propagating mode with period 98 hrs (just over 4 days) and an e-folding time of 96 hrs. The mode has a similar structure to the 4-day wave. It is a high latitude southern hemisphere mode, with peaks in temperature at around 55 km and 75 km. A double peak in temperature for the 4-day wave has been seen in observations (Allen *et al.*, 1997)[6], but at somewhat lower altitudes than shown in Figure

[6]The observed out of phase structure of the two temperature peaks is also reproduced by this mode, and can be seen when plotting the individual components instead of the amplitude.

5.11. For zonal wavenumber 2 the fastest growing mode is an eastwards propagating mode with period 54 hrs. Its spatial structure is shown in Figure 5.12, it has similar structure to k=1 mode, with amplitudes peaking somewhat more equatorwards (i.e., at 70°S rather than 80°S). Finally for zonal wavenumber 3, the fastest growing mode is an eastwards propagating mode with period 36 hrs (Figure 5.13). Again the spatial structure of the mode resembles the 4-day wave, with amplitudes peaking at around 60°S now.

5.4.2 August background state

Since the polar winter 4-day wave is also seen in August in the EUGCM, mean temperature and zonal winds for August were tried as well. Different time means were tested, finally a time mean from the 6th of August 1995 to the 9th of August 1995 was used. Figure 5.10b shows the zonal mean u-wind, interpolated onto 35 latitudes. Potentially unstable regions are seen at the core of the northern hemisphere easterly jet, and at polar latitudes in the southern hemisphere above 70 km. Although the flow does not change much by taking longer time means (monthly or a 15 day mean for example), the eigenvalues are sensitive to the background flow.

The e-folding times and periods of the fastest growing modes for k=1, k=2 and k=3 are shown in Table 5.2. Again disregarding the inertial-instability-like modes, the most unstable mode for k=1 has a period of 98 hrs and an e-folding time of 92 hrs (it has a very similar structure to the mode found for September background fields, Figure not shown). It is an eastward propagating mode with a period close to the 4-day wave. Its amplitude is confined to high latitude in the southern hemisphere, with double peak in temperature at around 60 km and 70 km. The zonal wind amplitude has a maximum at 60°S and 85°S, and meridional wind has a maximum at 80°S. This structure agrees well with the observed structure of the 4-day wave (see Figure 4.4). For k=2 there are 3 unstable modes. The fastest growing mode has a period of -52 hrs and an e-folding time of 85 hrs and the structure has very localized peaks in the northern hemisphere (Figure not shown). The second mode has a period of -86 hrs. Its spatial structure (shown in Figure 5.14) resembles the Rossby normal mode (2,1) mode, the 4-day wave. The last mode has a period of 49 hrs (Figure not

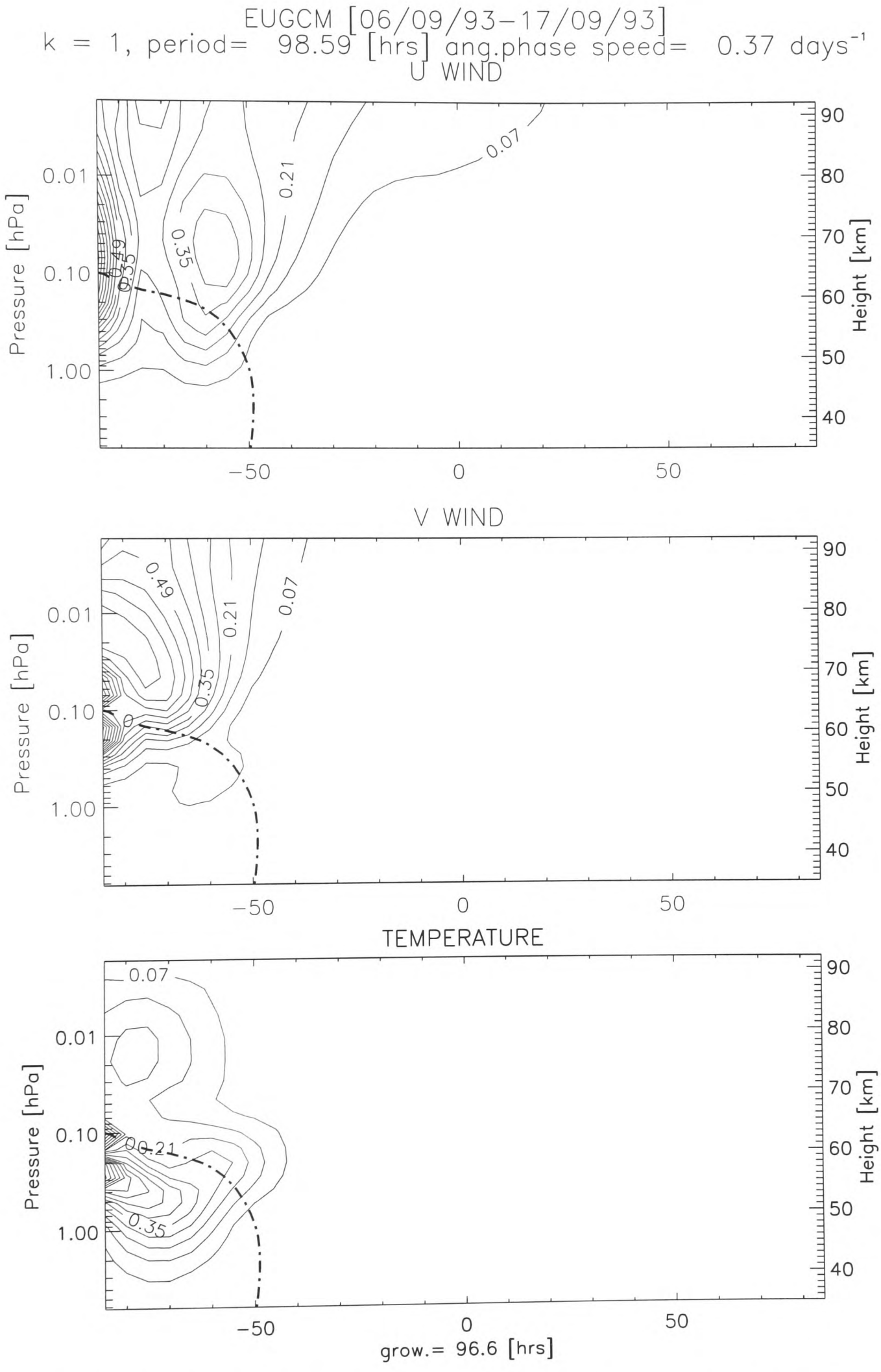


Figure 5.11: Amplitude of the fastest growing mode for k=1 for September background conditions. In bold dot-dashed line is the critical line for the mode.

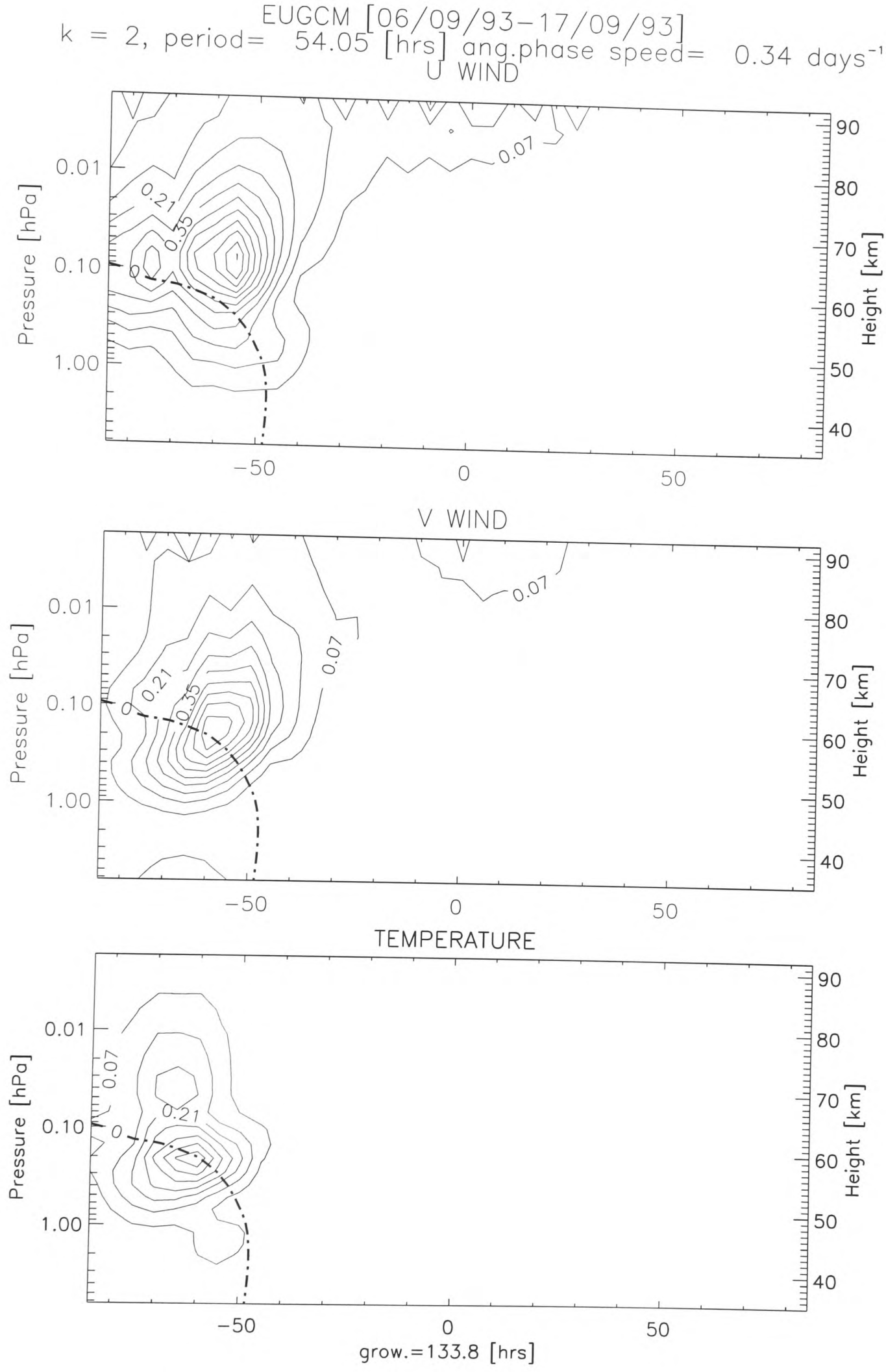


Figure 5.12: Same as Figure 5.12, but k=2.

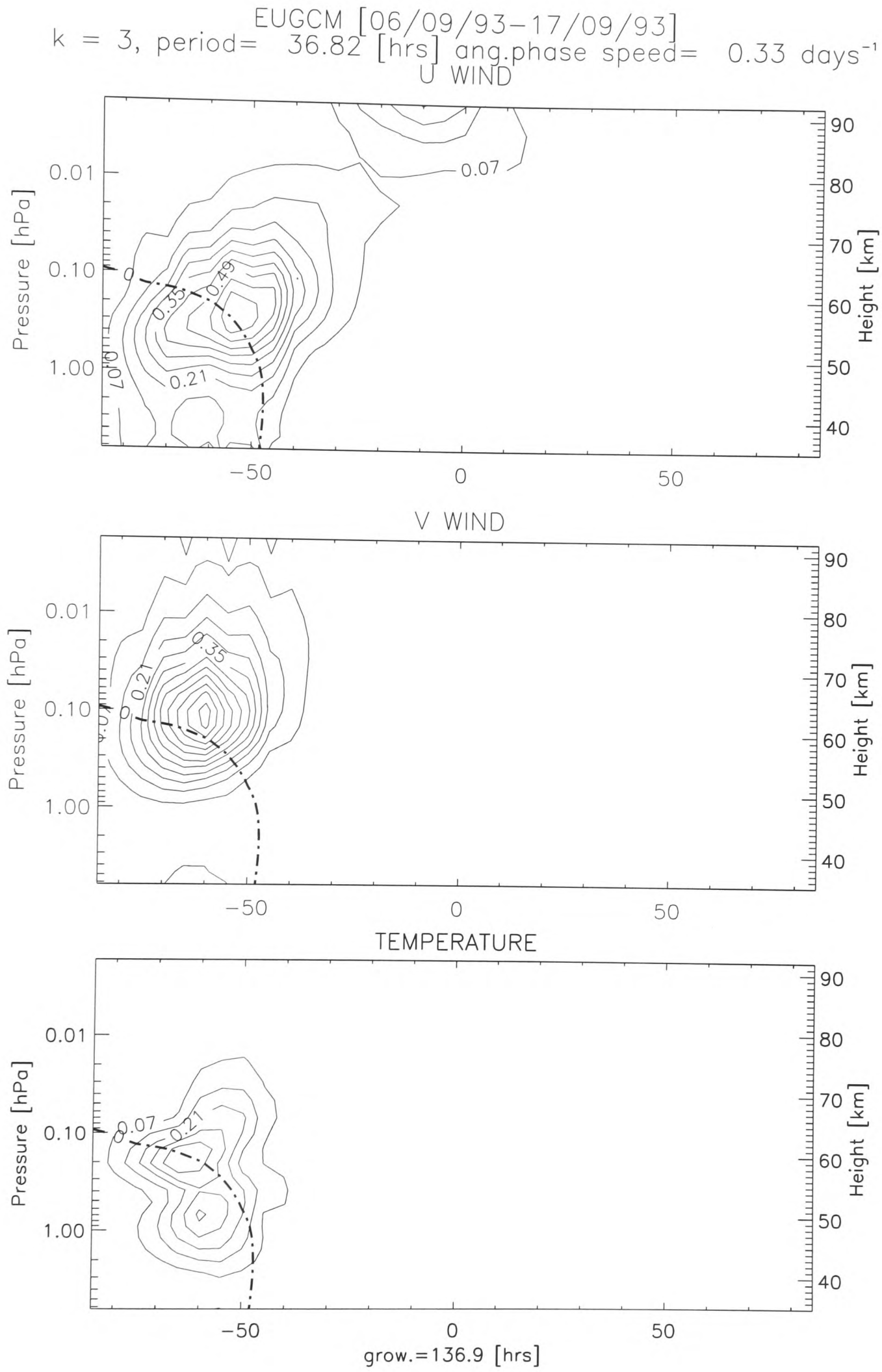


Figure 5.13: Same as Figure 5.12, but k=3.

shown), it is an eastward propagating mode with amplitude in the southern hemisphere. Its spatial structure resembles the fastest growing mode for k=1. For k=3 there are 3 unstable modes. The fastest mode has a period of -36 hrs and a spatial structure similar to the fastest growing mode found for July background conditions (localized at high latitudes in the northern hemisphere, see Figure 5.4). The second mode has a period of -40 hrs and is confined to the northern hemisphere high latitudes. The next unstable mode has period of -53 hrs and its structure resembles the quasi 2-day wave (and therefore also the (3,0) mode, Figure not shown). It is global, with meridional wind peaking at the equator. The zonal wind peaking in the midlatitudes of both hemispheres and the temperature structure is more global over the northern hemisphere. These findings might indicate that under this background state, stable Rossby modes have been perturbed to become unstable. This question will be addressed in the next section.

5.5 Calculation of stable modes

The instability code can also be used to calculate stable modes instead of unstable modes. As explained above, the instability code calculates first all the eigenvalues of the matrix and then the eigenvectors for particular eigenvalues. For the purpose of studying stable modes the code is run calculating the eigenvectors corresponding to eigenvalues with frequencies (periods) between some given values (i.e., whose imaginary part of the eigenvalue lies between some values).

As described in section 5.2, the normal modes for an isothermal atmosphere with no background wind are Hough functions and the temperature component of $\Theta(1,1)$ was shown in Figure 5.1.

The idea behind calculating stable modes is to investigate the evolution of the Rossby normal modes to the background fields slowly varying from the isothermal, no background wind state, to the full EUGCM background states used in sections 5.3 and 5.4. The June, July and August background states showed unstable modes that had spatial structures, as well as wavenumber and period, resembling Rossby normal modes. The aim of the

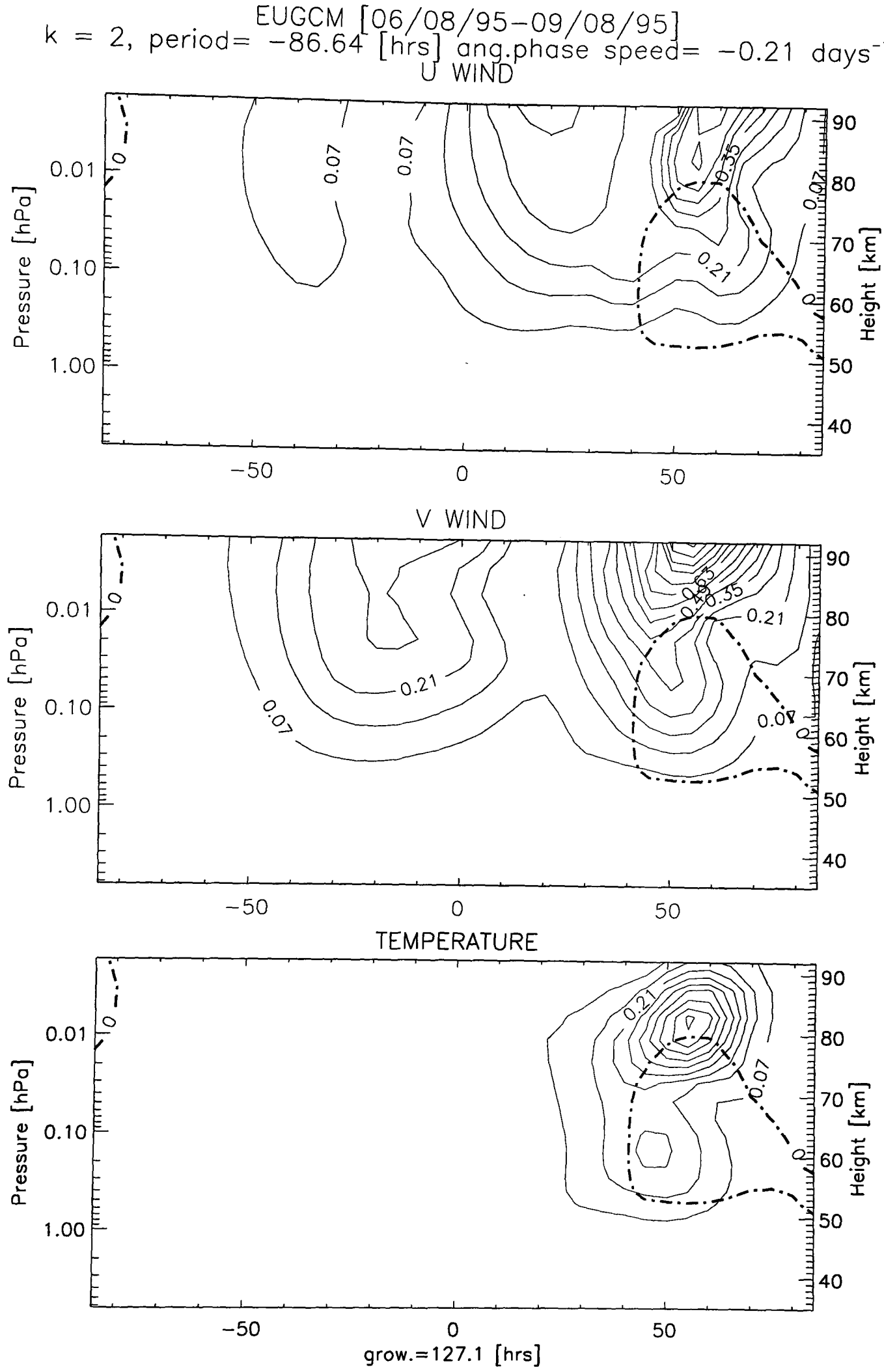


Figure 5.14: Unstable mode for k=2 from the 2-dimensional instability calculation. August background state.

exercise described below is therefore to study the relation between the unstable modes and the stable Rossby normal modes. Particularly important is the evolution of the (3,0) mode under realistic background winds and temperature, since some authors believe that the quasi 2-day wave is a manifestation of this mode. In addition to the (3,0) mode, the evolution of the (2,1) mode will be investigated as well. Three different background states are used, first the June and July mean (the states used to study the quasi 2-day wave in section 5.3), and then the August background state (used to study the polar winter 4-day wave).

In Figure A.4 the structure of the (2,1) mode, the first symmetric mode for zonal wavenumber 2, is shown (which has been identified with the normal mode 4-day wave). Figure A.5 shows the third Rossby-Gravity (3,0). To describe the different modes that will appear in the discussion below, the following notation will be introduced: a given mode will be be determined by 3 indices (k,n;m), where k and n are as usual the zonal wavenumber and the number of zeros between the poles for the meridional wind respectively. The third index (m) will represent the number of zeros in the vertical domain. So, for example, in this notation the third Rossby-gravity mode with the largest vertical wavelength will be referred to as (3,0;0).

To see whether stable normal modes persist under realistic background conditions, the instability code is run with varying background wind and temperature. The wind ($\bar{u}$) and temperature ($\overline{T}$) are changed as follows;

$$\overline{T} = \alpha \overline{T}_E + (1 - \alpha)240, \tag{5.17}$$

$$\bar{u} = \alpha \overline{U}_E, \quad \text{with} \quad \alpha \in [0, 1], \tag{5.18}$$

where $\overline{U}_E$ and $\overline{T}_E$ are the EUGCM mean zonal-mean fields and $\bar{u}$ and $\overline{T}$ are the background fields used in the instability calculations. So, $\alpha = 0$ corresponds to the isothermal, no background wind case and $\alpha = 1$ corresponds to the full EUGCM temperature and wind field.

5.5.1 June background state

The most unstable mode found for the June background state was a mode whose spatial structure (Figure 5.8) resembled the quasi 2-day wave, and therefore also the (3,0;0) mode. The experiment described above is performed with this background state to investigate the relationship between the unstable mode and the (3,0;0) mode. In this experiment eigenvectors are calculated corresponding to eigenvalues of periods between 40 hrs and 58 hrs. For α=0, the (3,0;0) mode has a period of -53 hrs, the (3,0;1) and the (3,0;2) mode, have periods around -55 hrs and -58 hrs, respectively. With increasing α, the period of these modes decreases and their structure is changed. Especially the temperature field shows, even from small values of α, suppression of the southern hemisphere amplitude. The meridional wind is in all cases the least altered field. The (3,0;0) mode survives as a stable mode for relatively large values of α. For $\alpha \leq 0.6$, although quite distorted the (3,0;0) mode appears as a stable mode with no critical line. For $\alpha = 0.6$ the meridional wind component is the most persistent, and the temperature structure has changed the most, with all the southern hemisphere amplitude disappearing. For α=0.7 the (3,0;0) mode is still stable, but has a critical line, although the amplitude is very much reduced in this region. For α=0.8 the mode finally becomes weakly unstable. The higher order modes (3,0;1) and (3,0;2) become unstable as well by α=0.7. None of the three modes survives as a stable mode with realistic temperatures and winds. Finally the fastest growing mode for α=1 (Figure 5.8) has a structure similar to the (3,0;0) mode, but it is not absolutely clear if this is an unstable version of the (3,0;0) mode because it is very difficult to exactly trace the mode with varying α [7]. Figure 5.15 shows the u-wind component of the (3,0;0) mode

[7]The classification of solutions of eigenvalue problems in the context of the atmosphere have only been done for the barotropic vorticity equation (Drazin *et al.*, 1982; Held, 1985). They found that the solutions belonged to either of 8 different classes, which might or might not be empty. Although for the complete primitive equations this classification has not been done, most of the solutions will belong to the same classes. Some of the classes are enumerated here. (i) A finite number of non-singular unstable modes, and an equal number of non-singular damped stable modes, whose eigenvalues and eigenvectors are complex conjugates. (ii) A finite number of marginally stable modes. (iii) A countable number of non-singular

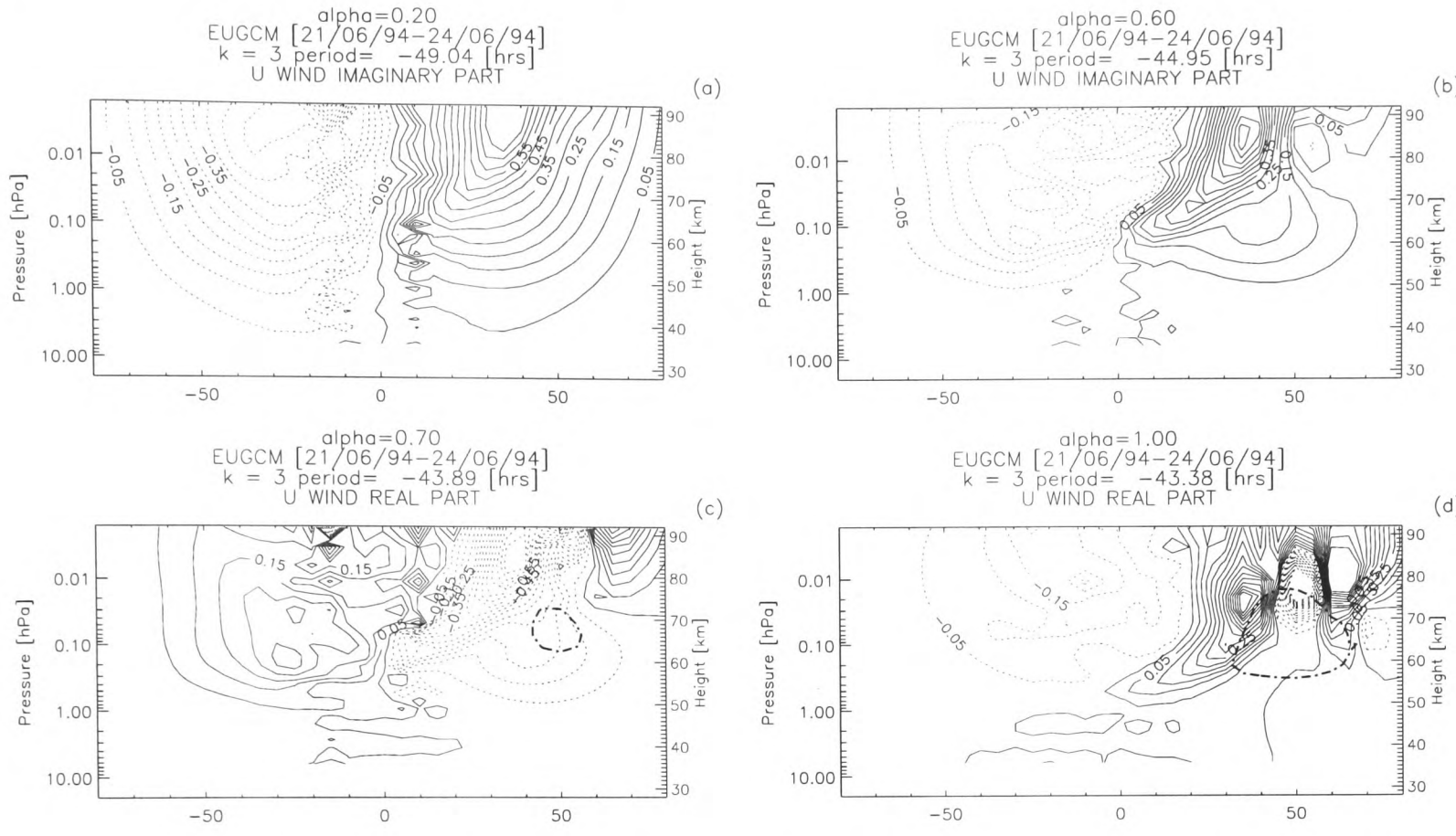


Figure 5.15: (a) Amplitude of u-wind of the (3,0;0) mode with background conditions corresponding to α=0.2, (b) for α=0.6, (c) for α=0.7, (d) Unstable mode.

for α=0.2, α=0.6, α=0.7, Figure 5.15 shows the u-wind component for α=1, this could be the unstable (3,0;0) mode.

5.5.2 July background state

In this section the evolution of the (3,0) under the July background state will be investigated. The eigenvectors of eigenvalues with period between 40 hrs and 59 hrs are calculated. For zonal wavenumber 3 the (3,0;0), (3,0;1) and (3,0;2) modes are followed. For increasing values of α's the period of all the modes decreases. As for the June background state, the spatial structure changes, especially the temperatures amplitude, which is suppressed in the southern hemisphere. At α=0.6, the (3,0;1) and (3,0;2) modes get slightly unstable and critical lines appear. For α=0.7 the (3,0;0) mode has a critical line and becomes weakly unstable. For $\alpha \geq 0.8$ the three modes disappear. The unstable

stable modes modified by the basic shear (these are Rossby waves). (iv) A continuum of singular neutrally stable modes.

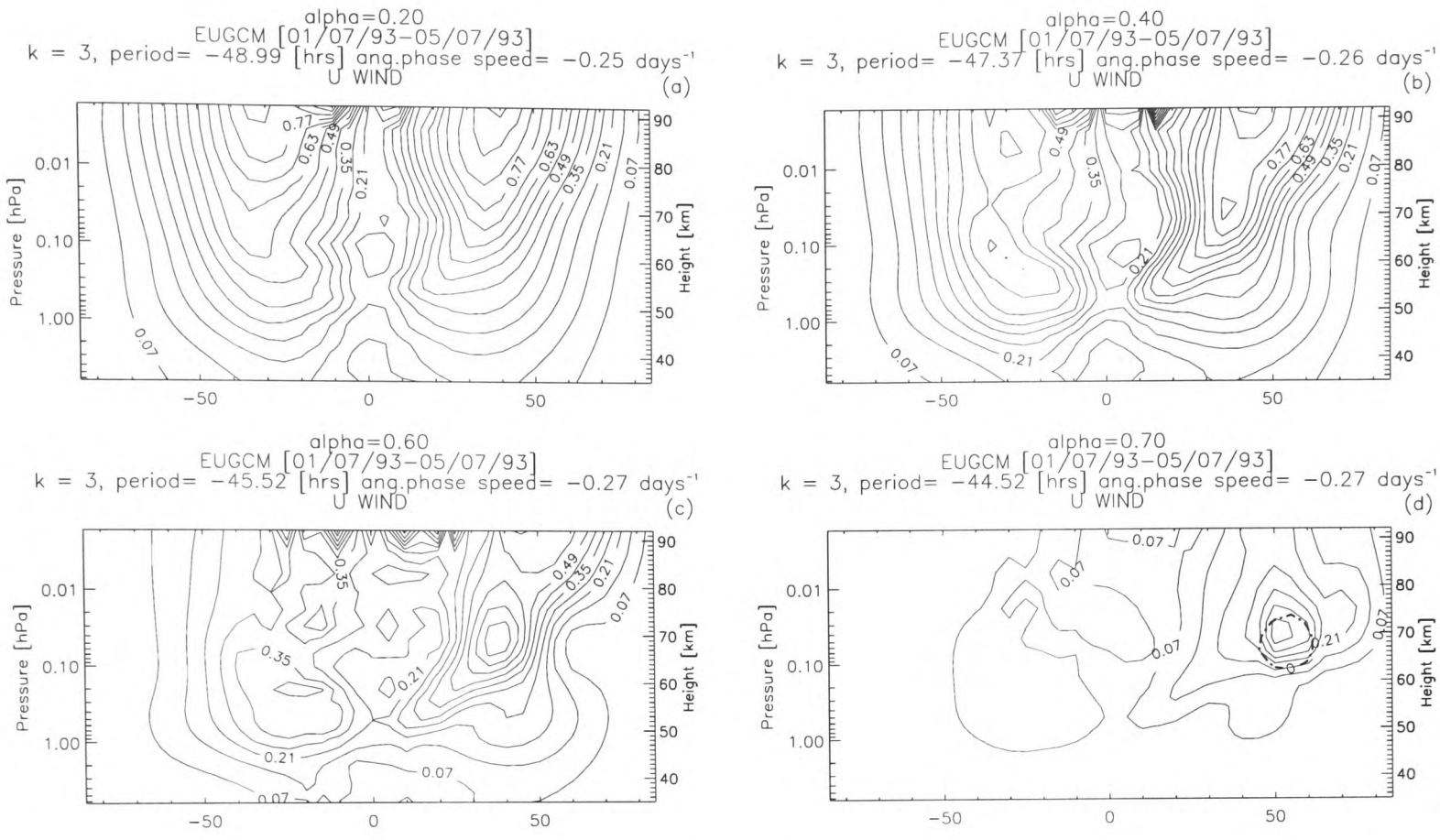


Figure 5.16: (a) Amplitude of u-wind of the (3,0;0) mode with background conditions corresponding to α=0.2, (b) for α=0.4, (c) for α=0.6, (d) for α=0.7.

mode for α=1 with period -42 hrs and a spatial structure similar to the quasi 2-day wave is therefore not any of the above stables modes that had become unstable. Nor do any of the above modes remain as a stable mode for full EUGCM background fields.

Figure 5.16 shows the evolution of the zonal wind amplitude of the (3,0;0) mode for α=0.2, 0.4, 0.6 and 0.7. The mode stays stable up to α=0.6, then it becomes very weakly unstable (e-folding time changes from 'infinite' to about 100 days).

5.5.3 August background state

The instability code was run for different values of α for zonal wavenumber 2 and 3. For zonal wavenumber 3 the results can be summarized as follows: The third Rossby-gravity mode, (3,0;0), disappears rapidly for increasing α. However, the higher order mode with a similar horizontal structure, but a smaller vertical wavelength, the (3,0;1) mode, survives realistic background conditions for much longer. The (3,0;1) mode starts with a period of about 53 hrs. As occurs for all the modes, the period decreases with increasing α. By α=0.7

the (3,0;1) mode becomes very weakly unstable (the growth rate changes from 'infinite' to 70 days), the period is now 51.7 hrs, and the spatial structure is less symmetric about the equator, the southern hemisphere amplitude being suppressed especially in temperature. For higher values of α the modes (3,0;1) becomes unstable. The unstable mode found for α=1 corresponds to a (3,0;1) like mode.

In the same exercise applied for k=2, the (2,1;0) can clearly be identified until α=0.4. For α=0.5, the mode's amplitude is greatly reduced at higher levels, but comes back for α= 0.7 and 0.8 very distorted. From $\alpha \geq$0.7 the (2,1;1) mode becomes weakly unstable, and stable modes with a horizontal structure similar to the (2,1;1) mode appear with a singular region. The periods of these modes are found between 85 hrs and 99 hrs. The (2,1;1) mode becomes unstable from $\alpha \geq 0.8$, and this is the mode found as unstable with α=1.

5.6 Summary of chapter

Instability calculations for various background fields were performed and presented in this chapter. A June and a July background state were used to study the quasi 2-day wave, and an August and a September background state were used to study the 4-day wave. For the quasi 2-day wave, the instability calculations for both of the background states gave unstable modes, the fastest growing were found for zonal wavenumber 3. For the July background state the fastest growing mode had a period of 33 hrs and a very localized spatial structure at around 60°N. The position of the maximum amplitude coincides with the region where $\bar{q}_y < 0$ and where the strongest shear zone in the background wind is seen. However, there is a slower growing mode with period 42 hrs and with a spatial structure more global, which resembled more closely the quasi 2-days wave. For the June background state, the fastest growing mode had a period of 44 hrs and a spatial structure resembling the quasi 2-day wave. The quasi 2-day wave is seen in the EUGCM around June/July for all the model years. Although the two background states used for the instability calculations are similar, the fastest growing modes obtained are different. However, both the June

and July, as well as the August background state, gave unstable modes that resembled in structure and period the quasi 2-day wave. The eigenvalues are more sensitive to the background state than the eigenvectors, which are more robust. The conclusion drawn from these calculations is therefore that the summer mesosphere is unstable, and the observed large-scale quasi 2-day wave grows from this instability.

In the EUGCM waves with periods around 35 hrs were found, their spatial structure resembled remarkably the fastest growing mode from the July background state. Waves with these periods can also be seen in the meteor-radar data. Another wave seen in all the EUGCM years in June is a wave with k=4 and similar structure than the quasi 2-day wave, but less global. No unstable mode was found with similar characteristics to that k=4 wave.

For the 4-day wave the four background states used in this chapter show unstable modes for zonal wavenumber 1 with spatial structure resembling the 4-day wave. In addition the September background state, unstable modes for zonal wavenumber 2 and 3 were found that resemble the $\sim$ 2 day, k=2 wave and the $\sim$ 1.5 day, k=3 found in observations to travel with the 4-day, k=1 wave. The conclusion is therefore that the 4-day wave, as well as the k=2 and k=3 waves with similar phase speeds arise from an instability process of the winter jet.

It should be noted that when running the code with 17 latitudes, the structure of the eigenvectors were less global in the case for quasi 2-day wave. All the modes with the more global structure, resembling the quasi 2-day wave, appeared when the instability code was run with 35 latitudes. In the case of the 4-day wave, the 35 latitudes were necessary to resolve the two peaks in zonal wind.

The other important result from in this chapter is the relationship between unstable modes obtained in the different instability calculations to the stable Rossby normal modes. The conclusions from the instability runs described in section 5.5 can be summarized as follows. For none of the background states used (June, July and August) does the (3,0;0)(or one of the shorter vertical wavelength modes) survive as a stable mode the varying perturbation from an isothermal atmosphere to the full EUGCM background conditions.

At some point critical lines appear and the waves become either unstable or disappear. The unstable modes with quasi 2-day wave-like structure are not the (3,0;0) mode becoming unstable. For the August background state the unstable mode found is a (3,0;1) like mode.

Results for the normal mode 4-day wave (the (2,1;0)) mode are the following. For June and July background conditions, as for the (3,0;0), mode the (2,1;0) does not survive as a stable mode the full EUGCM background conditions. The mode becomes either unstable or disappears. For the August background state it is a mode with shorter wavelengths, the (2,1;1) mode, that becomes unstable and is seen as the unstable mode for α=1.

In chapter 3 it was discussed, that although the 4-day wave could be identified with the (2,1) mode, the appearance of a critical line and the large amplitude of the wave in the region of the critical line was not in agreement with it been a stable Rossby normal mode. It was then suggested that the forcing mechanism of the normal mode 4-day wave in the EUGCM was associated with an instability of the summer easterly jet, this idea can be confirmed by the results of this chapter.

Chapter 6

SMM runs for the quasi 2-day wave

In chapter 5 instability calculations for certain background states were performed and unstable modes were found. The calculations were based on linear theory and are only valid for small amplitudes. To investigate the non-linear evolution of the modes found in the instability calculations, a mechanistic model, the SMM, is used to do initial value experiments. The initial conditions are the same zonally symmetric flows used in the instability code runs. Small amplitude noise is added in order to excite any unstable modes and the SMM is run for several weeks to study the evolution of the flow.

In chapter 5 two background states were used to study the quasi 2-day wave; the first corresponding to a July mean, and a second state corresponding to a June mean. The unstable modes found for the July background state included a localized structure in the northern hemisphere high latitudes, and a slower growing mode with a more quasi 2-day wave-like structure. For the June conditions the most unstable mode found had a more quasi 2-day wave-like structure. Both of the background states are now used to initialize the SMM, and results of those runs will be presented here. Sections 6.3, 6.4 and 6.5 describe different runs initialized with zonal mean u-wind and temperature from an EUGCM 1-5 July 1993 mean. In section 6.6 the initial fields are EUGCM 21-24 June 1994 time mean.

6.1 Description of the model

The model used throughout the experiments described in this and the following chapter is a version of the UK Meteorological Office Stratosphere Mesosphere Model (e.g. Fisher, 1985; hereafter referred to as the 'SMM'). The SMM is a mechanistic model used for process studies in the middle atmosphere and does not have a troposphere, but can be forced by perturbations at the lower boundary (typically at 100 hPa). It is a computationally cheap, portable, global, 3-dimensional, primitive equation model of the middle atmosphere written in FORTRAN. The equations are solved to fourth order accuracy in the horizontal and second order in the vertical and in time using energy conserving 'box' type finite differences and leapfrog integration with a four minute timestep. The SMM also uses Fourier truncation near the poles and a Shapiro filter to avoid numerical instability. The prognostic variables of the SMM are zonal wind (u), meridional wind (v) and temperature (T) held on an Arakawa A-grid (Arakawa and Lamb, 1977), which is a regularly spaced grid in longitude, latitude and log-pressure height, with all prognostic variables stored at the same locations. The SMM grid used for all the experiments described in this thesis has 72 longitudes, 36 latitudes and 35 levels, i.e., it has a resolution of 5° by 5° in the horizontal (from 87.5°S to 87.5°N and from 0°E to 355°E) and in the vertical, levels are approximately every 2 km, from 28 km to 96 km (17 hPa to 0.001 hPa).

The vertical velocity (w) and diabatic heating rate (J) are calculated at each timestep as follows; w is obtained on half levels by integrating the continuity equation downwards, with $w = 0$ half a grid space above the top boundary. J is obtained using the MIDRAD[1] radiation scheme, which will be described below.

The SMM parameterizes a number of sub-grid physical processes. The parameterization of gravity wave drag can be done in two ways. The first is a simple 'Rayleigh friction' scheme, where the zonal and meridional winds are relaxed back to zero with some damping coefficient (inverse timescale) $\alpha(z)$,

$$\frac{\partial(u,v)}{\partial t} = -\alpha(z)(u,v), \tag{6.1}$$

[1]MIDRAD stands for Middle Atmosphere Radiation scheme.

where the coefficient is given by;

$$\alpha(z) = a \quad \text{for} \quad (z < z_o), \quad \text{and}$$

$$\alpha(z) = a + b\left[1 - exp\left(\frac{1}{40}(z_o - z)\right)\right] \quad (z > z_o).$$

Typical values for the constants above are, a=1 $\times$ $10^{-7}s^{-1}$, b between 1 $\times$ $10^{-7}s^{-1}$ and 1 $\times$ $10^{-5}s^{-1}$ and z_o is between 50 km and 70 km.

More recently the more sophisticated 'Hines' scheme has been implemented by Lawrence (1997), but this is not used in the experiments described in this thesis.

The SMM has a dry convection scheme, which simulates the convective adjustment which occurs when the stability criterion of potential temperature is violated[2].

The SMM uses the MIDRAD scheme (Shine, 1987) to calculate heating rates in the middle atmosphere. For this it requires the temperature distribution and the radiatively-active constituents. These include O_3 and O_2, for the short-wave component (solar heating) and CO_2, H_2O and O_3, for the long-wave component (infrared). The ozone distribution is a climatological average, the rest of the constituents are assumed to have constant concentration. The linearized radiative transfer equation is solved using Curtis matrices. The heating rates are obtained by the multiplication of the Curtis matrix by the Planck function integrated over the appropriate wavelength region. The Curtis matrices are calculated only once per day, it is computationally too expensive to calculate them more often.

The SMM requires initial three dimensional fields of the horizontal winds (u and v) and temperature and geopotential height at the bottom boundary. The SMM's lower boundary is typically set at about the tropopause height ($\sim$100 hPa), where geopotential height field is read in daily, providing a continuously varying field representing waves propagating up from the troposphere. The geopotential height has to be specified at one level below the lowest SMM level (at 100 hPa for the standard configuration). The SMM writes output files of the prognostic variables plus the vertical velocity at specified intervals, and daily diabatic heating rates.

[2]The stability criterion is that potential temperature has to be an increasing function of height.

6.2 Set up of the SMM for quasi 2-day wave experiments

The description in the previous section corresponds to the standard configuration of the SMM. A few changes have been implemented in order to investigate the generation of the quasi 2-day wave. The aim is to use the SMM to examine the non-linear evolution of unstable waves from a given initial condition, with no wave forcing at the bottom boundary. The initial states are the EUGCM 'June' and 'July' means (zonal mean u-wind and temperature) used in section 5.3 and interpolated onto the SMM grid. The initial meridional wind is set to zero. These fields are shown in Figures 5.2 and 5.6.

The other initial field which is supplied to the SMM is the zonal mean daily geopotential height at the bottom boundary. To avoid having this updated every day, all the calls to the subroutine that changes the bottom boundary geopotential (UDPBDY) have been commented out.

Another modification to the SMM is the vertical domain, to match the instability calculations, the boundaries have been changed to 28 km and 96 km. Output files are written every 6 hours, so that waves with a minimum period of 12 hours are resolved. In most of the SMM runs described in this chapter, the SMM is run without the radiation scheme, i.e., there is no annual cycle.

When the SMM is run with the zonal mean initial conditions taken from the EUGCM, large values of the meridional wind develop near the top of the model as a result of the initial conditions not being in balance (in the EUGCM there are other body forces, e.g. from the parameterized gravity wave drag, which are important in the momentum equations). Hence a short initial run is carried out where the winds throughout the whole domain are strongly relaxed back to the initial conditions. By this process balanced initial fields are obtained. This run, SMM0, is described in the next section.

6.2.1 Initial balancing run, SMM0

The zonal and meridional wind are relaxed back to initial conditions ($\bar{u}_o$, $\bar{v}_o$) at every timestep, with a damping coefficient of α=1.15$\times 10^{-5}\,s^{-1}$, which corresponds to an e-folding time of approximately 1 day. This adds a tendency term in the momentum equations;

$$\frac{\partial u}{\partial t} = -\alpha(\bar{u} - \bar{u}_o), \tag{6.2}$$

$$\frac{\partial v}{\partial t} = -\alpha(\bar{v} - \bar{v}_o). \tag{6.3}$$

Note that in the initial condition $\bar{v}_o = 0$. In equation 6.2 $\bar{u}$ is the zonal mean part of the SMM zonal wind, and is calculated at every timestep. When using equations 6.2 and 6.3, instead of equation 6.1 for calculating the tendency terms, the 'wave' part of the winds is not affected. In this first run, where the initial state is axisymmetric and no perturbation is added, the fields stay zonally symmetric.

The SMM fields come into balance with a very small meridional wind field after a few days, the zonal wind field is very close to the initial values, and the temperature has changed slightly to achieve balance. Fields from SMM0 are then used as the initial conditions for further SMM integration where white noise, with maximum absolute value of 0.1, is added to the zonal wind and temperature at all gridboxes. This white noise is to seed the growth of unstable waves.

For studying the quasi 2-day wave a series of SMM runs with two different initial states and different SMM configurations were performed and are summarized here:

- The first initial state corresponds to the 1-5 July 1993 time average. This time mean will be referred to as SMM day 185, which corresponds to the 3rd of July, or simply 'the July mean'. SMM0 starts on day 185 and is then run for a few days. Four runs with the initial state taken from SMM0 are described in this chapter.

  SMM1: run with no radiation nor Rayleigh friction, started with initial state taken from SMM0, day 189.

SMM2: run with constant Rayleigh friction, started on day 189.

SMM3: run with the radiation scheme, started on day 189.

SMM4: run with radiation scheme and Rayleigh friction, started on day 189.

- The second initial state corresponds to the 21-24 June 1994 time mean. This mean is named after the 22nd of June, which corresponds to SMM day 174. Only one SMM run was performed with this background state. First a run was initialized on day 174 and run for a few days to bring the winds into balance (SMM00).

  SMM5: run with no radiation nor Rayleigh friction, started with initial state taken from SMM00, day 180.

In subsequent sections the SMM runs performed to study the non-linear evolution of the unstable modes found with the instability calculation will be described.

6.3 Experiment 1: SMM1, run day 189

After the short run with strong Rayleigh friction to bring the zonal mean fields into balance (SMM0), different days to initialize the SMM were tried. Since the idea is to study the development of the fastest growing normal mode found in section 5.3.1 (July background state), the initial fields should not differ too much from the July state. Day 189 was chosen, i.e., 4 days into the SMM0 integration. Figure 6.1 shows the difference between winds on day 189 and the winds from the EUGCM (day 185). Small changes are seen at the upper part of the easterly jet north of 60°N.

The SMM1 integration starts on the 7th of July (labelled as SMM day 189), and is 100 days long. The setup used in this experiment does not include the radiation scheme, i.e., no annual cycle is included and therefore dates should be taken as time references only.

After some 10 days into the SMM1 run, waves of different zonal wavenumbers can be seen growing from the initial conditions. Figure 6.2 shows the time evolution versus latitude at 70 km of the temperature amplitude for wavenumbers 1, 2, 3, and 4 respectively.

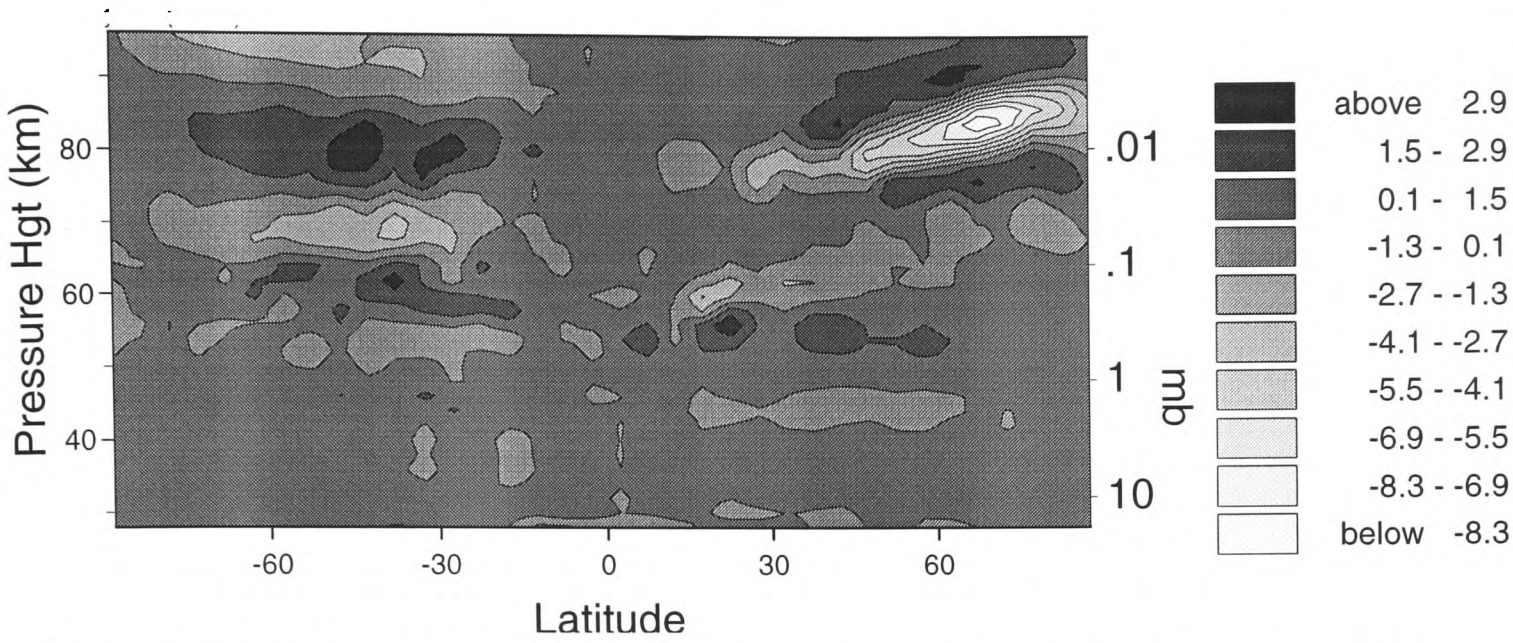


Figure 6.1: Difference between zonal mean u-wind field at day 189, and the initial zonal mean u-wind (day 185), SMM0.

Amplitudes for zonal wavenumbers 1 and 2 are confined to a narrow latitude band in the southern hemisphere. The k=1 wave appears around day 227, later than k=2, which is the first wave component to emerge with a significant amplitude at around day 210. The largest amplitudes are seen for k=3 in the northern hemisphere. Three periods of wave 3 activity can clearly be distinguished in Figure 6.2c. A first smaller amplitude wave is present between day 210 and day 224 at around 55°N, then the wave moves southwards and two bigger amplitude waves at around 40°N are present for days 224-247 and 247-263. Finally a very small amplitude k=4 wave is present between days 210 and 220 at about 55°N, the same position but earlier than the first period of wave 3 activity.

The three periods of wave 3 activity will be analysed separately in the following sections.

6.3.1 Period: day 200 - day 224

Figure 6.3 is a frequency versus zonal wavenumber plot calculated for zonal wind at 70 km and 52.5°N for the period day 200 to day 224. The largest peak is clearly at zonal wavenumber 3 (k=3) and frequency -0.7 cycles per day, which corresponds to a period of 35 hrs (the 35 hrs wave hereafter). A second smaller peak at k=3 can be seen at frequency -0.58 cycles per day, which corresponds to a period of 42 hrs (the 42 hrs wave hereafter). The spatial structure of the 35 hrs wave is shown in Figure 6.4. The structure is very similar

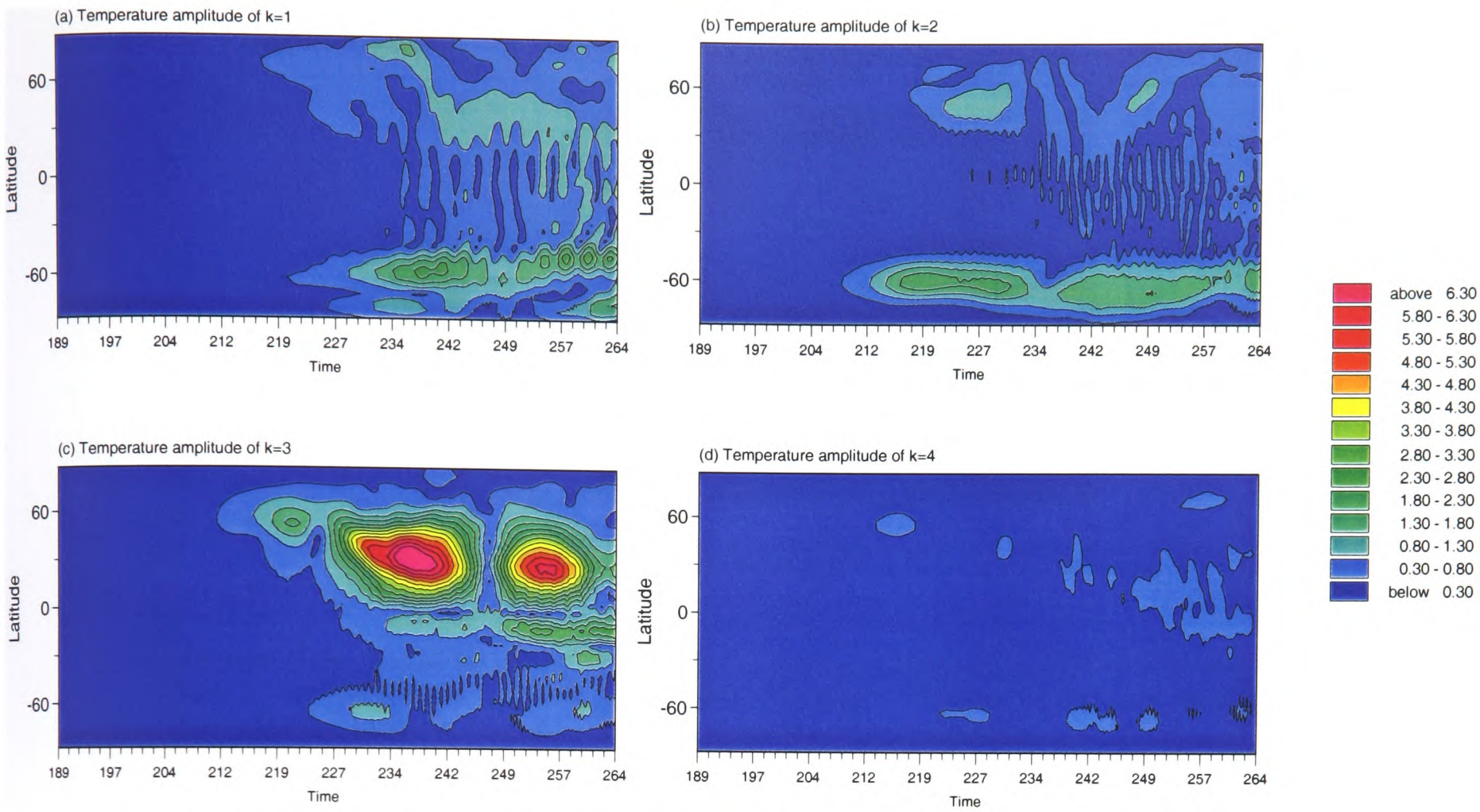


Figure 6.2: Time evolution versus latitude at 70 km of temperature amplitude for first four zonal wavenumbers in SMM1.

to the fastest growing k=3 mode found in the instability calculation (compare with Figure 5.4). It is a localized mode with largest amplitude at around 60°N and 80 km height. The bold dot-dashed line on the figure is the critical line. The wave has large amplitude in the critical region, as had the unstable mode from the instability calculation. In Figure 6.3 smaller peaks are seen at zonal wavenumbers 2 and 4. The k=4 wave has the same phase speed as the k=3 wave with frequency -0.9 cycles per day. The temperature amplitude for k=4 is shown in Figure 6.5a and again resembles the fastest growing mode for k=4 found in the instability calculation. The k=2 wave (Figure not shown) also corresponds to the fastest growing mode for k=2 from the instability calculation (Figure 5.3).

The 42 hrs wave has a somewhat more global structure than the 35 hrs wave. Figure 6.5b shows the meridional wind component. The wave can be identified as the third fastest growing k=3 mode in the instability calculation. The small amplitude found during this period is presumably because of the slower growth rate of the wave.

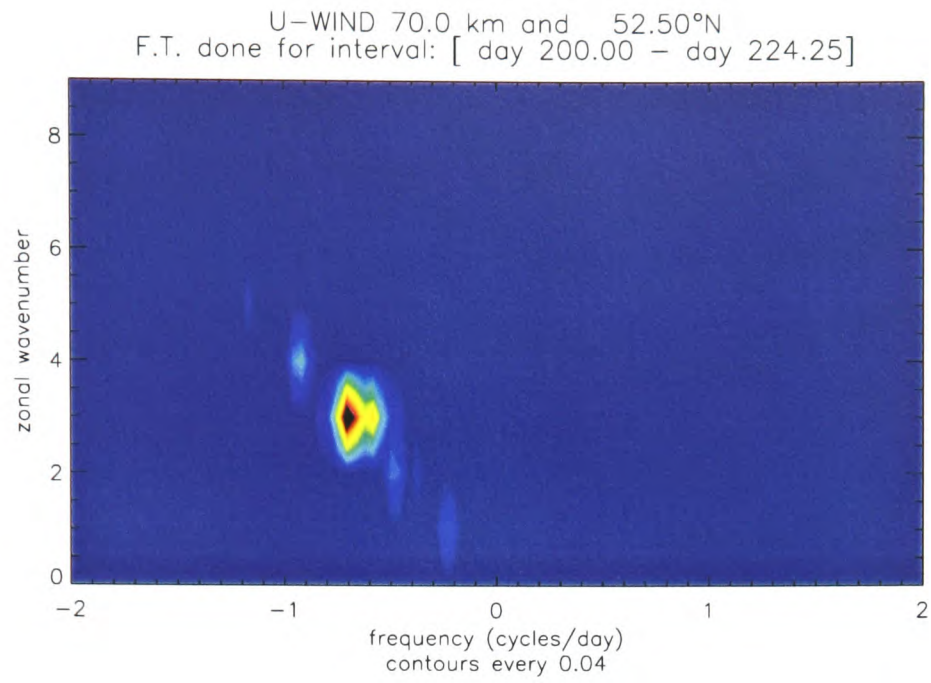


Figure 6.3: Zonal wavenumber versus frequency spectra of u-wind at 70 km and 52.5°N for the period day 200-224, SMM1. Negative frequencies indicate westward propagation, positive frequencies indicate eastward propagation.

6.3.2 Period: day 224 - day 247

During this period the waves reach their largest amplitudes, the zonal wavenumber 3 wave being the most important feature. A frequency versus wavenumber calculation done for this period for zonal wind at 70 km and 52.5°N (Figure 6.6) shows that the frequency of the dominant wave is −0.57 cycles per day (period of about 42 hrs), i.e., there is a change in period of the dominant wave at the same time as there is a shift of maximum amplitude from 55°N to 40°N. The latitude-height section of the amplitude of the wave shows large changes as well compared with the previous period. Figure 6.7 shows the spatial structure of the 42 hrs wave. Apart from the much larger amplitude seen during this period, the wave is also much more global. The meridional wind shows large amplitude in the southern hemisphere and the zonal wind component shows a second peak in the southern hemisphere. Figure 6.7 also shows the critical line of the wave; again the wave has large amplitude in the critical region, as expected for an unstable wave. In general all these characteristics of the 42 hrs wave are in better correspondence with the quasi 2-day wave.

The relation between the three zonal wavenumber 3 waves found up to now in this run is not clear. The 42 hrs wave present between days 224-247 could be the large amplitude

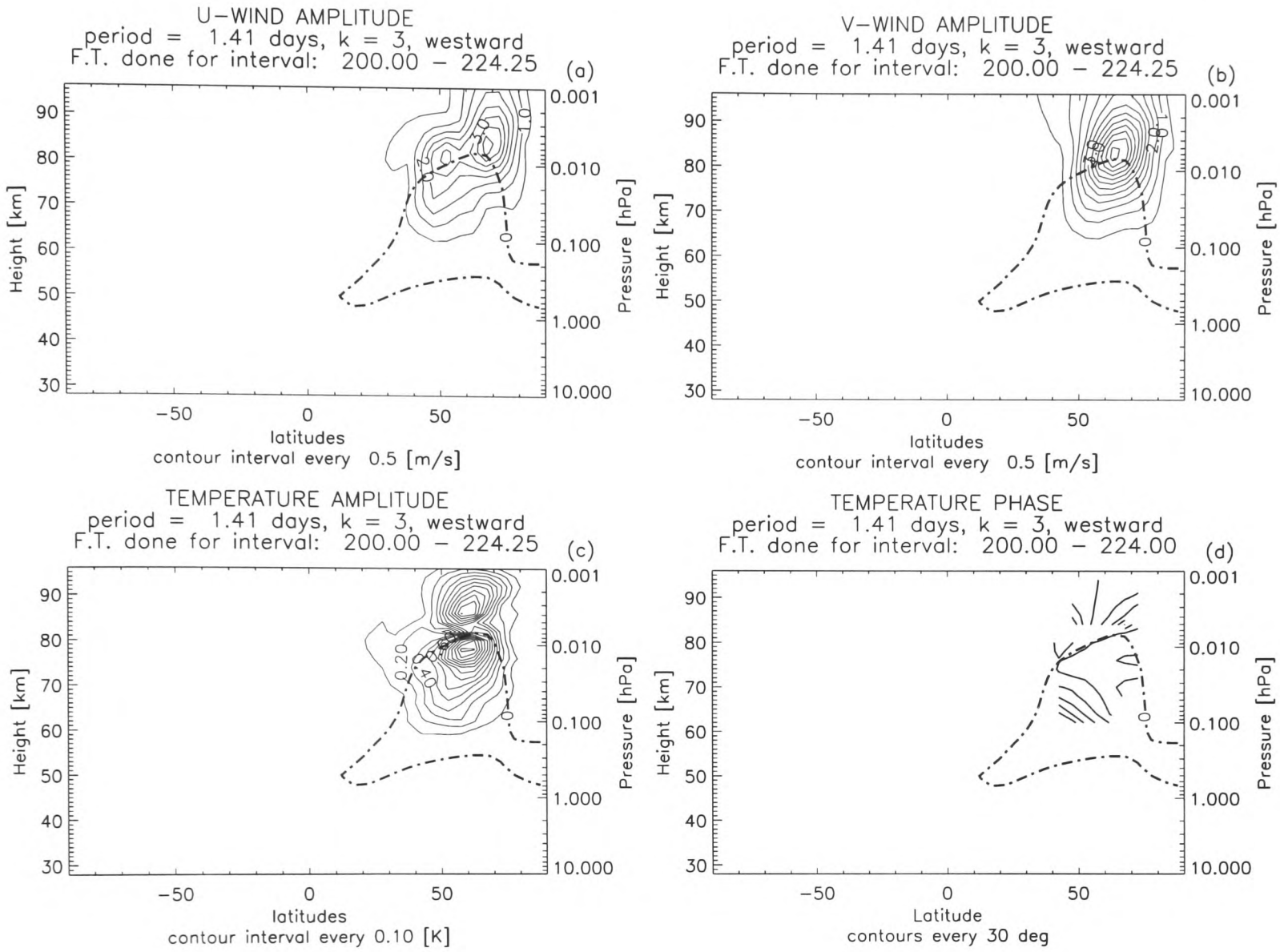


Figure 6.4: (a) u-wind amplitude of the westward propagating 35 hrs wave in SMM1. In bold dot-dashed line is the critical line for this wave ($u - c$=0). (b) v-wind amplitude, (c) temperature amplitude and (d) temperature phase.

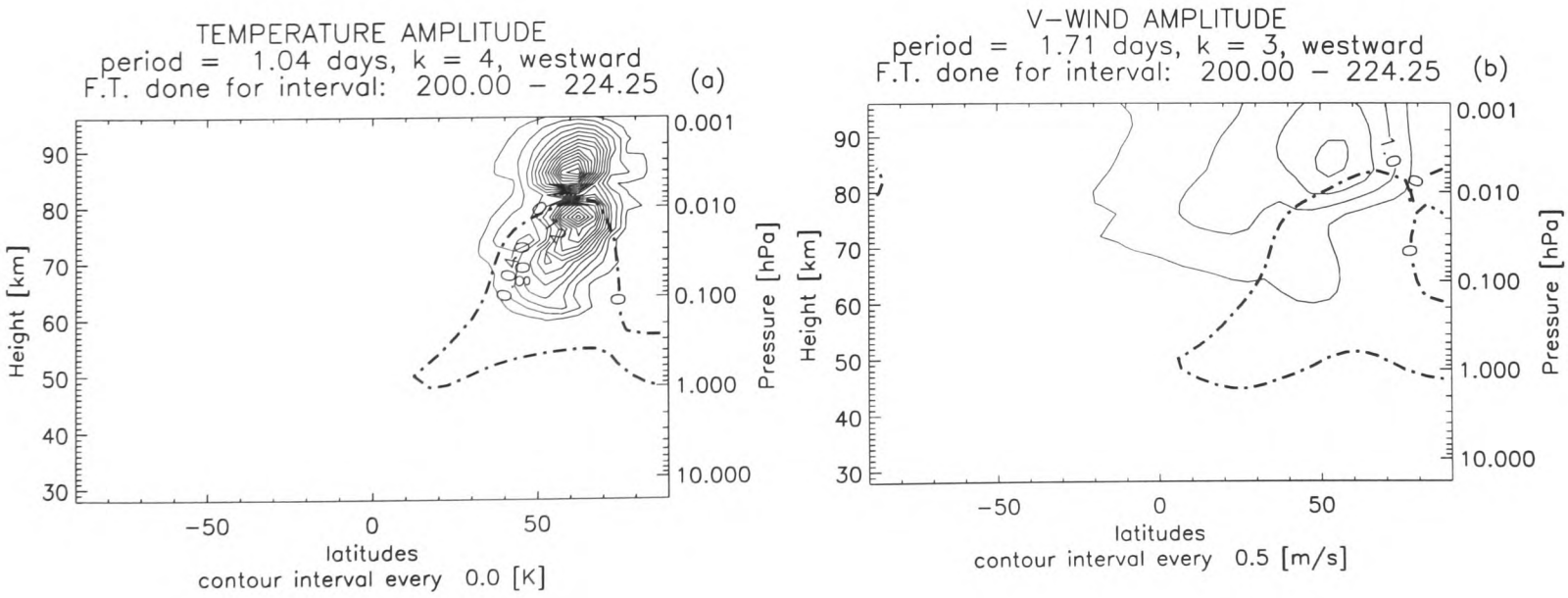


Figure 6.5: (a) Temperature structure for k=4, 25 hrs wave. (b) Meridional wind structure for k=3, 42 hrs wave, SMM1. In bold dot-dashed line is the critical line for these waves ($u - c$=0), SMM1.

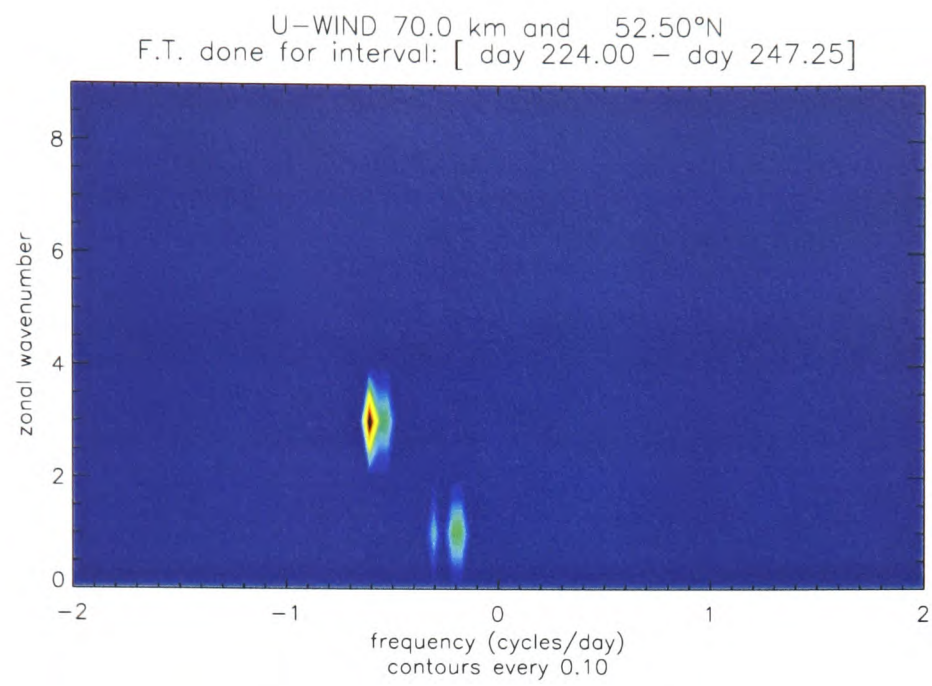


Figure 6.6: Zonal wavenumber versus frequency plot for u-wind at 70 km and 52.5°N for the period day 224-247, SMM1.

version of the 42 hrs wave found during the first wave 3 'blob', although the identification just by 'eye' is difficult. Another possibility could be that the 42 hrs wave is in some way forced or triggered by the wave present during the first 'blob'.

For this same period a k=1 and k=2 wave are observed in the southern hemisphere (Figure 6.2a and 6.2b). Spectral analysis indicates that these waves are both eastward propagating. The period of the k=1 wave is between 4.5 and 5.5 days. Figure 6.8 shows the zonal mean wind amplitude (6.8a), the meridional wind amplitude (6.8b), the temperature (6.8c) and the temperature phase (6.8d) of this wave at a period of 5 days. In temperature its structure shows a double peak at around 55 km and 80 km at 60°S. The zonal wind shows two maxima at around 70 km, 45°S and 85°S. The meridional wind has a maximum at the pole at 70 km. This wave resembles remarkably the polar winter 4-day wave in the EUGCM, apart from the somewhat longer period (compare with Figure 4.18). Comparison with UKMO analysis data is also very good, although the peaks of the wave in the SMM are at higher altitudes compared with the structure seen in the observational data (compare with Figure 4.4). The period of the k=2 wave is slightly over 2 days (figure not shown). The spatial structure of this wave is very similar to the k=1 wave. The k=2 wave has a

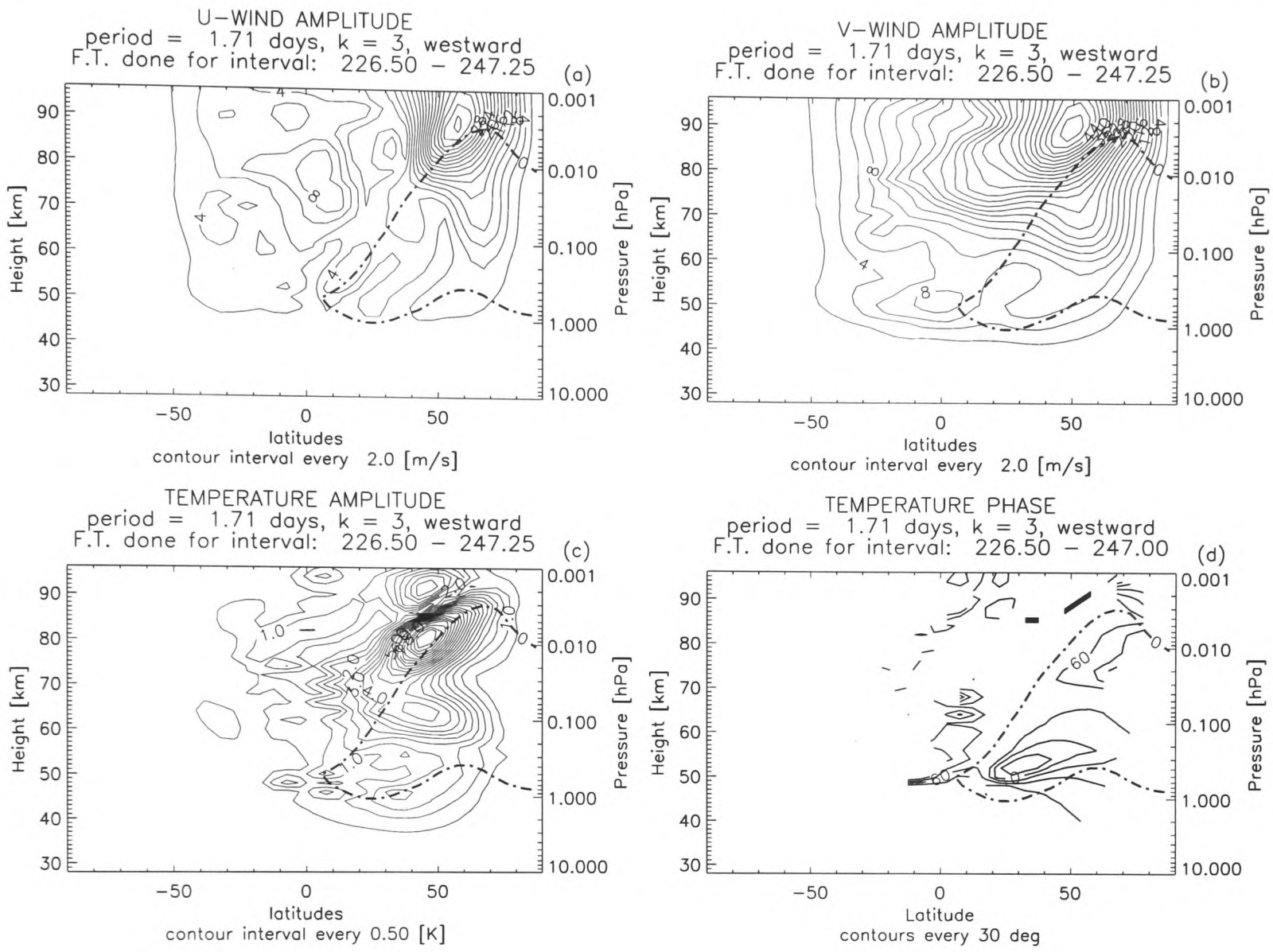


Figure 6.7: (a) u-wind amplitude of the westward propagating 42 hrs wave in SMM1. In bold dot-dashed line is the critical line for this wave ($u - c$=0). (b) v-wind amplitude, (c) temperature amplitude and (d) temperature phase.

meridional wind amplitude much smaller than the zonal wind component, whereas for the k=1 wave, both wind components show similar values.

6.3.3 Period: day 247 - day 265

In Figure 6.2c there is a clear minimum in the wave 3 amplitude visible around day 247. However there is no significant change in the structure of the wave after day 247. The wave 3 component has a period of approximately 42 hrs and the same spatial structure as the wave during the previous period. After day 260, the SMM run shows repeated periods of k=3 activity of smaller amplitude (Figure not shown).

Figure 6.9 shows PV on the 5000 K isentrope (about 70 km); the consecutive plots are

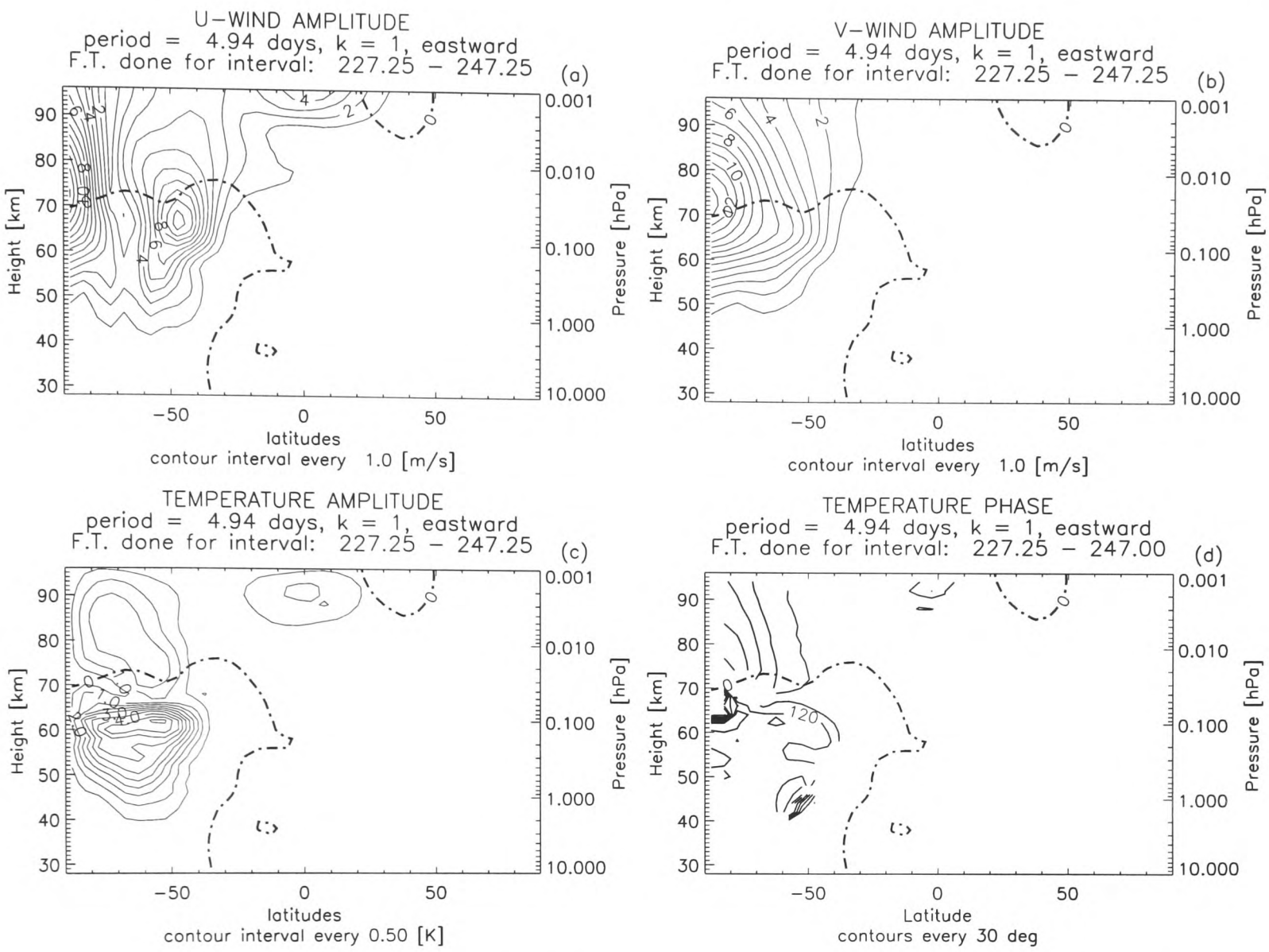


Figure 6.8: (a) u-wind amplitude of the eastward propagating 5 day wave in SMM1. In bold dot-dashed line is the critical line for this wave ($u - c$=0). (b) v-wind amplitude, (c) temperature amplitude and (d) temperature phase.

at 4 day intervals. The evolution of the flow in SMM1 can be seen from these plots. A clear wave 3 pattern starts to develop at around day 226 from the initial axisymmetric flow. Three vortices grow from the main 'triangle' shape PV by day 230 (at the time when the 42 hrs wave emerges as the largest wave), they break at day 234, and merge at day 246, which coincides with the minimum seen in Figure 6.2c. The wave 3 structure then emerges again and remains until the end of the integration. This 'life-cycle' of growing, breaking and merging of vortices resembles calculated baroclinic life-cycles of waves in the troposphere (e.g. Thorncroft *et al.*, 1993).

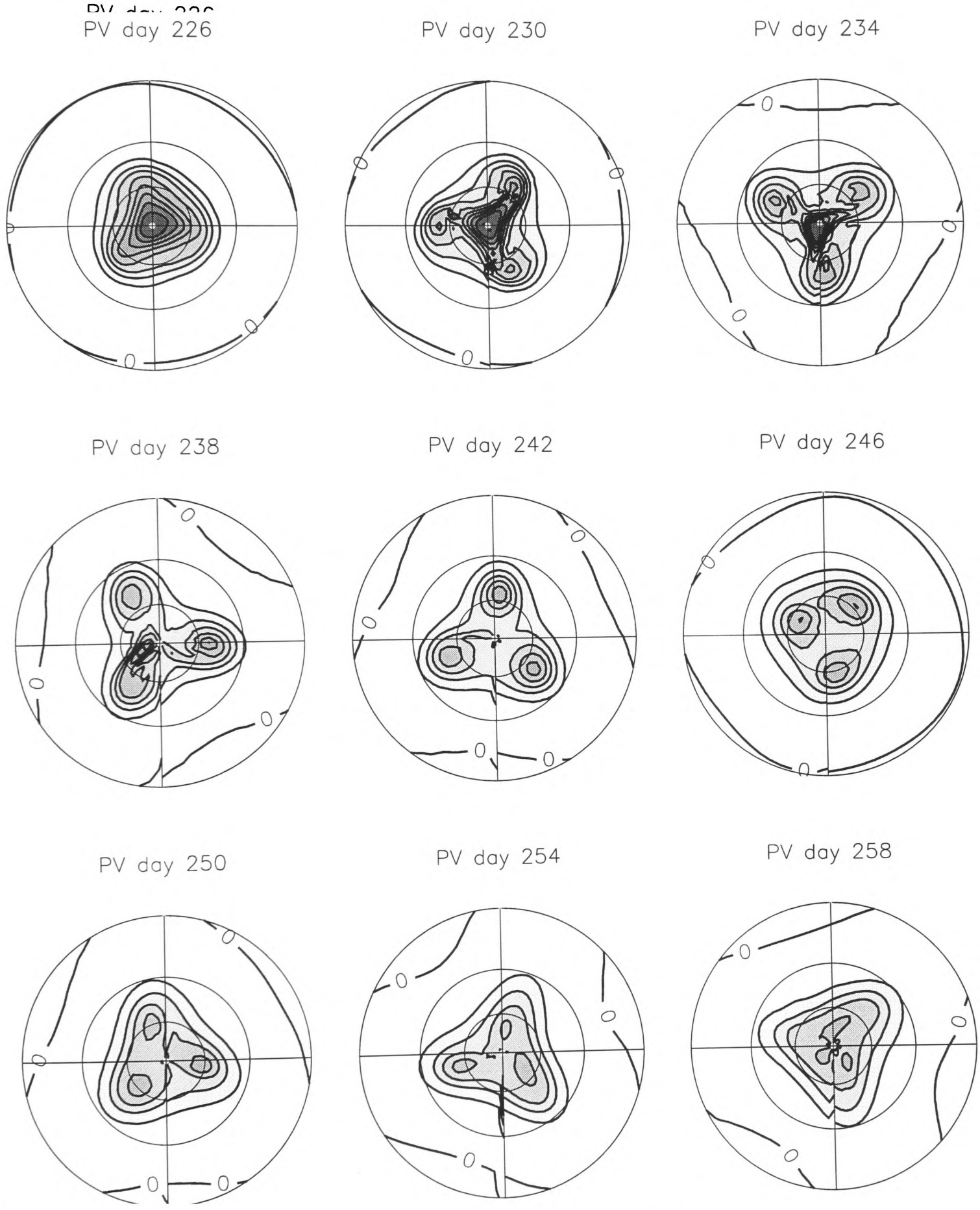


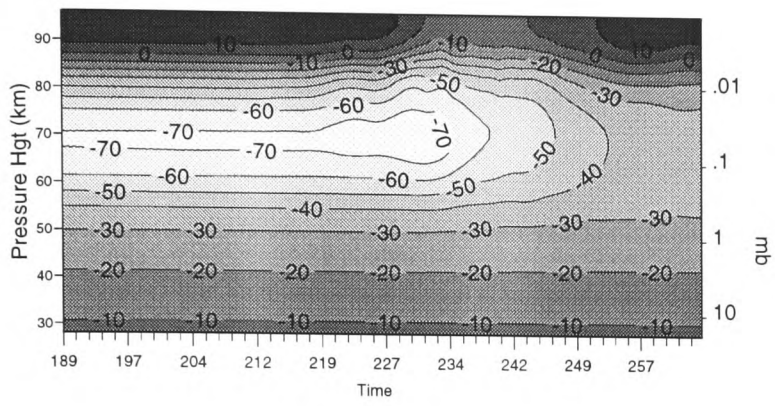
Figure 6.9: PV on the 5000 K isentrope ($\sim$ 70 km) from SMM1, run initialized on day 189.

6.3.4 Changes to the mean flow

Figure 6.10a shows the time evolution of the zonal mean u-wind at 57°N as a function of altitude. During the first wave event (days 210-224) there is no change of the mean flow; only when the second wave starts to grow in amplitude (at around day 230) are there observable changes. The summer jet gets decelerated, the easterlies penetrate much higher, pushing the mesospheric westerlies equatorwards and upwards. The jet maximum is moved polewards and the shear zone steepens in the vertical northwards of 60°N. By day 250 the deceleration of the core of the jet stops, now the maximum is at around 25°N and 50 km height. The westerly winds start to appear again in the higher levels of the SMM, and no further changes to the zonal mean u-wind occur, even though there continue to be periods of k=3 wave activity later in the run (although these are of smaller amplitude). In Figure 6.10b a latitude-height section of the zonal mean wind at day 189 is shown in solid contours, together with the zonal mean wind at day 235 in dashed contours. At day 235 the vertical shear has been reduced in most of the northern hemisphere middle to high latitudes, but stronger horizontal gradients have developed. Most of the forcing to the zonal mean wind occurs above 55 km and in the northern hemisphere. Much smaller changes to the zonal-mean flow are found in the southern hemisphere.

Together with these changes in the zonal mean wind, there are changes in the meridional gradient of the background quasi-geostrophic potential vorticity ($\overline{q}_y$). Figure 6.11a shows the time evolution of $\overline{q}_y$ at 70 km as a function of latitude. The region of most negative values of $\overline{q}_y$ coincides with the core of the easterly jet (about 55°N and 70 km height). The evolution of the field is associated with the changes observed in the zonal mean u-wind. The most negative region starts to decrease by day 235 and shifts towards higher latitudes, where the steepening of vertical wind shear is found. The influences of the eddies on the mean flow can be seen by examining the divergence of the EP flux per unit mass ($\nabla \cdot F/(\rho_0 a \cos\phi)$). Figure 6.11b displays the EP flux diagram for day 235. Contours indicate the divergence of the EP flux per unit mass. The negative contours between 40°N and 60°N at 80 km, indicate where the waves produce a westward force on the mean flow. The positive contours at 55°N and 65 km, indicate where the waves produce an eastward

(a) Zonal mean u-wind



(b) Zonal mean u-wind day 185 and day 235

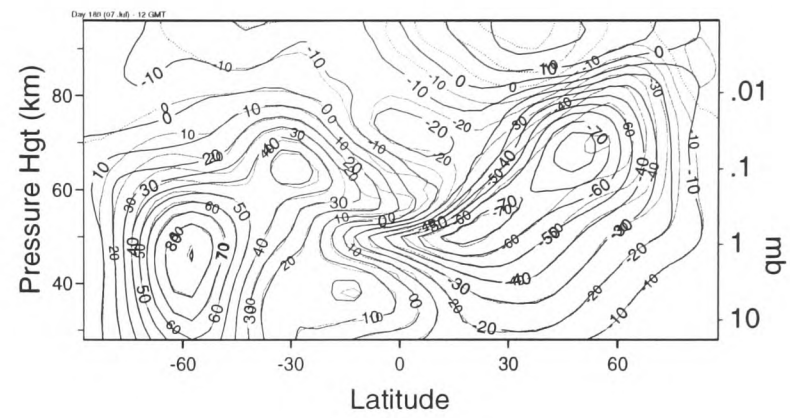
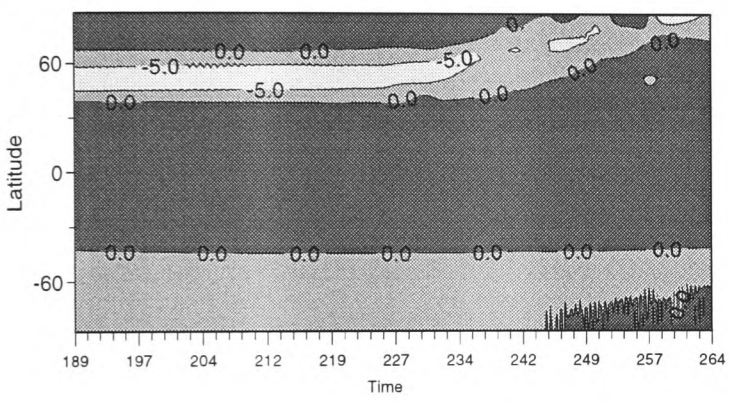


Figure 6.10: (a) Time evolution of zonal mean u-wind at 57°N, SMM1. (b) Zonal mean u-wind on day 189 (solid contours) and zonal mean u-wind on day 235 (dashed contours), units of $\mathrm{m\,s^{-1}}$, SMM1.

(a) $\overline{q}_y$



(b) day 235

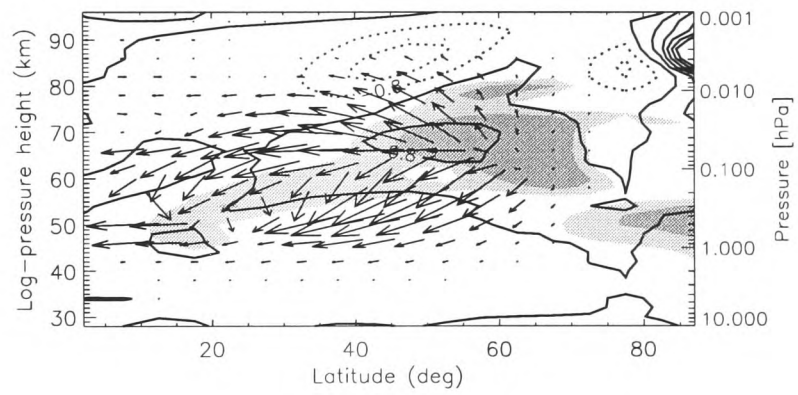


Figure 6.11: (a) Timeseries versus latitude at 70 km of $\overline{q}_y$ $[\mathrm{m^{-1}s^{-1}}]$, scaled by $1 \times 10^{+11}$, SMM1. (b) $\nabla \cdot F/(\rho_0 a \cos\phi)$ in units of $1 \times 10^4\,\mathrm{m\,s^{-2}}$. EP flux (arrows) scaled by $\cos\phi$, multiplication factor is applied such that when plotted in the $\phi - z$ plane, the flow will appear nondivergent when $\nabla \cdot F = 0$ (after Dunkerton, 1980). Shading indicate regions where $\overline{q}_y$ is negative, light grey for values between 0 and $-1.5 \times 10^{+11}$, dark grey for values less than $-1.5 \times 10^{+11}$, SMM1

force on the mean flow. The net effect of this wave forcing of the mean flow is to reduce the vertical shear in the region between 40°N and 60°N, consistent with the waves stabilizing the baroclinic instability which is driving the growth of the wave in the first place.

6.3.5 Growth rates

In the previous sections of this chapter, the latitude-height structure was presented of the dominant waves which developed during the integration. The growth rates of these waves are now examined by assuming that the zonal wavenumber of the meridional wind

amplitude[3], V_k, can be represented by a sum over the N dominant waves,

$$\mathrm{V}_k(\phi, p, t) = \sum_{n=0}^{N} a_n(t) A_n(\phi, z) e^{i\omega_n t}, \tag{6.4}$$

where, for the *nth* wave, a_n is the complex non-sinusoidal part of the time variation (which will represent the growth and decay of the wave), A_n is the latitude-height structure (which is assumed constant over the run, and is determined as in section 6.3), and ω_n is the frequency. The a_n in equation 6.4 are determined by assuming they are constant over a 4-day period and a best fit V_k is obtained by multiple regression over all latitudes, heights and N waves. A timeseries of a_n is determined by examining successive 4-day periods. The result of this procedure for the SMM1 run, where the regression is performed for $k = 3$ and both the 35 hrs and the 42 hrs waves is shown in Figure 6.12. The solid line in the Figure is the time evolution of $|a_1|$ (the 35 hrs wave) and the dotted line is the time evolution of $|a_2|$ (the 42 hrs wave). The solid curve shows exponential growth up to day 220, which corresponds to the time when the first wave 'blob' in Figure 6.2c can be seen. The 42 hrs wave has a much slower growth rate, during the day 200-224 period, when only a very small amplitude 42 hrs wave was found. Then the 42 hrs wave grows to large amplitude until day 235. The amplitude then decays sharply and re-emerges for the period of the third wave 'blob' (between days 245 and 265). The results show that both $k = 3$ waves are independent unstable modes. It can be seen that their initial growth appears exponential. To obtain a value for their initial growth, γ, a least-squares fit is performed to the logarithm of the curves. The time interval used for the this depends on the specific wave for which the curve is fitted. In table 6.1 the growth rates (γ) for the different waves found in SMM1 are presented.

The fits to exponential growth are all very good, with the correlation coefficient for the linear regression all above 0.98, for both the wavenumber 3 and for the southern hemisphere k=1 and k=2 waves. For zonal wavenumber 4 the fit is not very good, with lower correlation coefficient obtained for the least-squares fit.

[3]The meridional wind was chosen because this is the field in which the two k=3 waves in SMM1 differ most.

zonal wavenumber k	frequency ω [cycles/day]	period [hours]	growth rate γ [days^{-1}]	e-folding time γ^{-1} [days]
1	0.2	120	0.171	5.85
2	0.37	63	0.273	3.65
3	0.68	35	0.261	3.81
3	0.57	42	0.201	4.97
4	0.96	25	0.254	3.93

Table 6.1: Fitted growth rates and e-folding times for the different waves grown in SMM1.

The growth rates compare well with those obtained by the linear instability calculation: The e-folding time for the k=1 wave in the SMM1 is 5.8 days and the linear instability calculation gives 5.7 days. For k=2 the values are 3.7 days and 3.9 days from the SMM and the instability calculation respectively. For the 35 hrs wave the values are 3.8 days compared to 3.2 days. The values for the 42 hrs wave differ more, the SMM giving an e-folding time of 5 days and the instability calculation giving 4 days. Finally for k=4, the values are 4 days and 3.5 days respectively.

6.3.6 Sensitivity to initial conditions

To study the sensitivity to initial conditions of the SMM integrations, different runs with very similar initial conditions were performed. The same background fields were used (day 189 from SMM0) but different noise were added to these fields (the noise being generated with a random number function from IDL). Five runs of equal length were performed for this purpose. The general results and conclusions drawn from this exercise will be given here.

In all of the five runs performed, the unstable waves that grow from the initial perturbation are predominantly wavenumber 3. In four of the runs the three 'blob' pattern of the wavenumber 3 temperature amplitude is observed. This means a 35 hrs like-wave and a 42 hrs like-wave grow in four runs, with similar characteristics in growth rates, period

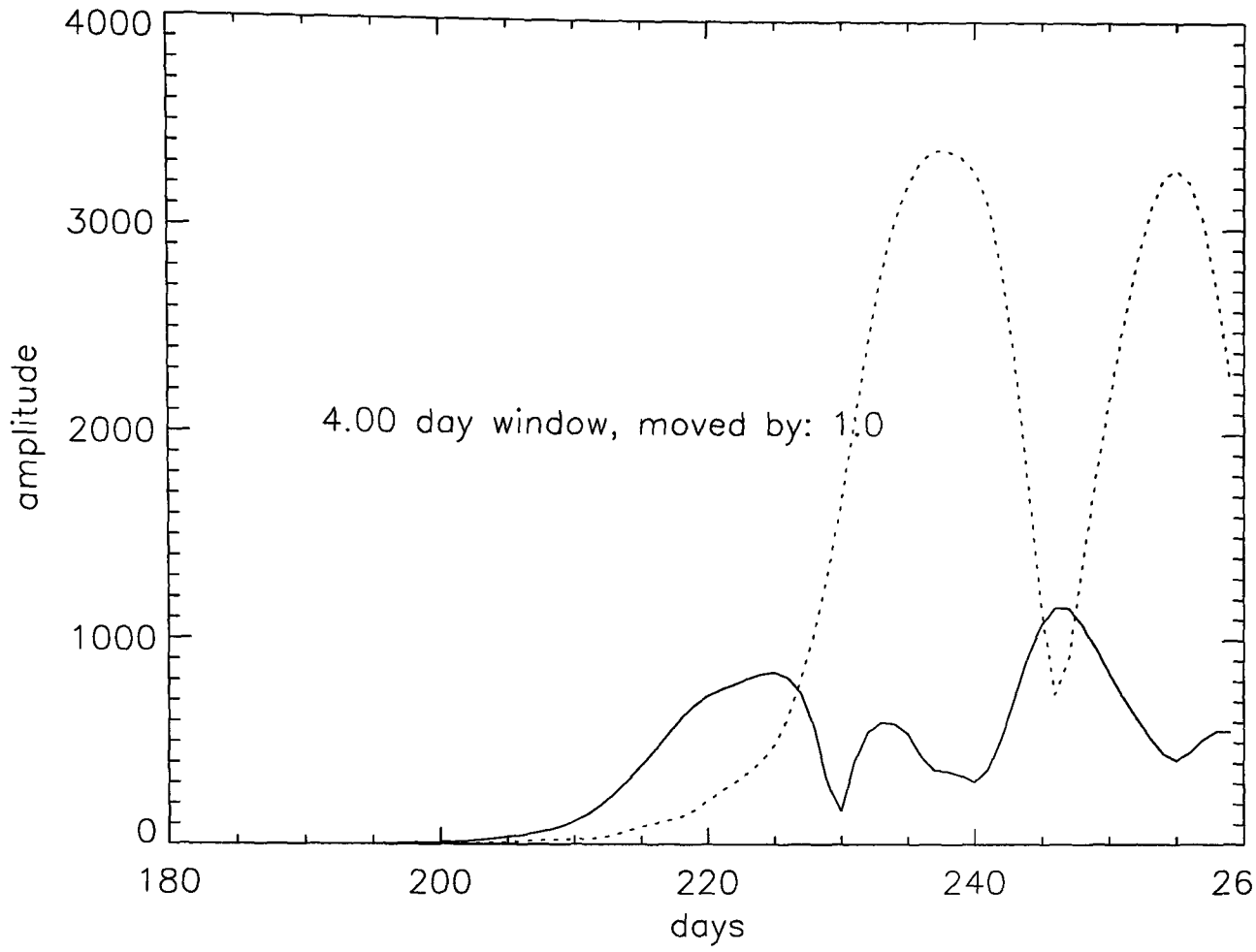


Figure 6.12: Time versus amplitude of fitted curves for the non-sinusoidal time dependence of the two k=3 waves: solid contour for the 35 hrs wave, dashed contour for the 42 hrs wave. Amplitude is in arbitrary units.

and spatial structure to SMM1. The contribution of other wavenumbers varies, and in particular two of the runs exhibit more wavenumber 1 in the northern hemisphere. In one run the first 'blob' is not present, and therefore the main wavenumber 3 mode is the larger amplitude global wave with period around 42 hrs.

6.4 Experiment 2: runs with Rayleigh friction (SMM2)

In this experiment the SMM is initialized with the same background state as SMM1, but instead of allowing the winds to change freely, uniform Rayleigh friction is applied over the whole domain. Again the SMM is run without radiation. The zonal mean u-wind is relaxed back to initial conditions with a relaxation time of about 2.5 days (this is $\alpha = 2.5 \times 10^{-6}\,\mathrm{s}^{-1}$). The meridional wind is relaxed back to zero. Note that only the

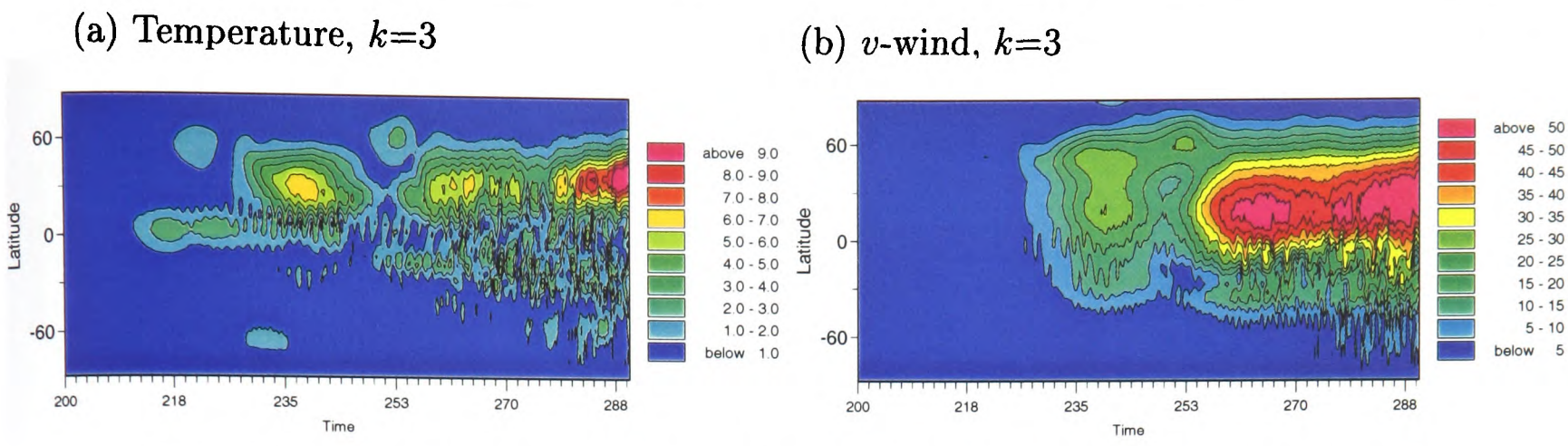


Figure 6.13: (a) time versus latitude at 70 km of k=3 temperature amplitude. Run with constant Rayleigh friction, α=4.5 $\times$ 10^{-6}s^{-1}, SMM2. (b) same as (a), but for v-wind.

zonal mean flow is relaxed back to initial conditions, so that waves can still develop (as described by equations 6.2 and 6.3).

The aim of this experiment is to see how the waves develop by 'clamping' the zonal mean state to the initial condition, and in this way restricting the feedback of the waves onto the zonal mean winds. No restriction is imposed onto the background temperature, but because of the thermal wind relation (equations 2.14 and 2.15), the zonal mean u-wind and zonal mean temperature are in close balance, thus forcing the winds to a particular state also constrains the temperature.

SMM2 is run for about 100 days. After 15 days, waves of different zonal wavenumbers can be recognized. Waves with zonal wavenumber 3 are the dominant component of the wave spectra in this run, as was the case in SMM1. No large-scale waves grow at other wavenumbers, only a small amplitude wave is seen for k=2 in the southern hemisphere. Figure 6.13a shows the time evolution from day 200 to day 290 of the temperature amplitude of k=3 at 70 km. This is to be compared with Figure 6.2c. The time evolution of the k=3 amplitude again shows three wave 'blobs'. Because the winds are 'clamped' to the initial state, the growth of the waves is exponential for longer, and they reach larger amplitudes. A first wave develops at around 60°N during days 210-224. After that a much larger amplitude wave at around 30°N emerges between days 230 and 250. From about day 260 onwards, a larger amplitude k=3 wave is present until the end of the run, with maximum amplitudes reaching 13 K (in comparison with maximum amplitudes of about

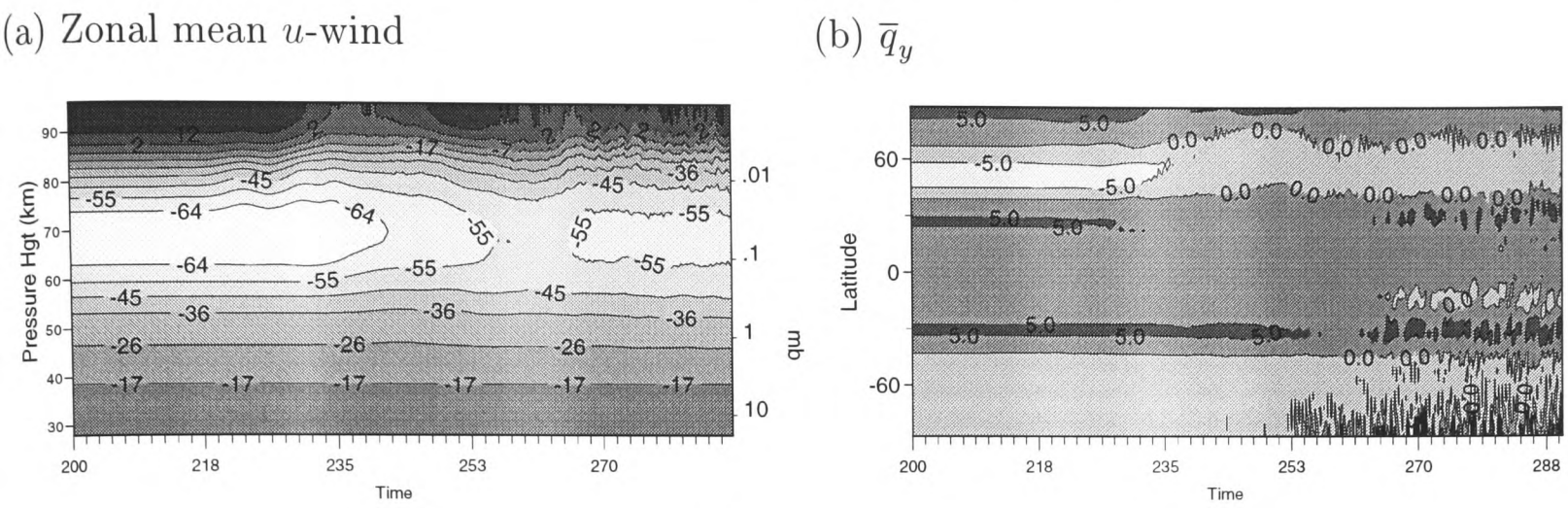


Figure 6.14: (a) time versus height plot at 57.5°N of zonal mean u-wind, SMM2. (b) Time evolution of $\overline{q}_y$ [$\mathrm{m}^{-1}\mathrm{s}^{-1}$], scaled by 10^{+11} at 70 km, SMM2.

7 K found in SMM1). Figure 6.13a also shows short period oscillations at lower latitudes and in the southern hemisphere from day 230 onwards. These short period oscillations considerably disturb the longer lasting midlatitude wave amplitudes (Figure 6.17a).

The spatial structure of the waves are similar to the waves obtained in SMM1. The first wave (days 210-224) is a westward moving wave with period of about 35 hrs (Figure not shown). For the second period, there are again two different waves with k=3. The periods are 35 hrs and 45 hrs, respectively.

Figure 6.14a shows a time versus height plot of zonal mean wind at 57.5°N from day 200 to day 278. No changes to the wind are seen until day 235, when the 42 hrs wave has grown to large amplitude. Then, as seen in SMM1, the mesospheric easterlies are decelerated as well as the core of the midlatitude jet (which is at about 70 km). By day 255 the zonal mean zonal winds above 80 km recover to their initial values, and after that (by day 270) the winds remain unchanged with high frequency oscillation superimposed upon them. Figure 6.14b shows a time versus latitude plot of $\overline{q}_y$ scaled by 10^{+11} at 70 km for the same time extent. At the beginning of the run there is a region where $\overline{q}_y$ is significantly negative (values less than $-5\,m^{-1}\,s^{-1}$) at around 55°N, but this particular region of very negative $\overline{q}_y$ is removed by day 235 (at the time when the changes in zonal wind are seen). However, the wider band (from 40°N to 65°N) where $\overline{q}_y$ is negative remains so for the rest of the SMM integration, with the same 'vacillations' as seen in the zonal wind in Figure 6.14a from day 250 onwards.

Plots of potential vorticity show a very similar behaviour for SMM2 as for the run without Rayleigh friction (SMM1). PV on the 5000 K isentrope for days 219 to 259, at a 5 day interval are shown in Figure 6.15. In the run without Rayleigh friction it is possible to observe how the initial triangular vortex develops into 3 vortices which then merge and finally decay (Figure 6.9). In this run, potential vorticity plots show a similar behaviour: a clear wavenumber 3 pattern emerges from the axisymmetric initial state, three vortices grow and then start to merge, but grow again and persist until the end of the run.

A run where the Rayleigh friction coefficient, α, was set to relax the winds back with an e-folding time of the order of 1 day showed waves growing to such large amplitude that the SMM finally crashed because of an overflow. In SMM2 the growth of the waves is controlled by the induced changes to the zonal mean wind. Usually waves grown from instabilities tend to stabilize the flow, by removing the unstable regions in the flow once they acquire large enough amplitudes. A time versus height plot of zonal mean u-wind at 62°N (see Figure 6.16b) for the stronger Rayleigh friction run ($\alpha = 1 \times 10^{-5}$) shows similarities with SMM2 up to day 260. Then the jet core intensifies and the easterlies push away all of the upper westerlies in the northern hemisphere. By then no coherent waves exist any more.

Returning to Figure 6.13, the other interesting thing seen here is the behaviour at the equator. Firstly, there is a wave amplitude at the equator between days 210 and 240 seen in temperature (Figure 6.13a), but not in meridional wind (Figure 6.13b); the wave is identified with a Kelvin wave. Secondly, as mentioned before, there is an amplitude modulation of the wave 3 amplitude; this can also be clearly seen from Figure 6.17a, where the wavenumber 3 amplitude of temperature at the equator is plotted in a time-height section. The amplitude oscillates from day 225 onwards, with lines of large amplitude (dark greys) tilting downward with time. Another interesting thing to observe in Figure 6.17a are the horizontal oscillations between days 225 and 235. These are alternating maxima and minima between 85 km and 95 km. This structure will be referred to as a 'pancake' structure and is identified with inertial instability.

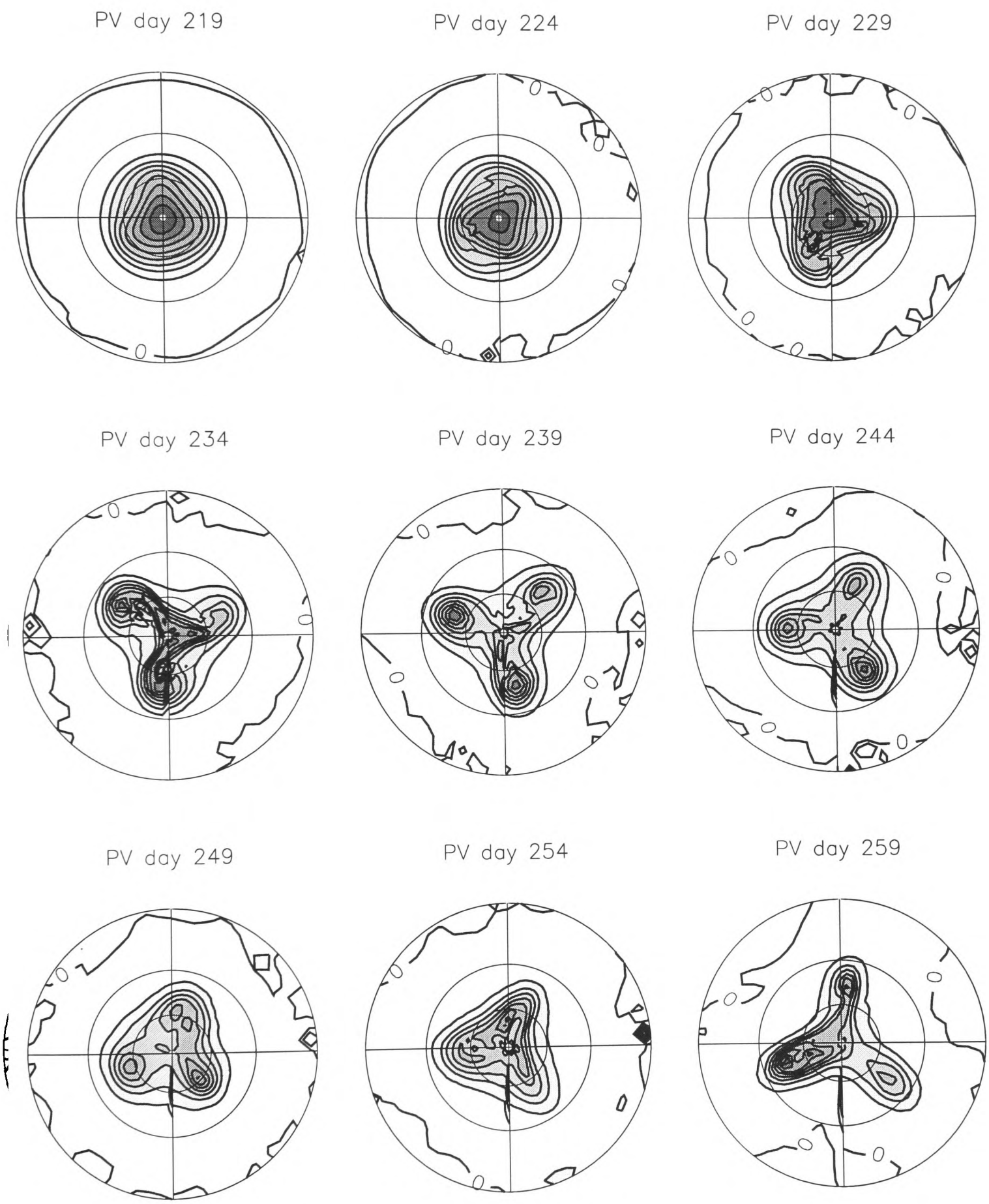


Figure 6.15: PV on the 5000 K ($\sim$ 70 km) isentrope from SMM2.

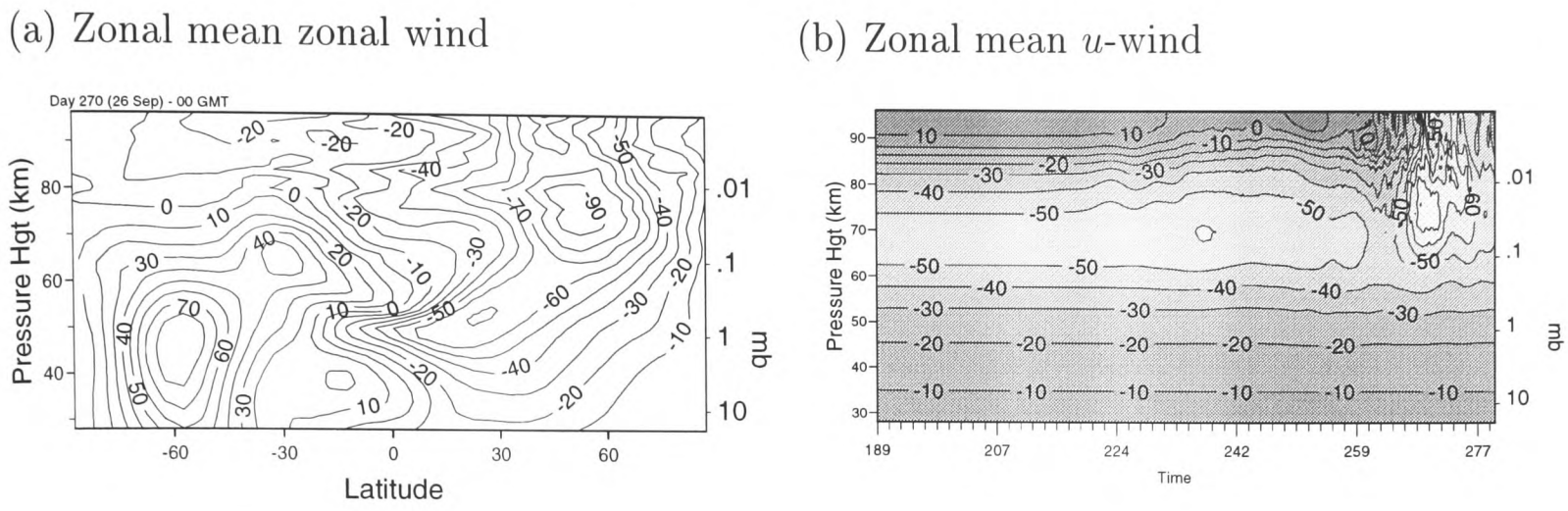


Figure 6.16: (a) Zonal mean u-wind at day 270 of run with Rayleigh friction, α=1 $\times 10^{-5}\mathrm{s}^{-1}$ (about 1 day). (b) for the same run, time evolution of zonal mean u-wind at 62°N.

6.4.1 Inertial instability

The characteristic 'pancake' structure can be seen mostly in meridional wind and is localized in time and location. Pancake structures over some 10-15 km vertical extent are found for day 234 at 90°E and 180°E and at around 5°S (Figure 6.17b). Inertial instability starts appearing around day 220. It is localized in longitude depending on the latitude at which one chooses to look. As was found in Iwi, (1998), inertial instability tends to happen with a vertical wavelength of twice the grid spacing used, i.e., in these experiments where levels are approximately 2 km apart, the vertical wavelengths is 4 km. This can be seen in Figure 6.17b, which shows meridional wind at 90°E in a latitude height section for day 234. Between 0°S and 15°S, alternating maxima and minima with a wavelength of 4 km can be seen. One can expect inertial instability to occur when there is displacement of low PV into higher latitudes. However, no indication could be found of negative PV (characteristic of the southern hemisphere) displacing into the northern hemisphere during the times of these 'pancake' structures.

6.4.2 Kelvin Wave

A Kelvin wave is an equatorially trapped wave with a small meridional wind component. Some of the theoretical characteristics, which have been confirmed from observations

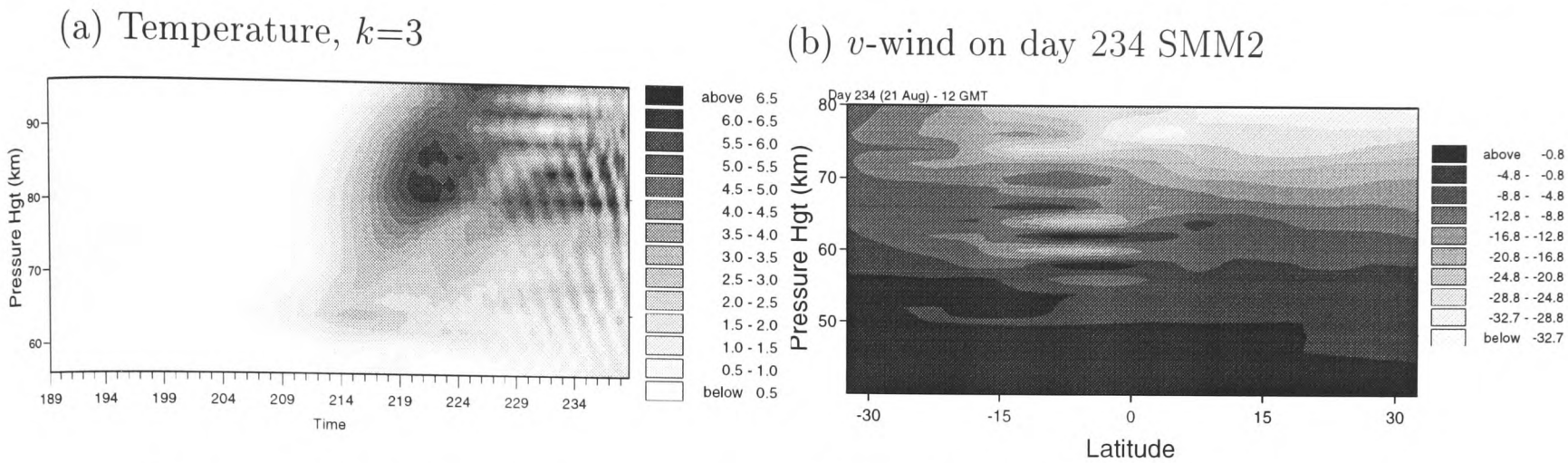


Figure 6.17: (a) time versus height plot at 2.5°N of temperature amplitude for k=3, SMM2. (b) latitude versus height section at 90°E and day 234 of v-wind, SMM2.

include the following: zonal wind, temperature and geopotential components of the wave are confined to low latitudes centered around the equator; they propagate eastward, with surfaces of constant phase tilting eastward with height and downward with time.

Spectral analysis at the equator shows that the wavenumber 3 wave seen in Figure 6.13a is an eastward propagating wave with period around 10 days. Observations of Kelvin waves in the stratosphere and mesosphere have usually been found with periods between 10 and 20 days and zonal wavenumber 1-2 (e.g. Andrews *et al.*, 1987). Figure 6.18a and 6.18b show the spatial structure of the zonal wind amplitude and temperature amplitude respectively; the meridional wind component is negligible. From a time versus longitude plot close to the equator (not shown), one can see that the zonal wind perturbation is in phase with the geopotential perturbation, as expected for this wave. The characteristics of the SMM wave are in good accordance with what is known about Kelvin waves.

With respect to the amplitude modulation seen for wavenumber 3 close to the equator in Figure 6.13a and 6.17a, this is due to interference with the Kelvin wave, which has zonal wavenumber 3 as well. Because the period of the Kelvin wave is much slower than the other wave (10 days compared to about 2 days), one can think of the Kelvin wave being stationary; the 42 hrs wave then moves westward and passes regions of alternating positive and negative anomalies with a zonal structure of wave 3, so that the period of the modulation is almost 2 days. This idea can also be confirmed by finding that no such oscillations are seen in a timeseries of wave number 3 of meridional wind (Figure 6.13b).

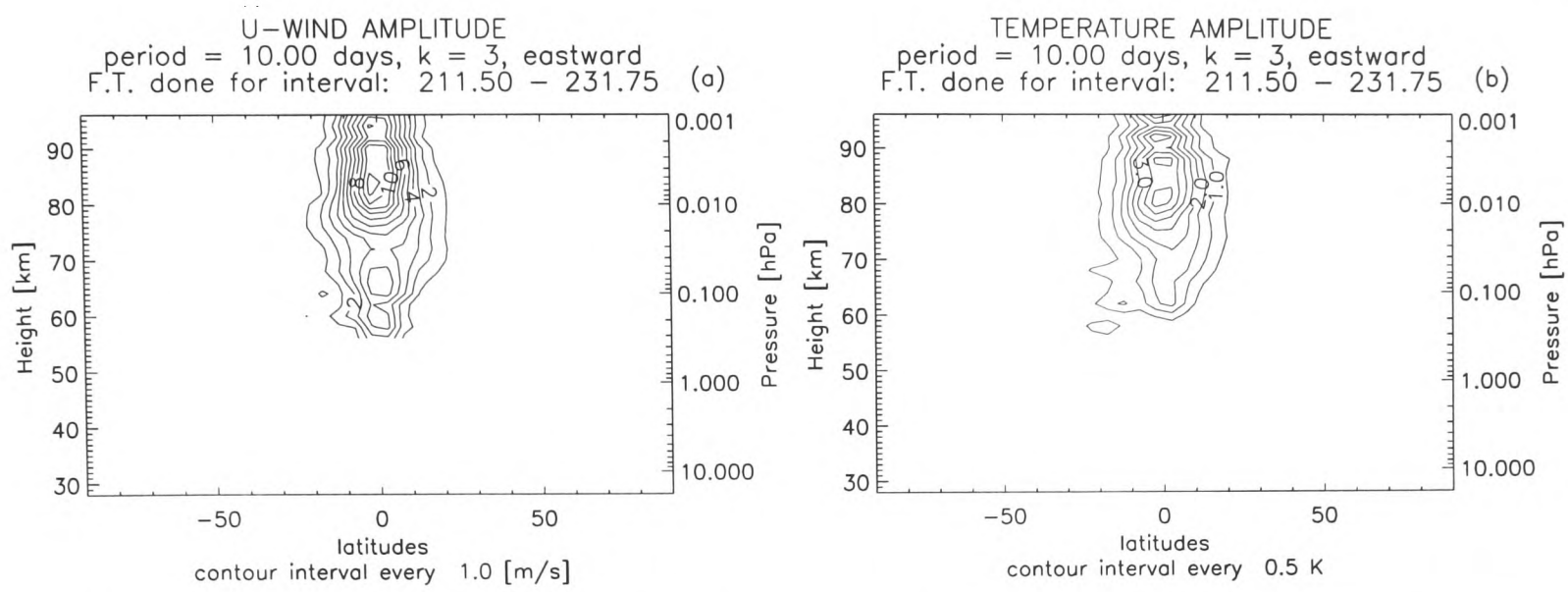


Figure 6.18: (a) u-wind amplitude of the eastward propagating 10 day Kelvin wave in SMM2. (b) same as (a) but temperature amplitude

Previous work with the SMM (Drysdale, 1998) showed that Kelvin waves had to be forced at the lower boundary. The source of the Kelvin wave in this experiment has not been found.

6.5 Experiment 3: runs with radiation

This section describes the results of a few SMM runs where the radiation scheme is included. In the runs described below the radiation was included in a 'perpetual July' mode, so no annual cycle is considered. MIDRAD requires, among other things, the date of the current day of integration. In the version run here, this date is given as the 7^{th} of July.

6.5.1 SMM3: run with radiation and no Rayleigh friction

For SMM3 the setup includes the radiation scheme. The radiative damping in the upper stratosphere and mesosphere decelerates the zonal mean summer jet very quickly in the absence of a gravity wave drag parameterization (see Figure 6.19a). Figure 6.19b shows a latitude height section of zonal mean u-wind at day 200. The core of the summer jet moves from about 50°N and 70 km to 10°N and 50 km and in a narrow height range close to 50 km the summer easterlies penetrate into the southern hemisphere, above which the winds are almost completely vertical. The flow stays mainly zonally symmetric, i.e., there

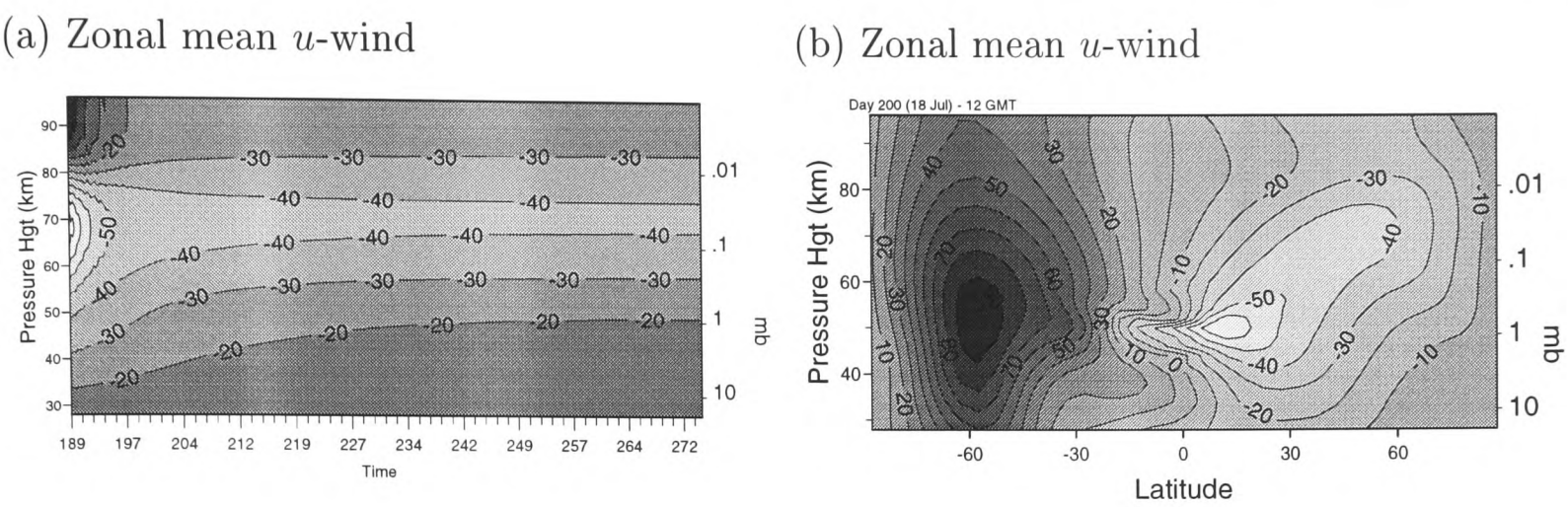


Figure 6.19: (a) time evolution versus height of zonal mean u-wind at 47.5°N, SMM3. (b) latitude height section of zonal mean u-wind on day 200, SMM3.

is no development of waves of any wavenumber in this run in either of the two hemispheres. The temperature field is warmed in the northern hemisphere; this again occurs in the first days of the SMM run. In the southern hemisphere there is a slight warming at all levels.

The time evolution of meridional gradient of the potential vorticity shows how the unstable region in the summer jet is rapidly quenched. However, at low latitudes at around 50 km height there are regions of alternating positive and negative $\overline{q}_y$ in the horizontal direction (this is the location where the northern hemisphere easterlies penetrate into the southern hemisphere). As a result of the acceleration of the winter jet there is a strong horizontal shear at the poleward flank of that jet. Here also is positive $\overline{q}_y$ next to negative $\overline{q}_y$.

6.5.2 SMM4: run with radiation and Rayleigh friction

In SMM4 the radiation scheme and a Rayleigh friction profile which relaxes the winds back to initial conditions are included. As was seen in the previous section, with no parameterization of the gravity wave drag the stratospheric jets cannot maintain their observed structure due to the effect of the radiation. This is true in the summer hemisphere, where the gravity wave drag counter-acts the damping effects of the radiation.

The Rayleigh friction profile used during this run is the one described by equations 6.2 and 6.3 with a relaxation coefficient $\alpha = 2.5 \times 10^{-5}\mathrm{s}^{-1}$ (e-folding time of about 2 days)

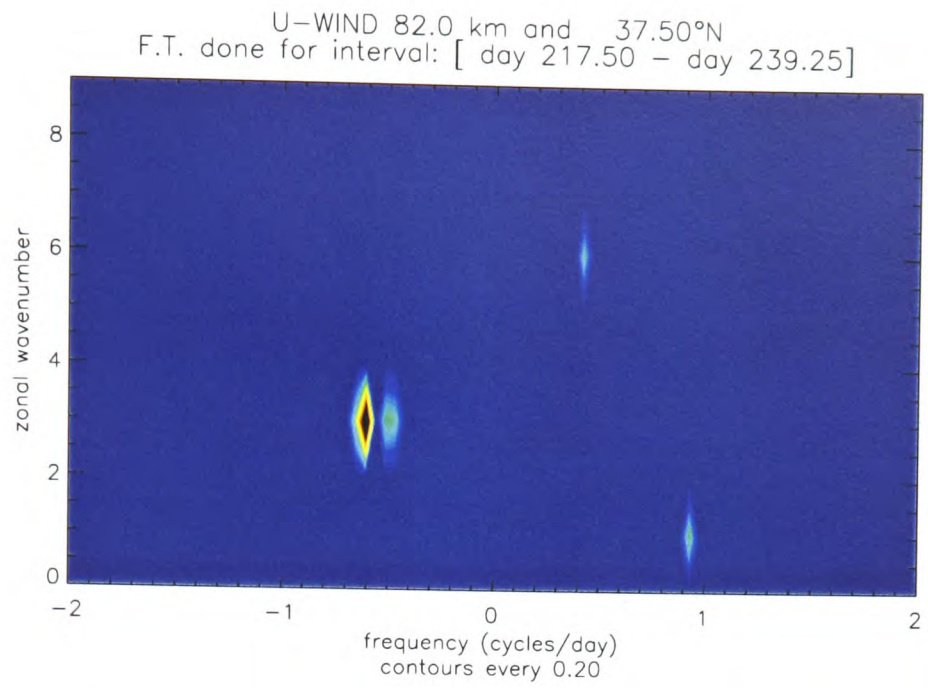


Figure 6.20: Zonal wavenumber versus frequency spectra of u-wind at 82 km and 37.5°, SMM4.

with a=1 × 10^{-7}, b = 2.5 × 10^{-5} and z_0=60 km. The imposed relaxation of the winds allows the SMM to maintain the summer jet close to its initial shape but penetrating all the way up to the top levels of the SMM (Figure 6.22a). Even though for the summer jet no considerable changes are observed, the winter jet accelerated to maximum values of about 150 m s^{-1} (from the initial maximum of 80 m s^{-1}), losing its double peak structure to a much broader and vertical shape.

With the midlatitude jets maintaining their shape, waves can develop in this run. Time evolution versus latitude plots show very noisy amplitudes for wavenumbers 1 to 6 (not shown), but largest values are found for zonal wavenumber 3. The amplitude of wave 3 seen in a time versus latitude section shows little large-scale coherence, with no localized maxima (in contrast to all the other cases described above). There are also intermittent oscillations in time of period about 2 days throughout the whole integration.

The waves start to appear in the run at around day 210. PV on the 5000K isentrope evolves from the initial zonally symmetric state into a wave 3 pattern by this date. Here again the pattern is very noisy and no individual vortices are created, as was the case in

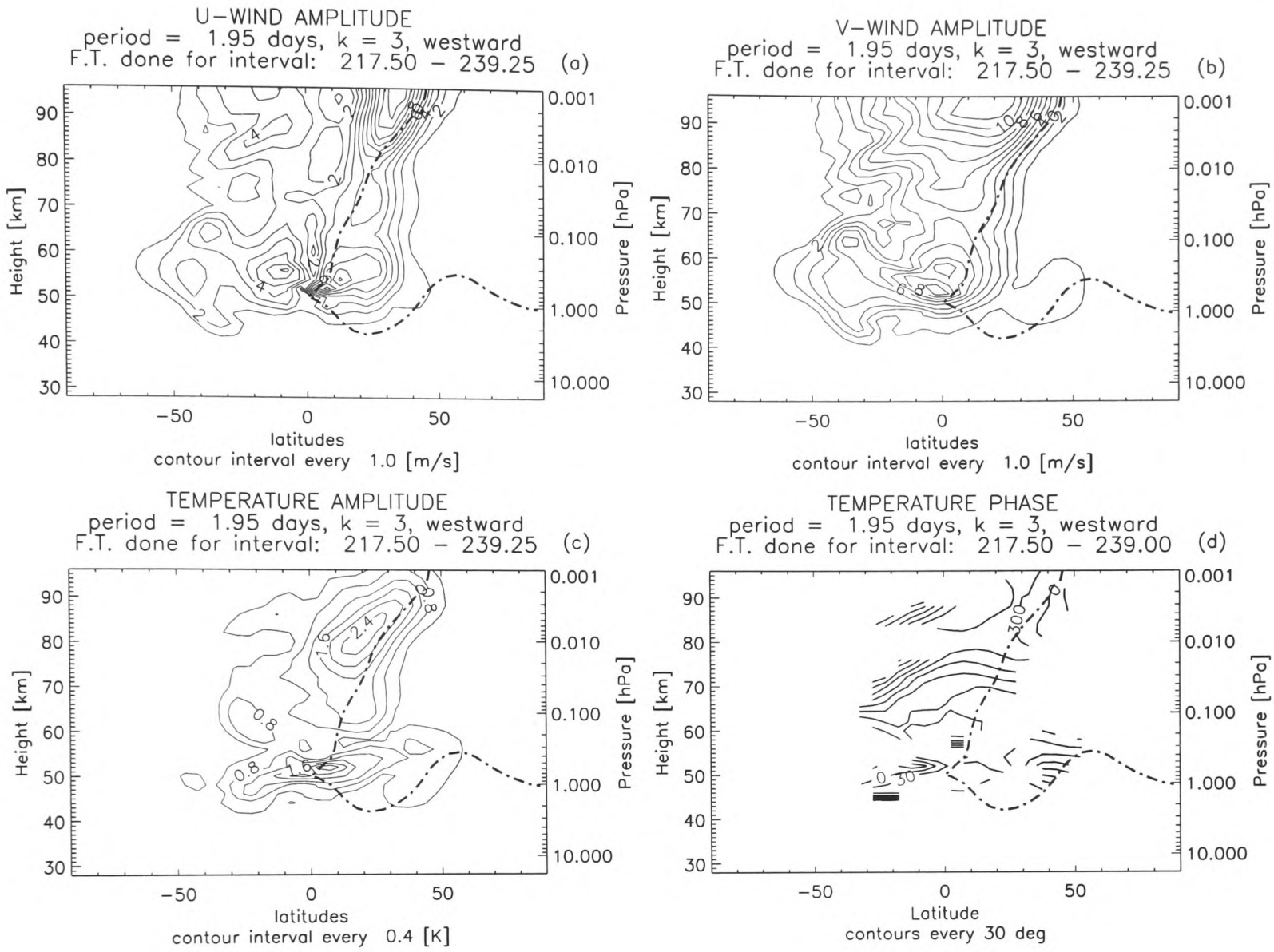


Figure 6.21: (a) u-wind amplitude of the westward propagating 47 hrs wave, SMM4. In bold dot-dashed line is the critical line for this wave ($u - c$=0). (b) v-wind amplitude, (c) temperature amplitude and (d) temperature phase.

SMM1, but a 'triangular' shape is maintained throughout the run (similar to that shown in Figure 6.9 on day 258).

Although no clear wave structure seems to exist as seen from a time versus latitude plot, spectral analysis reveals two peaks for wavenumber 3 (Figure 6.20), at frequency −0.6 cycles per day and at −0.51 cycles per day (periods of 40 hrs and 47 hrs respectively). The wave associated with the first peak has larger amplitude (40 hrs period wave). The spatial structure of both waves is similar, the difference being that the 47 hrs wave goes down to lower altitudes, showing large amplitude between 1 hPa and 0.1 hPa around the equator in the three fields, which is not seen in the 40 hrs wave. Figure 6.21 shows the spatial structure of the 47 hrs wave. Both waves have critical lines, but the 40 hrs wave has large

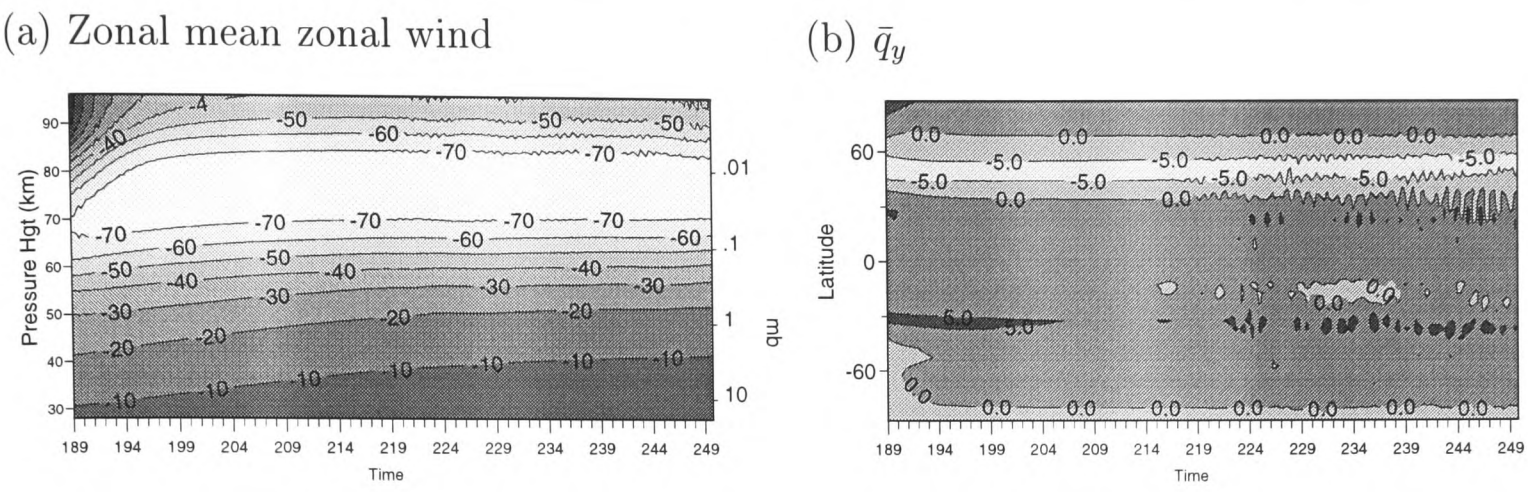


Figure 6.22: (a) Time evolution of zonal mean u-wind at 57°N, SMM4. (b) Timeseries versus latitude at 70 km of $\bar{q}_y$ [$m^{-1}s^{-1}$], scaled by $1 \times 10^{+11}$.

amplitude inside the critical region, whereas the 47 hrs wave is overall more equatorwards with large amplitude just outside the critical line (see Figure 6.21). Maximum amplitude of temperature is located at 20°N, and at 15°N for meridional wind.

The e-folding times of both waves were calculated as described in section 6.3.5. Both waves have a similar e-folding time of about 3 days, but the 40 hrs wave grows to larger amplitudes. In general the correlation coefficients from the REGRESS function were lower than for any fit done in SMM1.

Although the two waves grow to large amplitude, they do not force changes to the zonal mean flow (see Figure 6.22a). The distribution of $\bar{q}_y$ in the northern hemisphere stays unchanged throughout the run (Figure 6.22b). In the southern hemisphere, where the jet is accelerated considerably, the initial region where $\bar{q}_y$ is negative becomes larger.

6.6 Experiment 4: SMM5, run day 180

In this section the results of run SMM5 will be presented. The background state used for this experiment comes from the EUGCM 21-24 of June 1994 mean. In section 5.3 it was shown that running the instability code with this background state gave as the fastest growing mode a wavenumber 3 with a global structure and a period of 43 hrs. This is a different result from the one obtained with the July background state. With this run

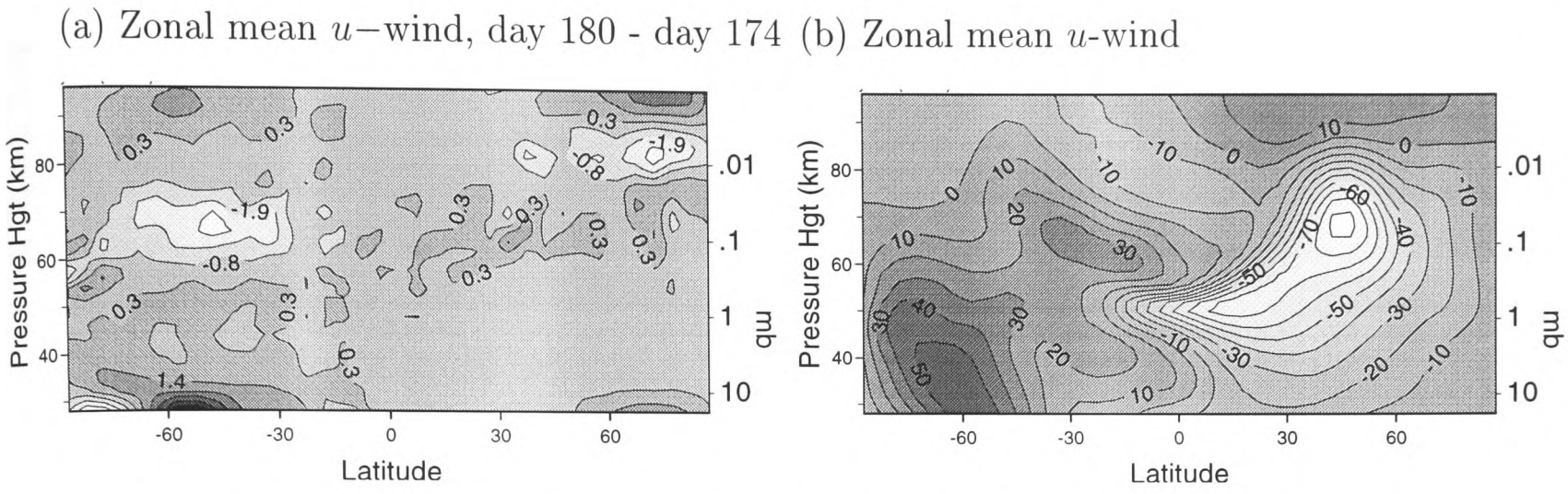


Figure 6.23: (a) Difference between zonal mean u-wind at day 180, and the initial zonal mean wind (day 174), SMM00. (b) contours of the zonal mean u-wind on day 180 SMM5, units of $\mathrm{m\,s^{-1}}$.

the non-linear evolution of the 43 hrs wave will be investigated, since this has a stronger resemblance to the quasi 2-day wave.

As before, a short initial run with strong Rayleigh friction is needed to balance the winds and temperature (SMM00). Day 180 from SMM00 was then chosen as the initial condition for SMM5, i.e., six days after the initial date of day 174. The SMM is then integrated for some 80 days with no radiation and no Rayleigh friction. Figure 6.23a presents the change in the zonal mean zonal wind (day 180 - 174) induced by the strong Rayleigh friction run. Small differences can be seen at the top and bottom of the SMM domain. Values up to $6\,\mathrm{m\,s^{-1}}$ are found for the lowest levels in the southern hemisphere. There are no large changes in the summer jet, which is the dynamically important region. In fact no changes in $\bar{q}_y$ are observed. Figure 6.23b shows the initial zonal mean u-wind of SMM5, day 180.

Figure 6.24 shows the time evolution at 80 km of the v-wind amplitude for the first four zonal wavenumbers. Only the k=3 wave amplitude grows in SMM5. Four 'blobs' of consecutive larger and smaller amplitude are found. For the first, days 200-218, the maximum of meridional wind at 80 km is seen at about 25°N. The second period of wave amplitude is between days 220 and 233; here the amplitude of the wave is reduced to almost half of the observed values of the previous period, and is still at about 25°N. A third period of k=3 wave amplitude is seen between days 235 and 253. Finally, a smaller wave amplitude

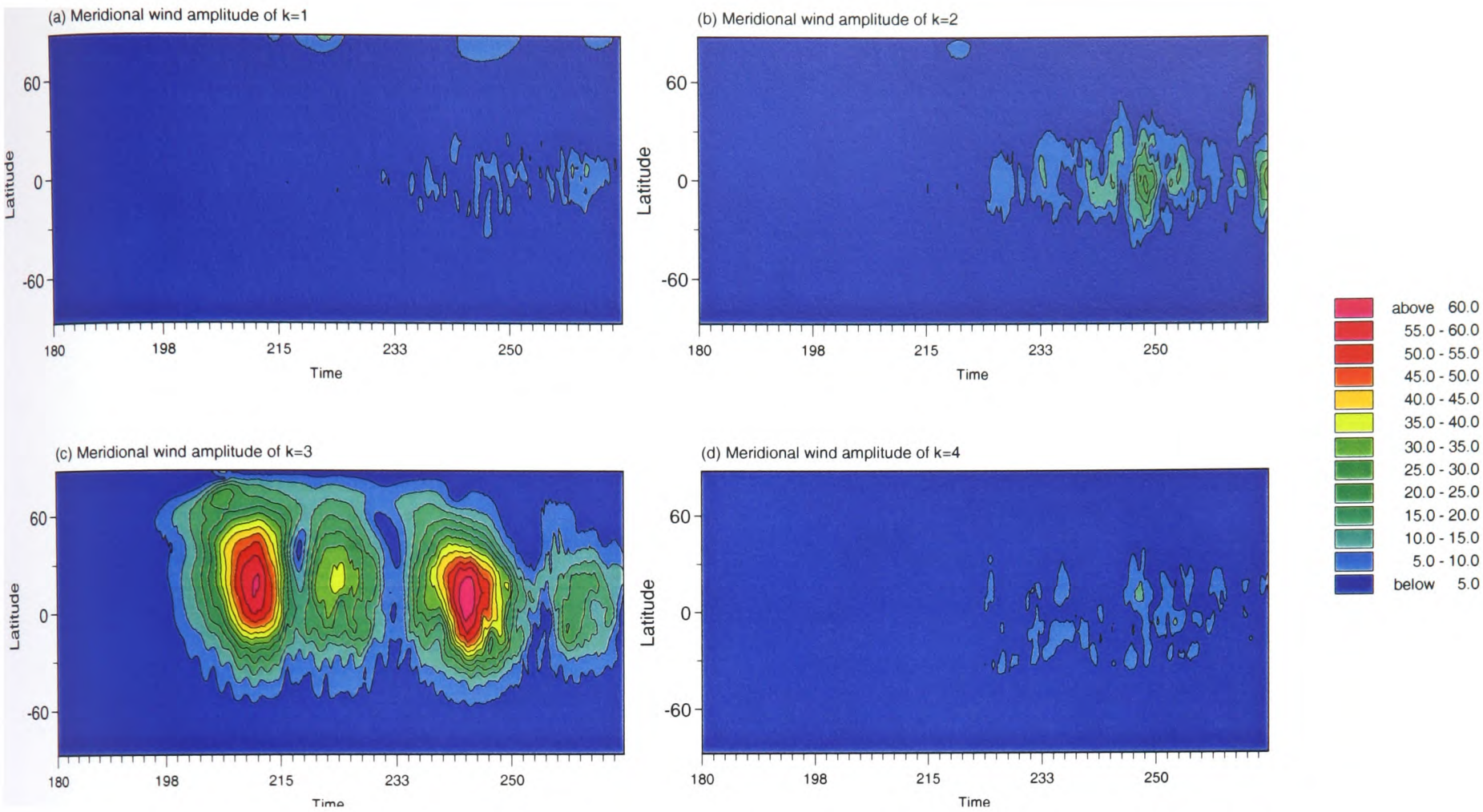


Figure 6.24: Time evolution versus latitude at 80 km of v-wind amplitude for different wavenumbers for run initialized on day 180, SMM5.

is present between days 255 and 270. The location of the wave maximum (at 80 km) has moved to about 10°N, and in general the wave is seen to be more symmetric about the equator, as is the case for the meridional wind in the quasi 2-day wave. From spectral analysis it is found that the four 'blobs' of k=3 wave activity are westward propagating waves with period 42 hrs, although, as seen in Figure 6.24c, the structure evolves during the run. In Figure 6.25 the spatial structure of the wave as calculated for the period days 230-250 is shown. The zonal wind and temperature show amplitude maxima at either side of the equator with larger values in the northern hemisphere. The meridional wind has a maximum at the equator. The e-folding time of the wave is 3.75 days, close to the 3.5 days given by the instability calculation. Note that the wave only has significant amplitude inside the critical region in the temperature field.

Changes to the mean flow start to be noticed by day 205 (Figure 6.26a), when the waves start to reach larger amplitude. The core of the easterly jet, which is initially at about 45°N

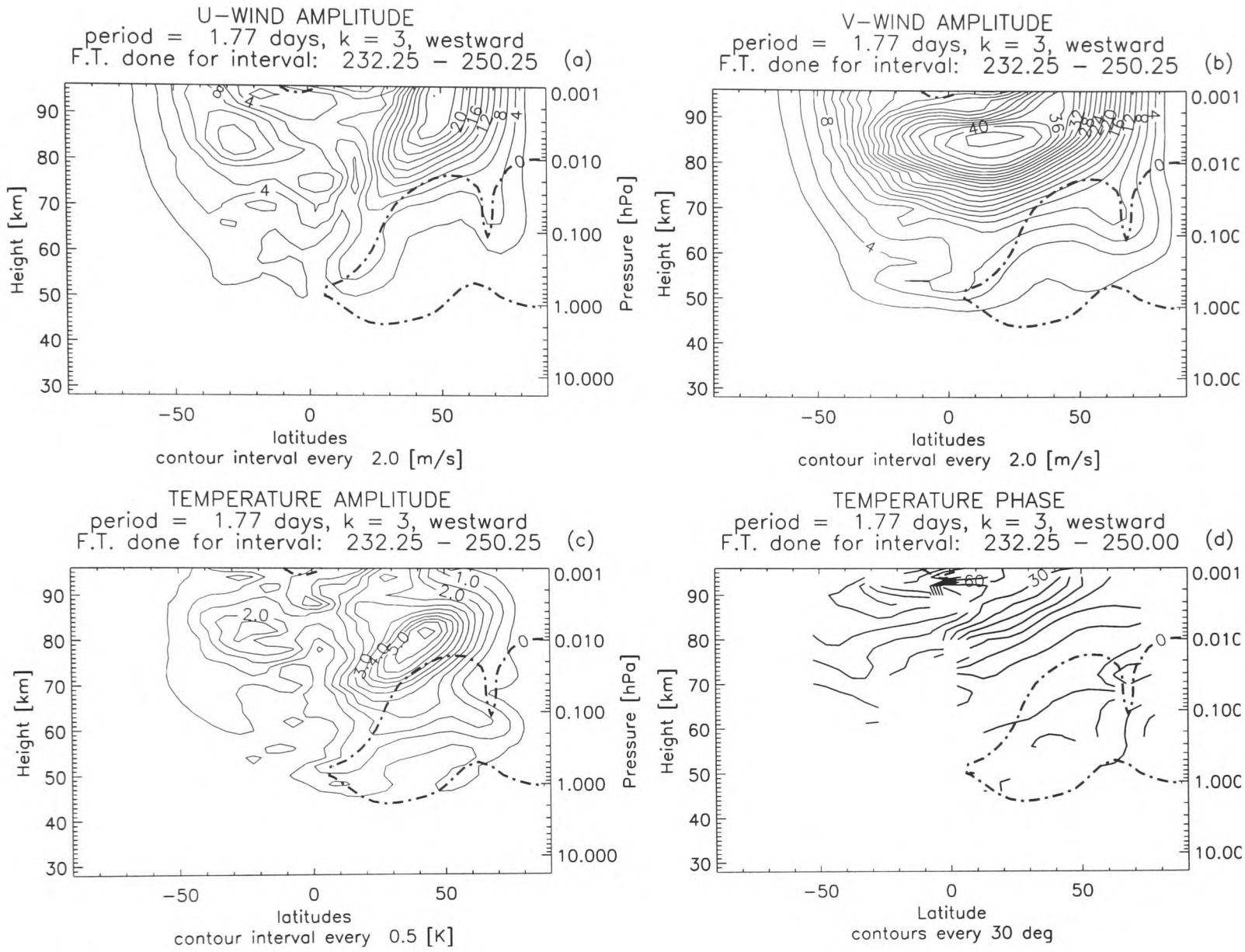


Figure 6.25: (a) u-wind amplitude of the westward propagating 42 hrs wave, SMM5. In bold dot-dashed line is the critical line for this wave ($u - c$=0). (b) v-wind amplitude, (c) temperature amplitude and (d) temperature phase.

and 68 km, gets decelerated and split into two. One maxima moves to 50°N with maximum values of 70 m s^{-1}; the other part moves equatorwards and to lower altitudes. This happens at around day 210. By day 220 the high latitude maximum has completely disappeared, but the easterlies reach the top SMM levels at 70°N. There are still mesospheric westerlies between 80 km and 96 km south and north of 70°N, but by now the vertical shear is very much reduced. The flow continues to evolve until day 240; after which the amplitude of the waves is too small to force the background flow. The changes found in the temperature field include a reduction of the very cold polar summer mesopause. Minimum temperatures are initially about 140 K, but by day 220 these have warmed to 160 K. The meridional gradient of background potential vorticity initially has a region of very negative values at the core

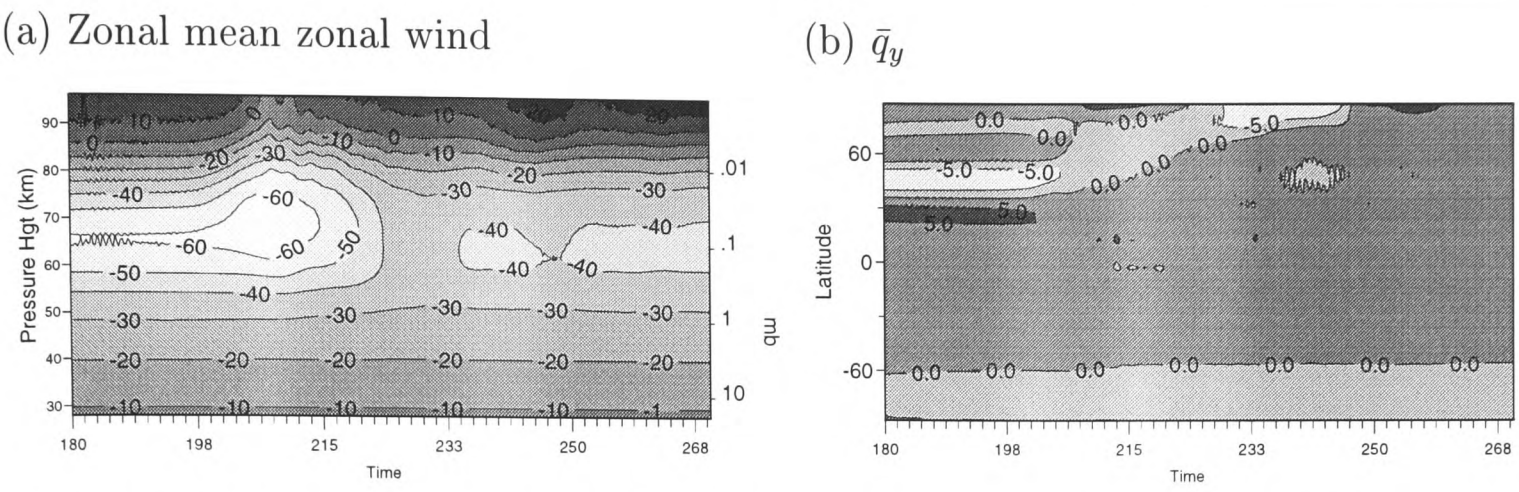


Figure 6.26: (a) Time evolution of zonal mean u-wind at 57°N, SMM5. (b) Timeseries versus latitude at 70 km of $\bar{q}_y$ [$\mathrm{m}^{-1}\mathrm{s}^{-1}$], scaled by $1 \times 10^{+11}$, SMM5.

of the summer jet. This region is removed by day 210. Negative values are still present after this but they are moved polewards. Between days 230 and 245 there is a region at the pole at 70 km where values $\bar{q}_y$ are less than $-1 \times 10^{-11}\mathrm{m}^{-1}\mathrm{s}^{-1}$. This is associated with a localized maximum of the zonal mean zonal wind in the same region.

6.7 Summary of chapter

Various SMM runs were performed for the two background states used in for the instability calculation described in section 5.3. From all the SMM runs initialized with July zonal background conditions various waves grow to finite amplitude — wavenumber 3 being the dominant wave. In SMM1 the most unstable modes obtained from the instability calculation for k=1, k=2, k=3 and k=4 grew to finite amplitude after some 20 days of the SMM integration. The northern hemisphere modes k=2 and k=4 grow but do not reach large amplitude. The southern hemisphere modes k=1 and k=2 develop into large scale waves, very much resembling the observed polar winter 4-day wave and its accompanying 2 day wave.

For zonal wavenumber 3 two different waves grow. The first to appear is the 35 hrs wave with a localized northern hemisphere spatial structure and is identified with the fastest growing mode of the instability calculation. The second wave to appear has a period of 42

hours and is identified with the third unstable mode from the instability calculation[4]. Its spatial structure is initially similar to the 35 hrs wave, changing to a more global structure during the integration, with quasi 2-day wave like characteristics. It is this wave which interacts with the background flow, decelerating the jet and removing the unstable region, during its non-linear phase. The instability calculation with the July background state did not give as the most unstable mode a mode that sufficiently resembled the quasi 2-day wave to conclude that that wave is an unstable mode. Nevertheless the SMM experiment shows how it is not the most unstable mode that reaches the largest amplitude. It is the less rapidly growing mode that reaches the largest amplitude and interacts with the background state.

In the above described results, the SMM was used in a very simplified configuration, excluding most of the physics. To see the waves in a physically more complete manner, other experiments in which the SMM is run with Rayleigh friction and the radiation scheme were performed. They showed similar results: the dominant wave which grows from an initial state representing July conditions is zonal wavenumber 3. However, these changes did not lead to a much closer representation of the quasi 2-day wave.

A final run with a background state, representing June conditions, shows the growth of a zonal wavenumber 3 mode with a period of 43 hrs, with quasi 2-day wave characteristics.

[4]the second mode has a very similar period and spatial structure to the 35 hrs mode.

Chapter 7

SMM runs for the 4-day wave

Chapter 6 described SMM runs performed to study the quasi 2-day wave. In this chapter a series of SMM runs will be presented to study the polar winter 4-day wave. Most of the previous theoretical work on the polar winter 4-day wave has assumed that an instability is the forcing mechanism of this wave. However, for the 4-day wave diagnosed in the EUGCM (NT97), some characteristics might indicate that upward propagating planetary waves may play a role in the onset of the wave. The experiments described in this chapter will try to address this question.

A description of the setup used in the model experiments (section 7.1) will be given. Then four different experiments are analysed in sections 7.2, 7.3 and 7.4 and in section section 7.5 a summary of the results are given.

7.1 Setup of the SMM for 4-day wave experiments

For studying the polar winter 4-day wave the setup of most of the runs is the same as for the 2-day wave runs (described in section 6.2). The bottom boundary is maintained constant and the vertical domain spans from 28 km to 96 km. The model is initialized with the relevant fields. Different initial field are taken from the EUGCM, they correspond to a time mean of:

- 9-15 of September 1993, referred to as model day 243. A short run with Rayleigh

friction is used to balance the fields. Afterwards day 248 is used to initialize SMM6. The background state is perturbed by adding small noise to it.

- 6-9 August 1995, referred to as model day 221. Again a short run with Rayleigh friction is performed to bring the fields into balance. Runs are afterwards initialized on day 226. SMM runs initialized on day 226 are SMM7, SMM8 and SMM9.

For SMM7 the basic state is perturbed by adding noise to $\overline{u}$ and $\overline{T}$. For SMM8 and SMM9 the model was run with the perturbation to the initial geopotential field in the form of waves added at the bottom boundary. This is done via the GEOPER subroutine included by Bryan Lawrence to the main model. The aim of these experiments is to simulate upward propagating Rossby waves from the troposphere into the stratosphere, as is known to occur during the winter months.

The geopotential at the bottom boundary is specified as:

$$\Phi(\lambda, \phi, t) = \Phi_{init} + A(t) sin(k\lambda) exp - \left(\frac{\phi - \phi_o}{\phi_1}\right)^2, \tag{7.1}$$

here Φ_{init} is the initial geopotential field at the bottom boundary. The perturbation is centred around latitude ϕ_o, which is chosen as 60°S, and ϕ_1 is the radius of influence taken as 30°. A(t) allows the waves to be 'turned on' over a suitable time, it is given by:

$$A(t) = A_o \left(1 - exp\left(-5(\frac{t}{5days})^2\right)\right),$$

for the first 5 days (this is the turn on time). From then onwards $A(t)$ is given by:

$$A(t) = A_o(1 - exp(-5)).$$

For SMM8 a stationary wave of zonal wavenumber 1 was used, and for SMM9 the perturbation had the form of a stationary wave of zonal wavenumber 2. The amplitude of the perturbation (A_o) was set to 300 m in both experiments. This is a relatively small perturbation for 28 km (where the bottom boundary is), but proved to be sufficient for the waves to reach large amplitude in the upper stratosphere.

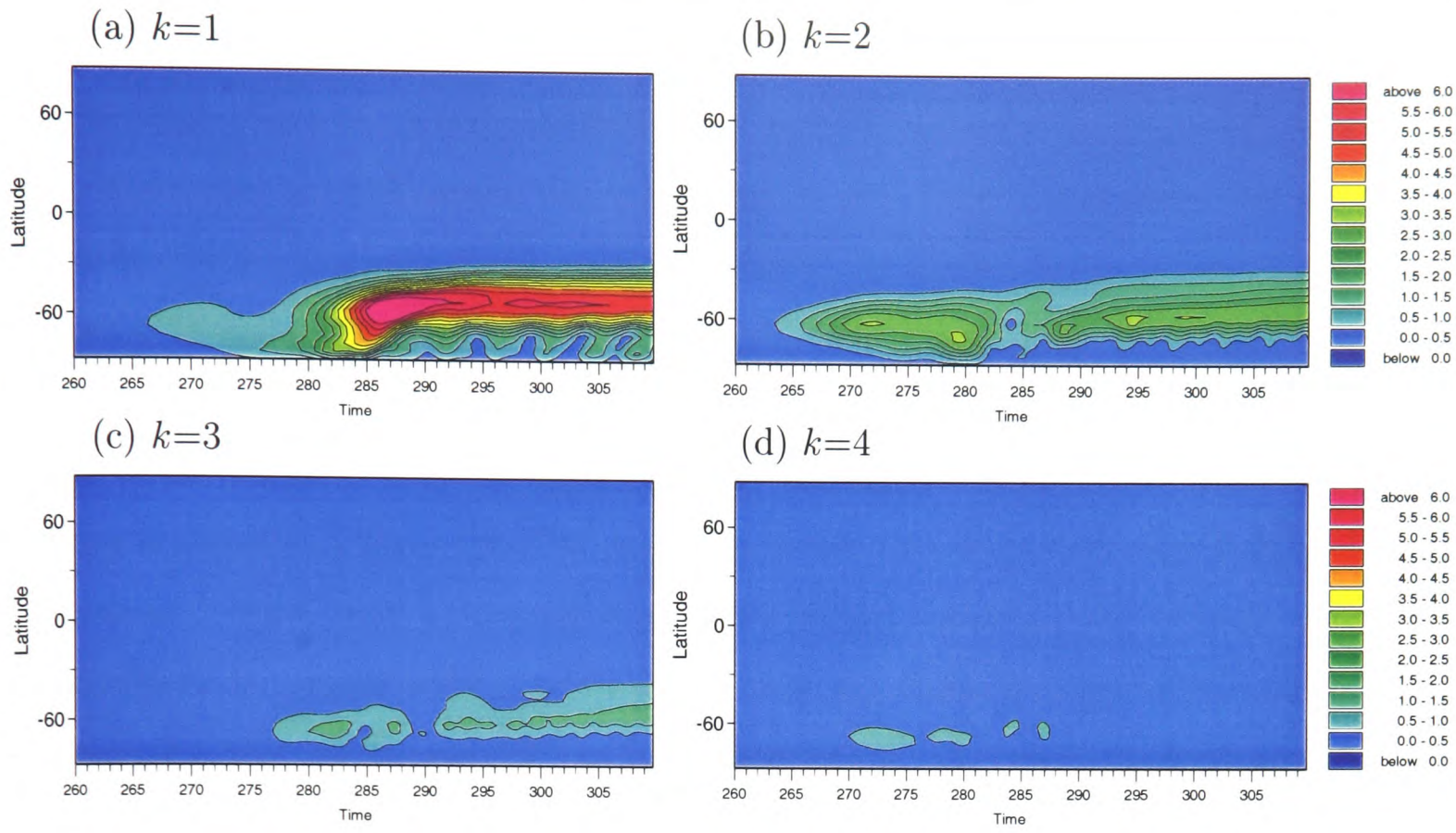


Figure 7.1: Time evolution versus latitude at 60 km of temperature amplitude for k=1, k=2, k=3 and k=4, SMM6.

7.2 SMM6: day 248

The experiment with September background flow was run with Rayleigh friction for 5 days to bring the winds and temperature into balance. SMM6 then starts on day 248, and is integrated for 80 days. The model is run without radiation and Rayleigh friction. The initial background state (Figure 5.10b) shows for the southern hemisphere the characteristic double peak shaped jet (corresponding to the polar night jet and the mesospheric midlatitude jet). The core of the polar night jet is centred at 60°S and 40 km height with values up to 90 m s^{-1}. The core of the mesospheric midlatitude jet is localized at 30°S and 65 km. Whereas in the winter hemisphere the jet is still strong, the summer jet has completely disappeared in September. The potentially unstable regions (i.e., where $\bar{q}_y$ is negative) are at the poleward flank of the winter jet (polewards of 80°S and between 30 km and 55 km), and above the core of the jet (60°S and 65 km). In general there are negative values of $\bar{q}_y$ in most of the region south of 40°S and above 60 km.

The background state proves to be unstable to the small perturbations, and waves of different zonal wavenumber grow in time. The waves growing in this model integration

are all confined to the southern hemisphere. There are two wavenumbers where large-scale waves develop, these are zonal wavenumber 1 and 2 (Figure 7.1). The k=2 wave is the first to appear at around model day 264, then a wave with k=1 follows few days later and reaches larger amplitude. The k=1 wave shows the characteristics of the polar winter 4-day wave (Figure 7.2), and has a very similar spatial structure to the 4-day wave found in SMM1.

The wavenumber 2 wave is identified with the polar winter 2-day wave, its spatial structure is shown in Figure 7.3. The spatial structure of the 2.2-day wave is similar to the wavenumber 1 wave, with an overall more equatorward structure. Meridional wind peaks at 65°S and 65 km, zonal wind has two peaks at 56 km centred around 50°S and 70°S and temperature peaks are around 65°S at 60 km and 70 km. The wave has large amplitude in the critical region.

Throughout the run the k=1 wave suffers various changes to its spatial structure as well as period. At the beginning of the integration (between days 260 and 270), the period of the wave ranges between 3.6-4.0 days. During this phase the maximum amplitude of meridional wind is at high latitudes and about 60 km height. The characteristic double peak structure in the temperature component of the wave has maximum amplitude at 80 km and 60 km. The lower peak being a warm pool of air, whereas the upper peak corresponds to a cold temperature anomaly. This is in agreement with findings by Allen *et al.*, (1997), where satellite data revealed a double peak with an out of phase structure in the vertical for the temperature component of the wave. However, in the SMM the phase lines of the temperature (Figure 7.2d) are not vertical as found in observations. The cold and warm anomaly pattern remains throughout the run. After some 20 days (between days 270-280) the period of the wave has changed to 4.8 days, and later in the run the period slows down to over 6 days. Figure 7.2 shows the spatial structure of the 4-day wave for the period day 277-296. Associated with these period changes, the meridional wind maximum amplitude shifts upwards at the pole. The temperature structure also shows differences. The lower peak at 60 km splits into 2 peaks with smaller amplitude at around 50 km and 62 km. These altitudes are closer to observations of the amplitude peaks of the 4-day wave,

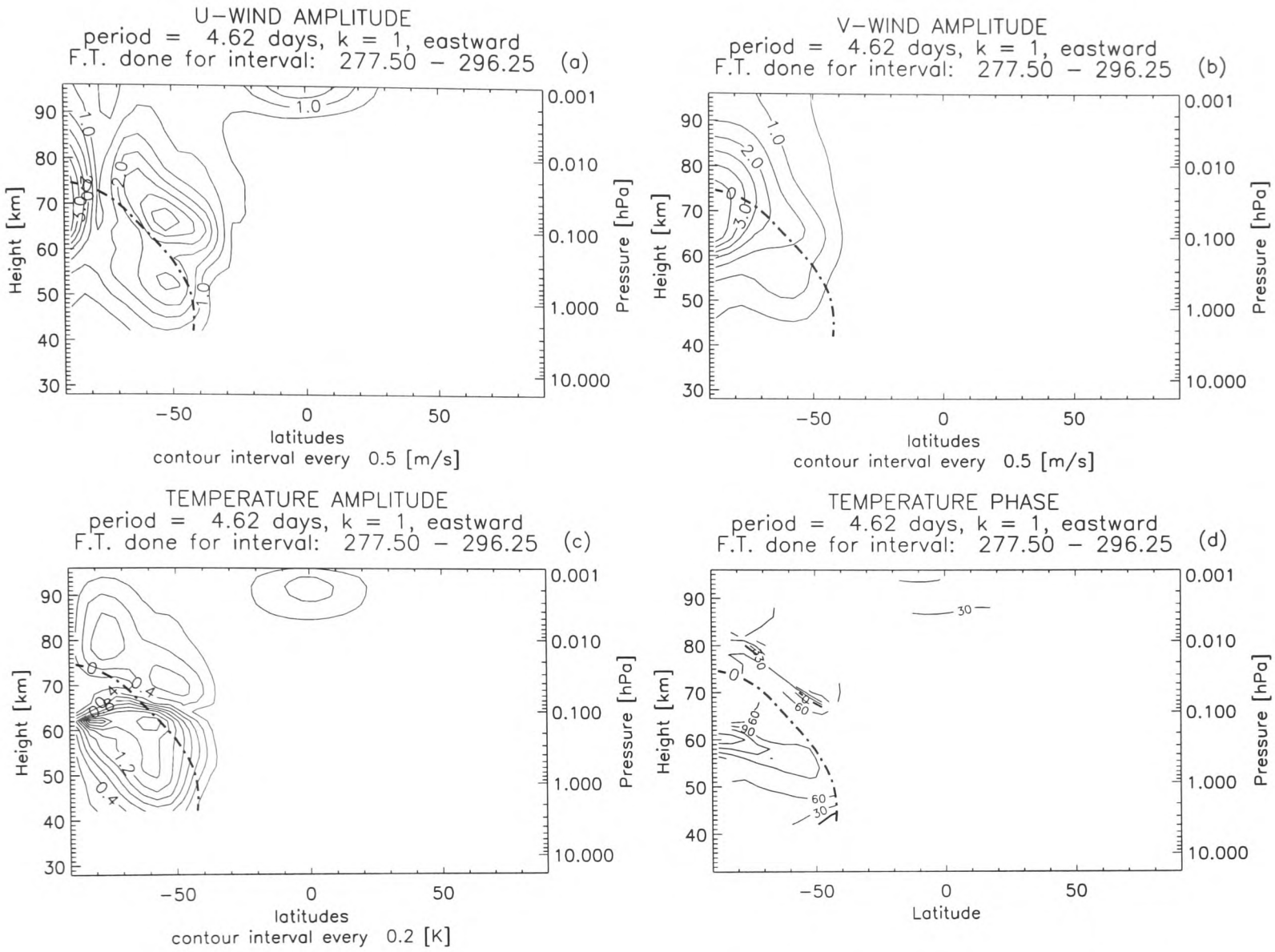


Figure 7.2: (a) u-wind amplitude of the eastward propagating 4.2 day wave, SMM6. The bold dot-dashed line is the critical line for this wave ($u - c = 0$). (b) v-wind amplitude, (c) temperature amplitude and (d) temperature phase.

but in the SMM these two peaks are in phase and not out of phase as found by Allen *et al.*, (1997). However, overall the spatial structure of the polar winter 4-day wave and the polar winter 2-day wave are in good agreement with observations, apart from the longer periods in the SMM.

The vacillations in the amplitude seen south of 60°S in Figure 7.1a, seem to be tongues of warm air from the wavenumber 1 component separating from the mean pool. Figure 7.4 shows the temperature anomaly from the pole to 60°S for three consecutive days. Tongues in the temperature anomaly periodically move towards the pole, curving round it (so that a wavenumber 1 pattern is recognizable) and then dissipating. A similar explanation can account for the amplitude vacillations seen in zonal wind and meridional wind.

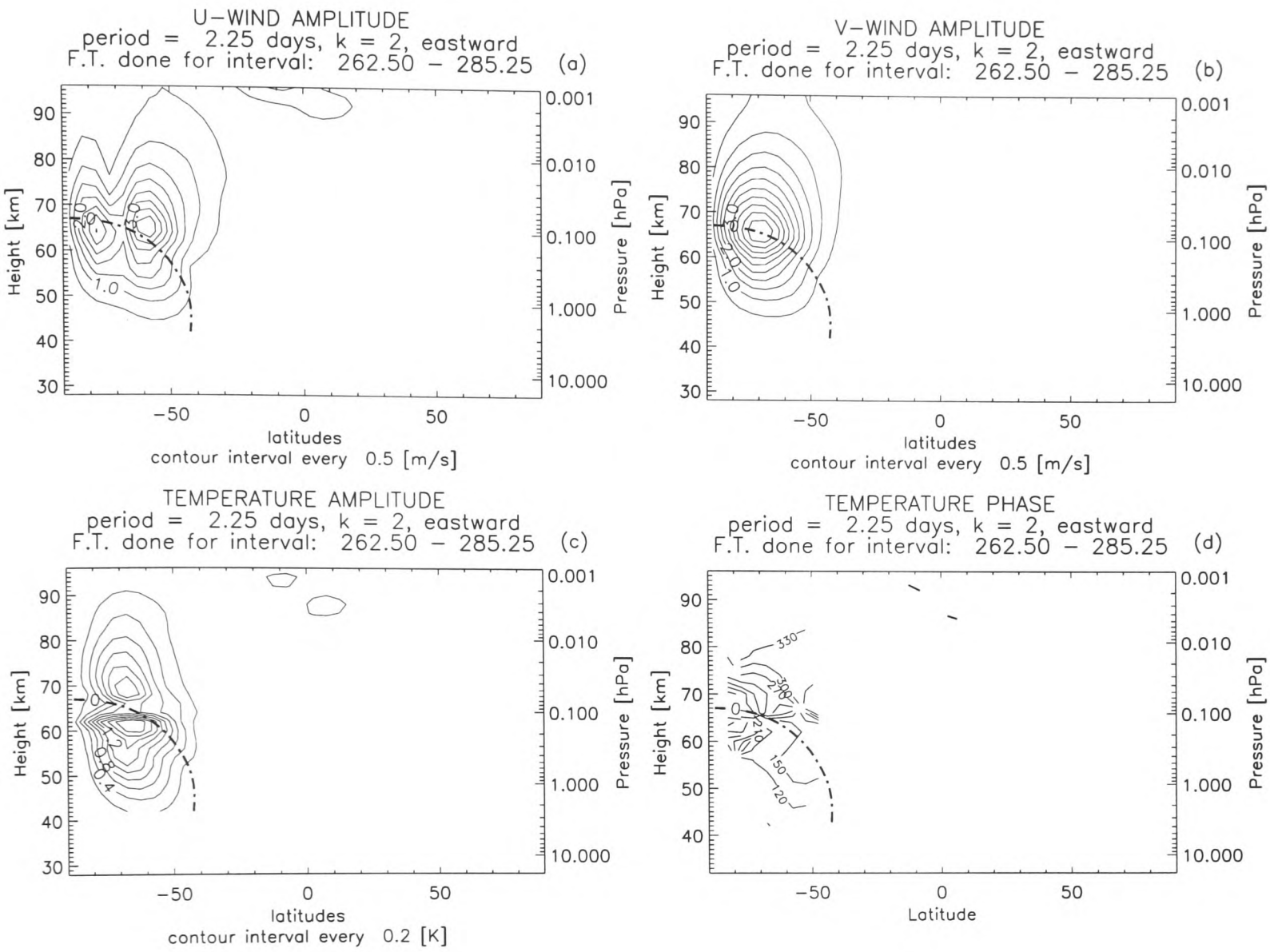


Figure 7.3: (a) u-wind amplitude of the eastward propagating 2.2 day wave, SMM6. The bold dot-dashed line is the critical line for this wave ($u - c = 0$). (b) v-wind amplitude, (c) temperature amplitude and (d) temperature phase.

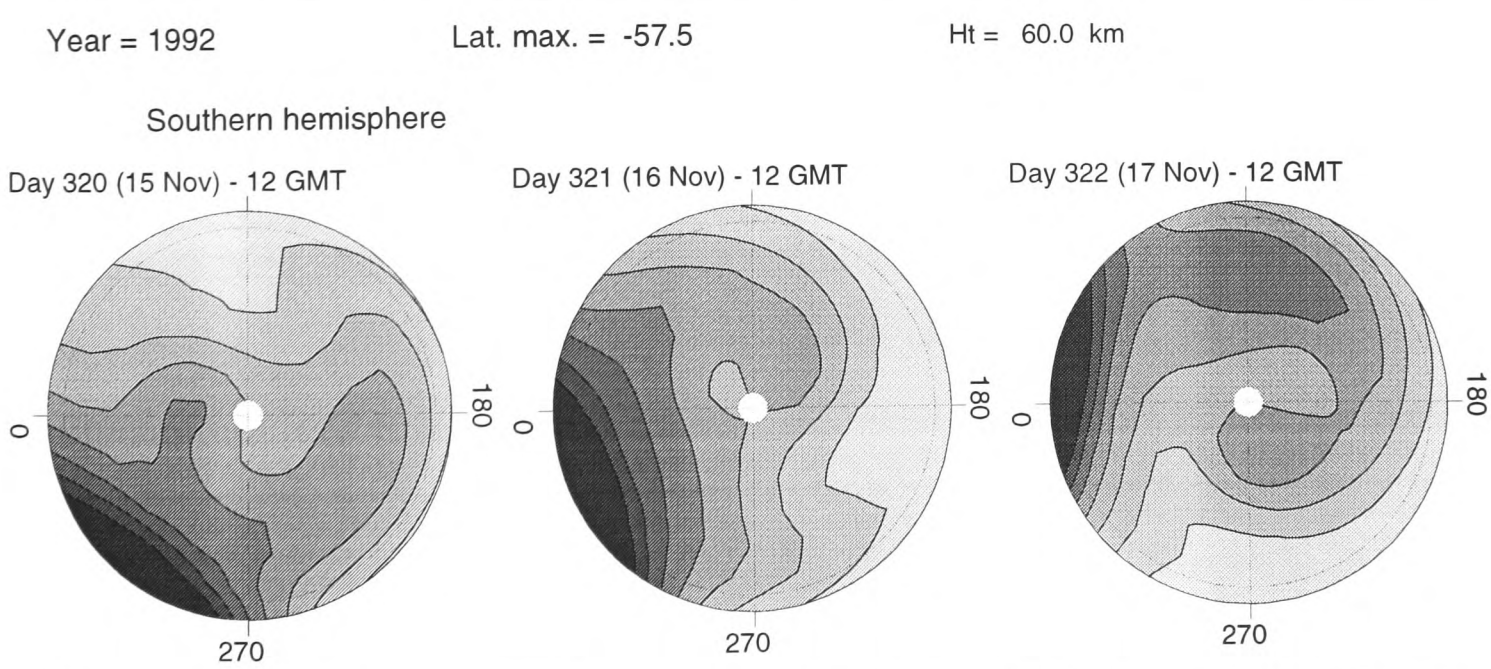


Figure 7.4: Southern hemisphere temperature anomalies for consecutive days at 60 km, SMM6. Dark colours for positive values, maximum contour is 4 K. Outer circle is 60°S.

Synoptic maps of the temperature anomaly at 60 km for the southern hemisphere are shown in Figure 7.5. The field is dominated by the wavenumber 2 disturbances until day 279, then the anomaly acquires a clear wavenumber 1 shape. The wavenumber 1 pattern goes round the pole with a period close to 6 days from day 280 onwards. After day 279 the warm anomaly is more localized than the cold anomaly, so that it looks like a warm pool of air moving eastwards, as has been reported from observations (e.g. Prata, 1984). The warm temperature anomaly reaches up to 10 K amplitude at 60 km, whereas the cold anomalies are less than 3 K.

7.2.1 Effects on the mean flow

Observational as well as theoretical studies on the 4-day wave have usually identified the forcing mechanism of the wave with barotropic instability of either the polar night jet or the double peaked structure of the mesospheric jet. The SMM6 initial state has in both these regions negative values of $\bar{q}_y$, and are therefore potentially unstable. In SMM6 both momentum fluxes and temperature fluxes are found, indicating that probably both barotropic and baroclinic instability play a role in the onset of the wave. In fact, longitude versus height plots at a given latitude clearly show the vertical tilt with height of the wave, whereas in most observations the structure of the wave has been found to be in phase with height, indicating the barotropic character of the disturbance.

From day 272 onwards small changes to the mean flow are detected. The changes are seen between 60 km and 70 km, with an acceleration of the flow around 70°S and a deceleration at 50°S (Figure 7.6a). This pattern intensifies and accelerations up to 15 $m\,s^{-1}$ are found by day 285. In general the poleward flank of the westerly jet penetrates higher into the higher mesosphere. The changes at the equatorward side of the jet, where the effect of the eddies is to decelerate the flow, are smaller, with changes reaching only up to 4 $m\,s^{-1}$. The effect of the wave on $\bar{q}_y$ is to remove the negative region present in the initial flow at polar regions, at about 75 km and at 60 km between 70°S and 45°S. The location where the zonal wind is decelerated stays slightly unstable (Figure 7.6b).

Both eddy momentum and temperature fluxes are found during the growth of the

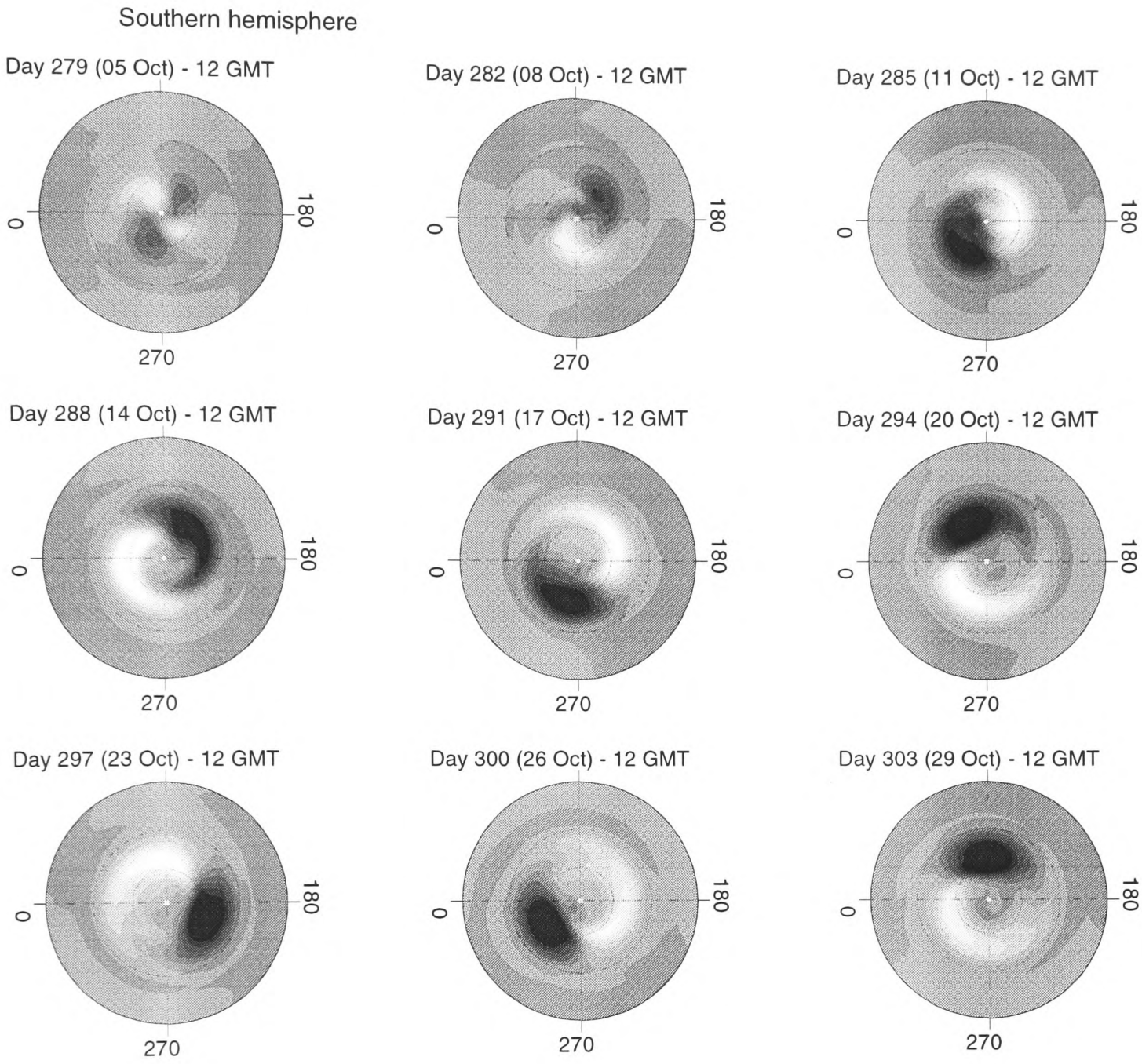


Figure 7.5: Southern hemisphere temperature anomalies 60 km, SMM6. Dark colours for positive values, maximum contour is 6 K.

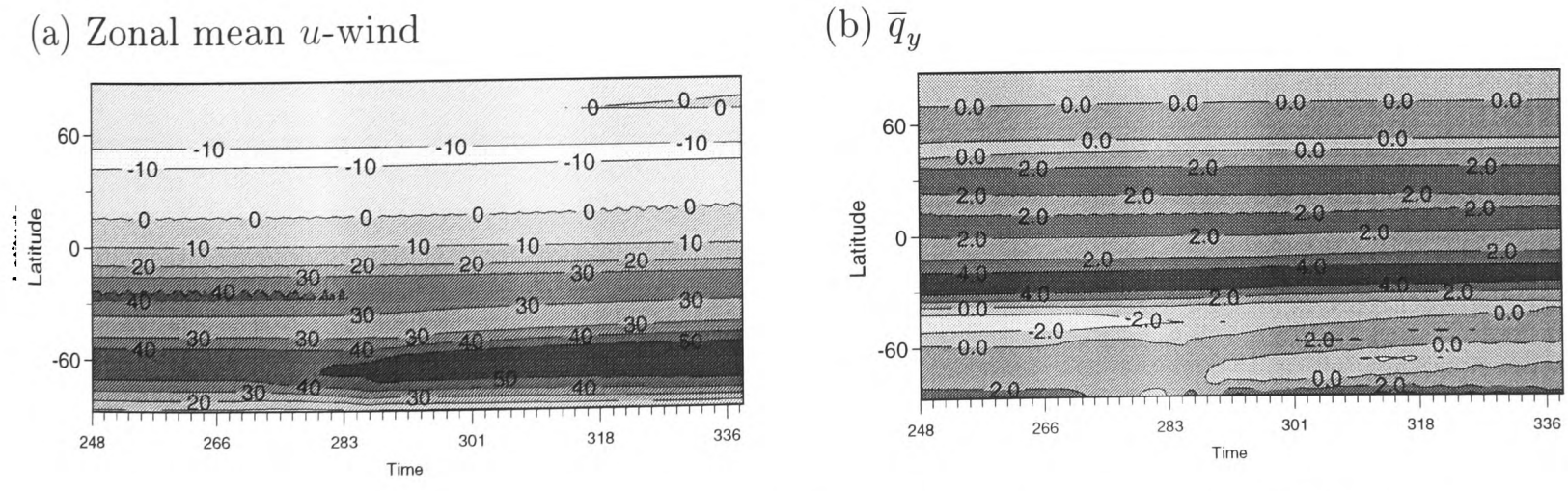


Figure 7.6: (a) time versus latitude at 60 km of zonal mean u-wind, SMM6. (b) time evolution of $\overline{q}_y$ [$m^{-1}s^{-1}$], scaled by 10^{+10} at 60 km, SMM6.

waves. They are of comparable magnitude, indicating that probably in the run both baroclinic/barotropic processes are involved in the instability. Latitude versus time section at different heights reveal that temperature fluxes are mainly poleward throughout the run; large values are seen between days 280 and 290. The momentum fluxes are polewards between days 270 and 288 and after this they change to equatorwards.

Studies of the polar winter 4-day wave, where poleward momentum fluxes are seen, find that the poleward momentum fluxes are correlated with zonal mean u-wind being unstable to so called 'polar modes'. For the 'polar modes' it is the poleward flank of the jet which is unstable (e.g. Manney, 1991). In these cases it was also found that the wave showed a southeast to northwest tilt. The other region of instability is associated with the midlatitude mesospheric jet ('midlatitude modes'); here the fluxes are found to be equatorwards and the wave tends to tilt northeast to southwest.

Although temperature fluxes of similar mangitude to the momentum fluxes are found in SMM6, the wave is probably a mix of a 'polar mode' and 'midlatitude mode'. At the beginning of the run the wave development seems consistent with the polar mode, where the momentum fluxes are poleward and the unstable region poleward and above the jet are removed by the wave. A southeast to northwest tilt in the temperature anomaly is also found for the wave in the SMM. In Figure 7.7 the divergence of the EP flux in shown in contours and the components of the EP flux (which are related to the momentum and temperature fluxes) are represented by arrows for days 282 and 296. The regions where $\overline{q}_y$ is negative are shaded. For day 282, $\overline{q}_y$ is still negative at the poleward flank of the polar night jet and the region above 60 km south of 40°S. Regions of divergence overly regions where $\overline{q}_y$ is negative, an indication of a wave activity generating region (see equation 2.45). By day 296 the whole pattern has moved equatorwards, finding divergence of the EP flux between 60°S and 40°S. The negative region of $\overline{q}_y$ close to the pole has disappeared.

Assuming that the waves found in this model integration can be modelled by equation 6.4, the growth rates of the waves were calculated in the same way as described in section 6.3.5. For the k=1 wave, assuming a period of 5 days for the wave, the e-folding time was found to be 4.9 days, somewhat slower than the value of 4 days from the instability

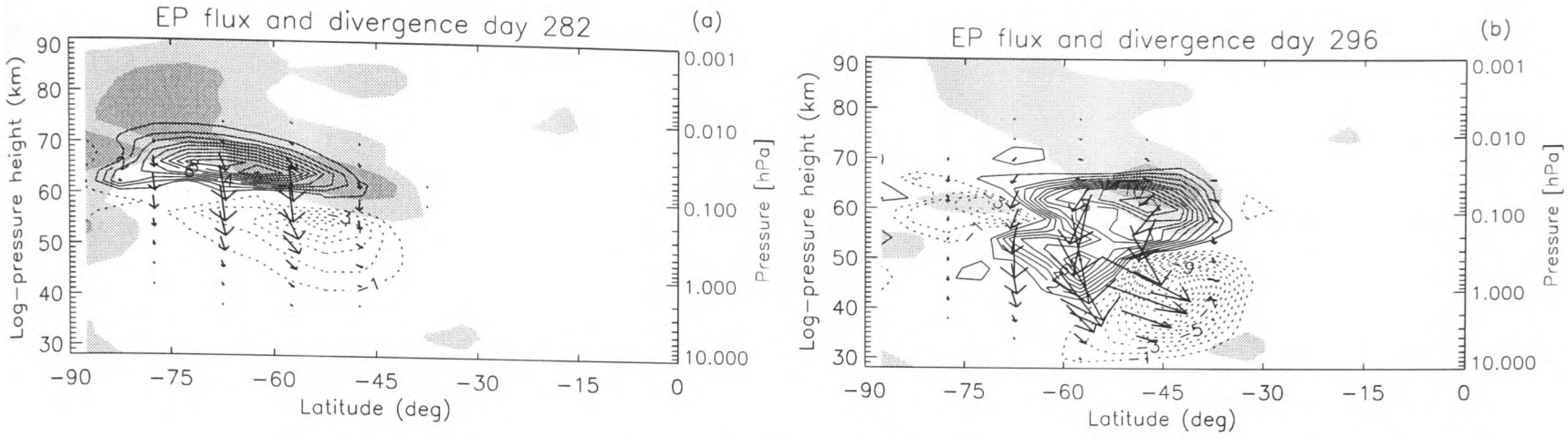


Figure 7.7: (a) Contours of $\nabla \cdot F$, scaled by 1×10^3 in units of $\mathrm{kgm^{-1}s^{-2}}$, arrows of the EP flux for day 282 SMM6. Shaded region are where $\overline{q}_y < -1 \times 10^{-11}$ $[\mathrm{m^{-1}s^{-1}}]$, with light grey for values between -1 to-5×10^{-11} and dark grey for values less than -5×10^{-11}. (b) same as (a) but for day 296 SMM6. Same contour interval and shading used for both Figures.

calculation. For the k=2 wave the e-folding time was found to be of 4 days, faster than the e-folding time for the 2 day wave found in the instability calculation, which was 6 days (see Table 7.1 in section 7.5).

7.3 SMM7: day 226

This run was initialized with August mean background fields (model day 221). The initial fields are balanced by applying strong uniform Rayleigh friction to the zonal and meridional mean winds. After a few days, the meridional wind values at the top levels, which would otherwise grow to large values in that region, are close to zero. Day 226 is chosen to initialize SMM7, i.e., 5 days of strong Rayleigh friction has been applied to the winds. Small perturbations are added to the zonal-mean flow and the model is integrated for some 100 days. In this run no parameterization of the gravity wave drag nor radiation is included.

In Figure 7.8a the difference between the original zonal mean wind (day 221) and 226 is shown. There are small difference in the northern hemisphere in the last few model levels and in the bottom levels (values a less than $5\,\mathrm{m\,s^{-1}}$). The zonal mean u-wind in the southern hemisphere on day 226 (Figure 7.8b) has a characteristic winter jet with a double peak at around 60°S and 40 km height, and at 35°S and 65 km. The potentially unstable

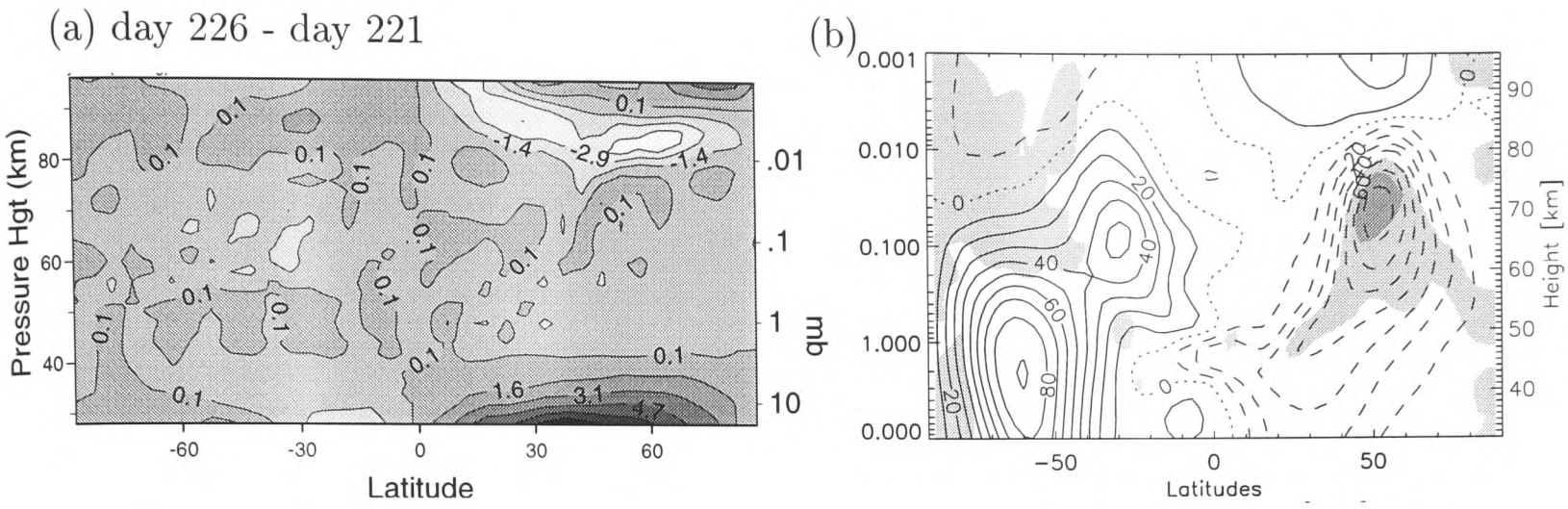


Figure 7.8: (a) Difference between zonal mean u-wind field at day 226, and the initial zonal mean wind (day 221). (b) Zonal mean u-wind for day 221, units of $\mathrm{m\,s^{-1}}$. Shaded region are where $\overline{q}_y < -1 \times 10^{-11}$ $[\mathrm{m^{-1}s^{-1}}]$, with light grey for values between -1 to -5×10^{-11} and dark grey for values less than -5×10^{-11}.

regions (where $\overline{q}_y$ is negative) are around the northern hemisphere jet and at the poleward flank of the polar night jet, and above 60 km south of 45°S.

Again a number of waves grow out of the initial perturbation. In contrast to SMM6, global-scale waves grow to large amplitude in this run. Figure 7.9 shows the time evolution of the meridional wind amplitude at 80 km for zonal wavenumbers 1, 2, 3 and 4[1]. The waves present in this run are, firstly, from day 240 onwards, as for SMM6, a southern hemisphere wavenumber 1 mode at very high latitudes. Later, large amplitude can be seen in the northern hemisphere. Large amplitudes at zonal wavenumber 2 and 3 appear later. A spectral analysis of the data indicates that the zonal wavenumber 1 are composed of two different waves. In the southern hemisphere the wave is an eastward propagating wave with a broad period between 4.3 and 5 days. The large amplitude seen in Figure 7.9a after day 280 is a westward propagating wave with period around 6 days. The large amplitude wavenumber 2 wave corresponds to a westward propagating mode with period about 3.6 days (seen from day 250 to day 280). With smaller amplitude, in the southern hemisphere there is also a zonal wavenumber 2 wave eastward propagating with a period of about 3.3 days. Finally, between the days 260 to 280, there is a large amplitude wavenumber 3 wave, this is an westward propagating mode with period just over 2 days.

[1]Meridional wind is the field which shows best all the waves that grow in SMM6 and was therefore chosen for this figure instead of temperature.

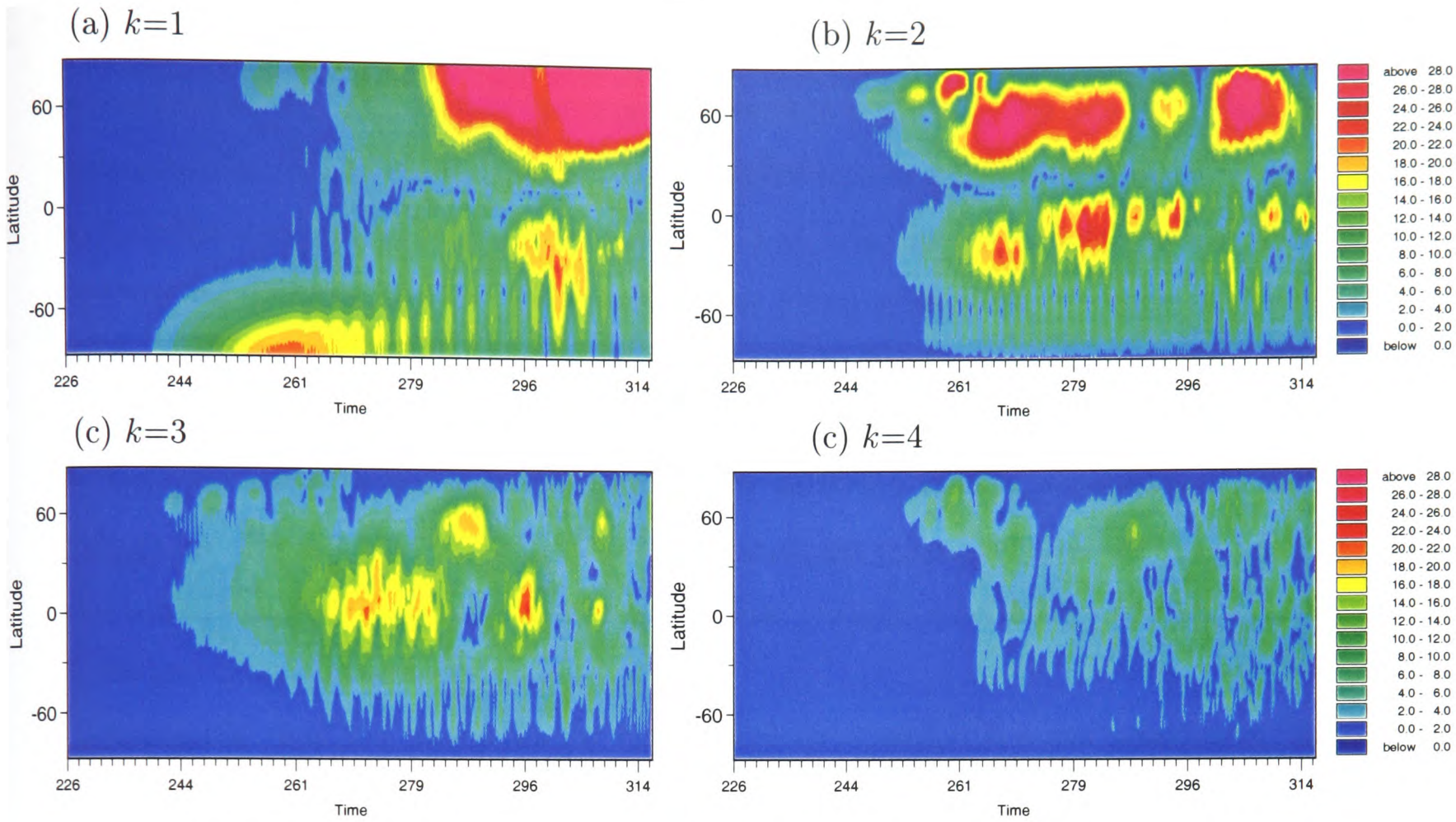


Figure 7.9: Time evolution versus latitude of meridional wind amplitude at 80 km for k=1, k=2, k=3 and k=4, SMM7.

From their spatial structures the waves have been identified with previously diagnosed waves. The eastward propagating k=1 wave (Figure 7.10) has the known characteristics of the polar winter 4-day wave, with a double peak in zonal wind around 45° and 85°S and 70 km height, double peak in the vertical in temperature, and meridional wind has its maximum at the pole and 75 km height. The wave has very similar characteristics to the k=1 wave in SMM6, and to the k=1 wave seen in SMM1 (chapter 6). The altitude at which the wave peaks is higher than found in observations, but similar to the polar winter 4-day wave in the EUGCM. The period is longer than the observed period and also longer than the period in the EUGCM. Later in Figure 7.9a (around day 280) in the northern hemisphere a second large amplitude zonal wavenumber 1 wave starts to grow. This wave is a westward propagating mode with period around 6 days (Figure 7.11). Its characteristics are consistent with that of a Rossby normal mode. In particular it has a spatial structure, zonal wavenumber and period resembling a higher order (1,1) mode (i.e., a mode with a shorter vertical wavelengths and longer period than the 5-day wave).

Figures 7.12 and 7.13 correspond to the spatial structures of the wavenumber 2 and 3 waves respectively. The 3.6 day wave can be identified with the (2,1;0) mode, and the 2 day wave with the (3,0;1) mode (the last index indicating the number of zeros of meridional wind in the vertical, as introduced in section 5.5). All the waves have critical lines, as expected for unstable modes. These modes were found as unstable modes in section 5.4.2 and in section 5.5 it was shown that these modes were Rossby normal modes that became unstable under the August background flow used to initialize run SMM7.

Synoptic maps of the temperature anomaly at 60 km show a wavenumber 1 pattern throughout the run (not shown). The warm anomaly (stronger than the cold anomaly) goes round the pole eastwards with a period that changes from 4 days to almost 11 days at the end of the integration.

Assuming that the waves can be represented by equation 6.4, the amplitude for the fastest growing modes for k=1, k=2 and k=3 is shown in Figure 7.14. The fastest growing wave in SMM7 is the southern hemisphere 4.4 day wave, with an e-folding time of 4.5 days, whereas the instability calculation gives a value of 4.1 days. Next is the normal mode 4-day wave, with an e-folding time of 4.9 days, somewhat faster than the value of 5.3 days given by the instability calculation. For the (3,0;1) mode the growth rate is only approximately exponential, and the e-folding time is between 6 days and 10 days. The instability calculation gave 6 days. Finally the 6 day wave has an e-folding time of about 8 days in the SMM. In the instability calculation this mode was found as well with an e-folding time of 8 days (see table 7.1).

7.3.1 Effects on the mean flow

The effect of the waves on the mean flow is considerably stronger in comparison with previously analysed runs. The Rossby normal modes in SMM7 reach very large amplitudes. For the southern hemisphere, the changes to the zonal mean u-wind are similar to those found in SMM6. Between days 240 and 255 the momentum fluxes are poleward and temperature fluxes negative. No significant changes to the mean flow are found until day

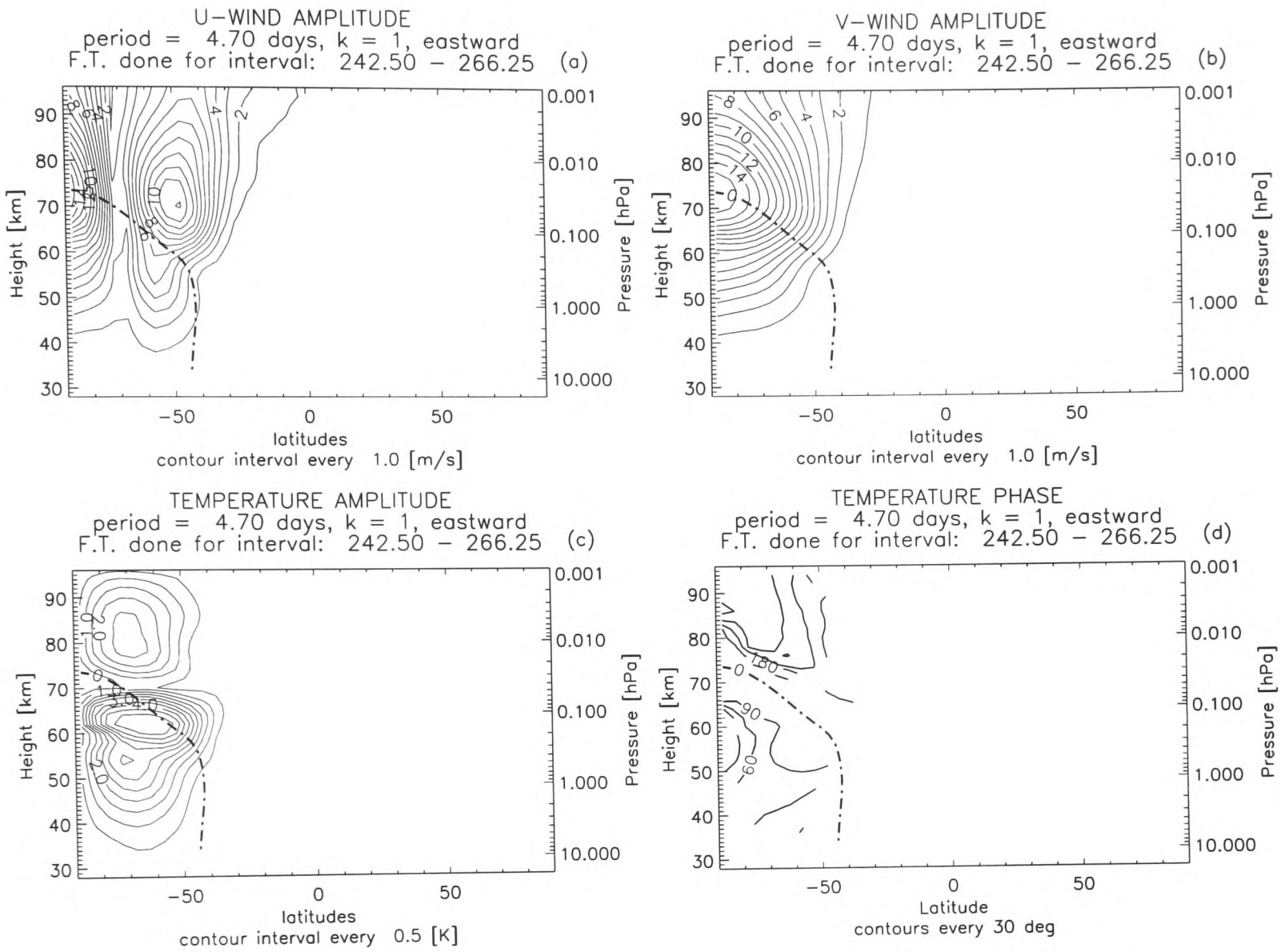


Figure 7.10: (a) u-wind amplitude of the eastward propagating 4.7 day wave, SMM7. The bold dot-dashed line is the critical line for this wave ($u - c = 0$). (b) v-wind amplitude, (c) temperature amplitude and (d) temperature phase.

255, then the upper mesospheric easterlies start to be pushed away by the winter polar night jet poleward flank, which penetrates into the upper mesosphere, accelerating that part of the jet. A minor deceleration is found of the midlatitude mesospheric jet. As in SMM6 the negative regions of $\overline{q}_y$ close to the pole between 40 km and 60 km are removed during the first stages of the growth of the 4-day wave (see Figure 7.8b for the initial state). By day 280 the southern hemisphere westerlies go up to the top level of the model (96 km).

The northern hemisphere background wind changes in a similar fashion as found in SMM1 (chapter 6). The main effect of the waves here is to decelerate the summer easterlies and to remove the strongly negative region of $\overline{q}_y$ lying just above the core of the summer jet (changes start to be visible around day 260). The core of the jet is also moved upwards and

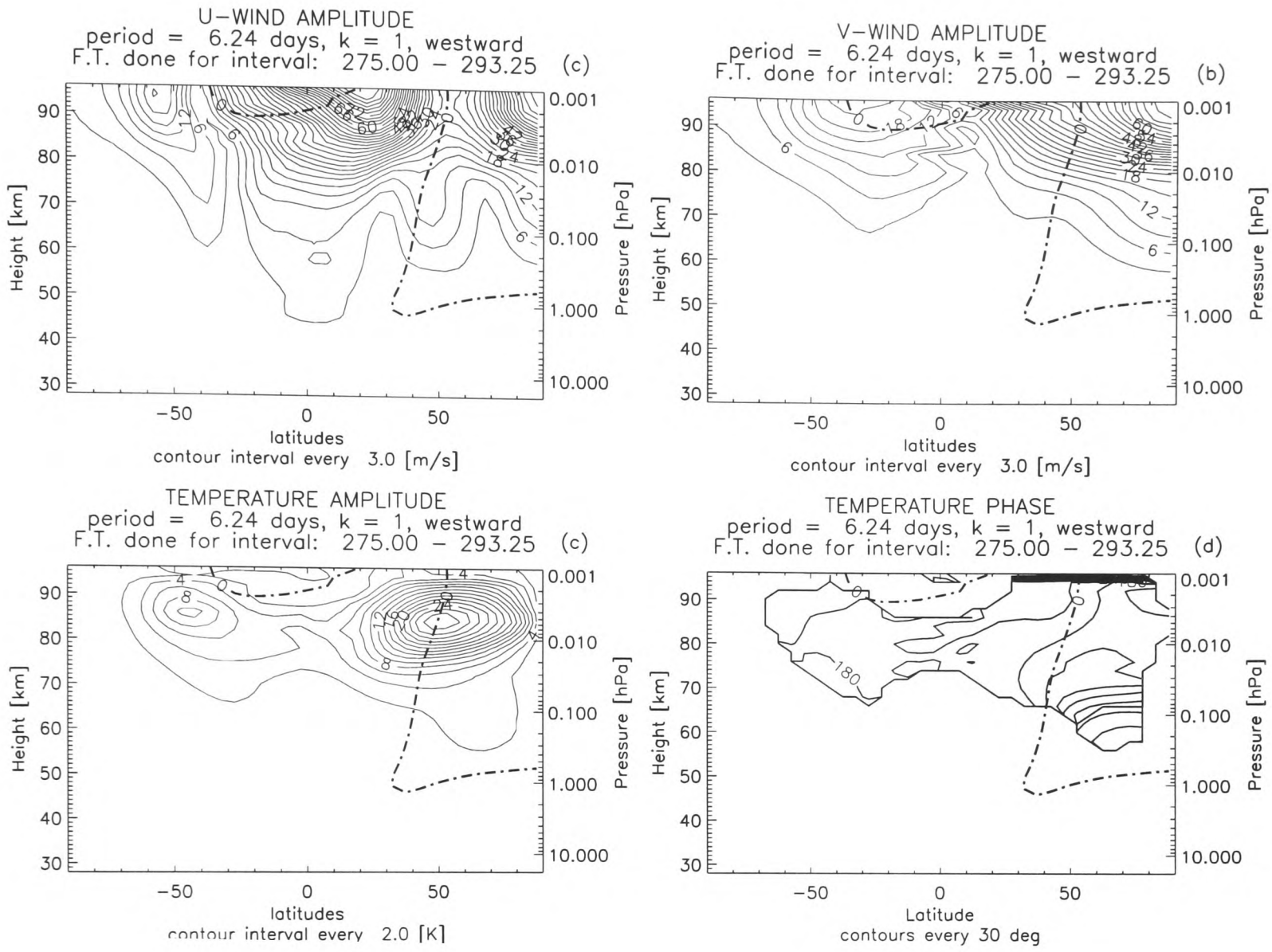


Figure 7.11: (a) u-wind amplitude of the westward propagating 6.2 day wave, SMM7. The bold dot-dashed line is the critical line for this wave ($u - c = 0$). (b) v-wind amplitude, (c) temperature amplitude and (d) temperature phase.

polewards, so that by day 270 the summer easterlies penetrate up to the top model levels, having pushed away the upper mesospheric westerlies to the region between 15°N and 45°N. The southern hemisphere upper mesospheric winds are also being shifted equatorwards. These changes occur during the onset of the (2,1;0) and the (3,0;1) modes. When these waves acquire very large amplitude (after day 270), there are easterly winds above 80 km and between 45°S and 30°N of -70 m s^{-1} (Figure 7.21a).

An additional SMM integration was performed with the same initial state as SMM7, but with a Rayleigh friction profile as in equation 6.2 and 6.3 (i.e., only the zonal mean part of the winds is relaxed back to the initial conditions), with $a = 1 \times 10^{-5}$ and z_0=50 km. The Rayleigh friction inhibits the extremely large values of the Rossby normal modes found in

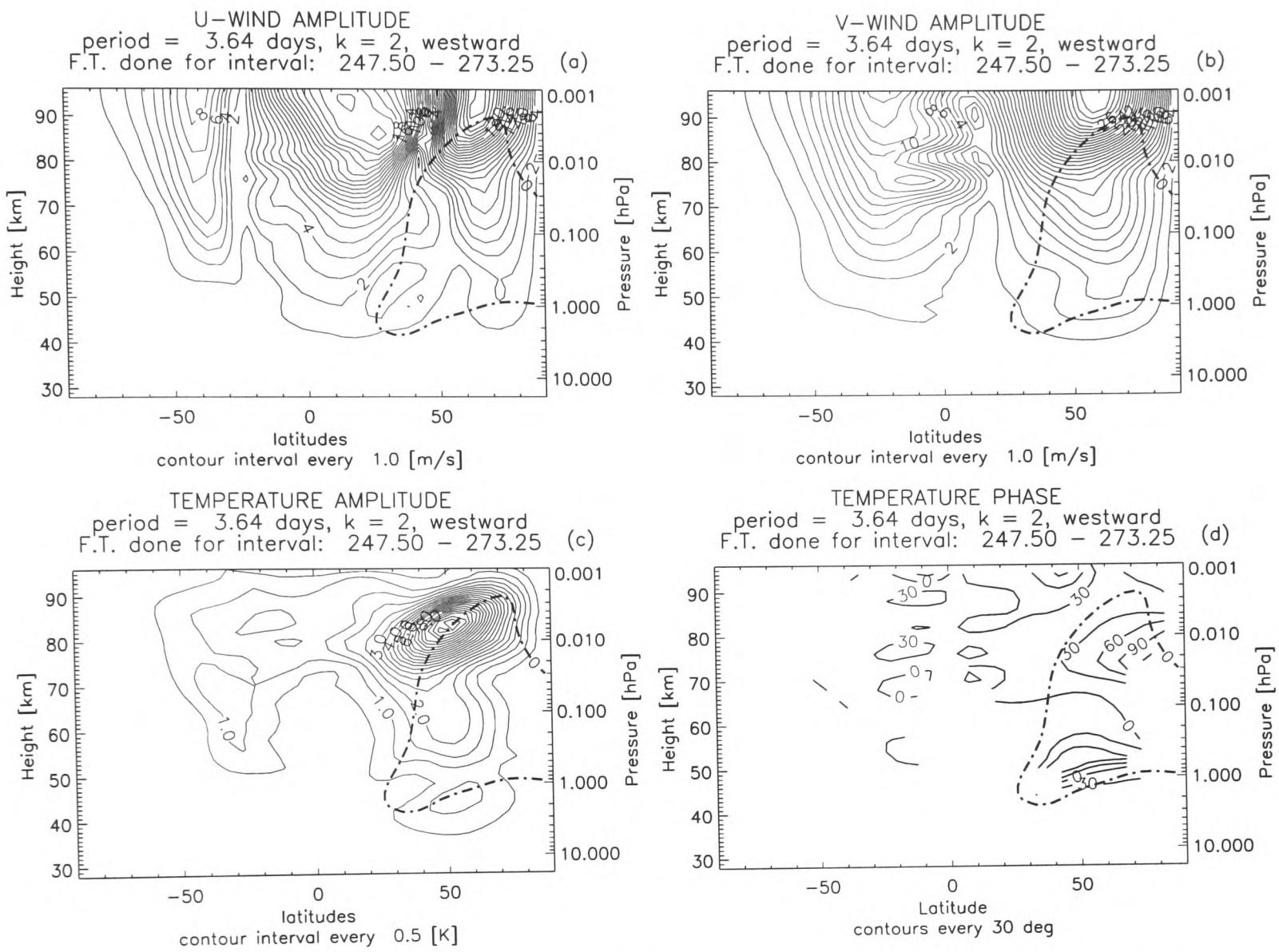


Figure 7.12: (a) u-wind amplitude of the westward propagating 3.6 day wave, SMM7. The bold dot-dashed line is the critical line for this wave ($u - c = 0$). (b) v-wind amplitude, (c) temperature amplitude and (d) temperature phase.

SMM7, and therefore the winds stay closer to the initial state. The same large-scale waves develop, but in particular the amplitude of the 6 day wave is reduced. Changes are seen mainly in the northern hemisphere. Because the aim of SMM7 was to study the southern hemisphere 4-day wave, and the Rossby waves have their largest impact in the northern hemisphere, it was decided to show the results from this SMM7 run without the Rayleigh friction, in spite of the unrealistic winds that develop at the top of the model.

7.4 Runs with perturbation at the bottom boundary

Two further SMM runs were performed, where instead of adding small perturbations to the initially axisymmetric state, as was done for all the previously described experiments,

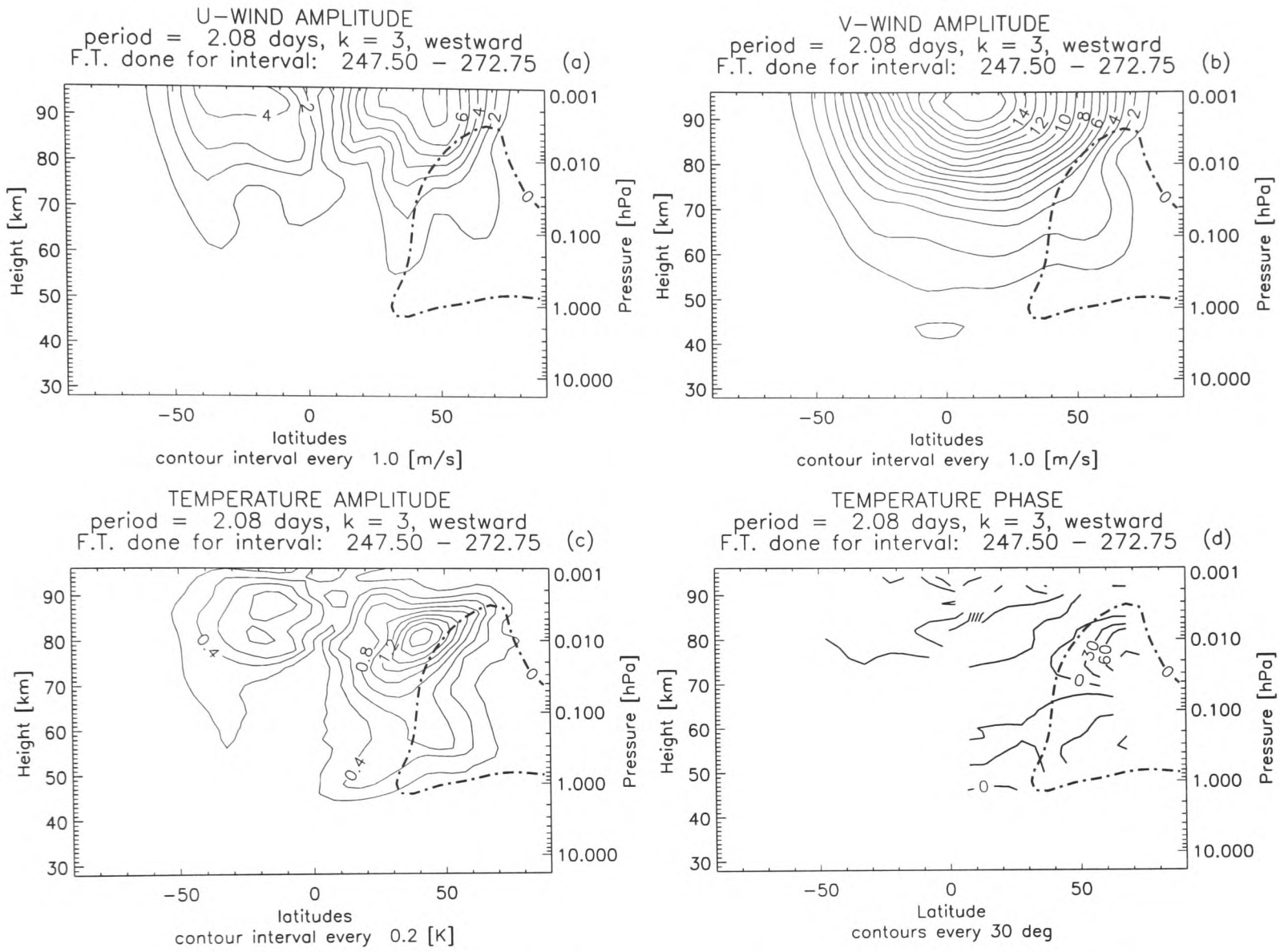


Figure 7.13: (a) u-wind amplitude of the westward propagating 2 day wave, SMM7. The bold dot-dashed line is the critical line for this wave ($u - c = 0$). (b) v-wind amplitude, (c) temperature amplitude and (d) temperature phase.

the atmospheric state is perturbed by adding a small wave component to the geopotential at the bottom boundary. SMM8 corresponds to the run where a zonal wavenumber 1 perturbation was used. In SMM9 a wavenumber 2 wave was used to perturb the initially axisymmetric state. The zonal mean u-wind and temperature are those from model day 226.

7.4.1 SMM8: wave 1 perturbation

A stationary zonal wavenumber 1 perturbation of 300 m amplitude is added to the bottom boundary in this run. The run is started on day 226 (same as SMM7) and run for about 80 days. Figure 7.15 shows the time evolution of the first four zonal wavenumbers for

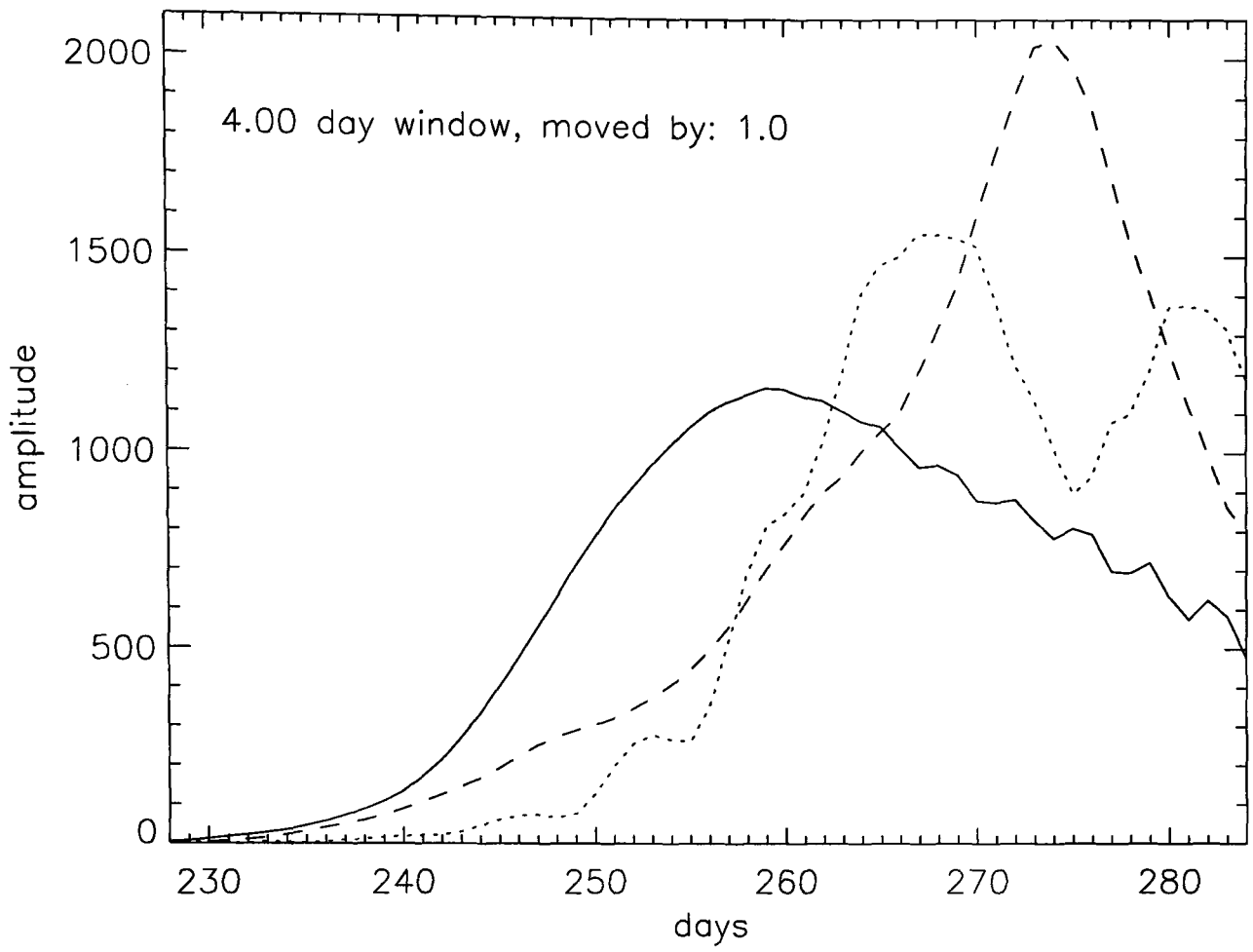


Figure 7.14: Time versus amplitude for the waves in SMM7. Solid contour for southern hemisphere 4.7 day wave. Dotted line is the growth of the (2,1) mode. Dashed lines are the growth of the (3,0) mode. Amplitude is in arbitrary units.

meridional wind in this run. Largest amplitude is found for k=1. First, large values are seen in the southern hemisphere with maxima at the pole, extending equatorwards to 30°S. By day 280 large values are seen in the northern hemisphere as well. Amplitude vacillations are found from day 260 onwards. Although in the latitude-time cross section the wave 1 component looks similar to the evolution found in the SMM7, when temperature anomalies are investigated in stereographic projections the wave in this run is found to be stationary throughout the model integration (Figure 7.16). The spectral analysis gives peaks at zonal wavenumber 1 symmetric about zero frequency for the 2 longest periods, i.e., the Fourier transform is representing a standing wave as an eastward plus a westward propagating wave (Figure 7.17).

The other wavenumbers growing in this run are large-scale waves. A spectral analysis at a northern hemisphere latitude reveals peaks at zonal wavenumber 1, 2 and 3, all at the same phase speed (Figure 7.18a). The amplitude of the zonal wind for all three

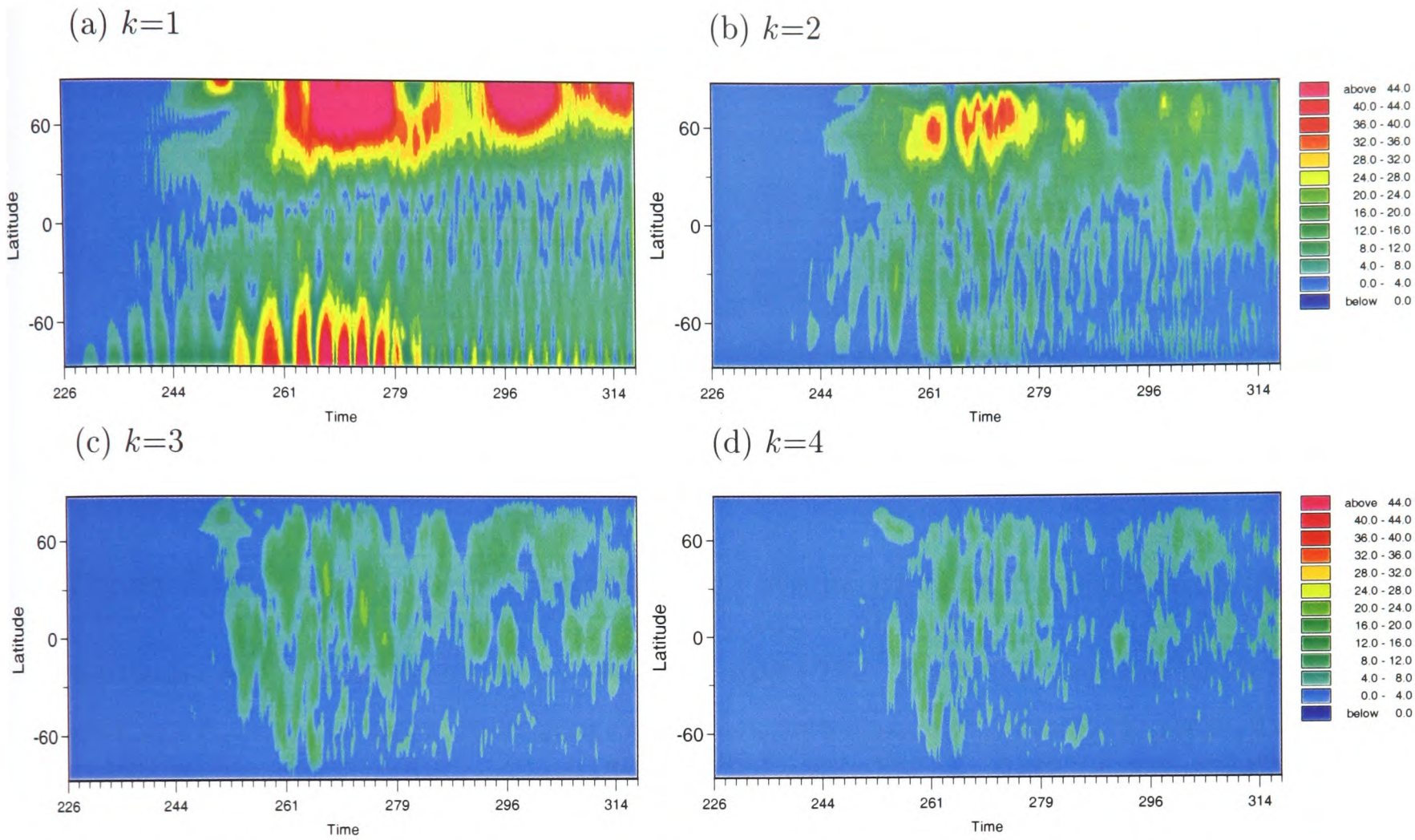


Figure 7.15: Time evolution versus latitude of meridional wind amplitude at 80 km for k=1, k=2, k=3 and k=4, SMM8.

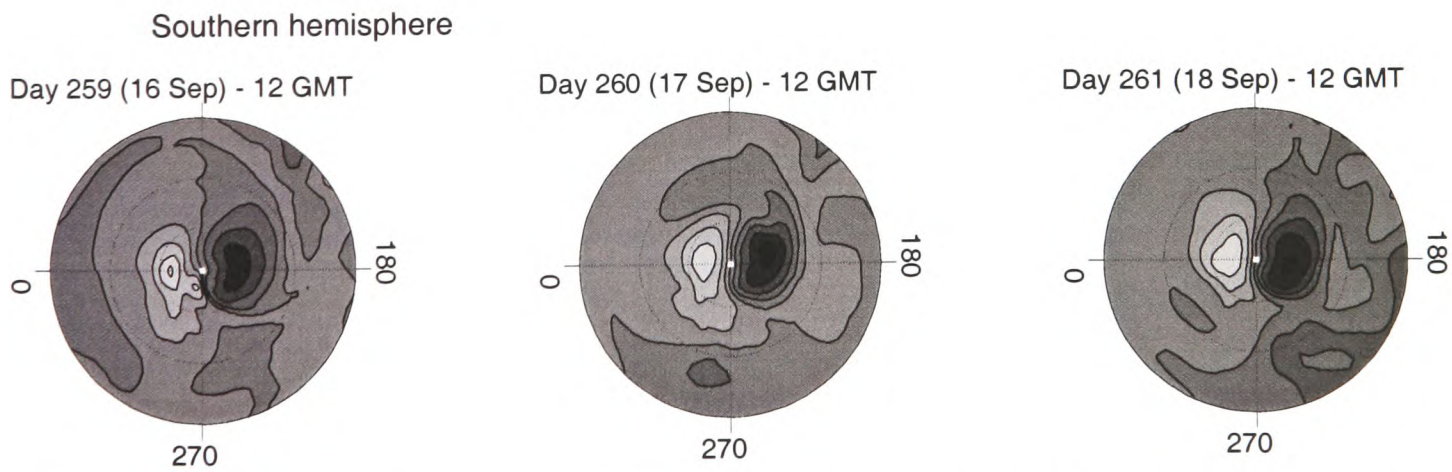


Figure 7.16: Southern hemisphere temperature anomalies for consecutive days at 60 km, SMM8. Dark colours indicate positive anomaly, maximum contour is 20 K.

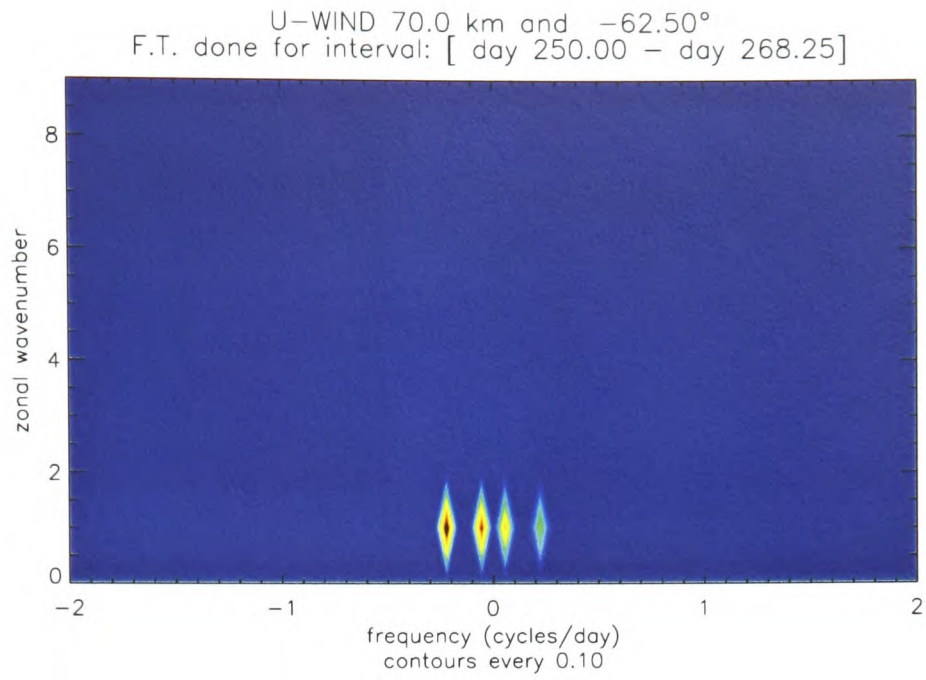


Figure 7.17: Zonal wavenumber versus frequency plot for u-wind at 70 km and 62.5°S, SMM8.

wavenumbers is shown in Figures 7.18b, 7.18c and 7.18d. The k= 1 wave can be identified with the (1,1) mode, the '5-day' wave (compare with Figure A.1). The k=2 and k=3 waves have smaller amplitude than the 5-day wave, but with a similar horizontal structure and a shorter vertical wavelength. All the waves show no amplitude at the critical lines, as expected for Rossby normal modes.

7.4.1.1 Effects on the mean flow

The effect of the wavenumber 1 perturbation at the bottom boundary on the mean flow is to produce a strong warming in the upper stratosphere. Large changes in the mean background flow in the southern hemisphere are seen. At the beginning of the integration the winter westerlies start to penetrate higher into the mesosphere south of 70°S, pushing the upper easterlies equatorwards at the start of the run (until about day 255). Together with this, the polar night jet develops a poleward tilt with height and separates from the midlatitude mesospheric jet, which by day 250 has disappeared. A few days later, the upper easterlies start to move downwards into the mesosphere and upper stratosphere. By day 270 the stratospheric westerlies are reversed to easterlies, as expected with a stratospheric warming (see Figure 7.19a). Values up to -150 $\mathrm{m\,s^{-1}}$ are seen at the top level of the model.

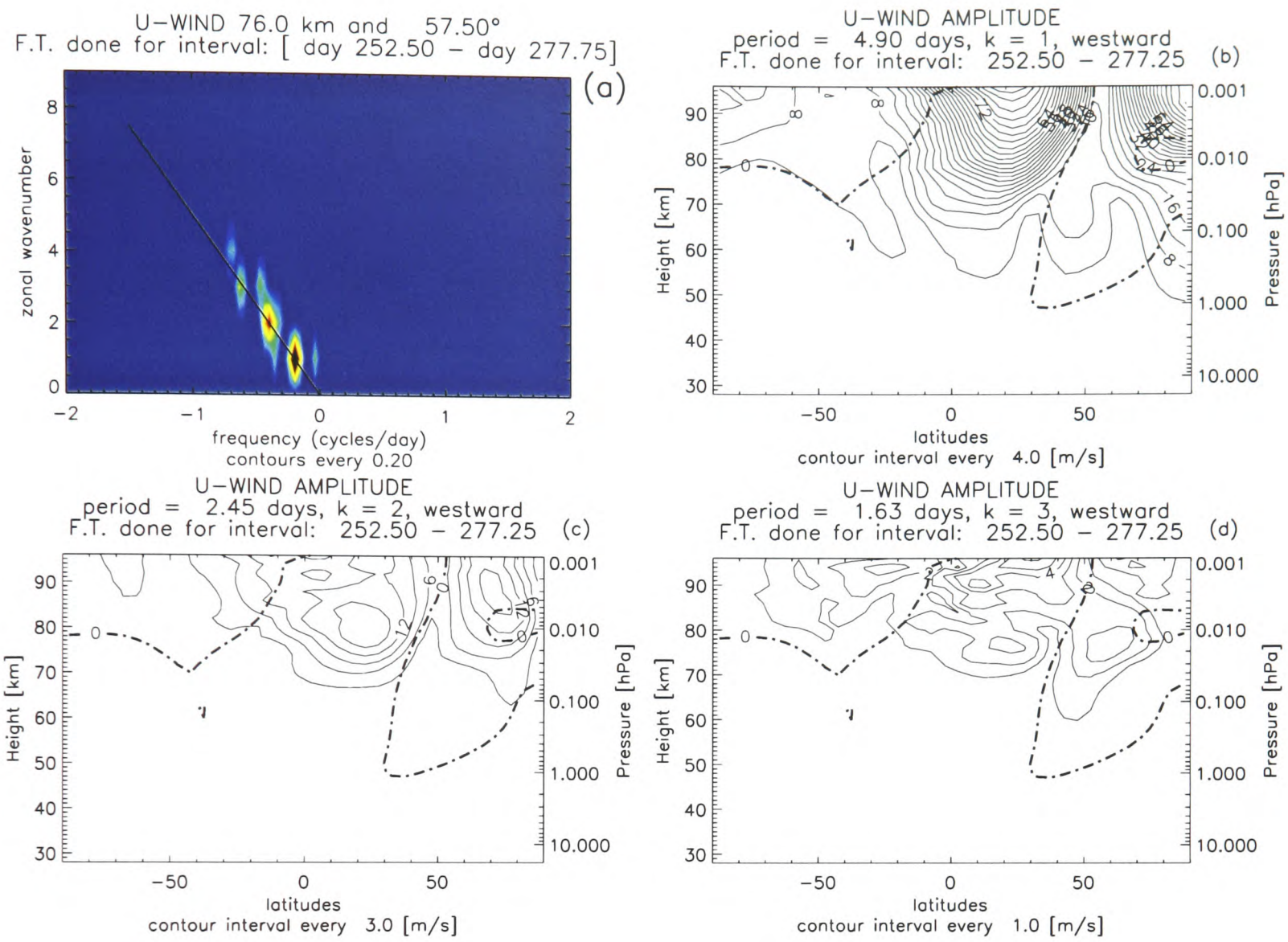


Figure 7.18: (a) zonal wavenumber versus frequency plot of u-wind at 57.5°N and 76 km. (b) Amplitude of u-wind for the k=1, westward propagating wave with period 4.9 days. (c) Amplitude of u-wind for k=2, westward propagating wave of period 2.45 days. (d) Amplitude of u-wind of the k=3, westward propagating wave with period 1.6 days, SMM8.

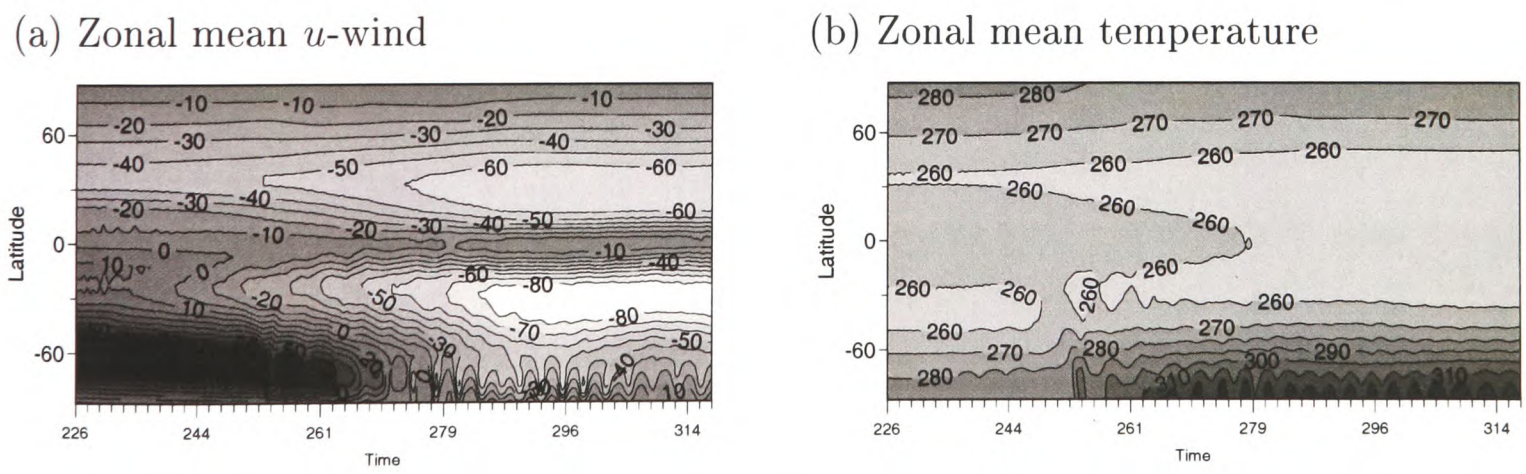


Figure 7.19: (a) Time evolution of zonal mean u-wind at 50 km, SMM8. (b) same as (a) but for temperature.

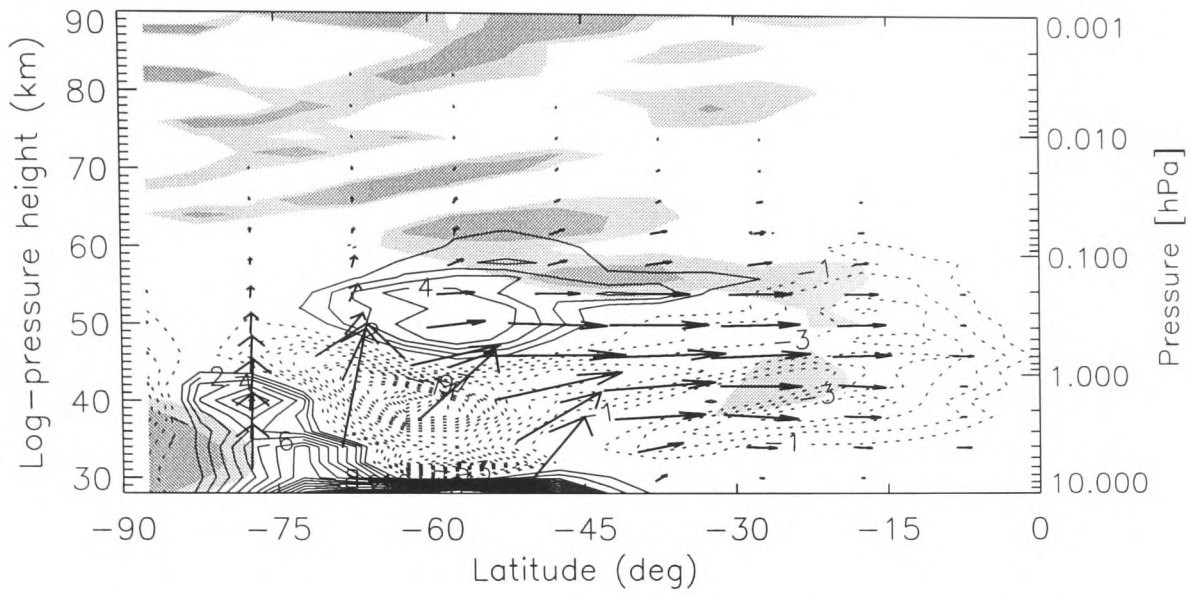


Figure 7.20: Contours of $\nabla \cdot F$, scaled by 1×10^3 in units of $\mathrm{kgm^{-1}s^{-2}}$, arrows of the EP flux for day 260 in SMM8. Shaded region are where $\overline{q}_y < -1 \times 10^{-11}$ $[\mathrm{m^{-1}s^{-1}}]$, with light grey for values between -1 to -5×10^{-11} and dark grey for values less than -5×10^{-11}.

Figure 7.19b shows the time evolution of the temperature as a function of latitude at 50 km. The strong warming can be seen in the southern hemisphere, just before the reversal of the zonal mean u-wind. In spite of the large values of the zonal mean u-wind at the top of the model, the integration finished normally without crashing.

The EP flux and the EP flux divergence are characteristic of upward propagating Rossby waves. Divergence of the EP flux is found at the bottom level of the domain and arrows (representing the EP flux components) point upwards and then equatorwards (Figure 7.20). This pattern of EP flux changes at around day 280, when the vectors south of 60°S point polewards (north of that latitude they still point equatorwards).

Fits to exponential growth for the waves in this run are not very good, the curves are much noisier than for any other waves analysed in this chapter or the previous chapter[2]. Nevertheless, the growth rates for the two normal modes found in SMM8 are given in Table 7.1, together with the growth rates of all the other waves found in the SMM runs described in this chapter.

[2] A correlation coefficient is obtained for each of the sliding windows where the data are fitted to equation 6.4, for the 40 fits performed the coefficients did in general not exceed 0.6.

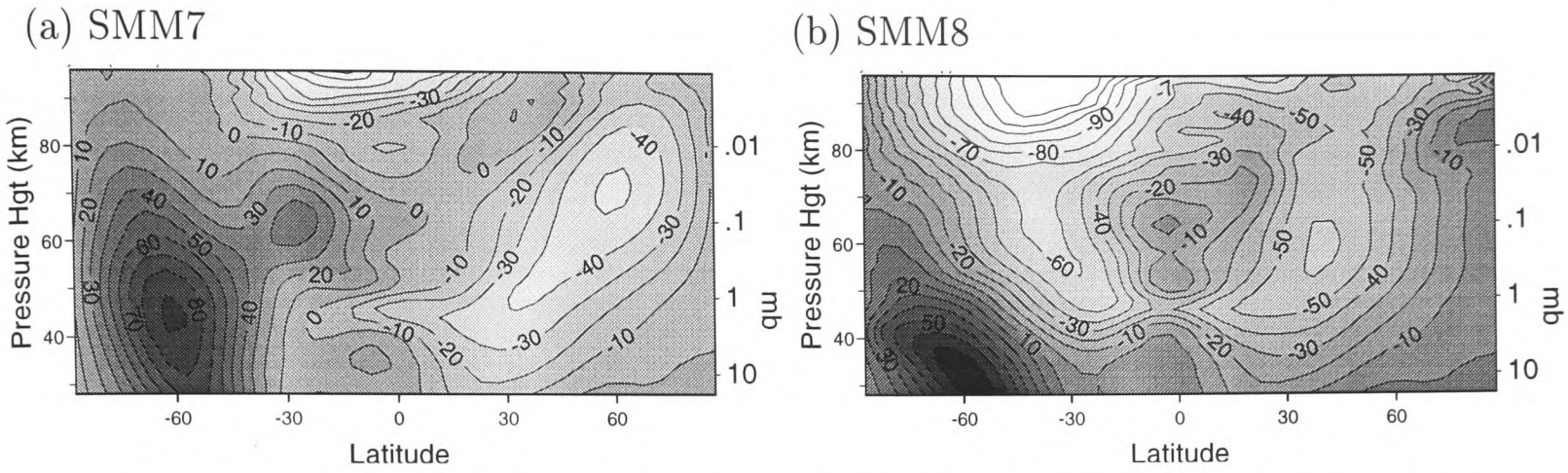


Figure 7.21: (a) Zonal mean u-wind at day 280 from SMM7. (b) Zonal mean u-wind at day 270 from SMM8, units of $\mathrm{m\,s^{-1}}$.

7.4.2 SMM9: wave 2 perturbation

In this experiment a perturbation in form of a stationary zonal wavenumber 2 wave is added to the geopotential at the bottom boundary with an amplitude of 300 m. Figure 7.22 shows the time evolution of the first four zonal wavenumber of meridional wind at 80 km. Wave amplitude can be seen for k=1 and k=2. In contrast to SMM8, where the zonal wavenumber 1 perturbation did not force travelling waves in the southern hemisphere, the zonal wavenumber 2 perturbation succeed in producing a polar winter 4-day wave. The wave has similar characteristics to the 4-day wave found in SMM1, SMM6 and SMM7. Figure 7.23a presents a spectral analysis of meridional wind at 62.5°S and 70 km showing the most important waves in SMM9. There are two eastward propagating waves in this run. For k=1 the wave has a period of about 4.5 days. For k=2 the wave has a period of about 2.1 days (the modes do not have the same phase speed). Their amplitudes are relatively small, but their structure agree very well with the previously modelled eastward propagating 4-day and 2-day waves. In addition, at zonal wavenumber 2, there is a westward propagating wave in Figure 7.23a with a period of 3.6 days. Zonal wavenumber, period, and spatial structure of the wave make it identifiable with the normal mode 4-day wave. Figures 7.23b, 7.23c and 7.23d show the amplitude of the zonal wind component of the relevant waves. All the waves have critical lines.

Plots in stereographic projection of the temperature anomaly in the southern hemi-

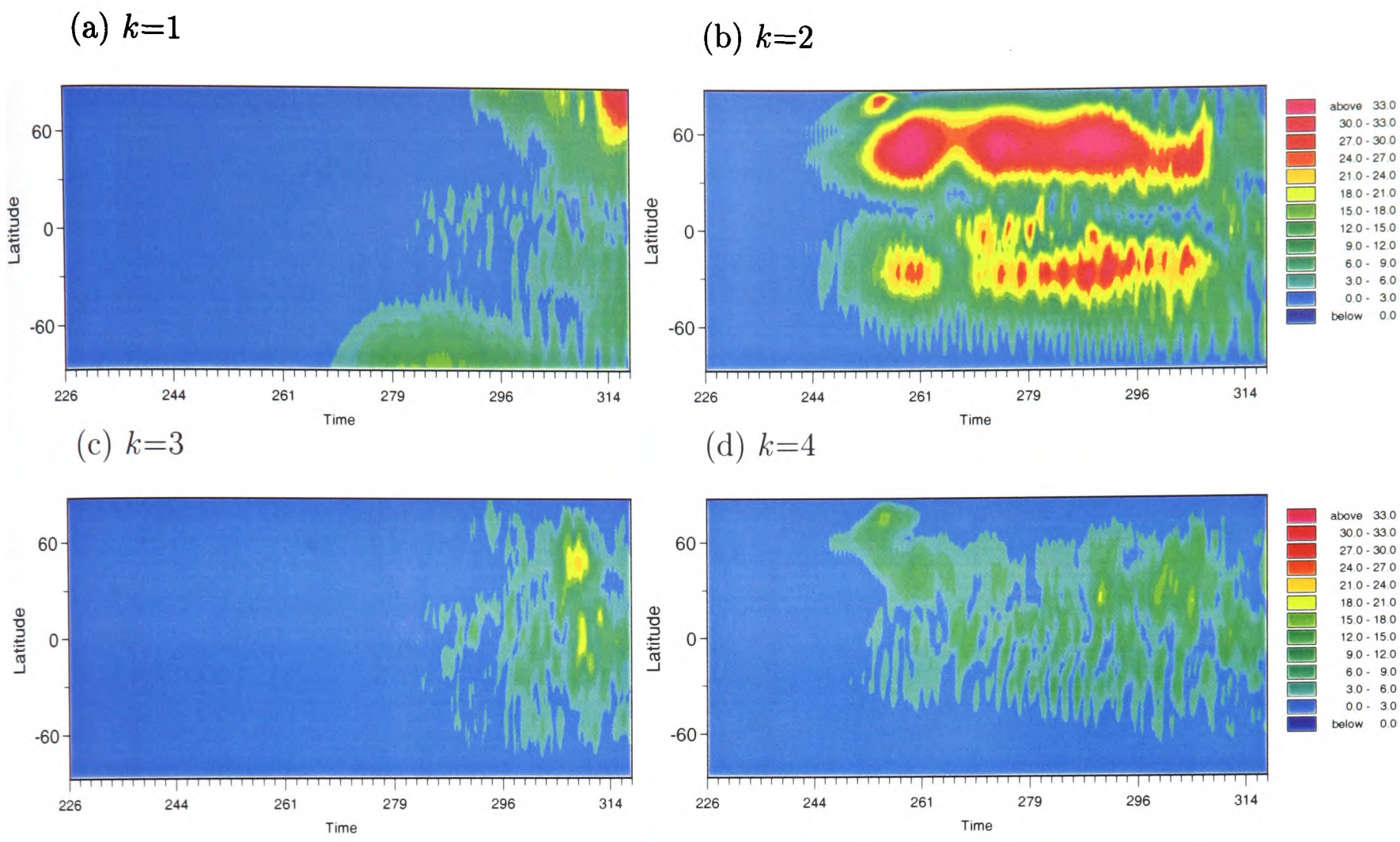


Figure 7.22: Time evolution versus latitude of meridional wind amplitude at 80 km for k=1, k=2, k=3 and k=4, SMM9.

sphere, show a stationary wavenumber 2 pattern up to day 250, then the travelling waves start to grow in amplitude (Figure not shown).

Divergence of the EP flux is predominately found in the lower levels of the model in the southern hemisphere. The EP fluxes point upwards and equatorwards, as expected for upward propagating Rossby waves, similar to what is seen in SMM8. Figure 7.24a shows the EP flux and its divergence for the southern hemisphere for day 280. To see the influence of the 4-day wave on the mean flow, the Eliassen-Palm flux was calculated just for zonal wavenumber 1. Because the magnitude of the wavenumber 1 component of the EP flux and its divergence is 2 orders of magnitude smaller than the total fluxes, they are not visible in the total fluxes. Figure 7.24b shows the wavenumber 1 component of the fluxes and they are very similar to those found for the 4-day wave found in SMM6 and SMM7 (Figure 7.7). The magnitudes are somewhat smaller, but also the amplitude of the 4-day wave in SMM9 is smaller in comparison to the other runs. The effect on the mean

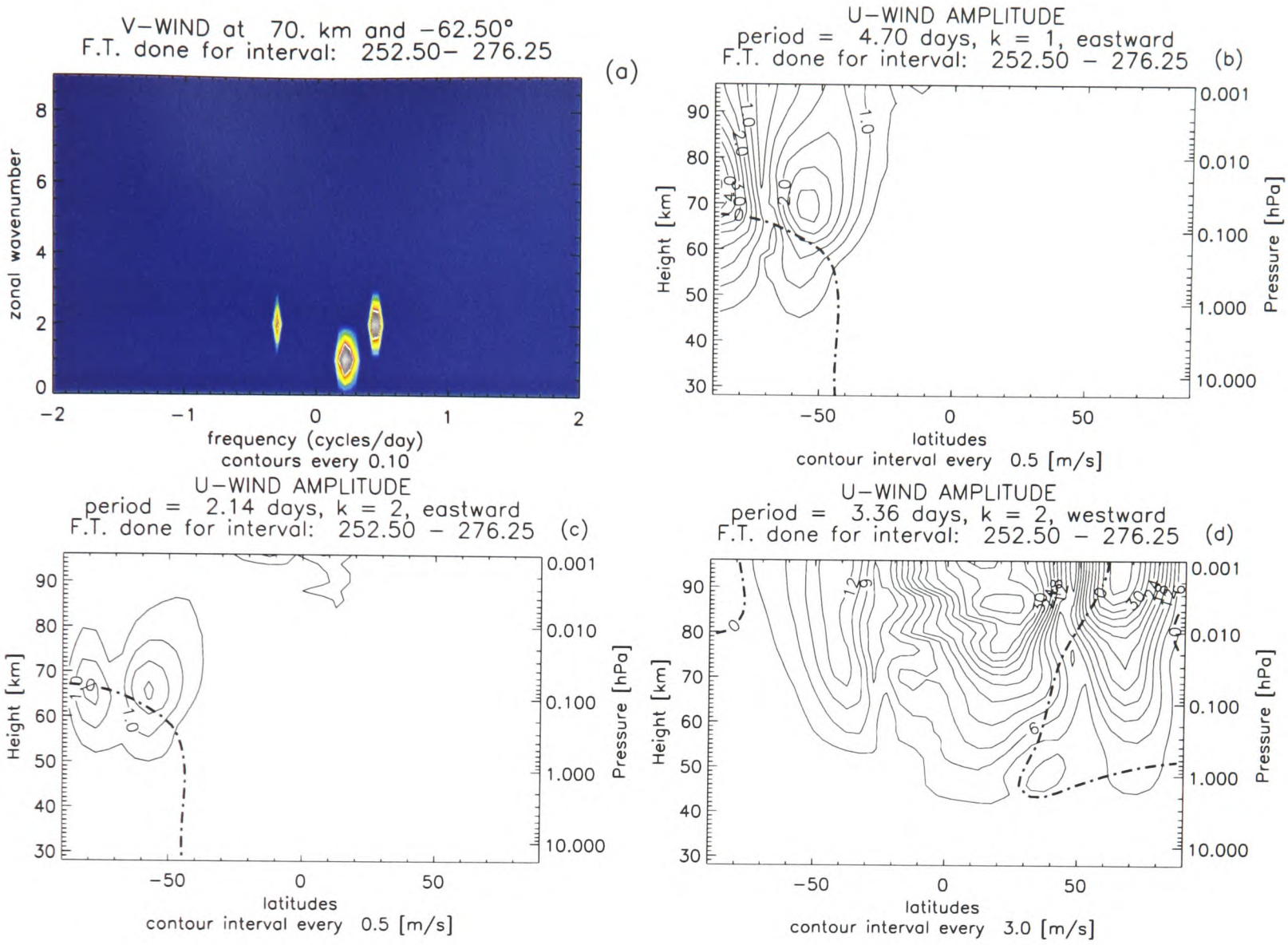


Figure 7.23: (a) zonal wavenumber versus frequency plot of v-wind at 62.5°S and 70 km. (b) Amplitude of u-wind for the k=1, eastward propagating wave with period 4.7 days. (c) Amplitude of u-wind for k=2, eastward propagating wave of period 2.1 days. (d) Amplitude of u-wind of the k=2, westward propagating wave with period 3.6 days, SMM9.

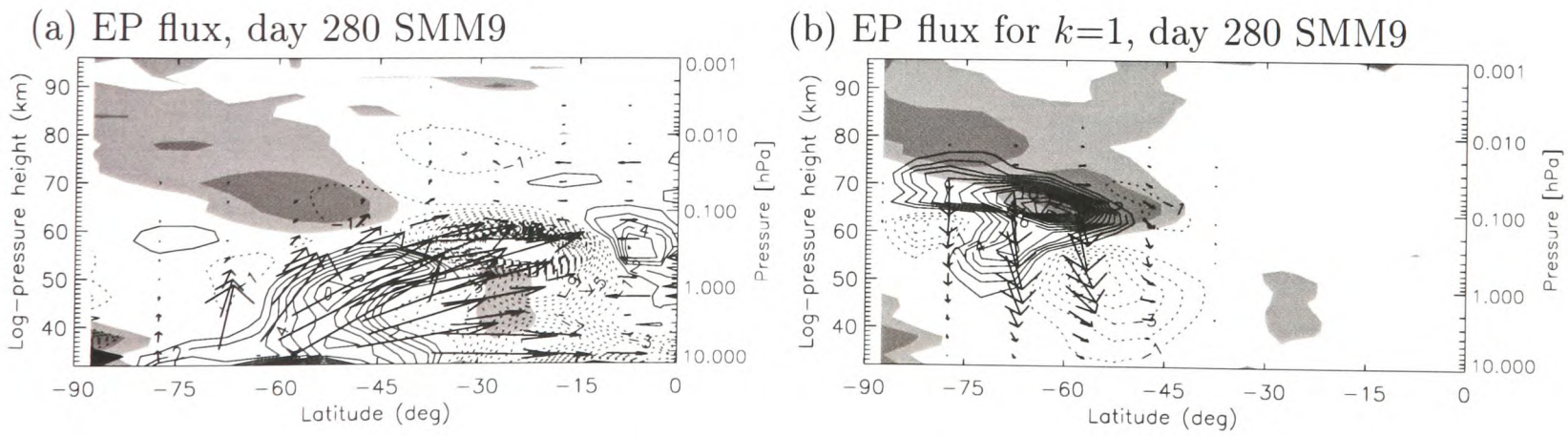


Figure 7.24: (a) Contours of $\nabla \cdot F$, scaled by 1×10^3 in units of $\mathrm{kgm^{-1}s^{-2}}$, arrows of the EP flux for day 280 in SMM9. Shaded region are where $\overline{q}_y < -1 \times 10^{-11}$ $[\mathrm{m^{-1}s^{-1}}]$, with light grey for values between -1 to -5×10^{-11} and dark grey for values less than -5×10^{-11}. (b) Same as (a) but here the EP flux and its divergence is calculated for the zonal wavenumber 1 only at day 280 in SMM9. $\nabla \cdot F$ is scaled scaled by 1×10^3, vectors are also scaled by 2×10^3. Same shading used for both Figures.

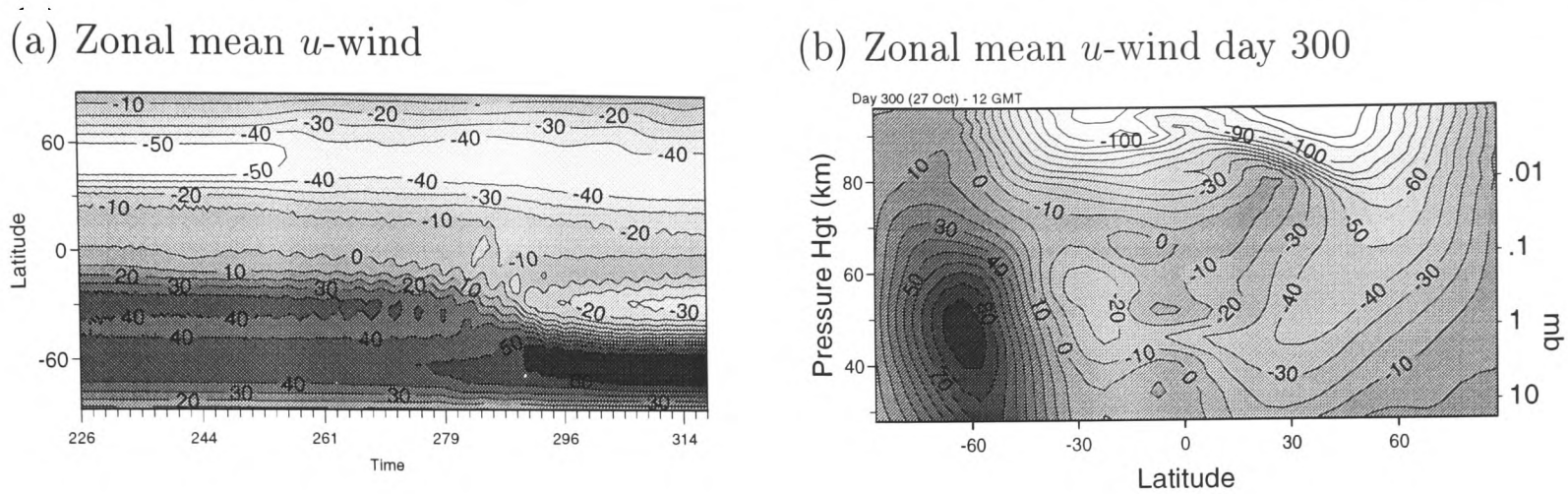


Figure 7.25: (a) Time evolution of zonal mean u-wind at 60 km, SMM9. (b) Zonal mean u-wind on day 300, SMM9.

flow of the wavenumber 1 wave, is to accelerate the background flow in the region south of 60°S at about 65 km, giving a very similar spatial distribution as found in SMM6.

7.4.2.1 Effects on the mean flow

Changes to the background state are not as dramatic as found in SMM8. No stratospheric warming is seen in SMM9. The zonal mean wind in the southern hemisphere shows small changes. By day 290 the midlatitude jet in the southern hemisphere disappears due to easterly winds in the upper SMM levels south of 30°S. The easterlies start to move downwards, as in SMM8, but only to about 80 km. At day 290 the polar night jet shows a small poleward tilt. No further changes develop in the southern hemisphere (Figure 7.25a). In the northern hemisphere the core of the summer jet start to move upwards at around day 270, until the strongest winds are found at the top level of the model. Easterly winds are seen above 80 km between 50°S and 70°N by day 300 with values up to -120 $\mathrm{m\,s^{-1}}$ (Figure 7.25b).

7.5 Summary of chapter

Various SMM runs were performed to study the polar winter 4-day wave in the southern hemisphere. Two different initial flows were used, a September average and an August average. For the September flow, the northern hemisphere jet had completely disappeared

SMM run	zonal wavenumber k	frequency ω [cycles/day]	period [days]	growth rate γ [days^{-1}]	e-folding time γ^{-1} [days]
SMM6	1	0.44	2.25	0.25	4.0
SMM6	2	0.2	5.0	0.205	4.9
SMM7	1	0.21	4.7	0.222	4.5
SMM7	1	-0.16	-6.25	0.130	7.8
SMM7	2	-0.27	-3.6	0.204	4.9
SMM7	3	-0.48	-2.1	0.170	6.0
SMM8	1	-0.21	-4.9	0.209	4.7
SMM8	2	-0.41	-2.45	0.256	3.9
SMM9	1	0.22	4.5	0.256	3.9
SMM9	2	0.44	2.25	0.051	19.4
SMM9	2	-0.29	-3.36	0.195	5.1

Table 7.1: Fitted growth rates and e-folding times for the different waves in the SMM runs described in this chapter.

so that only waves in the southern hemisphere developed. The largest amplitude was found for zonal wavenumber 1, although the zonal wavenumber 2 wave had a faster growth rate, but reached smaller amplitude than the wavenumber 1 wave. The wave is forced in the run by both barotropic and baroclinic processes. During the first stages of the growth of the wave it seems that it is the negative region of $\overline{q}_y$ at the poleward flank of the polar night jet that provides the wave activity of the growing wave. At this stage the wave shows many characteristics of the so called 'polar mode', with poleward momentum fluxes and temperature anomalies tilting from northwest to southeast.

Three different runs were performed using August time average background fields. SMM7 is a standard run; for SMM8 and SMM9, perturbations were added to the geopotential field at the bottom boundary in the form of zonal wavenumber 1 and 2 waves, respectively. For the standard configuration run (SMM7), again a 4-day wave grows in

the southern hemisphere with very similar characteristics to the wave found in SMM6. In the run there are momentum fluxes, as well as temperature fluxes associated with the wave, indicating the barotropic/baroclinic nature of the wave in the SMM. A wavenumber 2 wave, eastwards moving with a period close to 2 days, is also found. In SMM7 there are Rossby normal modes which grow to large amplitude and have strong effects on the mean flow. The instability calculations with the August background state showed a few Rossby normal modes becoming unstable. These modes' growth to large amplitude is seen in SMM7. In chapter 3 it was discussed that the normal mode 4-day wave in the EUGCM (seen in August Year 1) had characteristics of an unstable wave. The results from section 5.4.2 and from SMM7 indicate that the normal mode 4-day wave in the EUGCM is forced by an instability process.

In SMM8 no travelling waves in the southern hemisphere were found. But a large amplitude normal mode 5-day wave (and higher harmonics of the wave) grow, having a very strong effect on the background flow. The stationary wave 1 perturbation does not allow a travelling wave 1 to develop. This result could provide part of an explanation of why the 4-day wave is observed less in the northern hemisphere than in the southern hemisphere. Stationary wave 1 disturbances dominate the spectra of disturbances in the northern hemisphere winter, whereas in the southern hemisphere winter more stationary and transient wave 2 disturbances are found.

From these results one might conclude that the 4-day wave is forced by an instability of the winter stratospheric jet, but that a large amplitude stationary wave 1 disturbance inhibits the growth of the wave.

In SMM9 the wavenumber 2 perturbation produces a travelling wave in the southern hemisphere, with small amplitude but with the characteristics of the 4-day wave found in the other SMM runs. The EP fluxes associated with the wave are small, but have a similar distribution to the EP fluxes found in SMM6 and SMM7. Whereas the 4-day wave in SMM6 and SMM8 affects the mean flow in the southern hemisphere and removes the unstable regions, in SMM9 the unstable regions in the southern hemisphere remain throughout the run and the mean flow only shows very minor changes.

The e-folding times of the most relevant waves found in the SMM runs described in this chapter are given in table 7.1

In SMM8 and SMM9 Rossby normal modes are found. Normal models in the real atmosphere may be forced by perturbations produced in the troposphere. So the zonal wavenumber 1 perturbation forced a wavenumber 1 normal mode (the 5-day wave) and the wavenumber 2 perturbation equivalently forced a zonal wavenumber 2 normal mode (the 4-day wave). The 5-day wave in SMM8 did not have significant amplitude at the critical line, as expected for a normal mode. Also, no unstable 5-day wave was found in the instability calculations. The 4-day wave in SMM9 did, however, have large amplitude at the critical line, as did the 4-day wave in SMM7.

In SMM1 (chapter 6) a southern hemisphere 4 day wave was found as well and, although the amplitude of the wave is comparable with amplitudes found in SMM6 and SMM7, the wave in SMM1 has only a minor influence on the background winds in the southern hemisphere (see Figure 6.10b).

All the 4-day waves in the SMM runs have a baroclinic component, which is not found in observations; this is probably due to the too strong shear zones of the jets in the EUGCM. NT99 showed how the amplitude of the waves is influenced by the strengths and shape of the jets, which are related to the gravity wave drag in the EUGCM. The strong shear zone at the top of polar night jet seen for August (Figure 7.8) is too strong compared to observations. This can be seen for EUGCM winds for July (Figure 3.20a) compared with CIRA data, shown in Figure 1.2c for example.

Chapter 8

Conclusions

A complete study of travelling planetary waves in the middle atmosphere was performed for this thesis, and the origin of the diagnosed waves was investigated. This was done by examining the wave spectra in the Extended UGAMP GCM (EUGCM), and investigating the instability of the middle atmospheric jets as the forcing mechanism for the waves. Instability was tested in the linear regime by a 2-dimensional primitive equation linear instability calculation, and in the non-linear regime by a mechanistic middle atmosphere model, the UKMO Stratosphere Mesosphere Model (SMM).

Chapters 3 and 4 describe the wave spectra in the EUGCM compared with two different datasets. The representation of the middle atmosphere in EUGCM was analysed. A 3-year long integration of the EUGCM was performed, which allowed investigation of the waves present and also their interannual variability. The EUGCM produces a good simulation of the mean atmospheric state, including the structure and strength of the middle atmosphere jets and the very cold summer mesopause. The EUGCM also reproduces the observed wave spectra, including the polar winter 4-day wave, the quasi 2-day wave and various Rossby normal modes. Attention was paid especially to the quasi 2-day wave and the polar winter 4-day wave, as both these waves are thought to be forced by instability of their respective background flows.

In chapter 3 the EUGCM is compared with a 3-year long timeseries of meteor-radar data taken over Sheffield. The periods of wave activity were well reproduced by the EUGCM,

as well as the frequencies and amplitudes of the waves. In the winter and equinox months wave activity is mainly found at low frequencies (less than 0.2 cycles per day), whereas during the summer months wave activity is found at frequencies between 0.2 and 0.5 cycles per day. The EUGCM reproduces this pattern, with somewhat smaller interannual variability compared with the meteor-radar data. In the JJA season the main wave seen in meteor-radar data and the EUGCM is the quasi 2-day wave.

In chapter 4 the EUGCM output was compared to UKMO assimilation data. UKMO data is a global dataset, which allows a more complete comparison, but only goes up to 0.3 hPa and is therefore not suitable for studying waves with large amplitude in the upper mesosphere, such as the quasi 2-day wave. Waves found in the UKMO data included some Rossby normal modes and the polar winter 4-day wave.

The waves in the EUGCM were carefully examined not only with respect to their spatial structure, but also to the background flow in which they were embedded. The appearance of critical lines, the sign of $\bar{q}_y$, the EP flux and its divergence are diagnosed. On theoretical grounds, regions where $\bar{q}_y$ is negative are potentially unstable regions. If, in addition, these regions coincide with regions of divergence of EP flux, and a wave has a critical line with large amplitude at that region, then the wave is probably forced by an instability of the background state. In the EUGCM, because of the easterlies found in the JJA season, all the waves found during these months had critical lines in the upper mesosphere, and the above pattern of negative $\bar{q}_y$ with divergence of the EP flux near the critical region was fulfilled. This includes the quasi 2-day wave and the normal mode 4-day wave. The waves found during the equinox months did not have critical lines and were all identified with Rossby normal modes. In the winter months, apart from some Rossby normal modes, the polar winter 4-day wave was identified and the hypothesis that an instability forces this wave could be confirmed.

The representation of the polar winter 4-day wave in the EUGCM is again very close to the observations. The EUGCM modelled the wave as an eastward moving pool of warm air circling around the pole with a period of about 4 days. In years 2 and 3 of the integration,

an eastward moving wave of k=2 and period close to 2 days can be seen accompanying the 4-day wave, and in year 3 a k=3 wave with period about 1.5 days is seen as well.

Several Rossby normal modes were identified in the UKMO data, including a wave with period around 7 days which is found in the EUGCM as well. In the UKMO most of the Rossby normal modes did not have a critical line. However, as in the EUGCM, they are seen during equinox month. However, in the UKMO a 5-day wave is seen during solstice conditions with amplitude in the region of the critical line. Previous observational and theoretical studies show that stable modes must dissipate when reaching a critical line, so that amplitude is greatly reduced at the regions bounded by the critical line. However, the Rossby normal modes found for the JJA season in the EUGCM did all have critical lines and large amplitude at them. In NT99, the amplitude of waves in their relation to the shape and strengths of the jets was investigated. Therefore, the EUGCM is probably too unstable and most of the wave found in the model during solstice conditions are forced by an instability.

From the representation in the EUGCM of the quasi 2-day wave, it was concluded that the dynamics of the wave in the EUGCM are consistent with an instability forcing this wave. This idea was then tested for two different stages of the wave. First a linear instability analysis was performed. If waves arise from an instability process, then at the beginning they can be modelled by small amplitude waves and linear theory can be applied, and numerical solutions to the linearized equations can be obtained.

In chapter 5 results for the linear instability calculations were presented. The code written for this purpose is a discretisation of the linearized primitive equations, reduced from 3-dimensions to 2-dimensions by imposing the zonal structure. Then the eigenvalue problem is introduced by assuming that the temporal part of the solutions are complex exponentials. In this way, the imaginary parts of the eigenvalues give information about the frequencies or periods of the eigenvectors, and the real parts give information about the growth rates or e-folding times. The background states used to test their stability were taken from the EUGCM. Four different background states were used to run the instability

code. For the quasi 2-day wave the code was run with a June and July time average, and for the 4-day wave with a August and September time average. All of the instability calculations showed unstable modes for different zonal wavenumbers.

The runs for the quasi 2-day wave all gave as the fastest growing mode modes which have zonal wavenumber 3, as has the quasi 2-day wave. For the June background state, the fastest growing mode has a period of 43 hrs and a spatial structure which resembles the most important features from the quasi 2-day wave. The meridional wind has a maximum at the equator, whereas zonal wind and temperature have minima at the equator and maxima at midlatitudes, with larger values in the summer hemisphere. For the July background state the fastest growing mode has a period of 35 hrs, and its spatial structure is localized in the northern hemisphere at high latitudes, with no resemblance to the known global structure of the quasi 2-day wave. However, a slower growing mode does again have a period and spatial structure closer to the quasi 2-day wave. The amplitude of the 35 hrs mode coincides with the region where $\bar{q}_y$ is negative and the background state has strongest shear. In the EUGCM waves with periods around 35 hrs and localized spatial structure are seen for two of the three years in June and August. In the meteor-radar data amplitude at these periods is also seen in June. Probably because these waves are only seen north of 50°N and because of their small latitudinal extent, these waves have not been reported before.

For the 4-day wave both of the instability calculations performed had fastest growing modes for zonal wavenumber 1. The periods and spatial structure of the modes showed excellent agreement with the observed structure of the 4-day wave as well as the representation of the wave in the EUGCM. Unstable modes for k=2 and k=3 with similar spatial structure as the 4-day wave are seen as well. In fact, the July, August and September background state had an unstable mode for k=1 with a spatial structure and period close to the 4-day wave. The August background state showed various unstable modes (with smaller growth rates) resembling Rossby normal modes. All the unstable modes obtained from the instability calculations had critical lines. In particular, large amplitude is found at the critical line in temperature and u-wind.

Because the quasi 2-day wave is thought by some authors to be the manifestation of the third Rossby-gravity mode, i.e. a normal mode, the instability code was used to investigate what happens to this mode, and other Rossby normal modes, under changes to the background conditions. Stable modes were calculated for slowly varying background conditions from an isothermal case with no background wind to the full EUGCM background state, and the evolution of the normal modes is followed. These experiments were performed for the June, July and August background states. For increasingly realistic background states the normal modes get distorted until they either become unstable or disappear. The results of these experiments show that the third Rossby-gravity mode does not to survive realistic background conditions. Under increasing changes to the temperature and zonal mean u-wind, the mode's structure gets distorted and finally disappears. For the June background state it was possible to follow the evolution of the mode from stable to weakly unstable, with the appearance of a critical line. For the August background state it is a mode with smaller vertical wavelengths that becomes unstable; this mode corresponds to the unstable mode found for the full August background state.

Because in the EUGCM the normal mode 4-day wave had large amplitude in the region of a critical line, which did not agree with a stable normal mode, the same experiments were performed to see what happens to this wave under changes to the background fields. The conclusion of that experiment was that the mode does not survive to the full EUGCM background flow. The mode either becomes weakly unstable or disappears. For the August background state it is a higher order mode (with smaller vertical wavelength) that becomes unstable, and is produced in the instability calculation and the SMM runs as the unstable mode. None of the experiments showed for the full EUGCM background state a stable normal mode. For all the normal modes, it is the temperature field which is most distorted, with greatly reduced values in the southern hemisphere.

The results of chapter 5 indicate that unstable modes with characteristics of the quasi 2-day wave and the polar winter 4-day wave can grow from different background states. The instability calculation with the August background state showed also a normal mode 4-day wave as an unstable mode. The instability calculation assumes exponential growth,

and therefore it is believed that these modes will reach largest amplitude in their non-linear phase. To test this, a mechanistic model is used to perform initial value problems. The SMM is initialized with the same zonal mean states used for the instability calculations. The flow is then perturbed by adding random noise to u and T at all grid points.

Chapter 6 describes the experiments performed with the mechanistic model to study the non-linear evolution of the quasi 2-day wave-like modes found earlier with the linear instability code. Several experiments were performed with the July background flow, with different configurations of the SMM. In all the experiments the largest amplitudes are seen for the zonal wavenumber 3. The simplest configuration was a SMM run where the radiation scheme and Rayleigh friction were not included. Unstable modes grow for the first four zonal wavenumbers. All of the waves could be identified with unstable modes from the instability calculation, with the same spatial structure in the initial stage at least, and similar e-folding times. The northern hemisphere unstable modes for k=2 and k=4 grow only to very small amplitude. The southern hemisphere k=1 and k=2 modes grow to large amplitude. The fastest growing mode is, as in the instability calculation, the 35 hrs mode, but this mode only reaches a certain amplitude and then disappears. It is the slower growing 42 hrs mode that reaches largest amplitude in the SMM run and interacts with background flow so as to remove the unstable region. Other experiments were performed with the July background state where Rayleigh friction and radiation were included. In all the runs only a wavenumber 3 wave grows to large amplitude. These SMM runs did not give a realistic representation of the quasi 2-day wave. A SMM run for the June background state was performed with the simple configuration. Only a wavenumber 3 wave grows here. The wave reaches large amplitude, and its spatial structure resembles all the characteristics of the quasi 2-day wave.

Finally chapter 7 describes the experiments and results of SMM runs performed to study the polar winter 4-day wave. Two runs were performed with the basic configuration, with no radiation and no Rayleigh friction. Both these experiments show a 4-day wave growing in the southern hemisphere. The waves grow to large amplitude and interact

with the background state by removing the unstable regions at the polar flank of the winter jet. From observations and other theoretical studies the wave is thought to be barotropic in nature. However, in the SMM experiments the wave has both barotropic and baroclinic elements. For the August background state, apart from the southern hemisphere waves, large-scale Rossby normal modes grow. It was shown in chapter 5 that under this background state various Rossby normal modes became unstable. These are the modes that grow to large amplitude in the SMM experiment.

Two other runs were performed where instead of perturbing the initial state by adding noise to the zonal mean state, a perturbation was added in the form of a wave at the bottom boundary in the southern hemisphere, simulating upward propagating Rossby waves as are observed during the winter months. In a first run a zonal wavenumber 1 wave was added to the bottom boundary, and a second run added a zonal wavenumber 2 wave. The zonal wavenumber 1 perturbation did not excite any travelling waves during the run; only a large amplitude stationary zonal wavenumber 1 wave is seen. The zonal wavenumber 2 perturbation, on the other hand, succeeded in exciting a 4-day wave in the southern hemisphere. The spatial structure as well as the associated EP fluxes are similar to the 4-day wave growing from the standard configuration experiments. From the evidence of the linear instability calculations and the SMM runs, it is concluded that the polar winter 4-day wave is an unstable wave forced by the stratospheric winter jet. Furthermore, the results from the SMM experiments with wave perturbations added at the bottom boundary suggest that the 4-day wave cannot exist in the presence of a stationary wavenumber 1 wave, but can in the presence of a stationary wavenumber 2 wave, and probably also in the presence of transient wavenumber 1 waves, as seen in NT97. This might explain why the 4-day wave is observed more in the southern hemisphere than in the northern hemisphere, where stationary wave 1 dominates during the winter.

In all the SMM runs the 4-day wave had a strong baroclinic component. This is probably due to the too strong shear zones at the top of the polar night jet in the EUGCM. This is another indication that the EUGCM might be too unstable.

For the quasi 2-day wave the conclusion is that the summer mesosphere is unstable and the large scale quasi 2-day wave can grow from this instability. However, in the EUGCM the normal mode 4-day wave is also forced by instability of the mesospheric summer jet. For the quasi 2-day wave there is observational evidence (e.g. Lieberman, 1999; Fritts *et al.*, 1999) that confirm the observed EP flux and unstable regions in the EUGCM.

For the normal modes 4-day and 5-day waves, however, no such observations have been made. It would therefore be necessary to have observations of the background state during solstice conditions. These and the EP fluxes associated with the waves are needed to confirm that these waves effectively show reduced amplitude in the regions of critical lines. It has to be said that the instability code does not include dissipation terms; this might be the reason for not finding stable modes for the background states used. However, in the EUGCM dissipation and reduction in amplitude at the critical lines for Rossby normal modes is possible but not observed.

Appendix A

Laplace's tidal equation

Analytical wave solutions to the general linearized primitive equations governing small perturbations can only found if an isothermal atmosphere at rest is considered ($\bar{u}$=0, $\bar{T}$=constant), because otherwise the horizontal and vertical part of the solution can not be separated. Under the conditions of an atmosphere at rest and isothermal, an important class of waves motions results, including Rossby normal modes, atmospheric tides and gravity waves. This study was started by Laplace when trying to understand tides in the ocean, and in this way arrived at the Laplace Tidal equation. However, he did not succeed in finding solutions to the equation. Some hundred years later Hough recognized the similitude of Laplace's tidal equation to the Legendre equations and in this way found many solutions to the equation, now called Hough modes.

Writing the linearized set of equations 2.47 – 2.51 for an isothermal atmosphere at rest, and taking X=Y=J=0, gives:

$$\frac{\partial u'}{\partial t} - fv' + \frac{\Phi'_\lambda}{acos\phi} = 0, \tag{A.1}$$

$$\frac{\partial v'}{\partial t} + fu' + \frac{\Phi'_\phi}{a} = 0, \tag{A.2}$$

$$\frac{\partial \Phi'}{\partial z} = \frac{RT'}{H}, \tag{A.3}$$

$$\frac{1}{acos\phi}\frac{\partial u'}{\partial \lambda} + \frac{1}{a}\frac{\partial v'}{\partial \phi} + \frac{1}{\rho_0}\frac{\partial(\rho_0 w')}{\partial z} = 0, \tag{A.4}$$

$$\frac{\partial T'}{\partial t} + \frac{\kappa \overline{T} w'}{H} = 0. \tag{A.5}$$

The method of solution separates the problem into horizontal and vertical functions. So let:

$$(u', v', \Phi') = e^{z/2H} U(z)[(\tilde{u}(\lambda, \phi, t), \tilde{v}(\lambda, \phi, t), \tilde{\Phi}(\lambda, \phi, t)], \tag{A.6}$$

and

$$w' = e^{z/2H} W(z) \tilde{w}(\lambda, \phi, t). \tag{A.7}$$

The exponential factor simplifies the manipulation of the equations. Without loss of generality we choose:

$$U = \frac{dW}{dz} - \frac{W}{2H}. \tag{A.8}$$

With this assumption we replace equation A.7 into equations A.4 and A.5 which leaves us with:

$$-\frac{(W_{zz} - \frac{W}{4H^2})}{N^2 W} = \frac{\tilde{w}}{\tilde{\Phi}_t} = (gh)^{-1}, \tag{A.9}$$

where $(gh)^{-1}$ is a separation constant which couples the horizontal and vertical structure, h has dimensions of length and is called equivalent depth[1]. The z dependent part of this equation gives the following equation:

$$\frac{d^2 W}{dz^2} + \left(\frac{N^2}{gh} - \frac{1}{4H^2}\right) W = 0. \tag{A.10}$$

[1]The name equivalent depth comes from the fact that Laplace's original study was for oscillations of an uniform ocean on a sphere, and h was the mean depth of the ocean. For the atmosphere h should, however, be considered simply as an eigenvalue.

This equation is called the "vertical structure equation". By replacing A.6 into A.1, A.2 and A.3 and using the separation constant gh three equations for the horizontal structure are obtained:

$$\frac{\partial \tilde{u}}{\partial t} - f\tilde{v} + \frac{\tilde{\Phi}_\lambda}{a\cos\phi} = 0, \tag{A.11}$$

$$\frac{\partial \tilde{v}}{\partial t} + f\tilde{u} + \frac{\tilde{\Phi}_\phi}{a} = 0, \tag{A.12}$$

$$\frac{1}{a\cos\phi}\frac{\partial \tilde{u}}{\partial \lambda} + \frac{1}{a}\frac{\partial \tilde{v}}{\partial \phi} + \frac{\tilde{\Phi}_t}{gh} = 0. \tag{A.13}$$

These three equations for the horizontal and time dependence are called the 'Laplace tidal equations' or 'shallow water equations' for depth h. The standard procedure for finding solutions to Laplace's tidal equations is to pose the sinusoidal forms:

$$(\tilde{u}, \tilde{v}, \tilde{\Phi}) = Re[(\hat{u}(\phi), \hat{v}(\phi), \hat{\Phi}(\phi)]e^{i(k\lambda - 2\Omega\sigma t)}, \tag{A.14}$$

where k is the spherical zonal wavenumber and the period is given by $2\pi/2\Omega\sigma$. Substituting equation A.14 into A.11, A.12 and A.13 the Laplace tidal equation is obtained:

$$\mathcal{L}\tilde{\Phi} + \gamma\tilde{\Phi} = 0, \tag{A.15}$$

where $\gamma = \frac{4\Omega^2 a^2}{gh}$ is called Lamb's parameter and

$$\mathcal{L} = \frac{d}{d\mu}\left[\frac{(1-\nu^2)}{(\sigma^2-\mu^2)}\frac{d}{d\mu}\right] - \frac{1}{\sigma^2-\mu^2}\left[\frac{-k(\sigma^2+\mu^2)}{\sigma(\sigma^2-\mu^2)} + \frac{k^2}{1-\mu^2}\right]. \tag{A.16}$$

This equation with suitable boundary conditions is an eigenvalue problem and can be solved numerically. Specifying k and σ, i.e. zonal wavenumber and frequency, a set of eigenvalues can be found (or equivalent depth) and the corresponding eigenvectors are called *Hough functions*, denoted by $\Theta(k,n)$[2]. This way of solving the equations is mostly

[2]a thorough analysis of the solutions of Laplace's tidal equation is given in Longuet-Higgins, 1968.

used for the study of atmospheric tides, where the zonal wavenumber and frequency are given by the forcing (solar heating). Another way of solving this equations is to specify h by solving the vertical structure equation, and for a given zonal wavenumber k, equations A.11 – A.13 are an eigenvalue problem for σ, the frequency of the oscillation. This last approach was used to calculate normal mode Rossby waves. Using the code written to do the instability calculation in chapter 5, some Rossby normal modes were calculated and their latitude height cross sections are shown here.

Figure A.1 shows the first symmetric mode (1,1), the 5-day wave. The second and third symmetric modes for zonal wavenumber 1 are shown in Figures A.2 and A.3. They are called the 10-day wave and the 16-day wave, respectively. In Figure A.4 the first antisymmetric mode for k=2 is presented, the 4-day wave. Finally the third Rossby-gravity mode (3,0) is shown in Figure A.5.

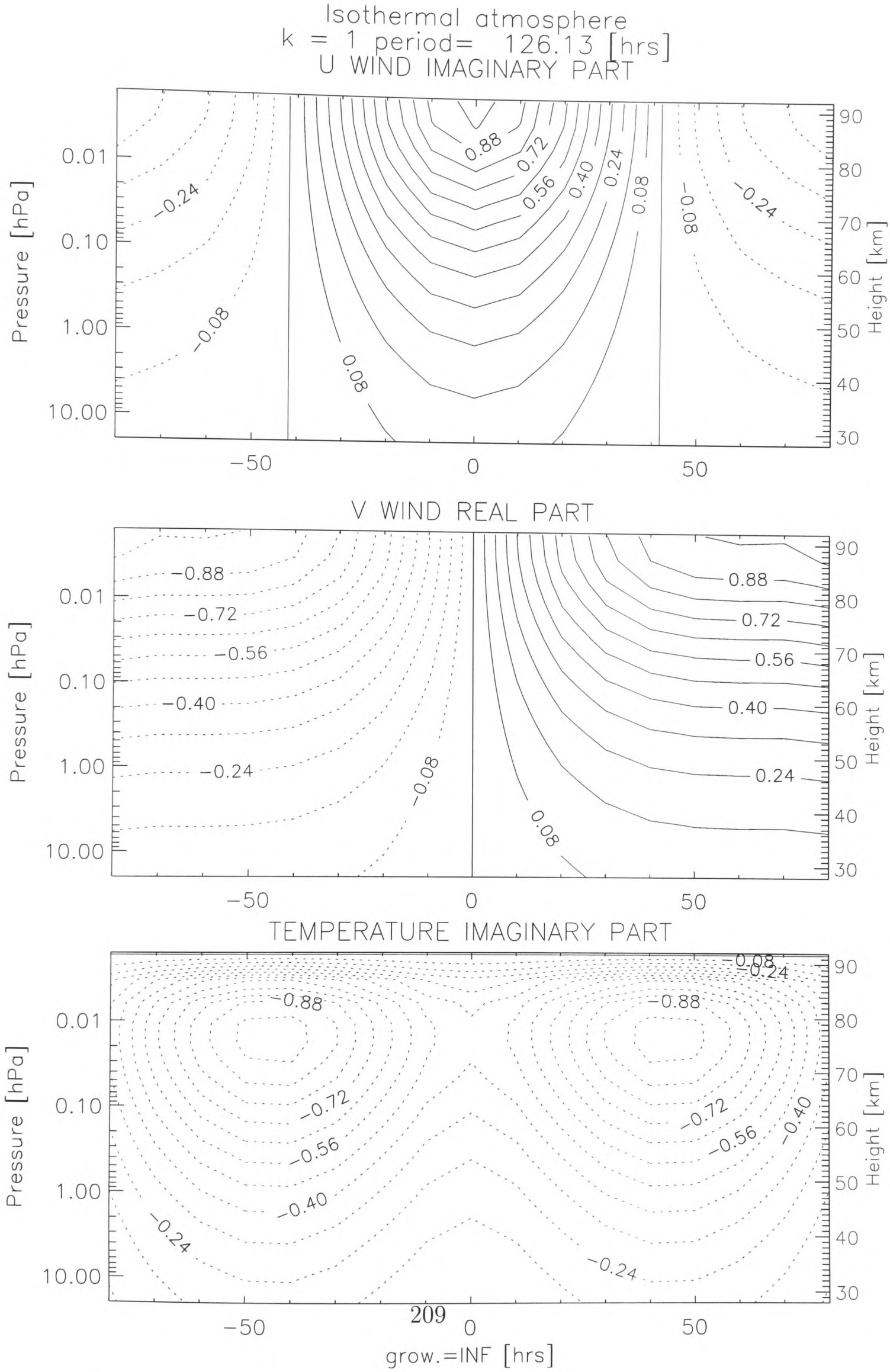


Figure A.1: First symmetric mode for k=1 (1,1), the '5-day' wave.

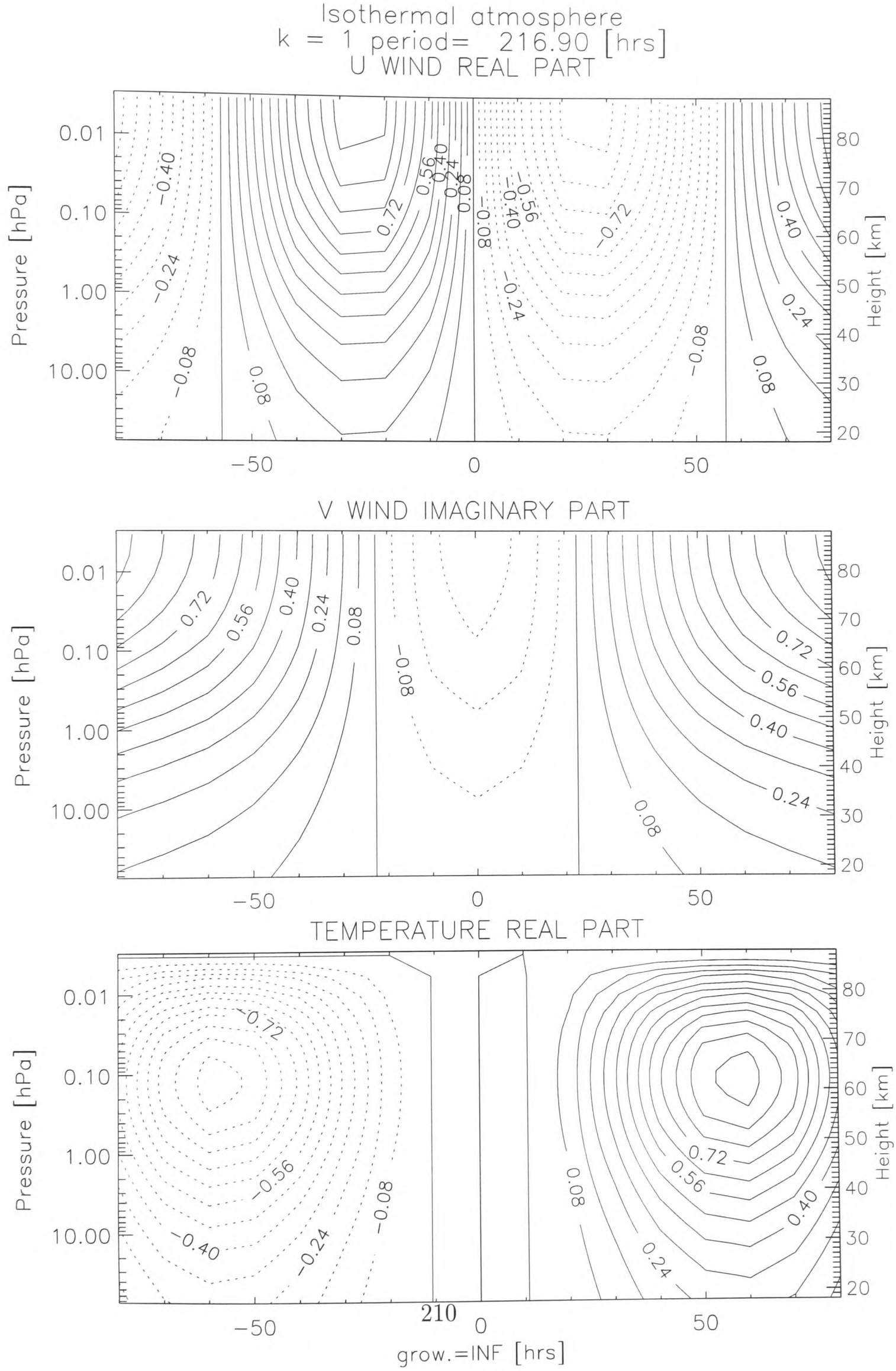


Figure A.2: Second antisymmetric mode for k=1 (1,2), the '10-day' wave.

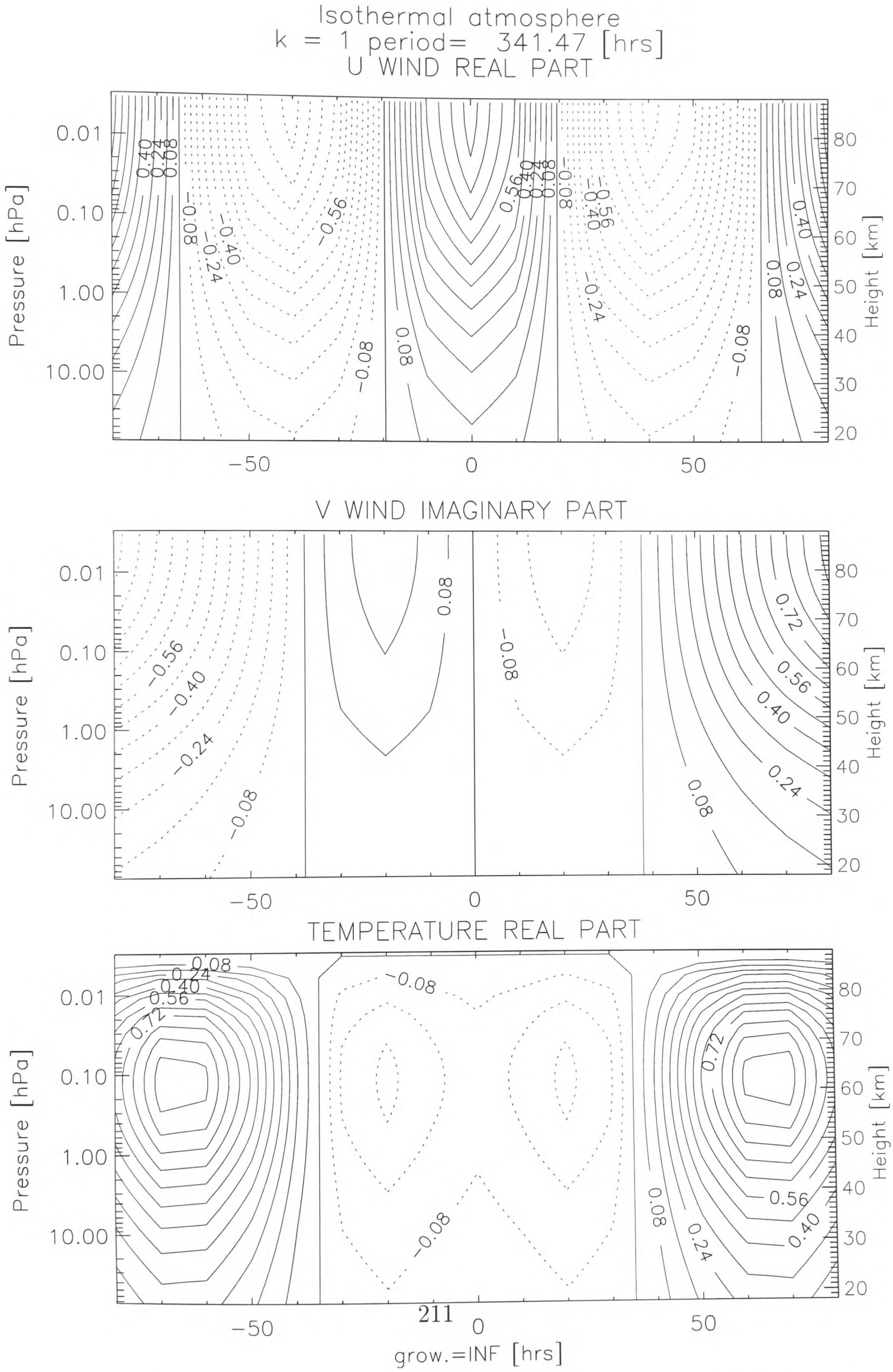


Figure A.3: Second symmeric mode for k=1, (1,3) Rossby mode, the '16-day' wave.

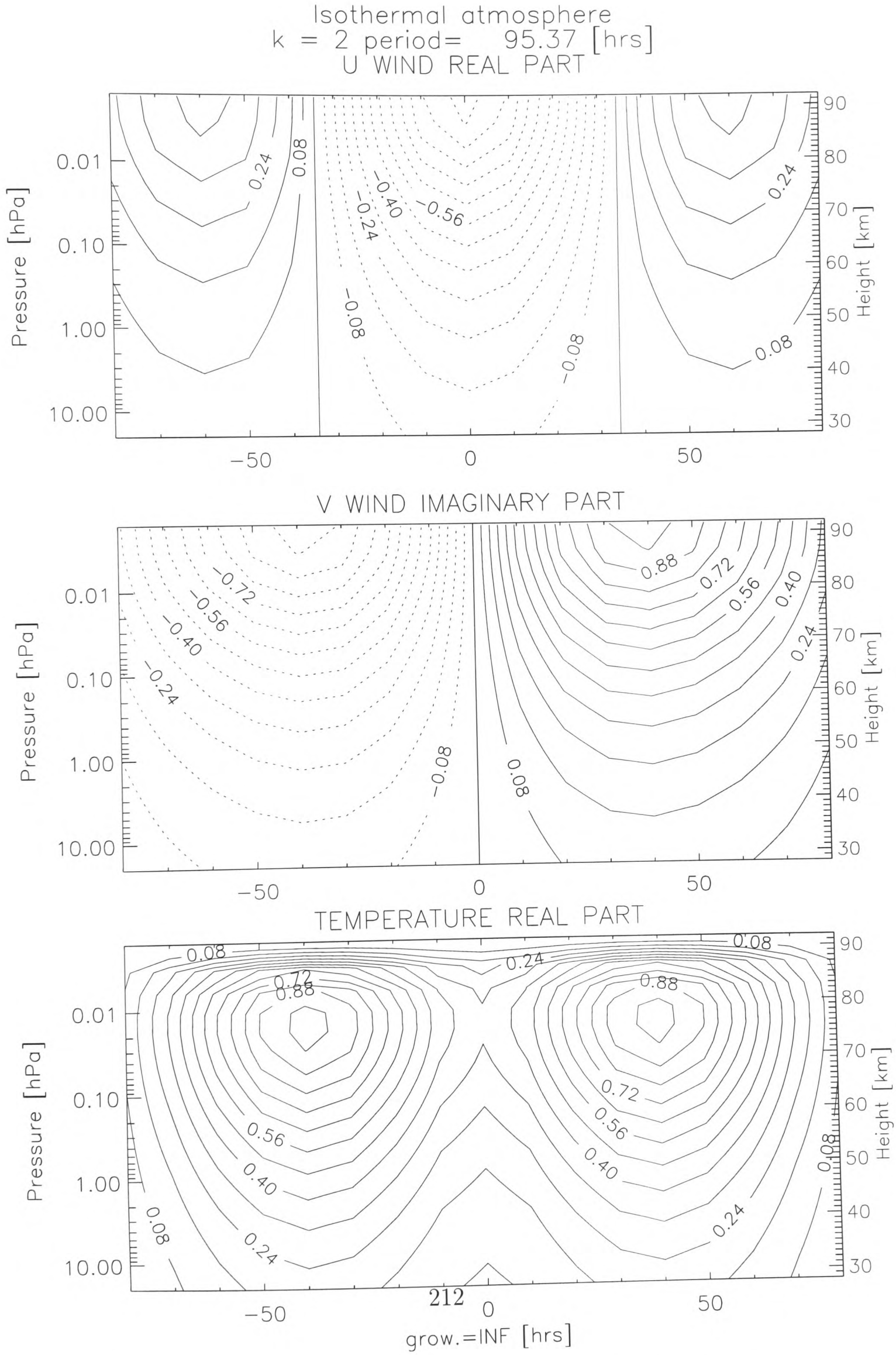


Figure A.4: First symmetric mode for k=2 (2,1), the '4-day' wave.

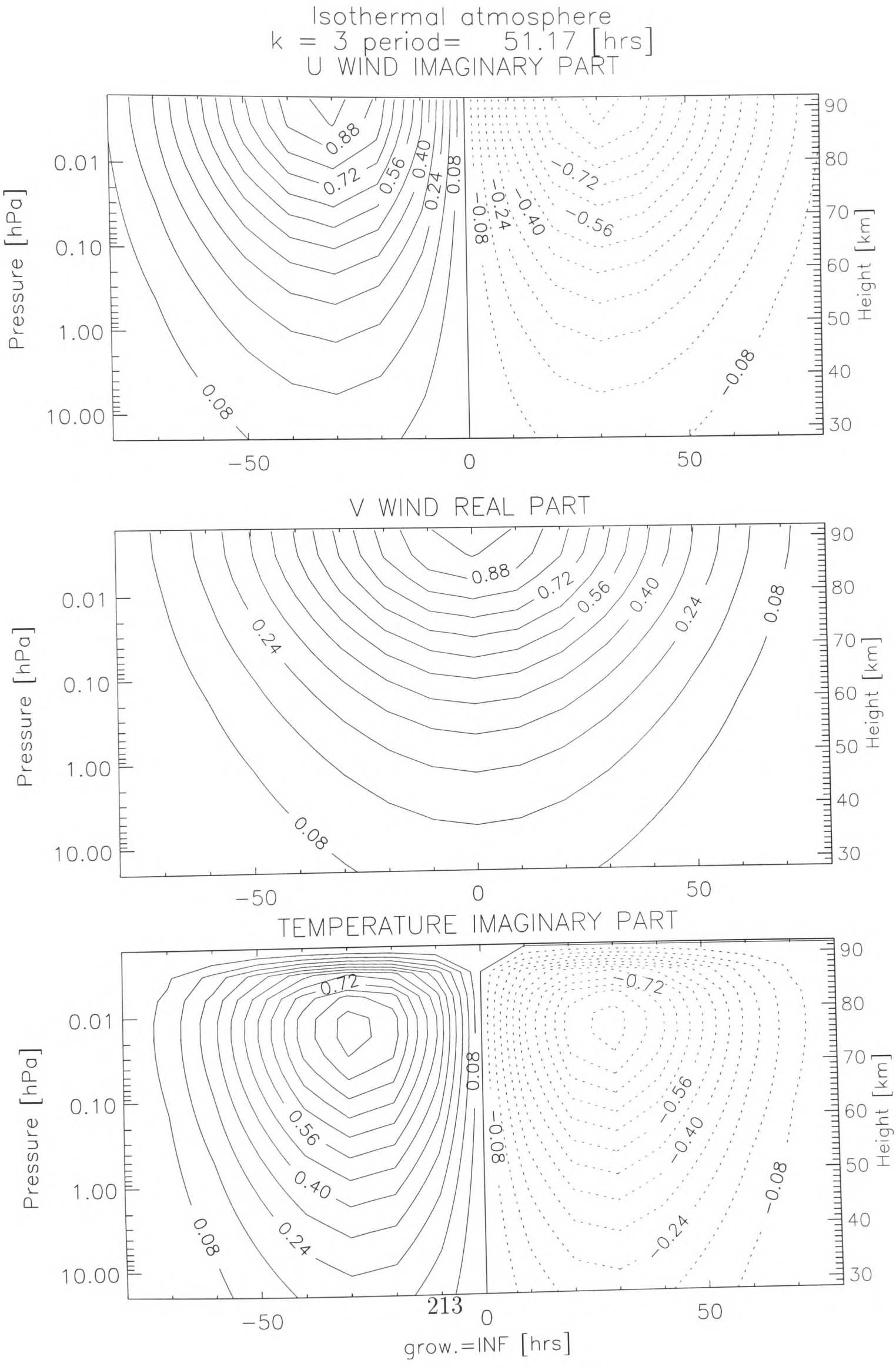


Figure A.5: Third Rossby-gravity mode (3,0).

Appendix B

List of symbols

Definitions of the startard symbols used in this thesis are given below:

a Mean radius of the Earth (about 6.371×10^6 m).

c phase speed of a wave, in $[\mathrm{m\,s^{-1}}]$.

c_p Specific heat capacity at constant pressure ($1.005 \times 10^3 \mathrm{J\,kg^{-1}\,K^{-1}}$, at 273 K).

c_v Specific heat capacity at constant volume ($7.17 \times 10^2 \mathrm{J\,kg^{-1}\,K^{-1}}$, at 273 K).

$\frac{D}{Dt}$ Material derivative in spherical coordinates,
$= \frac{\partial}{\partial t} + \frac{u}{a\cos\phi}\frac{\partial}{\partial \lambda} + \frac{v}{a}\frac{\partial}{\partial \phi} + w\frac{\partial}{\partial z}$.

f Coriolis parameter, $2\Omega \sin\phi$.

$\mathbf{F}$ Eliassen-Palm flux vector, units of $[\mathrm{kg\,s^{-2}}]$

$\nabla \cdot \mathbf{F}$ Eliassen-Palm flux divergence, in units of $\mathrm{kg\,m^{-1}s^{-1}day^{-1}}$

g Acceleration due to gravity ($9.81\,\mathrm{m\,s^{-2}}$)

H H=$\mathrm{RT_s/g}$, Scale height of the atmosphere, usually taken at 7 km.

J Net diabatic heating rate per unit mass / Photolysis rate

k Spherical zonal wavenumber

n Meridional index for Hough functions, indicates the number of zeros in the latitudinal direction for meridional wind.

N Buoyancy frequency, $[\mathrm{s^{-1}}]$.

p Pressure

p_s Pressure, usually taken as the Earth's surface pressure (1013 hPa).

P Ertel's potential vorticity

q Quasi-geostrophic potential vorticity

Q Net diabatic heating rate in units of potential temperature per unit time, $Q = (J/c_p)e^{\kappa z/H}$.

R Gas constant for dry air (287 $\mathrm{J\,kg^{-1}\,K^{-1}}$).

t Time

T Absolute temperature

u Zonal (eastward) wind velocity

u_g Geostrophic zonal wind

$\mathbf{U}$ Three-dimensional wind vector

v Meridional (northward) wind velocity

v_g Geostrophic meridional wind

$\bar{v}^*$ Transformed Eulerian mean meridional velocity

$\bar{w}^*$ Transformed Eulerian mean vertical velocity

x Distance in longitudinal direction

y Distance in latitudinal direction

z Log-pressure height, $z \equiv -H \log(p/p_s)$.

β Meridional gradient of coriolis parameter

θ Potential temperature

κ $\equiv R/c_p$, (0.286)

λ Longitude

ρ Density [$\mathrm{kg\,m^{-3}}$]

ρ_s Surface density (1.293 at STP[1] [$\mathrm{kg\,m^{-3}}$]

ρ_0 Basic density, $\rho_0 = \rho_s e^{-z/H}$ [$\mathrm{kg\,m^{-3}}$]

ϕ Latitude

Φ Geopotential

$\mathbf{\Omega}$ Earth's rotation vector, $\mathbf{\Omega}$=$\omega(0, \cos\phi, \sin\phi)$, its magnitude is 7.29 $\times 10^{-5}\,\mathrm{s^{-1}}$.

$\bar{X}$ Zonal mean of quantity X

X' $\equiv X - \bar{X}$

[1]Standard temperature and pressure (STP)= 1013hPa and 273 K.

Appendix C

Numerical solution

In this appendix the discretised, linear, primitive equations are shown. The equations are written in FORTRAN and are the basis of the instability code described in chapter 5. The subroutines to solve the resulting eigenvalue problem are given as well. Note that because k is used as the index for the levels, s is used for the zonal wavenumber. The discretised equations are as follows:

$$\begin{aligned} \mathrm{Du_{j,k}} &= -\frac{is}{a\cos\phi_j}\bar{u}_{j,k}u_{j,k} - \frac{\partial_p(\bar{u},J,K,j,k)}{\Delta p}w_{j,k} + 2\Omega\sin\phi_j v_{j,k} \\ &\quad -\frac{\partial_\phi(\bar{u},J,K,j,k)}{a\Delta\phi}v_{j,k} + \frac{\tan\phi_j}{a}\bar{u}_{j,k}v_{j,k} - \frac{is}{a\cos\phi_j}\Phi_{j,k}, \qquad \text{(C.1)} \\ \mathrm{Dv_{j,k}} &= -(2\Omega\sin\phi_j + \frac{2\tan\phi_j}{a})\bar{u}_{j,k}u_{j,k} - \frac{is}{a\cos\phi_j}\bar{u}_{j,k}v_{j,k} - \\ &\quad \frac{\partial_\phi(\Phi,J,K,j,k)}{a\Delta\phi}, \qquad \text{(C.2)} \\ \mathrm{DT_{j,k}} &= \frac{\kappa\bar{T}_{j,k}}{p_k}w_{j,k} - \frac{\partial_p(\bar{T},J,K,j,k)}{\Delta p}w_{j,k} - \frac{\partial_\phi(\bar{T},J,K,j,k)}{a\Delta\phi}v_{j,k} \\ &\quad -\frac{is}{a\cos\phi_j}\bar{u}_{j,k}T_{j,k}. \qquad \text{(C.3)} \end{aligned}$$

The geopotential is integrated in the following way:

$$\begin{aligned} \Phi_{j,1} &= \Phi_0 \quad \text{for} \quad \mathrm{k}=1, \qquad \text{(C.4)} \\ \Phi_{j,k} &= \Phi_{j,k-1} - \frac{R}{2}(T_{j,k}+T_{j,k-1})(\mathrm{logp_k} - \mathrm{logp_{k-1}}) \quad \text{for} \quad \mathrm{k}\neq 1. \qquad \text{(C.5)} \end{aligned}$$

where the geopotential at the bottom boundary Φo, is given by:

$$\Phi o = w_{j,1} R \frac{\bar{T}_{j,1}}{p_1}. \tag{C.6}$$

The vertical velocity is obtained by integrating the continuity equation downwards:

$$w_{j,K} = 0, \tag{C.7}$$

$$w_{j,k} = w_{j,k+1} - \frac{is\Delta k}{2a\cos\phi_j}(u_{j,k} + u_{j,k+1}) + \frac{\partial_\phi(vcos, J, K, j, k)}{\Delta\phi} + \frac{\partial_\phi(vcos, J, K, j, k+1)}{\Delta\phi}, \tag{C.8}$$

where

$$vcos_{j,k} = v_{j,k}\cos\phi_j. \tag{C.9}$$

The derivatives are calculated by calling the functions ∂_p and ∂_ϕ, these are the derivatives with respect to pressure and latitude respectively,

$$\partial_p = F_{j,k+1} - F_{j,k-1} \tag{C.10}$$

$$\partial_p = -3Fj, k + 4F_{j,k+1} - F_{j,k+2} \quad \text{for} \quad \text{k} = 1 \tag{C.11}$$

$$\partial_p = 3F_{j,k} - 4F_{j,k-1} + F_{j,k-2} \quad \text{for} \quad \text{k} = \text{K} \tag{C.12}$$

$$\partial_\phi = F_{j+1,k} \tag{C.13}$$

$$\partial_\phi = F_{j+1,k} - F_{j,k} \quad \text{for} \quad \text{j} = 1 \tag{C.14}$$

$$\partial_\phi = -F_{j-1,k} \quad \text{for} \quad \text{j} = \text{J} \tag{C.15}$$

Finally in equations C.2, C.3, C.3, C.8 and C.5 Δ is the following:

$$\Delta = L_{k+1} - L_{k-1} \tag{C.16}$$

$$\Delta = L_{k+2} - L_k \quad \text{for} \quad \text{k} = 1 \tag{C.17}$$

$$\Delta = L_k - L_{k-2} \quad \text{for} \quad \text{k} = \text{K}. \tag{C.18}$$

Once the matrix **M** is constructed by the process described in section 5.1 several NAG routines (Mark 18) are called to calculate the eigenvalues and eigenvectors.

- SUBROUTINE F01AVF

  This routine reduces the norm of a complex matrix by applying diagonal similarity transformations to the matrix. The subroutine balances the matrix in a norm different from the Euclidean norm. This is important because eigenvalue calculations usually produce results with errors proportional to the norm.

- SUBROUTINE F01AMF

  This routine transforms the balanced, complex unsymmetric matrix to a upper hessenberg form.

- SUBROUTINE F02ANF

  This routine uses the LR algorithm with shift of origin to calculate all the eigenvalues of the complex, upper hessenberg matrix.

- SUBROUTINE F02BLF

  This routine finds selected eigenvectors of the complex upper hessenberg matrix from prescribed eigenvalues using inverse iteration, i.e., the routine inverts the matrix.

- SUBROUTINE F01ANF

  This routine transforms the eigenvectors of the upper hessenberg matrix back to the eigenvectors of the balanced matrix.

- SUBROUTINE F01AWF

  This routine transforms the eigenvectors back to the eigenvectors of the original matrix **M**.

References

[1] Allen, D.R. *et al.*, 1997: The 4-Day Wave a Observed from the *Upper Atmosphere Research Satellite* Microwave Limb Sounder. J. Atmos. Sci., **54**, 420-434.

[2] Andrews, D.G. and McIntyre, M. E., 1976: Planetary waves in horizontal and vertical shear: the generalized Eliassen-Palm relation and the mean zonal acceleration. J. Atmos. Sci., **33**, 2031-2048.

[3] Andrews, D.G., 1987: On the interpretation of the Eliassen-Palm flux divergence. Q. J. R Meteorol. Soc., **113**, 323-338.

[4] Andrews, D.G. *et al.*, 1987: Middle Atmosphere Dynamics. Academic Press, 489pp.

[5] Betts, A.K. and Miller, M.J., 1993: The Betts-Miller scheme. Chapter in: The representation of cumulus convection in numerical models of the atmosphere. Eds. K.A. Emanuel and D.J. Raymond. American Meteorological Society.

[6] Charney, J. G., 1947: The dynamics of long waves in a baroclinic westerly current. J. Meteor., **4**, 135-163.

[7] Charney, J.G. and Drazin, P.G., 1961: Propagating of Planetary-Scale Disturbances from the Lower into the Upper Atmosphere. J. Geophys. Res., **66**, 83-109.

[8] Charney, J.G. and Stern, M. E., 1962: On the Stability of Internal baroclinic Jets in a Rotating Atmosphere. J. Atmos. Sci., **19**, 159-172.

[9] Clark, R., 1975: Meteor Wind Measurements at Durham, New Hampshire (42°N, 71°W). J. Atmos. Sci., **32**,1689-1693.

[10] Coy, L., 1979: A Possible 2-day Wave near the Tropical Stratopause. J. Atmos. Sci. **36**, 1615-1618.

[11] Craig *et al.*, 1980: The quasi 2-day wave in the Southern Hemisphere Mesosphere. Nature **28**, 319-320.

[12] Craig, R.L. and Elford, W.G., 1981: Observations of the quasi 2-day wave near 90 km altitude at Adelaine (35°S). J. Atmos. Terr. Phys., **43**, 1051-11056.

[13] Dikii, L. and Golistyn, G., 1968: Tellus, **20**, 314-317.

[14] Drazin, P.G. *et al.*, 1982: On Rossby waves modified by Basic shear, and barotropic instability. J. Fluid Mech., **124**, 439-456.

[15] Drysdale, E.F., 1998: Modelling of Equatorial Wave Motions in the Middle Atmosphere. DPhil thesis, University of Oxford.

[16] Dunkerton, T.J., 1982: On the inertial Stability of the Equatorial Middle Atmosphere. J. Atmos. Sci., **38**, 2354-2364.

[17] Eady, E. T., 1949: Long waves and cyclone waves. Tellus, **1** 33-53.

[18] Eliasen, E. and Machenhauer, B., 1965: A study of the atmospheric planetary flow pattern represented by spherical harmonics. Tellus, **17**, 220-238

[19] Eliassen, A. and Palm, E., 1961: On the transfer of energy in stationary mountain waves. Geofys. Pub., **22**, 1-23.

[20] Fisher, M., 1985: The Met. Office Stratosphere-Mesosphere Model. Internal report Met. Office.

[21] Fraser, G.J. *et al.*, 1993: Eastward-moving 2-4 day waves in the winter antarctic mesosphere. Geophys. Res. Lett., **20**, 1547-1550.

[22] Fritts *et al.*, 1999: Two-day wave structure and mean flow interactions observed by radar and High Resolution Doppler Imager. J. Geophys. Res., **104**, 3953-3969.

[23] Glass *et al.*, 1975: Comparison and interpretation of the results of simultaneous wind measurements in the lower thermosphere at Garchy (France) and Obninsk (U.S.S.R.) by meteor radar technique. J. Atmos. Terr. Phys., **37**, 1077-1087.

[24] Hagan *et al.*, 1993: Numerical Investigation of the Propagation of the Quasi-Two-Day Wave Into the Lower Thermosphere. J. Geophys. Res., **98**, 23,193-23,205.

[25] Harris, T.J. and Vincent, R.A., 1993: The Quasi-Two-Day Wave observed in the Equatorial Middle Atmosphere. J. Geophys. Res., **98**, 10,481-10,490.

[26] Hartmann, D., 1983: Barotropic Instability of the Polar Night Jet Stream. J. Atmos. Sci., **40**, 817-835.

[27] Held, I.M., 1985: Pseudomomentum and the Orthogonality of Modes in Shear Flows. J. Atmos. Sci., **42**, 2280-2288.

[28] Hirooka, T., 1999: Normal Mode Rossby Waves as Revealed by UARS/ISAMS Observations. Submitted to J. Atmos. Sci.

[29] Hirota, I., *et al.*, 1983: Upper stratospheric circulation in the two hemispheres observed by satellites. Q. J. R Meteorol. Soc., **109**, 443-454.

[30] Hirota, I. and Hirooka, T., 1984: Normal Mode Rossby Waves Observed in the Upper Stratosphere. Part I: First Symmetric Modes of Zonal Wavenumbers 1 and 2. J. Atmos. Sci., **41**, 1253-1267.

[31] Hirota, I. and Hirooka, T., 1985: Normal Mode Rossby Waves Observed in the Upper Stratosphere. Part II: Second Antisymmetric and Symmetric Modes of Zonal Wavenumbers 1 and 2. J. Atmos. Sci., **42**, 536-548.

[32] Hoskins, B. J. *et al.*, 1985: On the use and significance of isentropic potential vorticity maps. Q. J. R Meteorol. Soc., **111**, 877-946.

[33] Hunt, B.G., 1981: The 2-day wave in the middle atmosphere as simulated in a general circulation model extending from the surface to 100 km. J. Atmos. Terr. Phys., **53**, 1143-1154.

[34] Iwi, A.M., 1998: Tropical Dynamics and transport associated with stratospheric warmings. DPhil thesis, University of Oxford.

[35] Kubota, S. and Iida, M., 1954: Statistical characteristics of the atmospheric disturbances. Pap. Meteorol. Geophys., **5**, 22-34.

[36] Lahoz, W.A. *et al.*, 1996: Vortex dynamics and the evolution of water vapor in the stratosphere of the southern hemisphere. Q. J. R Meteorol. Soc., **122**, 423-450.

[37] Laplace, 1799: Mécanique Céleste, Paris.

[38] Lawrence, B.N. *et al.*, 1995: The 4-day wave in the Antarctic mesosphere. J. Geophys. Res., **100**, 18,899-18,908.

[39] Lawrence, B.N., 1997: The effect of parameterized gravity wave drag on simulations of the middle atmosphere during winter 1991/1992-general evolution. In: Gravity Wave Processes. Their Parameterization in Global Climate Models. NATO ASI Series. Springer-Verlag. Edited by K. Hamilton.

[40] Lieberman, R., 1999: Eliassen-Palm Fluxes of the 2-Day Wave. J. Atmos. Sci., **56**, 2846-2861.

[41] Longuet-Higgins, M., 1968: The eigenfunctions of Laplace's tidal equation over a sphere. Phil. Trans. R. Soc. Lond., Ser A, **262**, 511-607.

[42] Madden, R. A., 1978: Further evidence of traveling planetary waves. J. Atmos. Sci., **35**, 1606-1618.

[43] Madden, R.A., 1979: Observations of Large-Scale Traveling Rossby Waves. Rev. Geophys. Space Phys., **17**, 1935-1949.

[44] Manney, G.L. *et al.*, 1988: Barotropic Instability of Realistic Stratospheric Jets. J. Atmos. Sci., **45**, 2545-2555.

[45] Manney, G.L., 1991: The Stratospheric 4-day Wave in NMC Data. J. Atmos. Sci., **48**, 1798-1811.

[46] Manney, G.L. and Randel, W.J., 1993: Instability at the Winter Stratopause: A Mechanism for the 4-Day Wave. J. Atmos. Sci., **50**, 3928-3938.

[47] Manney, G.L. *et al.*, 1993: Instability at the Winter Stratopause: A Mechanism for the 4-Day Wave. J. Atmos. Sci., **50**, 3928-3938.

[48] Meek *et al.*, 1996: Global study of northern hemisphere quasi 2-day wave events in recent summers near 90 km altitude. J. Atmos. Terr. Phys., **58**, 1401-1511.

[49] Mitchell, N.J., 1991: PhD thesis, University of Sheffield.

[50] Mitchell, N.J., 1999: The 16-day planetary wave in the mesosphere and lower thermosphere. Unpublished manuscript.

[51] Morcette, J.-J., 1990: Impact of changes to the radiation transfer parameterizations plus cloud optical properties in th ECMWF model. Mon. Weather Rev., **118**, 847-873.

[52] Muller, H.G., 1972: Long-period meteor wind oscillations. Phil. Trans. R. Soc. Lond. A., **271**, 585-598.

[53] Muller, H.G. and Kinkley, S.P., 1974: On the scale sizes of wind systems in the meteor zone. J. Atmos. Terr. Phys., **36**, 1851-1861.

[54] Muller, H.G. and Nelson, N., 1978: A travelling quasi 2-day wave in the meteor region. J. Atmos. Terr. Phys., **40**, 761-766.

[55] Muller, H.G. *et al.*, 1995: A study of meteor winds from two locations in the British Isles. J. Atmos. and Terr. Phys., **57**, 979-993.

[56] Rodgers, C.D., 1976: Evidence for the 5-day wave in the upper stratosphere. J. Atmos. Sci., **33**, 710-711.

[57] Norton, W.A. and Thuburn, J., 1996: The Two-day wave in a middle atmosphere GCM. Geophys. Res. Lett., **23**, 2113-2116.

[58] Norton, W.A. and Thuburn, J., 1997: The mesosphere in the extended UGAMP GCM. In Gravity Wave Processes and Their Parameterization in Global Climate Models, vol 50, edited by K. Hamilton, pp. 383-401, Springer-Verlag, New York.

[59] Norton, W.A. and Thuburn, J., 1999: Sensitivity of mesospheric mean flow, planetary waves, and tides to strength of gravity wave drag. Submitted to: J. Geophys. Res.

[60] Orsolini, Y. and Simon, P., 1995: Idealized Life-Cycles of Planetary-Scale Barotropic Waves in the Middle Atmosphere. J. Atmos. Sci. **52**, 3817-3835.

[61] Palmer, T. N., *et al.*, 1986: Alleviation of a systematic westerly bias in general circulation and numerical weather prediction models through an orographic gravity wave drag parameterization. Q. J. Roy. Meteorol. Soc., **112**, 1001-1039.

[62] Pedlosky, J., 1986: Geophysical Fluid Dynamics. Springer-Verlag, second edition.

[63] Pfister, L., 1985: Baroclinic Instability of Easterly Jets with Applications to the Summer Mesosphere. J. Atmos. Sci., **42**, 313-330.

[64] Plum, A., 1983: Baroclinic instability of the Summer Mesosphere: A Mechanism for the Quasi-Two-Day Wave? J. Atmos. Sci., **40**, 262-220.

[65] Prata, A.J., 1984: The 4-Day Wave. J. Atmos. Sci., **41**, 150-155.

[66] Randel, W.J. and Lait, L.R., 1991: Dynamics of the 4-Day Wave in the Southern Hemisphere Polar Stratosphere. J. Atmos. Sci., **48**, 2496-2508.

[67] Randel, W.J., 1994: Observations of the 2-Day Wave in NMC Stratospheric Analyses. J. Atmos. Sci., **51**, 306-313.

[68] Rodgers, C.D. and Prata, A.J., 1981: Evidence for a Traveling Two-Day Wave in the Middle Atmosphere. J. Geophys. Res., **86**, 9661-9664.

[69] Rossby, C.-G., *et al.*, 1939: Relation between variations in the intensity of the zonal circulation of the atmosphere and the displacements of the semipermanent centers of action. J. Mar. Res., **2**, 38-55.

[70] Salby, M.L. and Roper, R.G., 1980: Long-period Oscillations in the Meteor Region. J. Atmos. Sci., **37**, 237-244.

[71] Salby, M.L., 1981(a): Rossby Normal modes in Nonuniform Background Configurations. Part I: Simple Fields. J. Atmos. Sci., **38**, 1803-1826.

[72] Salby, M.L., 1981(b): Rossby Normal modes in Nonuniform Background Configurations. Part I: Equinox and Solstice Conditions. J. Atmos. Sci., **38**, 1827-1840.

[73] Salby, M.L., 1981(c): The 2-Day Wave in the Middle Atmosphere: Observations and Theory. J. Atmos. Sci., **86**, 9654-9660.

[74] Shine, K.P., 1987: The middle atmosphere in the absence of dynamical heat fluxes. Q. J. Roy. Meteorol. Soc., **113**, 603-633.

[75] Shine, K.P. and Richaby, J.A., 1989: Solar radiative heating due to absortion by ozone. In: Ozone in the Atmosphere. Eds R.D.Bojkov and P. Fabian, Deepak Publishing Co., Hampton Virginia.

[76] Salby, M.L., 1984: Survey of Planetary-Scale Traveling Waves: The State of Theory and Observations. Rev. Geophys. Space Phys., **22**, 209-236.

[77] Stanford, J.L., 1997: The 4-day wave. Department of Physics and Astronomy, Iowa State University.

[78] Stenning *et al.*, 1976: Winds and Wave Motions to 110 km at Midlatitudes. VI. Tidal, Gravity and Planetary waves. J. Atmos. Sci., **35**, 2194-2203.

[79] Swinbank, R. and O'Neill, A., 1994: A Stratospheric-Tropospheric Data Assimilation System. Mon Wea. Rev., **122**, 686-702.

[80] Thorncroft, C.D. *et al.*, 1993: Two paradigms of baroclinic-wave life-cycle behaviour. Q. J. R Meteorol. Soc., **119**, 17-55.

[81] Thuburn, J. and McIntyre, M.E., 1997: Numerical advection schemes, cross-isentropic random walks, and correlations between chemical species. J. Geophys. Res., **102**, 6775-6797.

[82] Tiedtke, M. *et al.*, 1988: Tropical forecasting at ECMWF: the influence of physical parameterization on the mean structure of forecast and analyses. Q. J. R Meteorol. Soc., **114**, 639-664.

[83] Tsutsumi *et al.*, 1996: Wind Velocity and temperature fluctuations due to a 2-day wave observed with radio meteor echoes. J. Geophys. Res., **101**, 9425-9432.

[84] Venne, D.E. and Stanford, J.L., 1979: Observation of a 4-Day Temperature Wave in the Polar Winter Stratosphere. J. Atmos. Sci., **36**, 2016-2019.

[85] Venne, D.E. and Stanford, J.L., 1982: An Observational Study of High-Latitude Stratospheric Planetary Waves in the Winter. J. Atmos. Sci. **39**, 1026-1036.

[86] Waltershield, R.L. and Vincent, R.A., 1996: Tidal generation of the phase-locked 2-day wave in the southern hemisphere summer by wave-wave interactions. J. Geophys. Res., **101**, 26,567-26,576.

[87] Wu *et al.*, 1993: Observations of the quasi 2-day wave from the high resolution doppler imager on UARS. Geophys. Res. Lett., **20**, 2853-2856.